THE UNIVERSITY OF
WARWICK

Library Declaration and Deposit Agreement

1. STUDENT DETAILS

Please complete the following:

Full name: .....

University ID number: .....

2. THESIS DEPOSIT

2.1 I understand that under my registration at the University, I am required to deposit my thesis with the University in BOTH hard copy and in digital format. The digital version should normally be saved as a single pdf file.

2.2 The hard copy will be housed in the University Library. The digital version will be deposited in the University's Institutional Repository (WRAP). Unless otherwise indicated (see 2.3 below) this will be made openly accessible on the Internet and will be supplied to the British Library to be made available online via its Electronic Theses Online Service (EThOS) service.
[At present, theses submitted for a Master's degree by Research (MA, MSc, LLM, MS or MMedSci) are not being deposited in WRAP and not being made available via EthOS. This may change in future.]

2.3 In exceptional circumstances, the Chair of the Board of Graduate Studies may grant permission for an embargo to be placed on public access to the hard copy thesis for a limited period. It is also possible to apply separately for an embargo on the digital version. (Further information is available in the *Guide to Examinations for Higher Degrees by Research*.)

2.4 *If you are depositing a thesis for a Master's degree by Research, please complete section (a) below. For all other research degrees, please complete both sections (a) and (b) below:*

(a) Hard Copy

I hereby deposit a hard copy of my thesis in the University Library to be made publicly available to readers (please delete as appropriate) EITHER immediately OR after an embargo period of ..... months/years as agreed by the Chair of the Board of Graduate Studies.

I agree that my thesis may be photocopied. YES / NO (*Please delete as appropriate*)

(b) Digital Copy

I hereby deposit a digital copy of my thesis to be held in WRAP and made available via EThOS.

Please choose one of the following options:

EITHER My thesis can be made publicly available online. YES / NO (*Please delete as appropriate*)

OR My thesis can be made publicly available only after.....[date] (Please give date)
YES / NO (*Please delete as appropriate*)

OR My full thesis cannot be made publicly available online but I am submitting a separately identified additional, abridged version that can be made available online.
YES / NO (*Please delete as appropriate*)

OR My thesis cannot be made publicly available online. YES / NO (*Please delete as appropriate*)

3. GRANTING OF NON-EXCLUSIVE RIGHTS

Whether I deposit my Work personally or through an assistant or other agent, I agree to the following:

Rights granted to the University of Warwick and the British Library and the user of the thesis through this agreement are non-exclusive. I retain all rights in the thesis in its present version or future versions. I agree that the institutional repository administrators and the British Library or their agents may, without changing content, digitise and migrate the thesis to any medium or format for the purpose of future preservation and accessibility.

4. DECLARATIONS

(a) I DECLARE THAT:

- I am the author and owner of the copyright in the thesis and/or I have the authority of the authors and owners of the copyright in the thesis to make this agreement. Reproduction of any part of this thesis for teaching or in academic or other forms of publication is subject to the normal limitations on the use of copyrighted materials and to the proper and full acknowledgement of its source.

- The digital version of the thesis I am supplying is the same version as the final, hard-bound copy submitted in completion of my degree, once any minor corrections have been completed.

- I have exercised reasonable care to ensure that the thesis is original, and does not to the best of my knowledge break any UK law or other Intellectual Property Right, or contain any confidential material.

- I understand that, through the medium of the Internet, files will be available to automated agents, and may be searched and copied by, for example, text mining and plagiarism detection software.

(b) IF I HAVE AGREED (in Section 2 above) TO MAKE MY THESIS PUBLICLY AVAILABLE DIGITALLY, I ALSO DECLARE THAT:

- I grant the University of Warwick and the British Library a licence to make available on the Internet the thesis in digitised format through the Institutional Repository and through the British Library via the EThOS service.

- If my thesis does include any substantial subsidiary material owned by third-party copyright holders, I have sought and obtained permission to include it in any version of my thesis available in digital format and that this permission encompasses the rights that I have granted to the University of Warwick and to the British Library.

5. LEGAL INFRINGEMENTS

I understand that neither the University of Warwick nor the British Library have any obligation to take legal action on behalf of myself, or other rights holders, in the event of infringement of intellectual property rights, breach of contract or of any other right, in the thesis.

Please sign this agreement and return it to the Graduate School Office when you submit your thesis.

Student's signature: ..... Date: .....

Folding and Fibril Formation of Prions

Leszek Andrzej Gierusz

A thesis submitted in partial fulfilment of the requirements for the degree of

Doctor of Philosophy in Biochemistry

University of Warwick

School of Life Sciences

September 2012

Contents

Figures and Tables

Chapter 1: Introduction

Chapter 2: Expression and purification of mouse prion protein (MoPrP) and Syrian hamster prion protein (SHaPrP)

Chapter 3: Investigation of PrP folding kinetics by pressure-jump

Chapter 4: Fibrilisation and oligomerisation studies of Elk PrP

Acknowledgements

I would like to thank my supervisor Dr Teresa Pinheiro, for her invaluable help and support over the past four years and Dr Narinder Sanghera for overall training, day to day help in the lab and many useful discussions concerning my work. Furthermore, I thank Dr Philip Robinson for expression and purification training during the first year of my PhD.

I would also like to thank and Dr Ted King at TgK Scientific, for invaluable help on the continuous flow side of the project and general advice on kinetics and instrumentation. For the pressure-jump work I am very grateful to Professor Mike Geeves and Dr David Pearson in the Department of Biosciences at the University of Kent in Canterbury who allowed me access to their instrument and instructed me on data analysis.
Thanks to Dr Andy Gill for advice on fibrilisation and Dr Ian Portman for electron microscopy imaging.

I would also like to thank the Biological Mass Spectrometry Facility in School of Life Sciences, University of Warwick, for mass spectrometry analysis.

Thanks to all the members of the structural biology lab for a friendly and lively atmosphere in the laboratory, good humour, useful advice, and discussions on not-so-work-related topics.

Thanks to my friends at Warwick and further away, particularly John, Mike the local patriot, Dean, the other Mike, Cat, Vicky, Steve and Nathan.

Thanks to my family for support and motivation, especially my wife Maria for her love, understanding and patience, we both know I needed them.

Thanks to the EPSRC for funding.

Summary

Prions diseases are a group of fatal neurodegenerative disorders called the transmissible spongiform encephalopathies (TSEs), which include bovine spongiform encephalopathy in cattle, scrapie in sheep and Creutzfeldt-Jakob disease (CJD) in humans. TSEs are associated with the conversion of normal cellular form of the prion protein (PrP^{C}) to an altered pathological form (PrP^{Sc}). An important phenomenon known as the species barrier affects prion transmission, resulting in longer incubation time and lower incidence of disease upon transfer between species. Another feature of prion diseases is disease-modulating polymorphisms in PrP sequence which can alter individual's susceptibility to infection.

This thesis investigates two properties of PrP that may elucidate the mechanisms underlying both species barrier and disease resistance; (i) effect of disease-modulating mutations on folding kinetics of PrP and (ii) impact of disease-modulating mutations on formation of PrP fibrils.

Equilibrium and kinetic folding studies demonstrate that the folding pathway of PrP is affected by mutation Q167R which confers disease resistance, and mutations S170N, N174T and S170N/N174T characteristic for Chronic Wasting Disease in cervids, which are known to increase disease susceptibility.

The destabilising effect of Q167R mutation previously observed via equilibrium folding studies was confirmed through direct kinetic observations. Subsequent fibrilisation experiments suggested a possible link between the stability of mouse prion protein and its propensity to form fibrils, elucidating a potential mechanism of increased disease resistance conferred by Q167R mutation.

Equilibrium folding studies of S170N, N174T and S170N/N174T revealed a surprising correlation between the structural effects of these mutations and fibrilisation propensity.

Based on these findings, a disease resistance mechanism centred on decreased formation of neurotoxic particles in the organism as well as diminished ability of infectious oligomers from both inside and outside to propagate oligomerisation of PrP has been proposed.

Abbreviations

λ max	emission maximum
CCD	charge-coupled device
CD	circular dichroism
CF	continuous-flow
CJD	Creutzfeldt - Jakob disease
CWD	Chronic Wasting disease
$[D]_{50\,\%}$	midpoint of solvent denaturant
DTT	dithiothreitol
EDTA	ethylene diamine tetra-acetic acid
ER	endoplasmic reticulum
ESI-MS	electrospray ionisation mass spectrometry
F197W	mouse prion protein, residues 91-230, with a single tryptophan residue at position 197
F198W	Syrian hamster prion protein, residues 90-231, with a single tryptophan residue at position 198
GdnHCl	guanidine hydrochloride
GSH	reduced glutathione
GSSG	oxidised glutathione
HPLC	high performance liquid chromatography
huPrP	human PrP
IB	inclusion body
LB	liquid broth
MoPrP	mouse prion protein, residues 91-230
MES	2-(N-morpholino)ethanesulfonic acid
MOPS	3-(N-morpholino)propanesulfonic acid
N174T	mouse prion protein, residues 23-230, with N174T mutation
NATA	N-acetyl-L-tryptophanamide
NBS	N-bromosuccinimide
NMR	nuclear magnetic resonance
PDI	protein disulfide isomerase
PrP	prion protein

PrP^{C}	prion protein cellular isoform
PrP^{Sc}	prion protein scrapie isoform
Q167R	mouse prion protein, residues 91-230, with a single tryptophan residue at position 197 and Q167R mutation
RP HPLC	reversed-phase high performance liquid chromatography
S170N	mouse prion protein, residues 23-230, with S170N mutation
S170N/N174T	mouse prion protein, residues 23-230, with S170N and N174T mutations
SDS-PAGE	sodium dodecyl sulfate polyacrylamide gel electrophoresis
SEC	size exclusion chromatography
SF	stopped-flow
SHaWT	Syrian hamster prion protein, residues 90-231, with a single tryptophan residue at position 198
TFA	trifluoroacetic acid
ThT	thioflavin-T
TrisHCl	tris(hydroxymethyl)aminomethane hydrochloride
TSE	transmissible spongiform encephalopathy
UV	ultra violet
vCJD	new variant Creutzfeldt-Jakob disease

The standard single- and three-letter abbreviations of the amino acids are used

Chapter 1: Introduction

1.1 Prions

1.1.1 Transmissible spongiform encephelopathies

Prion diseases, also known as transmissible spongiform encephalopathies (TSEs), are a group of fatal neurodegenerative disorders affecting numerous species, including cattle (bovine spongiform encephalopathy, BSE), sheep (scrapie), cervids (chronic wasting disease, CWD), humans (Creutzfeldt-Jakob disease, Gerstmann-Straussler-Scheinker disease, and fatal familial insomnia), exotic ungulates (exotic ungulates encephalopathy) and cats (feline spongiform encephalopathy, FSE).
All of the transmissible spongiform encephalopathies are characterised by spongiform degradation, neuronal loss, brain vacuolation, astrogliosis and formation of large amyloid plaques composed of the prion protein in the brain (Collinge, 2005; Unterberger *et al.*, 2005).

1.1.1.1 Scrapie – first identified prion disease

First indications of recognition of scrapie as an infectious disease can be traced as far back as early 18th century. In 1772, scrapie was reported to be known for approximately 40 years in England, indicating that the earliest mentions of the disease originated around 1730. By 1750, a clear description of the disease was available in literature, presenting characteristics such as symptoms as well as possibility of horizontal transmission (Schneider *et al.* 2008).
Despite such early recognition of scrapie, it was not until 1936 that conclusive experimental evidence of natural transmission proved the infectious nature of the disease, supported by an accidental iatrogenic transfer through vaccination for looping-ill (Schneider *et al.* 2008). By 1960s, it was determined that scrapie can be successfully transferred to mice, which were recognised as a potential experimental model for

studies of disease transmission and progression (Chandler 1961). It was not until 1982 that famous experiments of Stanley Pruisner finally allowed scrapie to be categorised as prion disease.

1.1.1.2 Creutzfeldt-Jakob disease and Kuru

The earliest description of the human form of prion disease originates from 1920's when two German neuropathologists discovered an unknown neurodegenerative disorder. In 1957 the fatal neurological disease Kuru was discovered amongst the stone-age Fore people in New Guinea (Gajdusek and Ziggas, 1957). Studies of brain samples from individuals who had died of Kuru provided a link between pathogenesis of scrapie and CJD which were until then considered unrelated. This similarity was first described by Hadlow, who proposed that both diseases could be caused by the same agent, based on their pathology and epidemiology.

Subsequent transmission experiments demonstrated that both CJD and Kuru can be transferred to chimpanzees through intracerebral inoculation of infected brain material (Gajdusek *et al.*, 1966). Moreover, amyloid plaques resembling those found in brains of victims of Kuru were also found in CJD infected brains, providing further connection between the two conditions (Chou and Martin 1971).

The discovery that CJD, Kuru and scrapie all share common pathogenic traits such as degeneration of neurones, presence of amyloid plaques in the brain, lack of an inflammatory response and transmissibility to primates led to their common classification as transmissible spongiform encephalopathies (Adams, Beck *et al*. 1974). Chronic wasting disease affecting cervids and mink encephalopathy were later added to the group (Williams and Young 1980).

1.1.1.3 Bovine spongiform encephalopathy

Bovine spongiform encephalopathy, or “mad cow disease” is best known from the sudden outbreak in early 1990s. The disease itself, however, emerged as a new cattle disease in the United Kingdom almost a decade earlier, in the 1980s.

The symptoms of the disease resembled those of scrapie, which led to investigation of pathology and transmissibility. Scrapie-like fibrils were found in the brains of infected cows, which together with confirmed transmissibility to other laboratory animals allowed the disease to be grouped together with CJD and scrapie as transmissible spongiform encephalopathies (Hope *et al.* 1988; Fraser *et al.* 1988). Following the classification, a number of cases of BSE started to be monitored. While less than 2000 cases were observed in 1988, their number increased sharply in the following years, untill 37,011 cases of BSE were confirmed in UK in 1993, which is generally considered a peak of BSE epidemic. High economic impact of the disease including worldwide ban on British beef export introduced by European Union resulted in increased interest in BSE epidemics and transmission. While the exact origins of the disease are unknown, feeding cows with BSE-contaminated cattle meat and bone meal is a widely accepted cause (Weissmann and Aguzzi 1997). Introducing a ban on ruminant offal usage as a protein supplement for cattle allowed for curtailing the epidemic, leading to a gradual decline in cases since 1993 (Figure 1.1) (figures from the DEFRA website, www.defra.gov.uk).

1.1.1.4 Variant Creutzfeldt-Jakob disease (vCJD)

In 1996, the first case of new variant Creutzfeldt-Jakob disease (vCJD) was first reported in the UK (Will *et al*., 1996) as a result of a widespread monitoring action initiated by the fear that individuals who consumed contaminated beef during the outbreak of BSE could contract the human form of prion disease. The disease exhibited novel neuropathological features that distinguished it from sporadic CJD, as well as a much lower age of onset compared to its classical, sporadic form. Although origin of the disease was unknown at the time, the fact that all known cases were reported in the UK suggested that it could be linked to BSE. Transmission experiments provided conclusive evidence for the origin of vCJD demonstrating that the BSE could be transferred from cows to macaques and that upon transmission it induced similar pathological changes in the brain (Lasmezas *et al.* 1996).

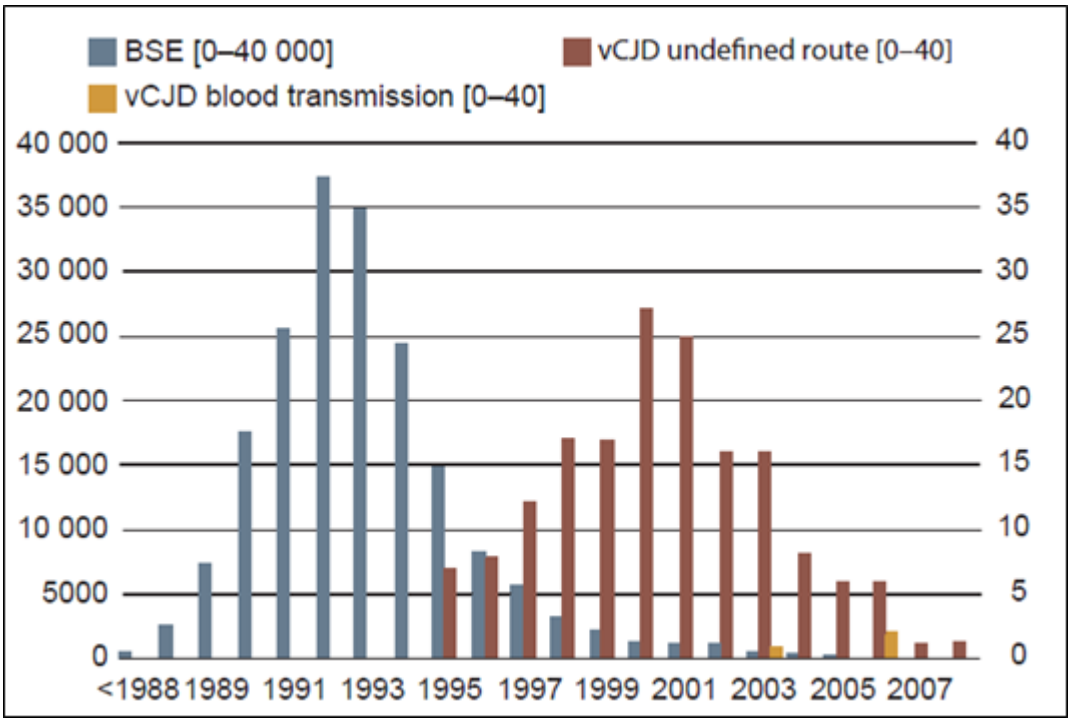

Figure 1.1 Cases of BSE, and vCJD in the UK from 1988 to 2007. The epizootic of bovine spongiform encephalopathy is represented by blue bars, the epidemic of variant Creutzfeldt-Jakobs disease in humans is shown by brown bars and three cases of transmission of vCJD between humans by blood transfusion are indicated with yellow bars.

Figure adapted from (Norrby, 2011).

1.1.1.5 Chronic wasting disease

Chronic wasting disease (CWD) is a prion disease of free-ranging wildlife, affecting a number of cervid species such as deer, elk and moose. It is the only prion disease identified so far which affects wild animals, which coupled with its high transmission rate and the fact that the exact prevalence remains currently unknown is of major concern in terms of epidemiology.

CWD was first reported in 1967 in a US research facility, but it was more than a decade later when pathologists recognized the brain lesions characteristic for a transmissible spongiform encephalopathy. The disease was subsequently demonstrated as a prion disease by neuronal changes, accumulation of aggregated prion protein (Spraker *et al*., 2002) as well as prion infectivity in the brain (Browning *et al*., 2004).

While originally thought to be limited to a small area in central United States, it proved to be spreading quickly. Only in the last decade it was identified in several more states of USA, as well as in southern Canada and even in South Korea, raising possibility of a widespread occurrence akin to that of bovine spongiform encephalopathy (BSE).

Since CWD affects wild animals, controlling its spread has proved to be particularly difficult. Moreover, it is likely that disease-associated prions are progressively accumulating in the environment due to the fact that PrP^{Sc} binds to soil and can retain its infectivity for a long period of time (Miller and Williams, 2004; Sigurdson and Aguzzi, 2007).

Since millions of North Americans hunt deer and elk, it is very likely that a large number of humans have been exposed to CWD-infected meat, either by contact or consumption (Sigurdson, 2008). While the possibility of transmission of CWD to other species remains unknown, only a handful of occurrences in human population could result in a new disease, much like transmission of bovine prions to humans resulted in an emergence of a variant of Creutzfeld-Jakobs disease. No clinical evidence linking humans exposed to CWD and patients suffering from CJD has been found, however, the autopsies on suspect human TSE cases were not performed until recently, hampering the diagnosis of new TSE strains (Sigurdson, 2008).

In transmission experiments, inoculation of squirrel monkeys with CWD prions induced the disease, yet transgenic mice expressing human PrP remained unaffected, indicating that the species barrier effect between humans and cervids is stronger than between cattle and humans (Kong *et al*., 2005; Sandberg *et al.*, 2010).

1.1.1.6 Inherited prion disease

Familial diseases such as Gerstmann-Sträussler syndrome (GSS) or familial CJD account for approximately 10-15 % of human TSE cases. Mutations in *PRNP* gene encoding prion protein which result in amino acid substitutions or additional insertions of the octapeptide repeat in unstructured N-terminus of PrP have been linked with the familial form prion disease.

First such mutation identified was a proline to leucine substitution at codon 102 (Hsiao *et al.* 1989) linked to GSS. Subsequently it was found that an additional range of amino substitutions, including a stop mutation at position 145 resulting in a truncated form of PrP could cause the disease (Kitamoto *et al.* 1993, Brown 2002).

Familial CJD-inducing mutations were first tracked to a point mutation resulting in substitution of Glu at position 200 for Lys (Goldfarb *et al.* 1990, Gabizon *et al.* 1993) and to date additional disease-associated mutations resulting in amino acid substitutions have been identified (Brown 2002).

While the link between PrP mutations and familial prion diseases provides strong support for the protein-only model, the mechanism by which these mutations facilitate the pathogenic process remains unclear. It has been postulated that these mutations may facilitate the pathogenic process by reducing the stability of the prion protein (PrP).

Interestingly, introduction of several point mutations such as P102L corresponding to Gerstmann-Straussler-Scheinker syndrome, E200K linked with Creutzfeld-Jakob disease and M129/D178N inducing fatal familial insomnia into the recombinant variants of human PrP(90–231) resulted in virtually no alterations in neither secondary structure nor thermodynamic stability. While E200K substitution induced a very small destabilization of the protein, it was deemed extremely unlikely that such a slight destabilizing effect alone could account for the pathogenicity associated with the mutation. These experiments, together with the predictive analysis of other familial mutations, indicate that the pathogenic mutations do not exert a uniform effect on the thermodynamic stability of the human prion protein, and consequently, not all hereditary forms of the disease may be rationalized through a common mechanism based on the mutation-induced decrease in global stability of PrP^{C}.

Especially intriguing in this context are GSS-associated mutations at residues 102, 105, and 117 which lie within the unstructured region of PrP, as their effect cannot be rationalized by a model based on an increase in the population of partially folded intermediates, as proposed for mutations within the C-terminal domain (14).
Another proposed pathogenic mechanism associated with these mutations postulates an increased amyloidogenic propensity of the unstructured N-terminal region (14) conferred by P102L and P105L mutations which replace a_β-sheet incompatible Pro residue as well as A117V and other mutations which introduce a branched hydrophobic side chains which are believed to increase the capability of amyloid formation (33–35). However, as demonstrated by experimental evidence (paper reference) the kinetics of amyloid fibril formation of several GSS-linked mutants are very similar to those of wild-type protein. Moreover, fibrils formed by GSS variants of prion protein are indistinguishable in conformation and seeding properties, indicating that these mutations do not affect the amyloidogenic properties of PrP.
Consequently, other factors, such as alterations in PrPC interactions with a complex cellular environment (36–38) or metabolic effects related to PrP trafficking (39–41) should be considered to explain how these familial mutations facilitate PrP conversion *in vivo*.

1.1.2 Chronology of prion discovery

Since the very first demonstration of transmissibility of scrapie a lot of interest in the disease has been generated due to the unique properties of the elusive infectious agent. The first attempts to investigate the nature of the causative agent date back to 1938, when spinal cord homogenate obtained from scrapie-affected sheep was shown to induce disease in unaffected animal, prompting speculations that the infectious agent was a “filterable virus” (Cuille and Chelle, 1938).
Irradiation experiments of brains from infected mice performed in 1966 revealed that very large doses of ultraviolet radiation of 253.7 nm wavelength, which was known to be specifically absorbed by DNA, do not inactivate the scrapie agent (Alper *et al.* 1966) Since only ionizing radiation at unusually high doses resulted in inactivation, it was concluded that the infectious agent is either a very short nucleic acid in the range of 800 bases, or other particle “of an unusual nature”.

Speculations on the nature of the scrapie agent involved replicating polysaccharides (Alper *et al*., 1967), replicating membrane fragments (Gibbons and Hunter, 1967), DNA-polysaccharide complex (Adams and Caspary, 1968), viroids (Diener, 1972) and even lipids (Alper *et al*., 1978).

1.1.2.1 Protein only hypothesis – introduction and supporting evidence

In 1967 a series of extraction and electrodialysis experiments with scrapie agent led to the conclusion that "the transmissible agent may be, or may be associated with, a small basic protein" (Pattison and Jones, 1967). In the very same year the mathematician J. S. Griffith presented a "protein only" theory which encompassed three ideas of modes of transmission, all of which required the prion protein to be host encoded. One of the theories, which is nearly identical to what is today believed to be the mode of transmission, suggested that upon introduction of a seed of modified prion protein, the native cellular prion protein molecules are prompted to attach to this seed which eventually splits into two new seeds, thereby giving rise to its exponential propagation (Griffith 1967).

Subsequent experiments demonstrated that inactivation of scrapie infectious agent can be achieved if it is subjected to compounds or environments that modify proteins or disrupt their structure, such as protease treatment or exposure to chaotropic agents (Prusiner, McKinley *et al.* 1981). This suggested that it is the protein itself that is an essential component of the infectious agent, supporting the protein-only hypothesis. Consequently, in 1982, based on the unusual resistance of the pathogen and experimental evidence indicating that it consists primarily of protein, Stanley Pruisner introduced the term "prion" which denotes proteinaceous infectious particle (Prusiner 1982). Due to lack of certainty at the time, two possibilities for the nature of prions were considered: a small nucleic acid surrounded by a tightly packed protein coat or a protein devoid of nucleic acid which is itself infectious. It should be noted that while at the time Pruisner himself admitted that the second idea is "clearly heretical", prions today are clearly defined as "proteinaceous infectious particles lacking a nucleic acid" (Prusiner 1998).

1.1.2.2 Purification and isolation of infectious material

Since Griffith proposed the "protein only" hypothesis to explain the unique features of scrapie infectious agent, numerous attempts have been made to identify the elusive particle. Analysis of protein associated with prion material allowed to determine its molecular weight, which was estimated to be 27–30 kDa (Bolton *et al.*, 1982).
The presence of rod-like structures in the brain referred to as "scrapie associated fibrils" was discovered during attempts to purify the scrapie agent from affected neural tissue (Merz *et al.* 1981). Eventually, prions were successfully isolated from brain tissue of infected hamsters following extensive purification by detergent extraction, proteinase K treatment, and sucrose density gradient (Prusiner *et al.*, 1983). Subsequent structural characterisation confirmed that they are composed of polypeptides, with no covalently bound nucleic acids. Moreover, isolation of a short N-terminal fragment of the protein allowed for sequencing and subsequent production of molecular probes, which were used to identify mRNA coding for the prion protein. It was quickly discovered that the prion protein was encoded by a cellular gene present in non-diseased brain tissue as well as other body tissues (Chesebro *et al.*, 1985; Oesch *et al.*, 1985).
Sequencing of the prion gene revealed that the cellular form of the prion protein called PrP^{C} had a molecular weight of approximately 33–35 kDa, which was later confirmed by determining the molecular weight of prion protein isolated from brain tissue without the use of proteinase K.
Analysis of scrapie associated fibrils determined that they were composed of the same host-encoded protein, which led to the conclusion that prion protein exists as a normal cellular form, which can be converted to a disease associated conformation names scrapie-isoform (PrP^{Sc}). This misfolded PrP could then be recruited into formation of fibrillar structures found in brain tissue of animals suffering from TSEs.
The PrP^{C}-PrP^{Sc} model was consistent with the protein-only hypothesis presented twenty years earlier by Griffith, which proposed that seed of modified prion protein (PrP^{Sc}) can induce autocatalytic conversion of the native cellular protein molecules (PrP^{C}) and subsequent formation of fibrils.
Further investigation confirmed that both PrP^{C} and PrP^{Sc} are encoded by the same single gene, indicating that the differences between isoforms are not caused by different primary structures, but a post-translational modification or change in conformation (Basler *et al.*, 1986). The idea of autocatalytic conversion of PrP^{C} by PrP^{Sc} was

supported by subsequent findings that knock-out mice mutants which do not express prion protein were completely resistant to scrapie (Bueler, Aguzzi *et al.* 1993), indicating that expression of the protein within the host is essential for disease progression.

1.1.2.3 Yeast prions – in support of proteinaceous nature of prions

The protein-only hypothesis is supported by observation of prion-like behaviour of proteins in the yeast *Saccharomyces cerevisiae*. While these proteins have no relation to PrP, they exhibit similar templating mechanism of autocatalytic conversion, as well as transfer of genetic elements between cells without the presence of nucleic acids. Two proteins: a nitrogen regulator Ure2p, and translation termination factor Sup35p, were determined to have a soluble form and an amyloid form ([URE3] and [PSI+], respectively). Moreover, both of the amyloid isoforms can cause their soluble counterparts to convert to the prion-like state and form long β-structured fibres, similarly to how PrP^{Sc} affects PrP^{C} (Caughey, 2000; Wickner *et al.*, 2004).
Other examples of prion-like behaviour in yeast involve Rnq1p soluble protein with its amyloid form [PIN+] (Patel and Liebman 2007), Swi1 subunit of SWI/SNF chromatin remodelling complex and its prion form [SWI+] (Du, Park *et al.* 2008), as well as global transcription repressor Cyc8, isoform of which (called [OCT+]) was also demonstrated to have prion activity upon overexpression (Patel, Gavin-Smyth *et al.* 2009).

1.1.3 Characteristics of prion diseases

Although, throughout many years of research, numerous aspects of prion diseases have been investigated and characterised, there still remain several characteristics lacking definitive proof or explanation. One such feature is the transmissibility of prion diseases and the fact that it has so far been impossible to isolate single neurotoxic agent responsible for neurodegeneration of infected neural tissue. Still, a growing body of evidence indicates that small, soluble oligomers are primary

cytotoxic mechanism as opposed to fibril formation and deposition on cellular membranes (Chisea *et al.,* 2001; Novitskaya *et al.,* 2005). Moreover, formation of fibrils and their aggregation as well as subsequent formation of plaques is considered a protective mechanism evolved to avoid high toxicity of soluble oligomers (Buccianti *et al*., 2002; Kirkitadze *et al.*, 2002; Caughey *et al.,* 2003).
Another interesting aspect of prion diseases is the fact that infectious material, composed only of PrP, can induce a disease with widely different incubation time, pathology, and other phenotypic aspects (Prusiner *et al.*, 1998), suggesting the existence of different "strains" of prions.

1.1.3.1 Prion strains

One of the most interesting features of prions is the existence of "strains" which induce different disease phenotypes differing in incubation time, brain pathology and other features and which can be transferred between hosts with surprisingly high fidelity (Safar *et al.,* 1998). Some of these aspects of strain phenotype do not depend on the host, leading to the conclusion that they must be encoded by the infectious agent (Bruce *et al.,* 1991). In such a case, the autocatalytic template mechanism through which
PrP^{Sc} propagates would allow it to impose its conformation onto the host expressed PrP^{C}, consequently dictating the strain phenotype of the disease (Telling *et al.,* 1996).

1.1.3.2 Species barrier

An interesting phenomenon associated with prion transmission is the apparent inability of infectious prions to induce a disease in certain species, while retaining full infectivity upon transferring to others. The species barrier, as it is known, results in a longer incubation time and lower incidence of disease upon transfer of the infection between individuals from different species (Bruce 1993). Through compelling experimental evidence, it has been demonstrated that the mechanism of the species barrier is directly controlled by the primary sequence of prion proteins. Transgenic mice expressing hamster PrP exhibited high susceptibility to hamster prion infection, a

feature absent in wildtype animals (Scott *et al.*, 1989; Moore *et al.*, 2005). Interestingly, mice expressing human prion protein demonstrated high resistance to bovine prion infection, while showing high susceptibility to vCJD (Bishop, Hart *et al.* 2006). This suggests an existence of a strong species barrier between humans and cattle which is likely to be a primary reason of very low vCJD incidence after the BSE outbreak in 1990s, compared to number of cases in cattle.

Since the structure of PrP is highly conserved, it is unlikely that structural differences between PrP from different species are directly responsible; however, the very fact that both primary sequence and structure are conserved does not mean that the folding mechanism itself is conserved (Robinson and Pinheiro, 2009).

1.1.3.3 Disease-associated mutations in humans – inheritance and increased susceptibility

Prion diseases in general can be classified as sporadic, inherited or acquired through transmission, although the most common reasons of occurrence vary greatly between the species. In humans, sporadic CJD accounts for 85% of all cases of disease, with around 10–15% of cases associated with the familial cause and less than 5% acquired through transmission (Collinge, 2005). All the familial forms of the disease are caused by mutations in the *PRNP* gene which encodes prion protein. Gene alterations which result in amino acid substitutions or insertions of additional octapeptide repeats in the N-terminus of PrP have been linked to familial CJD.

One of the genetic forms of human prion disease is a Gerstmann-Sträussler syndrome (GSS) transmitted in an autosomal dominant fashion. Several mutations have been linked with GSS, including substitution of proline residue at position 102 with leucine (Hsiao, Baker *et al.* 1989) and a stop mutation at position 145 which produces a truncated form of prion protein (Kitamoto, Iizuka *et al.* 1993).

Not all mutations in the *PRNP* gene result in spontaneous disease generation. Some of the alterations have been demonstrated to increase susceptibility to the disease acquired from external source. An example of such a mutation is a human polymorphism which results in presence of valine or methionine residue at position 129. It was discovered that 95% of patients suffering from a sporadic form of CJD are homozygous at codon 129. In comparison, 51% of the population not affected by CJD were found to be

heterozygous, indicating that homozygous mutation greatly increases susceptibility to sporadic form of the disease (Palmer, Dryden *et al.* 1991).

1.1.4 Diagnostics of prions and possible therapies

Increased interest in prion diseases generated during the BSE and vCJD outbreaks, as well as due to increased prevalence of CWD in the cervid population and concerns of possible transfer to humans resulted in a widespread search for possible methods of TSE diagnostics.

Although several *in vitro* methods have been reported, most have major limitations that would preclude their use in routine diagnostic or screening applications. Of particular interest are methods capable of detecting prions in blood or plasma, but these environments exhibit extremely low prion concentrations and contain inhibitors lowering the effectiveness of most sensitive prion tests (Orru *et al.*, 2011).

One of the methods capable of detecting prions of variant Creutzfeldt-Jakob disease (vCJD) in human plasma is a quaking-induced conversion (QuIC). It exhibits sensitivity similar to that of *in vivo* bioassays, yet is much more rapid and less expensive (Orru *et al.*, 2011). Another potential assay for PrP is the detection of glycated PrP by monoclonal antibodies specific for carboxymethyl lysine/arginine-modified prion protein (Dvorakova *et al.*, 2011).

The discovery of the proteinaceous nature of PrP allowed for focussing of the attempts to develop effective treatment of prion diseases. Thousands of compounds have been screened for anti-prion effect, and while many show promising results in *in vitro* studies, very few are equally effective *in vivo*, especially if administered in the later stages of disease (Sim, 2012).

The vast majority of potential therapeutic effects was limited to prolonged incubation periods, but required the treatment to begin near the time of infection, which is difficult to estimate particularly in sporadic or familial forms of human disease (Brown, 2009). However, development of new diagnostic techniques, together with experimental insight into the mechanism of prion pathogenesis, particularly the role of oligomers and fibrils in neuropathology, increases the chances of finding effective therapeutic strategies. Many of the proposed methods rely on redistribution, sequestering, or down-regulation of PrP^{C} by polyanionic or polycyclic agents, thus preventing conversion of

cellular form of PrP to PrP^{Sc}. Novel approaches include trapping the multimeric form of PrP^{Sc}, increasing clearance of scrapie isoform, targeting accessory molecules playing a role in conversion, targeting pathways which lead to neurodegeneration and even stem cell therapy (Sim, 2012).

1.1.4.1 Protein misfolding cyclic amplification

One of the potential diagnostic methods theoretically capable of detecting single molecules of PrP^{Sc} is a protein misfolding cyclic amplification (PMCA).
The method relies on autocatalytic conversion of PrP^{C} by small amounts of PrP^{Sc} isolated from scrapie brain homogenate. Scrapie isoform is diluted to very low concentration and incubated with PrP^{C} while the reaction mixture is subjected to short bursts of sonication. The amount of PrP^{Sc} increases with every cycle as a result of autocatalytic conversion of PrP^{C}, which is enhanced by sonication aimed to break up growing fibrils thus providing additional replication templates. The sensitivity of the assay is sufficient to detect several dozens of PrP^{Sc} monomers in the blood sample, which allows it to be used as effective diagnostic method (Castilla *et al.*, 2005; Saa *et al.*, 2006).

1.1.5 Biosynthesis and metabolism of prion protein

1.1.5.1 Expression and post-translational modification of PrP

Prion proteins are encoded by *PRNP* gene in a form of 253 amino acid long polypeptide chain (Basler *et al.*, 1986; Oesch *et al.*, 1985). During translation by cytoplasmic ribosomes, a signal recognition peptide (SRP) binds to an N-terminal signal sequence of the growing polypeptide chain, targeting the ribosome-PrP complex to endoplasmic reticulum (ER), where the signal sequence is cleaved. Following translation, a C-terminal sequence of the polypeptide forms a transmembrane helix which anchors the protein to ER membrane. The C-terminal transmembrane segment is then cleaved by an enzyme which attaches the protein to a GPI anchor, allowing it to

remain connected to the membrane. Two high mannose oligosaccharides are subsequently attached to N-linked glycosylation sites at positions 181 and 197 in case of human PrP. Finally, a disulfide bond is formed between two cysteine residues at positions 179 and 214 (Lawson *et al.,* 2005).

High sequence identity of PrP genes between different species as well as experimental observaions indicate that these modifications are highly conserved (Wopfner *et al.*, 1999).

Following the post-translational processing in the ER, the GPI-anchored PrP is directed to the Golgi body, where its glycosylations are processed to a range of variable glycosylations including un-glycosolyated, mono and di-glycosylated species (Lawson *et al.,* 2005). PrP is then directed from the Golgi body to the outside face of the cell membrane.

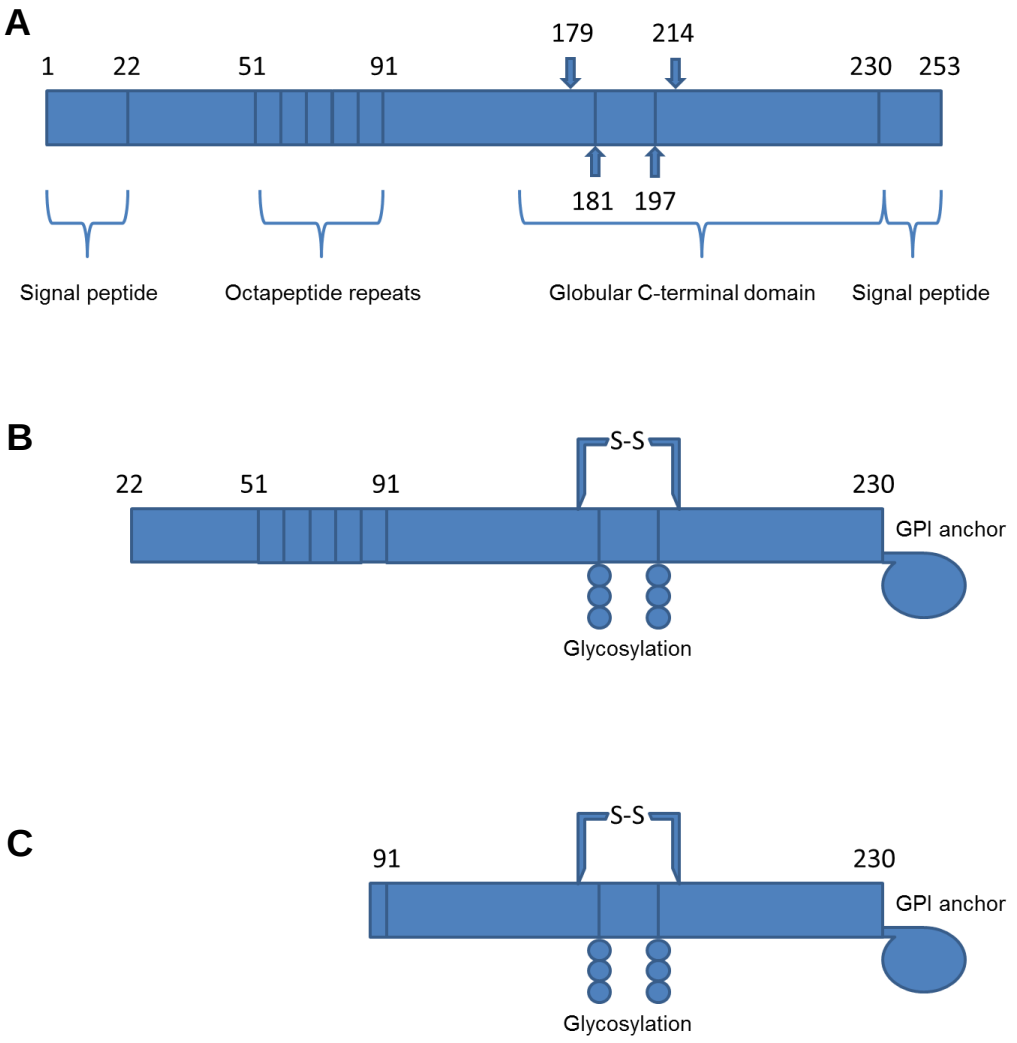

Figure 1.2 Schematic representation of biosynthesis, processing, and conversion of prion protein. The initial polypeptide chain (A) is 253 amino acids in length, including the signal sequences at the N- and C- termini.

A series of post-translational modifications yields cellular form of PrP (B). During the maturation process the signal sequences are removed, residues 181 and 197 are glycosylated, disulfide bond formed between cysteine residues 179 and 214 and the glycosylfosphatidylinositol (GPI) anchor added.

Upon conversion to PrP^{Sc} the primary structure remains unaffected, however extensive changes in secondary and tertiary structure result in formation of 142 amino acid-long proteinase-K resistant core (C).

1.1.5.2 Trafficking to cell membrane and endocytosis

Following the variable glycosylation in the Golgi body, mature PrP is transported to the plasma membrane attached via GPI anchor to the luminal side of the membrane of secretory vesicles. Upon reaching the membrane, the protein is localised to the to the lipid rafts on the external surface of the lipid bilayer. This localisation is independent of the GPI anchor, due to the fact that unstructured N-terminal region of PrP contains targeting sequence which directs protein to the lipid rafts even in absence of GPI anchor (Walmsley, Zeng *et al.* 2003). PrP remains attached to the external surface of lipid bilayer for approximately 3 to 6 hours (Caughey, Race *et al.* 1989) before it is internalised and trafficked between the cell surface and endosomal compartments (Shyng, Huber *et al.* 1993).

Like many other transmembrane proteins, PrP is internalised via clathrin coated pits. The unusual aspect of the process is the fact that prion protein lacks cytoplasmic domain, being GPI anchored (Shyng, Heuser *et al.* 1994), which should theoretically prevent its internalisation. N-terminal truncation provided some insight into the subject, demonstrating that partial removal of unstructured region reduces endocytosis, suggesting PrP interacts with a transmembrane protein that undergoes conventional endocytosis and is incorporated into clathrin coated pits along with it (Shyng *et al.*, 1994; Shyng *et al.*, 1995).

1.1.5.3 Physiological role of PrP

Although prion protein was first identified almost 20 years ago and ever since has been the subject of continuous research interest, its physiological function has remained uncertain.

Several lines of knockout mice not expressing PrP gene have been engineered to this date, displaying resistance to prion infection and no apparent anatomical abnormalities (Bueler *et al.*, 1992). While some of these animals exhibited subtle behavioural and cellular alterations, the molecular basis of those defects remained unknown (Steele *et al.*, 2007).

Compelling evidence for an involvement of PrP^C in cell adhesion has emerged recently from zebrafish research (Malaga-Trillo *et al.*, 2009). Two genes expressing PrP-like protein were discovered, playing important role in embryogenesis (PrP1 gene) and development of nervous system (PrP2). Depletion of PrP1-encoded protein resulted in gastrulation arrest, which could be rescued by PrP-1 and PrP-2 proteins as well as mouse PrP (Malaga-Trillo *et al.*, 2009), indicating very high conservation of biological activity. Subsequent research revealed that PrP-1 influences the delivery of E-cadherin to the plasma membrane, thus playing a role in cell adhesion modulation (Biasini *et al.*, 2012).

Another possible function of PrP is the regulation of ion channels and synaptic development in general, a role supported by its localization at synaptic sites (Moya *et al.*, 2000; Kanaani *et al.*, 2005) and the fact that variety of electrophysiological abnormalities have been described in neurons of PrP-knockout mice (Biasini *et al.*, 2012).

Extensive research into neuropathological effects of prion diseases revealed another, perhaps most surprising, possible function of PrP. Neuroprotective effects of PrP^C overexpression against several kinds of apoptotic stimuli have been demonstrated, together with its role in regulation of survival-mediating intracellular signaling cascades (Lo *et al.*, 2007; Biasini *et al.*, 2012).

Moreover, recent findings indicate that prion protein may be linked to self-renewal of neural progenitor and stem cells (Santos *et al.*, 2011) and regulation of neural precursor proliferation during mammalian neurogenesis (Steele *et al.*, 2006).

1.1.6 Structure of PrP

The discovery and sequencing of *PRNP* gene demonstrated that both PrP^C and PrP^{Sc} are in fact the same protein (Basler *et al.*, 1986; Stahl *et al.*, 1993). Consequently, it became apparent that vastly different behaviour and properties of the two isoforms can only be attributed to structural differences. This was confirmed through initial spectroscopic characterisation of both isoforms, which revealed predominantly α-helical structure of the cellular form of PrP and β-sheet rich conformation of PrP^{Sc} extracted from neural tissue of animals suffering from TSEs (Pan *et al.*, 1993).

High resolution studies of prion protein became possible upon successful cloning of PrP-encoding gene, which allowed for the induction of PrP expression in bacterial cells via PRNP-containing plasmids.
To this date intact prion protein could not be successfully crystallised, excluding the application of X-ray crystallography and limiting high resolution studies of PrP to nuclear magnetic resonance (NMR) and related techniques.

1.1.6.1 NMR structures of PrP^C

The first high resolution structure of PrP^C was determined through NMR studies of truncated construct of murine PrP (Riek *et al.*, 1996). The C-terminal fragment was found to contain three short α-helices designated helix A, helix B, and C, as well as a short antiparallel β-sheet composed of two short strands dubbed S1 and S2. A single disulfide bond was identified between first turn of the second helix (A2) and the last turn of the third helix (A3), in the hydrophobic core of the protein. Investigation of full length prion protein by fluorescence and circular dichroism revealed that the N-terminal region is composed solely of random coil and devoid of any structure (Hornemann, Korth *et al.* 1997), which was later confirmed through NMR studies (Donne *et al.*, 1997; Riek *et al.*, 1997).
NMR spectroscopy was also used to investigate the truncated construct of Syrian hamster PrP, the structure of which was found to be very similar to mouse prion protein (James *et al.*, 1997; Liu *et al.*,1999).
To this date, high resolution structures of cellular prion proteins from numerous mammalian species have been determined (Lysek *et al.*, 2005), all showing remarkable structure similarities with primarily α-helical C-terminal domain and a long unstructured N-terminus. Moreover, PrP structures from non-mammalian species sharing only 30% sequence homology with mammals were showed to be very similar, indicating high structure conservation (Calzolai *et al.*, 2005).
Recent studies of elk and bank vole PrP revealed a presence of highly rigid loop region between the β-strand B2 and the α-helix A2, not encountered in other species (Gorfe and Caflisch, 2007; Christen *et al.*, 2008). NMR analysis of mouse-bank vole hybrids and molecular dynamics simultions of elk-mouse hybrids show that replacing the loop

of mouse PrP with that from bank voles or elk results in increased stability and rigidity of the loop (Christen *et al.*, 2009; Scouras and Daggett, 2012). Experimental evidence demonstrates that increasing loop region stability induces spontaneous prion disease in mice (Sigurdson, Nilsson *et al.* 2009), indicating an important role of this region in disease susceptibility.

1.1.6.2 Structural models of PrP^{Sc}

While investigation of PrP^{C} structure from numerous species has been accomplished through a number of spectroscopic methods, the amount of information on structure of scrapie isoform PrP^{Sc} is much lower. Infectious species of prion protein are difficult to identify and extract due to multi-conformational nature of PrP^{Sc} deposits and the fact that isolation of scrapie isoform from brain tissue requires the use of detergents which may alter protein structure during purification. Moreover, amyloid fibrils are highly insoluble, preventing the use of X-ray crystallography and solution NMR.

First information on PrP^{Sc} structure was obtained through FTIR studies, which suggested a β-sheet rich conformation (Caughey *et al.*, 1991). Subsequent X-ray diffraction studies confirmed the overall nature of PrP^{Sc}, revealing cross β-structure of the isoform (Nguyen *et al.*, 1995).

Co-purification of negatively stained crystals and prion rods and their subsequent analysis via electron crystallography provided further information about PrP^{Sc}, allowing for extensive modelling of its structure. Currently available models suggest a β-helix fold which can assemble into trimers, consequently forming repeating subunits of prion fibrils (Wille *et al.*, 2002; Govaerts *et al.*, 2004).

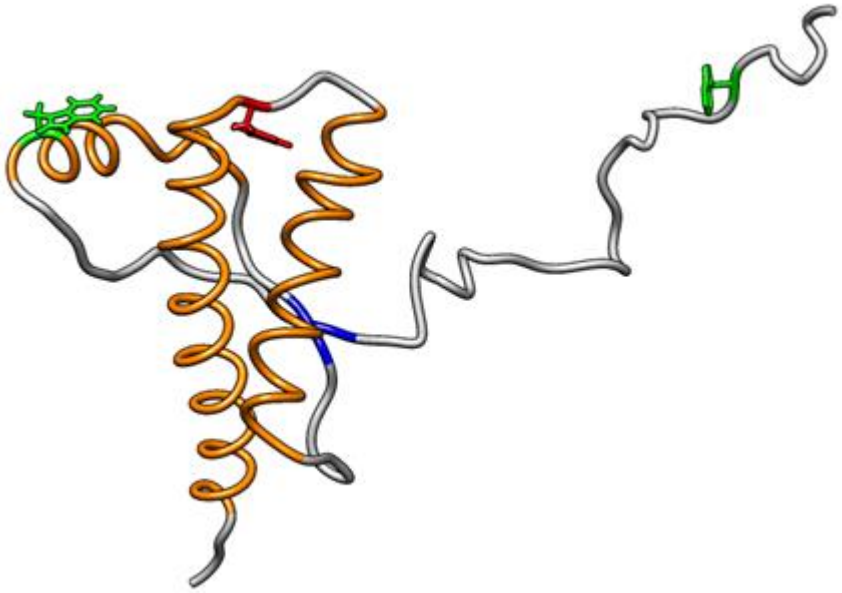

Figure 1.3 Ribbon representation of the structure of the C-terminal globular domain of mouse prion protein (residues 90-230) based on the NMR structure (Gossert *et al.* 2005). Main structural features are highlighted in colour with key residues shown using stick representation. Three main α-helices are shown in orange, with short antiparallel β-sheet S highlighted in blue. Native tryptophan residues at positions 98 and 144 are highlighted in green and phenylalanine residue at position 197 is highlighted in red.

The NMR structure was drawn from PDB file 1XYX using UCSF Chimera package from the Resource for Biocomputing, Visualization and Informatics at the University of California, San Francisco (supported by NIH P41 RR-01081).

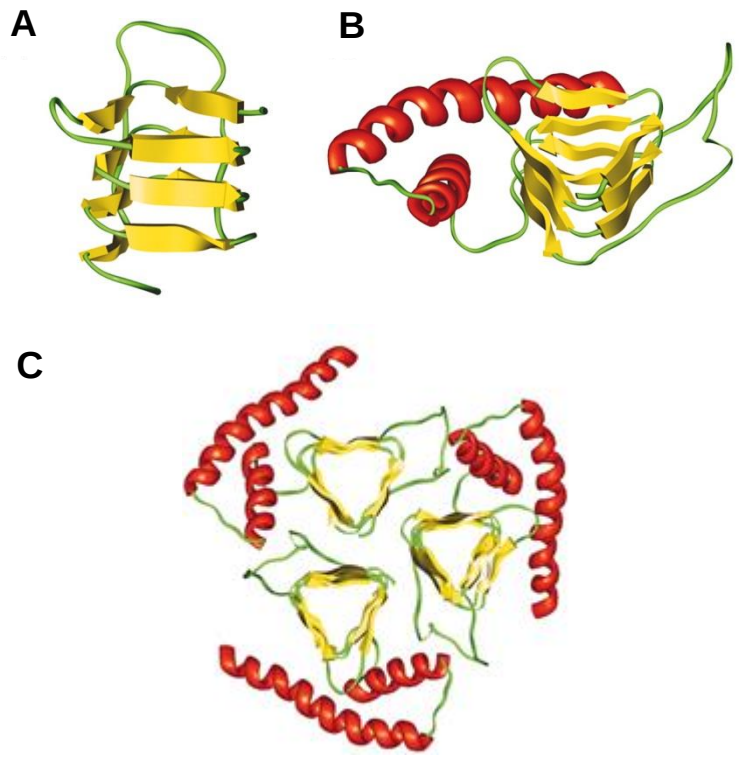

Figure 1.4 Modeling of β-helical conformation of residues 89-174 of PrP^{Sc} and its assembly into timeric subunits of prion fibrils. Panel A shows the β-helical model of the N-terminal part of PrP 27–30, panel B demonstrates the structure of PrP^{Sc} monomer, panel C depicts the trimeric model of PrP^{Sc} subunit present in fibrils.

Figure adapted from (Govaerts *et al.*, 2004).

1.1.7 Conversion of PrP^{C} to PrP^{Sc}

Structural studies of prion protein revealed dramatic structural difference between the cellular form PrP^{C} and disease-associated PrP^{Sc}. These findings, coupled with protein only hypothesis stating that the scrapie isoform can recruit and convert the cellular form of prion, sparked significant interest in the mechanism of such an extensive conversion.

Several models of conversion mechanism were presented over the years, including template mechanism, equilibrium conversion and recruitment of intermediate.

The template mechanism assumes that PrP^{Sc} binds directly to partially unfolded PrP^{C} and acts as a replication template, inducing conformational change in a catalytic fashion (Prusiner *et al.*, 1998). Second model implies existence of equilibrium between cellular and scrapie isoforms which can be shifted towards PrP^{Sc} upon formation of stable nucleus of the latter isoform (Jarret and Lansbury, 1993). Finally, PrP^{Sc} may be able to recruit an intermediate present in the folding pathway of PrP^{C} and force it down the alternative pathway leading to disease-associated conformation (Apetri *et al.*, 2004; Liemann and Glockshuber, 1999).

1.1.7.1 *In vivo* conversion

It is widely accepted that destabilising environment contributes greatly to the misfolding of PrP. Consequently, endoplasmic reticulum, lysosomal pathway and the plasma membrane have all been suggested as possible locations of PrP^{C} to PrP^{Sc} conversion, yet exact site of the process remains unknown (Campana *et al.*, 2005). Recent quantitative analysis of PrP^{C} and PrP^{Sc} distribution coupled with estimation of PrP^{Sc} levels in different trafficking-impired neuronal cells allowed to exclude the early and late endosomes from possible sites of prion conversion. At the same time, endosomal recycling compartment where PrP is trafficked following internalization from the cell surface has been suggested as the most likely location of the process (Marijanovic *et al.*, 2009).

Involvement of host-specific factor was suggested as an important aspect of prion conversion. The yet-uncharacterised ligand dubbed “Protein-X” has been proposed to bind to the loop region encompassing residues 165-171, facilitating pathogenic

conversion of PrP (Telling *et al.*, 1995, Kaneko *et al.*,1997). This hypothesis was based on the results of infectivity studies on transgenic mice expressing both murine and human prion protein, as well as mouse-human chimera based on mouse PrP with residues 90-167 of the human protein. Mice expressing human PrP and chimeric animals were found to be susceptible to human prions, while those expressing murine PrP were not, suggesting that a host-encoded protein with affinity for mouse PrP greater than that for human PrP binds in the loop region thus facilitating pathogenic conversion (Telling *et al.*, 1995).

1.1.7.2 *In vitro* conversion and fibrillization

Since the discovery of two dramatically different conformations of prion protein, considerable efforts have been made to characterise the process of conversion, with many studies focussing on replicating the process *in vitro*.

The conformational change from primarily α-helical form to a PrP^{Sc}-like structure rich in β-sheets was observed to occur under partially destabilising conditions such as presence of mild denaturant or low pH (Swietnicki *et al.*, 2000; Baskakov *et al.*, 2001). It was soon discovered that two distinct isoforms of PrP^{Sc} can be produced under slightly different experimental conditions: long, multimeric amyloid fibrils which were highly insoluble, as well as small oligomeric particles consisting of several (usually 8) monomers of PrP rich in β-sheet structure (Baskakov *et al.*, 2002; Bocharova *et al.*, 2005).

Subsequent studies revealed that both oligomers and amyloid fibres can be produced from full-length PrP (Bocharova *et al.* 2005) and that pre-formed fibrillous material can act as seeds for fibrilization, effectively eliminating the nucleation phase and decreasing the lag time of fibril formation (Baskakov 2004).

Interestingly, fibrilization pathways can be affected by minor structural features of PrP, as indicated by reports that even minor N-terminal truncations of full length PrP produces fibrils with distinctly different conformations (Ostapchenko *et al.*, 2008).

Successful generation of infectious prions *in vitro* have been reported in several studies where the use of protein misfolding cyclic amplification allowed for conversion of PrP^{C} to PrP^{Sc} (Castilla *et al.*, 2005) and subsequent adaptation of the *in vitro* produced prions (Castilla *et al.*, 2008). Hamster PrP^{C} misfolded by mouse PrP^{Sc} generated new prions infectious to wild type hamsters, with the inverse process yielding material infectious to mice. A detailed characterization of the species produced during the study indicated that their properties correspond to those of new prion strains (Castilla *et al.*, 2008).

Recent molecular dynamics simulations suggest that a compact loop encompassing residues 166-175 is necessary for aggregation and formation of the infectious particles in several species including bank vole, elk, sheep and mouse prion strains. Moreover, the stability of the loop region is decreased in a number of point mutations which are associated with increased disease resistance (Scouras and Daggett, 2012).

According to the modelling studies of infectious protofibrils, the stabilised turn is buried between two PrP monomers, allowing for oligomerisation. In the absence of stabilising mutations, the loop region is destabilised, and the resulting flexible, expanded loop disrupts the packing of the adjacent monomers, consequently impairing their incorporation into the protofibril (Scouras and Daggett, 2012). Another potential disease-resistance mechanism is based on the possibility that if the PrP variants carrying loop-destabilising mutations become parts of the infectious seeds, the altered stability of their conformation prevents further oligomerisation (Ott *et al.*, 2008).

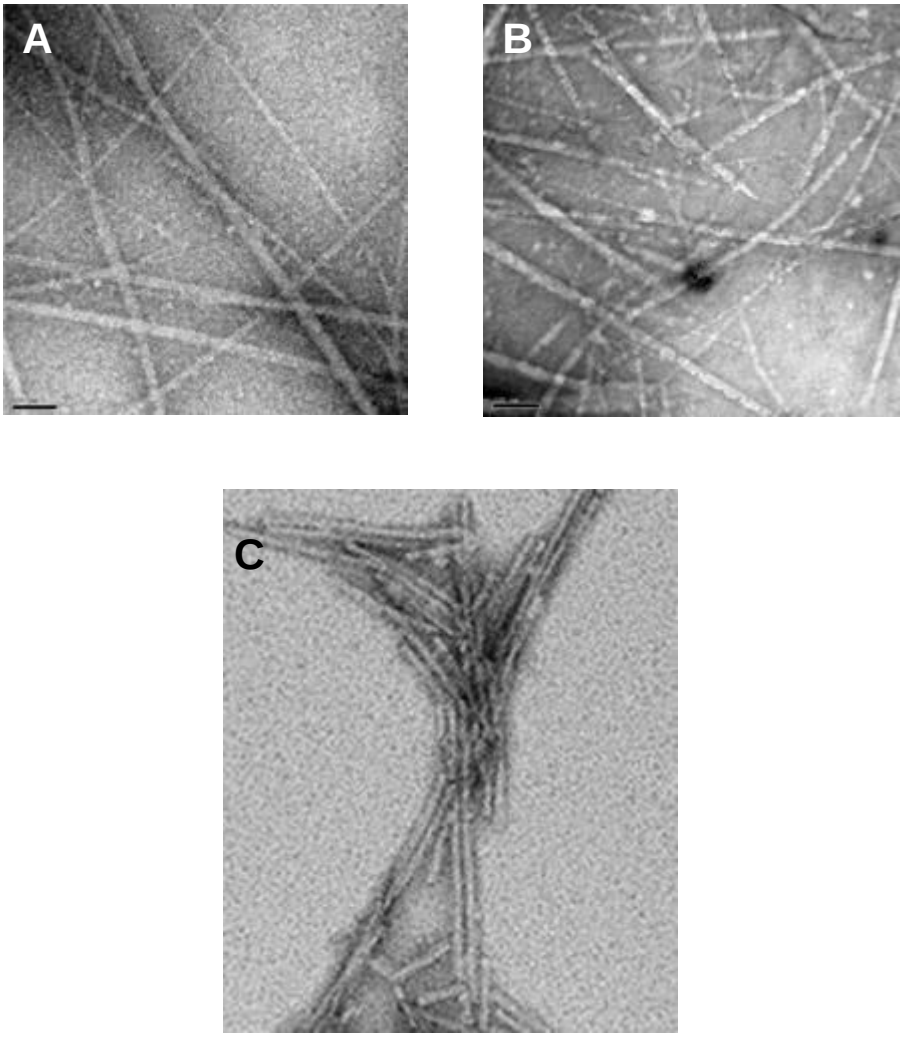

Figure 1.5 Electron microscope images of mouse PrP fibrils formed *in vitro* (A and B) and prion rods purified from brain extracted material(C) which co-purify with infectivity.

Images A and B were collected by the author following fibrilisation experiments (see Chapters 3 and 4), image C was reproduced from (Safar *et al.*, 2006)

1.2 Protein folding

1.2.1 Principles of protein folding

Proteins are biological macromolecules essential in virtually every process occurring within living cells including catalysis of biochemical reactions, transport of molecules and metal ions or role in structural framework.
They begin their life as long polypeptide chains which spontaneously adopt stable and active three-dimensional structure in order to perform their function within the cell (Jahn and Radford 2008). All of the structural information necessary for the polypeptide to adopt its native conformation is encoded in its amino acid sequence, also referred to as "primary structure" (Anfinsen, 1973).
While protein folding is a spontaneous, self-assembly process, it cannot occur completely at random, as demonstrated by simple calculation showing that a 100 amino acid long polypeptide may adopt 3^{198} different conformations. If such a protein were to adopt its tertiary structure by random sampling all of the possible conformations with highest physically possible rate, the process would take longer than the present age of the universe (Levinthal 1968). Consequently, protein folding must be a directed process which occurs via clearly defined pathways (Zwanzig *et al.*, 1992).

1.2.1.1 Polar opposites – native state and unfolded state

The final, fully functional structural conformation of the protein which is most thermodynamically stable is referred to as the native state. Physiological roles of proteins such as enzymatic catalysis or transport require structural flexibility, and due to this dynamic nature the native state often encompasses a population of near native structures rather than single rigid conformation (Jahn and Radford 2008).
Proteins can spontaneously adopt correct three-dimensional structure due to the fact that self-assembly is a thermodynamically favoured process characterised by a negative change in free energy between the unfolded and native states.
One of the major factors contributing to protein folding is the formation of thermodynamically favourable non-covalent interactions between side chains of amino

acids and the polypeptide chain backbone. Further stabilising effects are provided by formation of a complex network of hydrogen bonds as well as weaker electrostatic interactions between negatively and positively charged groups (Mathews *et al.*, 2000). Another factor crucial for overall stability of the native conformation is the so-called hydrophobic effect, which results in majority of hydrophobic residues being buried in the protein core, where they are shielded from aqueous environment.

The increase in entropy associated with the internalisation of hydrophobic regions induces a significant positive change in entropy of the system composed of the polypeptide chain and surrounding water molecules, contributing to the overall negative change in free energy and thus spontaneous nature of protein folding (Mathews *et al.*, 2000c).

The unfolded state of the protein can be defined as the conformation where all the backbone NH groups of a polypeptide chain are solvent-exposed (Dill and Shortle 1991), or alternatively as an ensemble of extended conformations, in which the protein chain is extensively hydrated and the individual residues do not interact with each other (Day, 1996).

Interestingly, experimental evidence indicates partial retention of native interactions such as the hydrophobic clusters of aliphatic and aromatic side chains even in very high denaturant concentrations (Klein-Seetharaman, Oikawa *et al.* 2002), rising questions whether "true" unfolded state can be attained in experimental conditions.

1.2.1.2 Intermediates and transition states

Extensive study of the mechanism and kinetic properties of protein folding provided considerable insight into the process through which proteins attain their fully functional structural conformation. Due to its complexity, protein folding occurs in a series of steps, each encompassing small populations of distinct, metastable conformations referred to as intermediate states which are transiently populated during the progression of folding process (Brockwell and Radford 2007).

A transition state, as opposed to an intermediate, is defined not as a metastable conformation but as a rate limiting step of the folding process corresponding to the highest point in the energy profile.

Intermediate states can be sampled by a variety of kinetic methods including techniques capable of following sudden shifts in the equilibrium of the system (Roder, Maki *et al.* 2006) or rapid mixing techniques such as stopped-flow, continuous-flow or pressure-jump capable of characterising protein folding on millisecond and microsecond timescale.

Transition states are often studied using psi-value analysis, a powerful protein engineering technique which provides information about the role of individual side chains in the folding transition state, describing its structure in terms of the presence of native interactions (Matouschek *et al.,* 1989; Oliveberg 2001).

Populations of folding intermediates and transition states are often represented in a form of energy landscape (see Figure 1.6) which reflects the free energy of each conformation attainable by a polypeptide chain as a function of its degrees of freedom. Each point on the energy landscape represents a single conformation the polypeptide chain can adopt, with denatured states possessing high internal free energy and wide variety of conformational states found at the "edge" and upper region of the energy funnel and native state conformations with lower energy and smaller range of conformations close to or within the deepest "well" of the landscape (Radford, 2000; Jenkins, 2006).

Representation of protein folding as an energy landscape is also useful in visualising both kinetic barriers and energy traps which can potentially slow, disrupt or even completely halt the process of spontaneous self-assembly of polypeptides due to the fact that molecule would have to revert to a higher energy state in order to proceed down the folding pathway, which is highly thermodynamically unfavourable.

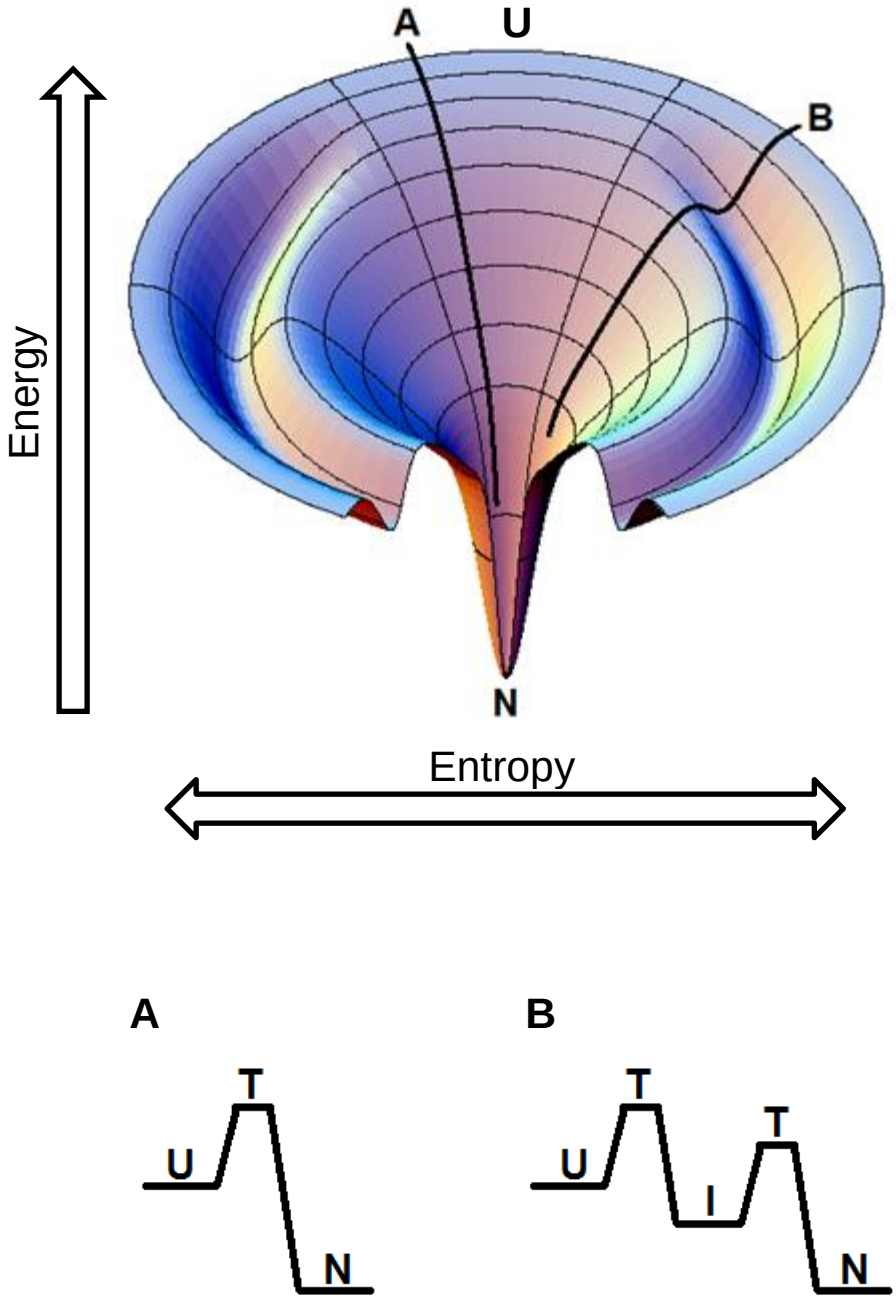

Figure 1.6 Schematic representation of a "funnel" energy landscape of a protein illustrating all possible conformations populated between the unfolded state (U) and native state (N). Black lines indicate two parallel folding pathways, illustrating how a protein might fold without (A) and with an intermediate state (B).

Reaction co-ordinates corresponding to pathways A and B illustrating the presence of unfolded state (U), transition state (T), intermediate (I) and native state (N) are presented below the energy landscape.

Image depicting energy landscape adapted from (Dill and Chan,1997).

1.2.2 Experimental approaches for the study of protein folding

Although numerous techniques have been employed to date to study the folding pathways of proteins, the *in vitro* studies can be divided into three general categories: kinetic studies, equilibrium studies and molecular dynamics simulations.

1.2.2.1 Kinetic studies of protein folding

Experimental techniques employed during kinetic studies of protein folding provide insight into the folding pathway in general, as well as specific events such as formation of intermediates and presence of transition states. A folding pathway devoid of any kinetic intermediates is referred two as two-state transition with conformational change occurring between unfolded and native states. Any deviations from a typical two-state model are typical for pathways which include the formation of one or more kinetic intermediates (Royer, 2006).

Kinetic studies rely on detecting and following dynamic changes in protein conformation and related physical properties as the polypeptide proceeds down the folding or unfolding pathway. Both folding and unfolding of investigated protein are typically induced by rapid application or removal of destabilising conditions such as chemical denaturant (stop-flow and continuous-flow techniques), pressure (presser-jump spectroscopy) or temperature (temperature-jump spectroscopy), or a combination of these factors. Changes in structural properties over the course of experiment can be monitored using a wide range of spectroscopic techniques such as fluorescence measurements, circular dichroism or NMR.

Fluorescence spectroscopy involves detecting and monitoring changes in emission of fluorescent probes (such as tryptophan residues) within the protein which are sensitive to changes in local environment providing information regarding alterations in tertiary structure of the protein (Lakowicz, 1999; Royer, 2006).

Far-UV circular dichroism is often employed to monitor changes in secondary structure of the polypeptide as it transits between native and unfolded states (Kelly and Price, 1997), allowing for detection of structurally distinctive conformations on the folding pathway such as intermediates.

NMR studies can complement both fluorescence and CD techniques, providing detailed information on specific residues within the protein, often revealing subtle but crucial changes undetectable by other methods (Kumar and Yu, 2004).

1.2.2.2 Equilibrium studies of protein folding

In contrast to kinetic studies, equilibrium techniques utilise incremental changes in destabilising conditions such as presence of denaturant or change in pressure or temperature (Fersht, 1999), rather than rapid and often total destabilisation of the structure employed by kinetic methods.

Structural alterations induced by changes in denaturating conditions result in gradual shift in conformation of the protein over the course of experiment, allowing for monitoring of the folding and unfolding process.

While differing in principles, equilibrium studies often utilise spectroscopic techniques similar if not identical to those employed in kinetic studies, including fluorescence spectroscopy, circular dichroism or NMR.

Structural data provided by these measurements allow for the construction of denaturant folding curves which illustrate conformational changes in relation to gradual shift in conditions. These curves can be analysed using a non-linear least-squares regression (Santoro and Bolen, 1988), allowing for calculation of a number of parameters such as the free energy of folding in the absence of denaturant.

Moreover, equilibrium folding curve analysis often indicates whether the folding pathway of the protein is highly cooperative and two-state or whether multiple states are present, indicating the presence of stable, partially-folded intermediates (Kim and Baldwin, 1982).

1.2.2.3 Models of protein folding

Over the years, studies of protein folding yielded two general models attempting to describe the sequential steps of the process.

These two classical models are the framework model and the hydrophobic collapse model, both detailed below.

The framework model first proposed in 1973 states that the formation of secondary structure is the initial step of protein folding, subsequently followed and stabilised by tertiary interactions which result in the formation of the native state (Ptitsyn, 1973)
In contrast, the hydrophobic collapse model predicts that the clustering of hydrophobic residues is the first event in folding, significantly restricting the space available in which defined tertiary structure can form, thus directing the process of folding along specific pathways.
In agreement with an old phrase that the "truth lies in between", experimental evidence suggests that folding of majority of the proteins follows a mechanism which shares the features of both models. This process is described as nucleation condensation, where secondary structure forms simultaneously with the hydrophobic collapse (Daggett and Fersht 2003).
All three models of protein folding can be represented as a folding funnel (see Figure 1.6), which encompasses all of the populations of intermediates and transitions occurring between unfolded and folded states.

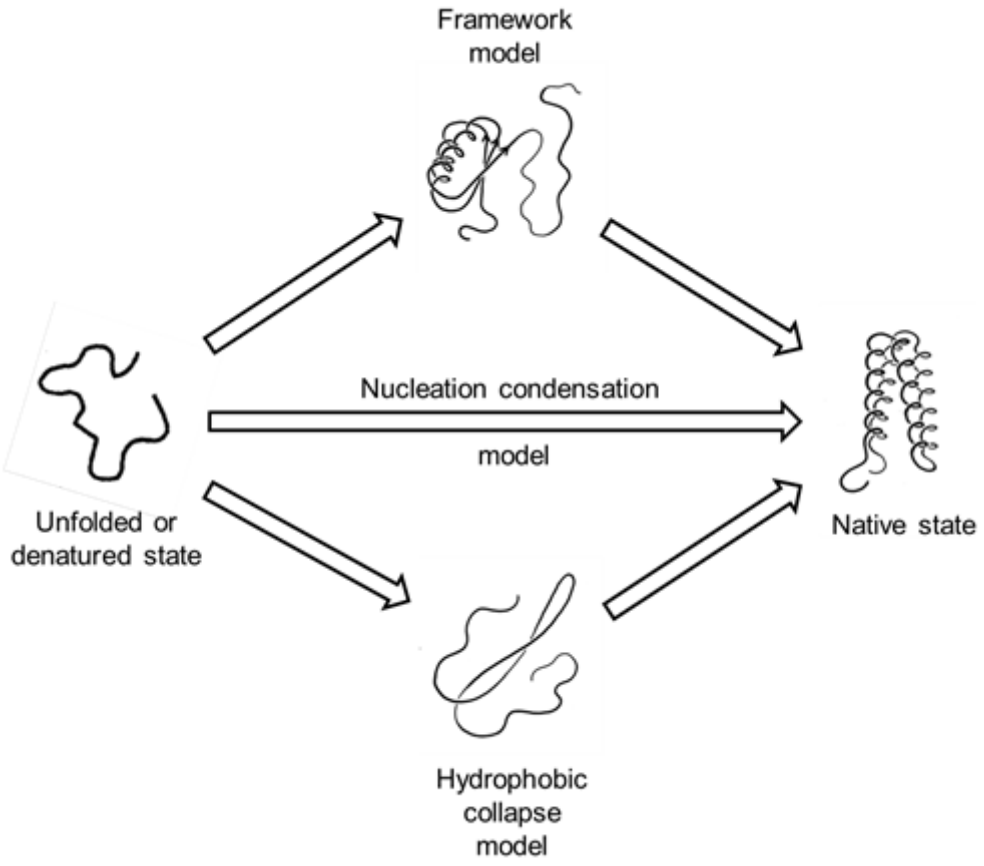

Figure 1.7 Schematic representation of three proposed mechanisms of protein folding.

In the framework model the formation of secondary structure is the initial step of protein folding, followed by tertiary interactions which resulting in the formation of the native state. According to the hydrophobic collapse model, the clustering of hydrophobic residues is the first event in folding, followed by formation of secondary and tertiary structure. The nucleation condensation model is the combination of the two previous models, in which secondary structure forms concurrently with the hydrophobic collapse.

1.2.3 Protein folding *in vivo*

In vitro folding studies of protein folding provided invaluable information about the mechanisms and pathways associated with the adoption of functional tertiary structures by a polypeptide chains. It must be remembered, however, that protein folding *in vivo* is very likely to differ from *in vitro* process due to discrepancy in environmental conditions.

In vitro studies of protein folding have been compared to observing behaviour of a single person in the desert, whereas *in vivo* conditions native to cellular proteins resemble a trip through a multimillion city at rush hour.

While protein folding studies usually employ aqueous environment which may or may not contain a range of co-factors such as salts, metal ions substrates etc., protein folding in the cell takes place in the environment occupied by 300-400 g l^{-1} of proteins and other macromolecules (Hartl and Hayer-Hartl, 2009). Such a crowded environment is certain to significantly restrict initial entropy of unfolded polypeptide chain which may translate to alterations of folding pathways (Ellis, 2001) such as accelerated folding kinetics (Tokuriki *et al.*, 2004).

Moreover, proteins begin to adopt their native conformation even before the polypeptide chain is fully synthesized on the ribosome (Netzer and Hartl, 1997), a property which cannot be reliably reproduced *in vitro*.

Another factor influencing protein folding *in vivo* is the interaction of polypeptide chain with molecular chaperones, a group of proteins capable of modulating the folding process (Ellis and van der Vies, 1991). Numerous chaperones are present in the ER, where they interact with folding proteins and prevent any incorrect interactions within and between polypeptides, ensuring adoption of a functional tertiary structure.

The action of chaperones is complimented by folding catalysts, a group of enzymes encompassing protein disulfide isomerases which catalyse the formation of disulfide bonds an rearrangement of the incorrect ones, as well as peptidyl-prolyl isomerases which catalyse the isomerisation of peptide bonds before proline residues (Wilkinson and Gilbert, 2004; Lu *et al.*, 2007).

Further chaperones await proteins outside the ER, providing further assistance in correct folding as well as “quality control” mechanism prior to transportation of the protein to its designated location. All of these interactions are virtually impossible to reproduce in a single experimental environment *in vitro*.

1.2.4 Protein misfolding and aggregation

Misfolding and subsequent aggregation of proteins have been linked to a number of human diseases including TSEs, Parkinson's disease, Alzheimer's disease and Huntington's disease, all of which are associated with formation and deposition of insoluble fibrils that exhibit birefringence when stained with congo-red (Lansbury, 1992; Howie and Brewer, 2009).

Aggregation is a general feature of proteins which can be observed in a number of denaturing conditions including presence of chemical denaturants, incubation at high temperature, presence of high salt concentration, pH change close to the isoelectric point of the polypeptide or presence of polar organic solvent or heavy metals (Ohnishi and Takano, 2004). While some of these conditions can increase the propensity of amyloid formation, fibrilisation in general remains strongly associated with adoption of stable, non-native conformation often referred to as misfolded state (Ohnishi and Takano, 2004).

1.2.4.1 Amyloid fibrils and models of fibrilisation mechanics

Due to its association with a number of human diseases, amyloid fibril formation has drawn a significant interest.

In vitro studies determined that formation of amyloid fibrils is a two-step reaction consisting of a slow nucleation phase also referred to as lag phase, followed by a much more rapid molecular assembly step (Jarrett and Lansbury, 1992; Lomakin *et al.,* 1996). It was soon discovered that addition of pre-formed fibrils results in significant reduction of the nucleation phase, indicating that nucleation itself plays important role in fibrilisation kinetics (Han *et al.,* 1995; Wood *et al.,* 1999).

Numerous studies highlighted the importance of partial unfolding of the protein for the formation of amyloid fibrils. While the mechanism of association of partially unfolded polypeptides into fibrils has in many cases not been fully described, several models have been proposed.

One of the fibrilisation models proposed as explanation to the role of expanded glutamine repeats linked to several inherited neurodegenerative diseases is the "polar

zipper" model, in which β-sheets are stabilized with a network of hydrogen bonds involving polar residues such as glutamine and asparagine (Perutz *et al.*, 1994). Another proposed mechanism of amyloid formation is the domain-swapping model in which two or more protein molecules form a dimer or oligomer by exchanging one or more of their structural domains (Liu and Eisenberg, 2002).

Interestingly, several experiments demonstrated that even non-pathogenic proteins may form amyloid fibrils under destabilizing conditions, supporting a hypothesis that the potential to form amyloid fibrils may be a common feature of all proteins (Guijarro *et al.*, 1998).

More recent results indicate that polythreonine, polyglutamate and polylysine are capable of forming amyloid fibrils, leading to hypothesis that amyloid fibril formation is driven by interactions between backbones and that side-chain interactions in the native state may be a limiting factor in fibrilisation (Fandrich and Dobson, 2002). These findings are consistent with the fact that *in vitro* fibrilisation is often achieved under destabilizing conditions where side-chain interactions are weakened, and that amyloid fibrils have a similar cross β-structure regardless of amino acid sequence (Ohnishi and Takano, 2004).

1.2.4.2 Fibrilisation of prion protein

Two models of amyloid fibril formation by prion proteins have been proposed: the nucleation-polymerization model and template-assistance model (see Figure 1.7). The nucleation-polymerization model assumes the existence of dynamic equilibrium between the PrP^{C} and PrP^{Sc} isoforms of prion protein. In the presence of an aggregate large enough to act as a stable nucleus, this equilibrium is shifted towards the PrP^{Sc} form, driving conversion and polymerisation of PrP^{C}.

In the template-assistance model, the conversion of PrP^{C} or its intermediate to PrP^{Sc} is extremely slow in the absence of scrapie isoform, but the process is essentially irreversible. Consequently, PrP^{Sc} is able to propagate itself by catalysing the conversion of folding intermediates to PrP^{Sc} confirmation.

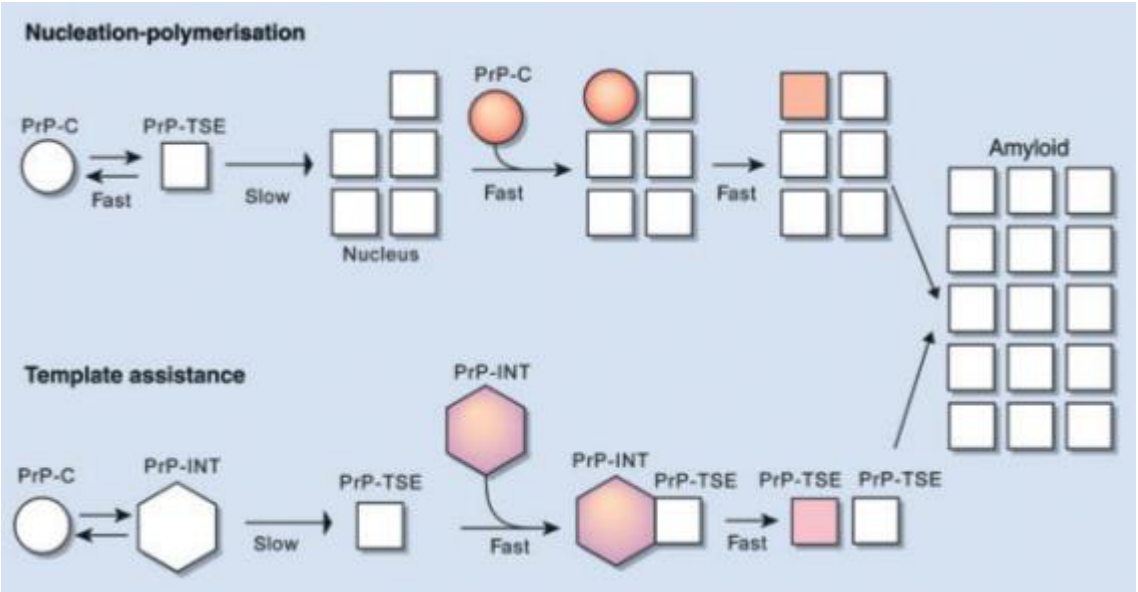

Figure 1.8 Schematic representation of two models describing conversion of cellular form of prion protein to disease-associated isoform: the nucleation-polymerization model (top) and template-assistance model (bottom).
Circles represent the cellular isoform of PrP, with scrapie isoform depicted with squares. In the nucleation-polymerisation model, multiple squares are used to represent stable nucleus capable of driving PrP^{C} conversion and polymerisation.
In the template-assistance model, the folding intermediate of PrP^{C} which can be recruited by PrP^{Sc} is represented as pink hexagon.

Figure adapted from (Norrby, 2011).

1.3 Aims of the thesis

The experiments described in this thesis utilised both truncated and full length forms of mouse prion protein and truncated form of Syrian hamster prion protein. Truncated constructs include the structured C-terminus and a short region of the unstructured N-terminus.

The aim of experiments detailed in Chapter 3 was to fully characterise folding kinetics of mouse and Syrian hamster PrP, as well as investigate whether the folding properties of mouse PrP are influenced by the Q167R mutation which is known to confer decreased disease susceptibility.This was achieved by comparing the unfolding and refolding kinetics of wild type mouse PrP and Q167R mutant under native and mildly denaturing conditions using pressure-jump spectroscopy. Moreover, possible kinetic mechanisms underlying the species barrier were investigated by comparing unfolding and refolding kinetics of both mouse constructs with those of Syrian hamster PrP in search of species variation.

Another aim of the thesis was to correlate the presence of possible intermediates in folding pathways of mouse and Syrian hamster prions with fibrilisation propensity. This was achieved through fibrilisation studies of truncated mouse PrP, Q167R mutant and Syrian hamster PrP detailed in Chapter 3, conducted at a range of denaturant concentrations and pHs known to induce PrP conversion into β-state intermediate, in an attempt to answer the question of species variation and disease-modulating mutations in the folding properties of the prion protein.

The aim of experiments detailed in Chapter 4 was to study the folding pathway of CWD mutations in mouse construct in order to investigate the importance of stability of the compact loop encompassing residues 166-175 of PrP which has been suggested to play an important role in aggregation and formation of the infectious particles of prion protein.

The impact of a number of point mutations known to affect the stability of the loop region was determined by equilibrium studies of a series of full length mouse PrP mutants carrying one or two loop-stabilising point mutations (S170N, N174T and double mutant S170N/N174T) and comparison of their folding properties with full length wild-type mouse PrP.

Another aim of the research detailed in this thesis was to characterise fibrilisation properties of CWD-related elk mutations in mouse constructs. To accomplish this goal, equilibrium studies were complemented by fibrilisation assays of the four full length constructs in an attempt to correlate the kinetic effects of loop-stabilising mutations with propensity to from fibrils, which should yield to our understanding of both the misfolding and fibril formation mechanisms associated with the occurrence of the disease and the phenomenon of the species barrier and varied disease susceptibility.

Final aim of the thesis as detailed in Chapter 5 was to develop and thoroughly evaluate a new continuous-flow instrument which could be used to study the earliest kinetic events of the prion folding pathway.

Chapter 2: Expression and purification of recombinant mouse prion protein (MoPrP) and Syrian hamster prion protein (SHaPrP).

2.1 Introduction

Biochemical studies such as protein folding often rely on repeating experiments multiple times in order to generate reliable and statistically valid data. Consequently, sample consumption can be high, driving the need for efficient and reliable material supply method.

Initial studies of prion proteins relied on material purified from hamster brain extracts – a method both time consuming and generating low yields. A suitable illustration of the issue is a fact that one of the most efficient protocols based on immobilised Cu^{2+} and cation exchange chromatography of detergent-extracted material provided yields in range of only 120 μg per 100 g of brain tissue (Pan *et al.*, 1992). Thus, structural studies of PrP benefitted greatly from development of bacterial overexpression systems. These recombinant expression systems provided an effective method of generating large yields in a much simpler manner, consuming less materials and labour.

Recombinant PrP from a number of species obtained from bacterial expression allowed for high resolution structural analysis of prions through NMR spectroscopy (Hornemann *et al.* 1996; Viles *et al.* 1997; Zahn *et al.* 2000). This, coupled with determination that the structure of native PrP purified from brain tissue is identical to recombinant one (Hornemann *et al.* 2004) allowed for recombinant prion protein to be widely used as a model of PrP^{C} behaviour.

Studies presented in this thesis focus on investigating folding pathways of prion proteins from different species via two primary methods: the study of early folding kinetics of mouse and Syrian hamster prion protein in order to investigate the influence of a disease preventing mutation Q167R on the folding pathway of PrP, and fibrilisation studies of hamster, mouse and elk PrP to determine the effects of disease-related mutations on formation of fibrils.

The early folding pathway of prion proteins was investigated using a number of spectroscopic and kinetic techniques such as circular dichroism and tryptophan fluorescence.

Tryptophan fluorescence measurements are particularly useful for studying protein folding pathways in aqueous solutions, since tryptophan residues within investigated protein can be selectively excited and act as a highly sensitive fluorescent probes responding to changes in their local environment induced by folding or unfolding of polypeptide chains. Upon unfolding of the protein, the tryptophan residues buried in hydrophobic core of the structure become solvent-exposed which is reflected in their spectral properties.

Application of tryptophan fluorescence to structural studies of PrP required carefully modified constructs to be used. The structure of prion proteins employed in fluorescence studies encompasses residues 90–231 of Syrian hamster and 91–230 of mouse proteins, representing the globular folded domain and short unstructured N-terminus section of PrP^{C} as well as proteinase K-resistant core of PrP^{Sc}. The remainder of the N-terminus containing residues 23–90 of MoPrP and 23–89 of SHaPrP is unstructured and thus unlikely to have any influence on the folding of globular domain. The two native tryptophan residues present in globular domain of PrP are solvent-exposed even in the folded state and thus unsuitable for protein folding monitoring by fluorescence. Consequently, both of the residues had to be removed by introducing point-mutations which replaced them with phenylalanines. Similarly, six tryptophans present in the unstructured domain would have to be removed if the N-terminus part of the protein was to be retained, a process both time and resource consuming. Since that particular region was deemed to be unimportant for folding of globular domain and consequently removed, only the residues in the globular domain were replaced. Following the removal of any undesirable native residues, site-directed mutagenesis can be used to introduce tryptophan residues in strategically important positions, allowing them to act as fluorescent reporters of structural changes. Such a strategy has been successfully employed by members of author's research group in kinetic and equilibrium folding studies of prion proteins (Sanghera and Pinheiro 2002, Kazlauskaite *et al.* 2003, Jenkins *et al.* 2008, Robinson and Pinheiro 2009).

Fibril formation by mouse, Syrian hamster and elk PrP was investigated in a series of fibrilisation and oligomeristaion studies using ThT fluorescence (Gill *et al.* 2009) involving both truncated and full length constructs. Positively charged ThT is known to bind to negatively charged nucleic acids as well as fibrils formed by α-synucleins and prion proteins. Upon binding, ThT molecules which exhibit low fluorescence emission upon excitation at 450 nm in water, show several-fold

enhancement in fluorescence intensity. This increase in emission is characteristic only for bound ThT and therefore is often used as a marker of fibril formation. Since ThT fluorescence measurements utilize different excitation and emission wavelengths than tryptophan fluorescence, both native tryptophans and unstructured N-terminus domain of PrP could be retained to investigate any effects they may have on fibril formation. This chapter details the methods used for expression and purification of recombinant constructs of mouse, hamster and elk prions, as well as their biophysical characterisation in order to confirm their identity, purity and structure for subsequent use in research detailed in experimental chapters of the thesis.

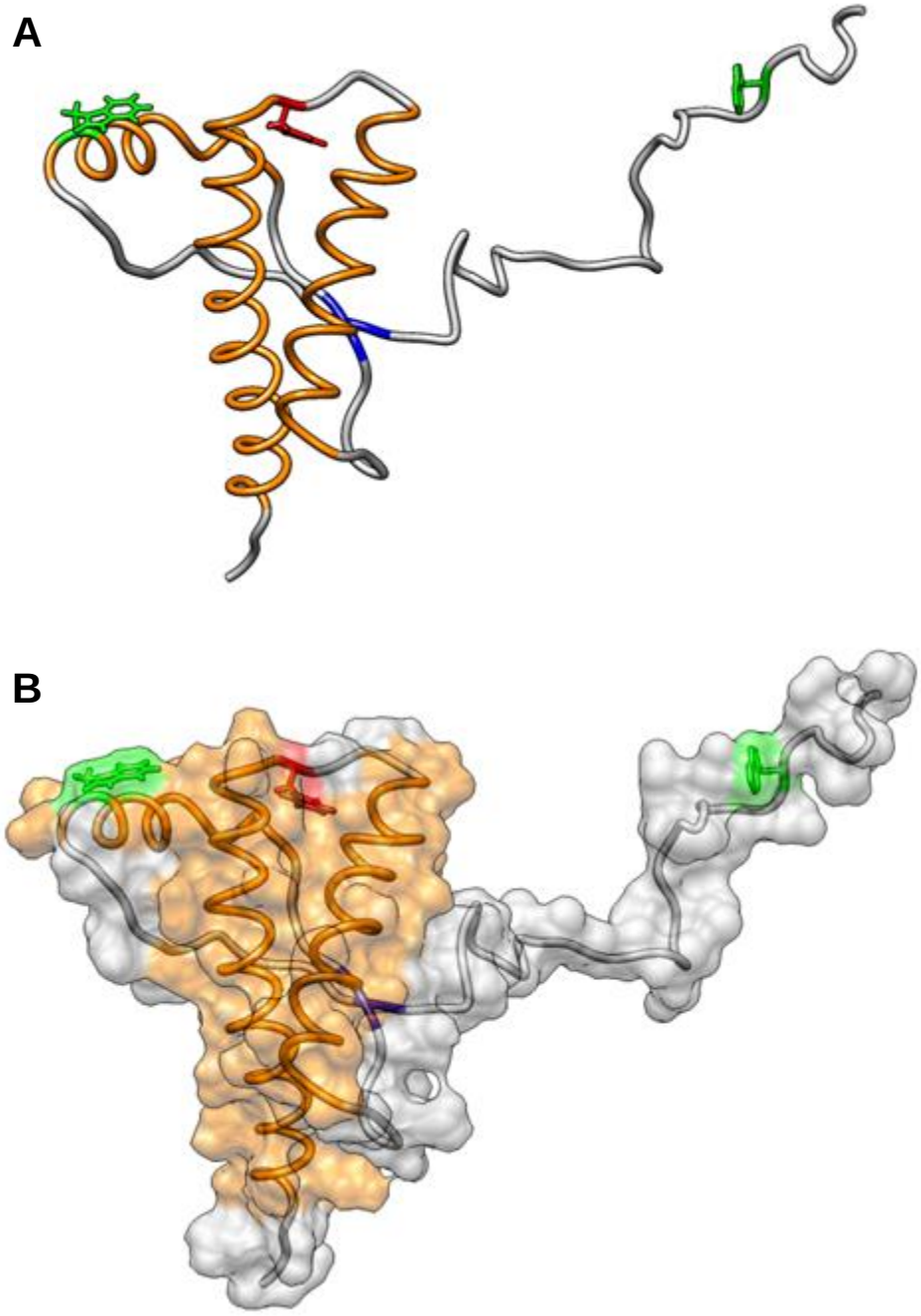

Figure 2.1 Ribbon representation (A) and space-filling model (B) of the structure of the C-terminal globular domain of mouse prion protein (residues 90–230) based on the NMR structure (Gossert *et al.* 2005). Main structural features are highlighted in colour with key residues shown using stick representation. Three main α-helices are shown in orange, with short antiparallel β-sheet S highlighted in blue. Native tryptophan residues at positions 98 and 144 are highlighted in green and phenylalanine residue at position 197 is highlighted in red.

The NMR structure was drawn from PDB file 1XYX using UCSF Chimera package from the Resource for Biocomputing, Visualization and Informatics at the University of California, San Francisco (supported by NIH P41 RR-01081).

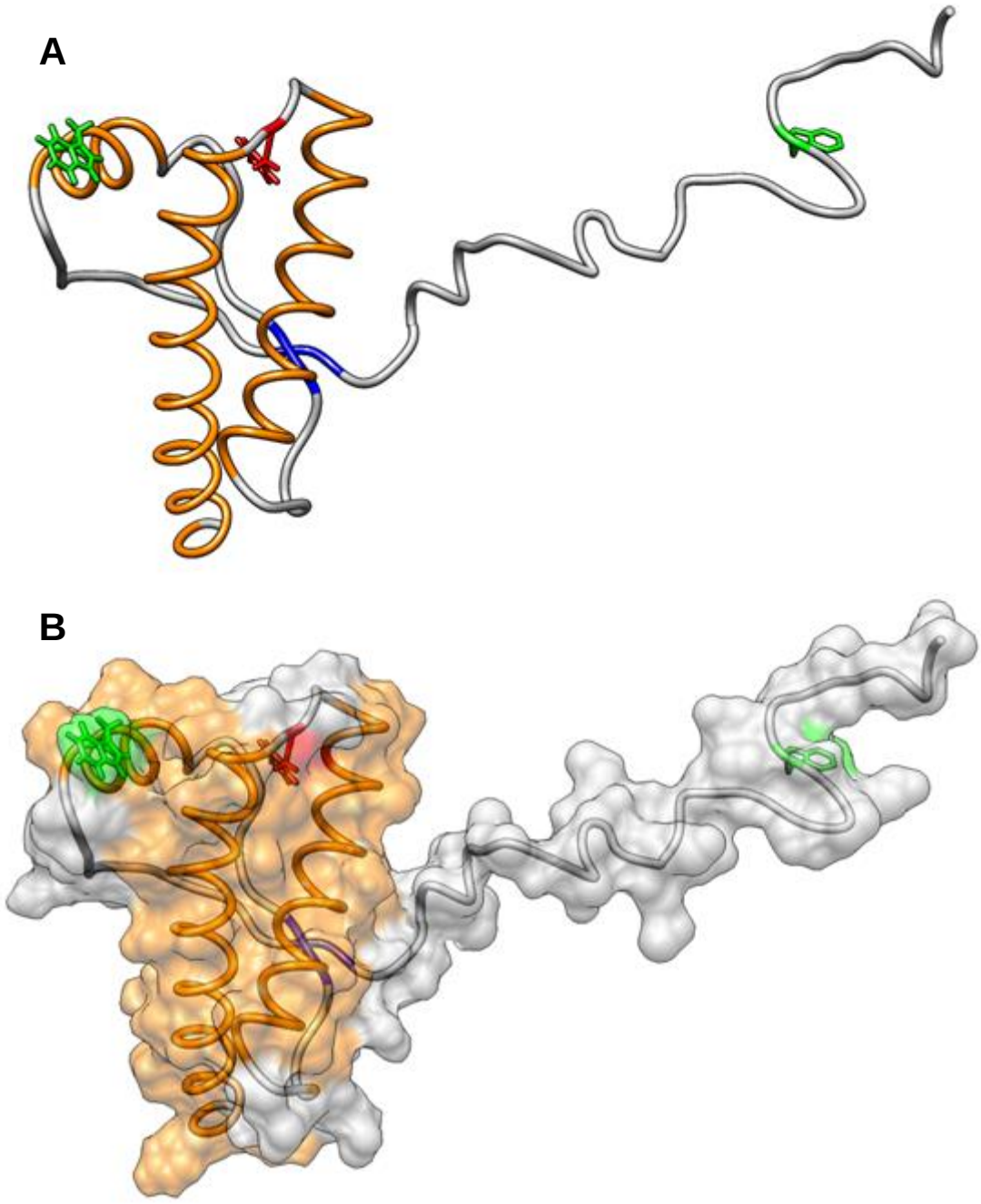

Figure 2.2 Ribbon representation (A) and space-filling model (B) of the structure of the C-terminal globular domain of Syrian hamster prion protein (residues 90–231) based on the NMR structure (James *et al.* 1997). Main structural features are highlighted in colour with key residues shown using stick representation. Three main α-helices are shown in orange, with short antiparallel β-sheet S highlighted in blue. Native tryptophan residues at positions 99 and 145 are highlighted in green and phenylalanine residue at position 198 is highlighted in red.

The NMR structure was drawn from PDB file 1B10 using UCSF Chimera package from the Resource for Biocomputing, Visualization and Informatics at the University of California, San Francisco (supported by NIH P41 RR-01081).

2.2 Materials and methods

2.2.1 Expression and purification of mouse and Syrian hamster prion proteins

2.2.1.1 Materials

Acrylamide/bis acrylamide was purchased from Geneflow (Stafforshire, UK).

Guanidine hydrochloride (GdnHCl) was purchased from Alfa Aesar (Heysham, UK).

2-mercaptoethanol, acetonitrile, ammonium persulfate, ammonium sulfate, EDTA, ethanol, glucose, glycerol, MgSO4, NaCl and potassium acetate were purchased from Fischer Scientific (Loughbotough, UK).

2-(N-morpholino)ethanesulfonic acid (MES), ampicillin, chloramphenicol, dithiothreitol (DTT) and isopropyl β-D-thiogalactoside (IPTG) were all purchased from Melford (Ipswitch, UK).

Peptone and yeast extract were purchased from Merck (Darmstadt, Germany).

SnakeSkin dialysis tubing was purchased from Pierce (Rockford, IL).

Triethanolamine was purchased from Lancaster (Morecombe, UK).

Trifluoroactic acid (TFA) was purchased from Acros Organics (New Jersey, USA).

All other materials and chemicals were purchased from Sigma-Aldrich (Poole, UK) unless stated otherwise.

2.2.1.2 Growth media

Lysogeny broth (LB) growth medium constituents: 10 g of peptone, 5 g of yeast extract and 10 g of NaCl, made up to 1 litre with distilled water and autoclaved prior to use.

AP5 growth medium constituents: 1.5 g glucose, 11 g casein acid hydrosylate, 0.6 g yeast extract, 0.19 g $MgS0_4$, 1.07 g NH_4Cl, 3.73 g KCl, 1.2 g NaCl, 60 ml 2 M triethanolamine pH 7.4 made up to 1 litre with distilled water.

Terrific Broth (TB) growth medium constituents: 12 g peptone, 24 g yeast extract, 4 ml glycerol, made up to 900 ml with distilled water and autoclaved. Following the autoclaving of the broth 100 ml of 0.17 M KH_2PO_4/ 0.72 M K_2HPO_4 was added.

NZY+ Transformation Broth constituents: 10 g casein acid hydrosylate, 5 g yeast extract, 5 g NaCl made up to 1 litre with distilled water (pH 7.5). Following the autoclaving of the broth 12.5 ml of 1 M $MgCl_2$, 12.5 ml of 1 M $MgS0_4$ and 10 ml of 2 M glucose were added. All solutions were filter-sterilised prior to their addition to autoclaved broth.

2.2.1.3 Competent cell buffers

TFB1 buffer constituents: 30 mM potassium acetate, 10 mM $CaCl_2$, 50 mM $MnCl_2$, 100 mM RbCl, 15 % (v/v) glycerol, pH 5.8.

TFB2 buffer constituents: 10 mM MOPS, 75 mM $CaCl_2$, 10 mM RbCl, 15% (v/v) glycerol, pH 6.5.

2.2.1.4 Purification solutions

Buffer A constituents: 25 mM TrisHCl, pH 8, 5 mM EDTA.

Buffer B constituents: 8 M Guanidine HCl, 25 mM Tris-HCl pH 8, 100 mM DTT.

Buffer C constituents: 6 M Guanidine HCl, 50 mM Tris-HCl, pH 8.

Solvent 1: 0.1 % TFA (v/v) in water.

Solvent 2: 0.09 % TFA (v/v) in acetonitrile.

2.2.1.5 SDS-PAGE solutions

Resolving Gel solution constituents: 375 mM Tris (pH 8.8), 15 % acrylamide, 0.1 % SDS, 0.1 % ammonium presulfate, 0.004 % TEMED.

Stacking Gel solution constituents: 100 mM Tris (pH 6.8), 5 % acrylamide, 0.1 % SDS, 0.1 % ammonium persulfate, 0.001 % TEMED.

Running Buffer constituents: 25 mM Tris base, 192 mM glycine, 0.1 % SDS, pH 8.3.

Sample Buffer constituents: 62.5 mM Tris-HCL pH 6.8, 10 % glycerol (v/v), 2 % SDS, 5 % 2-mercaptoehtanol, 0.05 % bromophenol blue.

Staining Solution constituents: 10 % ammonium sulphate, 0.1 % Coomassie G250, 20 % ethanol, 3 % phosphoric acid.

2.2.1.6 Expression plasmids

The pET23a plasmid encoding mouse PrP Met(91-230) (Figure 2.3, panel A) was provided by Professor David Brown, University of Bath. The plasmid was modified by Dr. Phil Robinson, University of Warwick to encode single-tryptophan mutant. Site-directed mutagenesis was used to replace native tryptophans at positions 98 and 144 with phenylalanines and introduce folding sensitive tryptophan at position 197 in place of native phenylalanine.

The pET23a plasmid requires bacteriophage T7 RNA polymerase for expression as it contains a T7 promoter (Studier and Moffatt 1986). Expression of T7 RNA polymerase in *E. coli* cells can be induced by addition of IPTG, consequently driving expression of the target gene encoded on the plasmid. It should be noted that the plasmid contains a "plain" T7 promoter with both *lacI* gene and *lac* operator absent.

The pIngPrP plasmid encoding SHaPrP(90-231) (Figure 2.3, panel B) was obtained from Professor Stanley Prusiner. This plasmid was a modified version of phGH1 (Chang, Rey *et al.* 1987). Modified version of the pIngPrP plasmid encoding single-tryptophan mutants was prepared by Dr. Ian Sylvester, Institute of Animal Health. Modified plasmids had their native tryptophans at positions 99 and 145 replaced with phenylalanines using site directed mutagenesis. Additional tryptophan was introduced at position 198 in place of native phenylalanine to act as fluorescent reporter of structural changes.

Since in pIngPrP plasmid expression of the PrP gene is under control of Ppho promoter from *E. coli* alkaline phosophatase A, the protein is expressed in high levels under low phosphate conditions. Expressed protein contains a signal sequence STII from the *E. coli* heat-stable enterotoxin II, which targets PrP to the periplasmic space of the *E. coli*. There, the signal sequence is cleaved (Mehlhorn, Groth *et al.* 1996) and mature protein forms insoluble aggregates – a property exploited by purification protocol.

Both pET23a and pIngPrP plasmids encode the ampicillin resistance gene (see Figure 2.3).

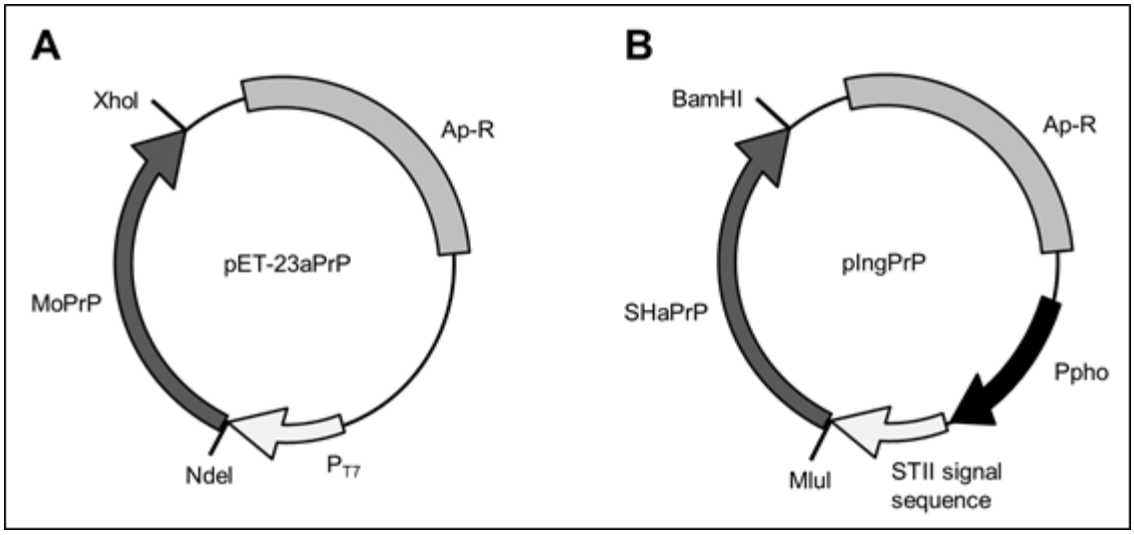

Figure 2.3 Expression plasmids pET23a (A) encoding Mouse PrP(Met91-230) and pIngPrP (B) encoding Syrian hamster PrP(90-231). The T7 promoter (P_{T7}, plasmid A) and phosphatase A promoter (Ppho, plasmid B) are indicated by white and black arrows respectively. Restriction sites used for PrP gene insertion are shown as black lines perpendicular to the plasmid and the genes themselves are represented by dark grey arrows. Ampicillin resistance genes (Ap-R) on both plasmids are highlighted in light grey.

2.2.1.7 Preparation of competent cells

Two strains of competent cells have been used throughout the project: Escherichia coli (*E.coli*) 27C7 cells obtained from ATCC (55244) used for Syrian hamster PrP expression and *E. coli*, BL21 Star obtained from Invitrogen, (Paisley, UK) used for mouse PrP expression. Competent cells of a given strain were streaked onto LB agar plate and incubated overnight at 37°C. The following day single colonies were selected and used to inoculate 2.5 ml cultures of LB medium which were subsequently incubated overnight at 37°C with shaking (200 rpm). The following morning starter 2.5 ml cultures were used to inoculate 250 ml of LB medium containing 20 mM $MgSO_4$. The cells were then incubated at 37°C with shaking until the absorbance of the culture at 600 nm wavelength (A_{600}) reached values of 0.4–0.6. Upon reaching the optical density of 0.4–0.6, cells in the liquid culture were harvested through centrifugation at 4,500 *g* for 5 minutes at 4°C. Resulting pellet was re-suspended in 100 ml of ice-cold TFB1 and incubated for 5 minutes on ice. Following incubation, the cells were again centrifuged at 4,500 g for 5 minutes at 4°C and the resulting pellet was re-suspended in 10 ml of ice cold TFB2. Re-suspended cells were incubated on ice for 30 minutes, flash frozen in liquid nitrogen and alliquoted for storage at -80°C.

2.2.1.8 Transformation of competent cells

Transformation of competent cells and any subsequent procedures involved in expression of prion proteins up to and including solubilisation of PrP-containing inclusion bodies were carried out in class-3 bio-containment suite.
50 µl aliquot of the appropriate competent cells (*E. coli* 27C7 cells for SHaPrP(90-231) expression and *E. coli* BL21* Rosetta cells for MoPrPMet(91-230) expression) was thawed on ice and 10 ng of relevant plasmid was added. Transformation mixture was gently mixed for approximately 1 minute and incubated on ice for 30 minutes. Following a 45 second heat shock at 37°C the transformation mixture was added to 0.5 ml of NZY+ medium and incubated for 45 minutes at 37°C with shaking. Transformed cells were selected by spreading a 100 µl aliquot of the transformation mix onto LB agar plate containing 100 µg/ml ampicillin and 35 µg/ml chloramphenicol for

MoPrPMet(91–230) or 100 μg/ml ampicillin and 25 μg/ml kanamycin for SHaPrP(90–231) and incubating the plate overnight at 37°C.

2.2.1.9 Expression of PrP

Single colonies of transformed cells were picked from selection plates and transferred to 5 ml of LB containing 100 μg/ml of ampicillin and 35 μg/ml chloramphenicol for MoPrP or 100 μg/ml ampicillin and 25 μg/ml kanamycin for SHaPrP. The cultures were incubated at 37°C overnight (14–16 hours) with shaking at 200 rpm. 5 ml overnight cultures were then used to inoculate 1 l flasks of appropriate growth media: terrific broth for MoPrP and AP5 medium for SHaPrP expression. One litre liquid cultures were incubated overnight at 37°C with shaking (150 rpm). MoPrP expression was induced when the cells reached optical density at A_{600} of 0.4–0.6 by the addition of 0.4 mM IPTG. Since expression of SHaPrP is auto-induced on phosphate depletion, the cultures were simply left to grow overnight for approximately 20–24 hours. Following overnight incubation, the cells were harvested through centrifugation at 3,250 g for 30 minutes at 4°C. Expression was confirmed through SDS-PAGE analysis of 500 μl aliquots of liquid cultures obtained prior to cell harvesting.

2.2.1.10 Isolation and solubilisation of inclusion bodies

The cell pellets isolated from liquid cultures through centrifugation were re-suspended in buffer A, pooled into two 250 ml centrifuge flasks and re-pelleted through centrifugation at 13,000 g for 30 minutes at 4°C. The supernatant yielded by centrifugation was discarded and the pellet re-suspended again in buffer A. The pellets were then sonicated for 20 seconds with 30 second rests between bursts to break open the cells. Sonication cycle was repeated three times and resulting cell paste was then centrifuged at 13,000 g for 30 minutes at 4°C. Obtained supernatant was discarded to remove soluble proteins and centrifugation was repeated to wash the inclusion bodies. Following second round of centrifugation, the pellets were solubilised in buffer B and sonicated by short 5-second bursts with 10 second intervals over a 5 minute period.

Sonicated cell extract was then centrifuged at 14,000 g for 30 minutes at 4°C and the soluble fraction containing PrP was carefully pooled. In order to ensure sterility of the inclusion body extract, a 100 µl sample was spread on a LB agar plate and only removed from the containment laboratory when no colonies could be observed on the plate after overnight incubation at 37°C.

2.1.1.11 Size exclusion chromatography

As a first step of purification, 4 ml aliquots of solubilised inclusion bodies were loaded onto a 26/60 sephacryl S-300 high resolution gel filtration column (Amersham Biosciences, Buckinghamshire, UK) equilibrated with buffer C over the night before. The column was attached to AKTA Prime chromatography system (GE Healthcare, Buckinghamshire, UK). During the purification 4 ml fractions were collected across the elution profile and 200 µl aliquots were removed for analysis through SDS-PAGE. Following the analysis, PrP-containing fractions were pooled for subsequent oxidation.

2.2.1.12 Oxidation of PrP

In order to maximize the yield of α-helical form of PrP, the disulphide bond present in prion protein had to be formed prior to further purification by HPLC. Oxidation of cysteine residues necessary for the formation of disulphide bridge was achieved using either Cu^{2+} ions or glutathione.. Mouse PrP(91-230) was oxidised using 30 µM copper sulfate. Syrian Hamster PrP(90–231) was oxidised using oxidised form of 0.2 mM glutathione in the presence of 5 mM EGTA. Both oxidation processes were accomplished by adding relevant oxidising agent directly to the pooled fractions and incubating them overnight at room temperature (20–25°C).

2.2.1.13 Reverse phase HPLC

Second step of purification protocol involved PrP separation on a 3 ml RESOURCE^{TM} RPC column (GE Healthcare). The column was attached to Jasco HPLC system consisting of two PU-980 pumps with a HG-980-30 solvent mixer and a UV-975 detector unit. During each HPLC run a 20 ml aliquot of the pooled size-exclusion fractions was injected onto the column, which was then washed with solvent A until UV signal returned to zero. In order to elute PrP bound to the column, an acetontirile gradient from 0 % to 100 % was applied over the course of 12 minutes. Eluting fractions were collected according to their UV absorbance trace and their PrP content verified by SDS-PAGE.

2.2.1.14 Refolding of PrP

Following purification, HPLC fractions containing PrP in acetonitrile and 0.1 % TFA were dialysed against 5 litres of 2 mM MES pH 5 at 4°C. The dialysis procedure was repeated twice to ensure no acetonitrile or TFA content in PrP-containing fractions. Dialysed PrP was then concentrated using Centriprep® centrifugal filter devices (Millipore, Billerica, MA). Concentration process involved centrifugation at 13,000 g at 4°C in a desktop centrifuge to remove any aggregates. Conformation of concentrated PrP was then determined using far-UV circular dichroism. Upon confirmation of α-helical structure of PrP, protein was aliquoted and flash frozen in liquid nitrogen for -20°C storage.

Prior to every experiment, PrP samples were thawed and their concentration determined spectrophotometrically using a molar extinction coefficient ε_{280} of 25,700 M^{-1} cm^{-1} for $MoPrP^{Wt}$ and $MoPrP^{Q167R}$, 20,100 M^{-1} cm^{-1} for $MoPrP^{F197W}$ and $MoPrP^{F197W/Q167R}$ and 24420 M^{-1} cm^{-1} for $SHaPrP^{Wt}$ (Gill and von Hippel 1989).

2.2.1.15 SDS-PAGE analysis

Following every step of purification, protein-containing fractions were analysed through SDS-PAGE (Laemmli 1970) to confirm the presence of PrP at various stages of the procedure and determine its purity. Prior to SDS-PAGE analysis, protein samples were diluted in sample buffer in 1:1 ratio and heated to 95 °C for 5 minutes. Boiled samples were then loaded onto 15 % polyacrylamide gels prepared from resolving and stacking solutions as stated in Section 2.2.1.5. Following electrophoresis, the gels were left in colloidal coomasie staining solution to visualise the proteins.

Samples of crude extract as well as those collected after size-exclusion chromatography but before the HPLC separation required additional processing prior to their analysis by SDS-PAGE. High concentrations of GdnHCl present in buffers B and C interfere with protein separation through SDS-PAGE due to their high salt concentrations which prevent SDS-binding to the protein and consequently disrupt electrophoresis. Consequently, these salts had to be removed by precipitating the protein in acetone (procedure referred to as acetone-wash). The procedure involved adding 300 µl of sterile water followed by 1 ml of 100% acetone to each 200 µl aliquot and freezing the sample on dry ice for 15 minutes. Frozen samples were then centrifuged at 13,000 g for 30 minutes at 4°C in a desk top centrifuge to pellet the precipitated protein. The pellets were then re-suspended in adding 500 µl of sterile water and 1 ml of 100% acetone, frozen on dry ice for 15 minutes and centrifuged at 13,000 g for 30 minutes at 4°C. Second step of the procedure was repeated two more times, after which precipitated samples were re-suspended in sample buffer and analysed through SDS-PAGE.

2.2.2 Characterisation of purified PrP

2.2.2.1 Mass spectrometry

Molecular weight of purified PrP was verified through positive electrospray ionisation mass spectrometry (ESI-MS) performed by Biological Mass Spectrometry Facility in the School of Life Sciences, University of Warwick.

2.2.2.2 Circular dichroism spectroscopy

Structural properties of purified PrP were determined by measuring the far-UV (190–260 nm) circular dichroism spectra using JASCO J-815 spectropolarimeter. All spectra were measured using 1 mm path length quartz cuvettes, with a scanning rate of 100 nm / minute, time constant of one second, bandwidth of 1.0 nm, and resolution of 0.5 nm. Typically 16 scans were averaged per spectrum and corresponding buffer backgrounds were subtracted from the final spectra. All measurements were carried out at 20 °C.

For far-UV CD measurements, mean residue ellipticity ($[\theta]_{MRW}$) was calculated using Equation 3.1:

$$[\theta]_{MRW} = \frac{\theta}{Ncl \times 10} \tag{3.1}$$

where θ is the observed ellipticity (millidegrees), *N* is the number of peptide bonds in the protein, *c* is the molar protein concentration, and *l* the pathlength of the cuvette used (cm).

2.3 Results

2.3.1 Expression and purification of PrP

Relevant strains of *E. coli* cells were transformed using plasmids containing PrP gene. Selection plates containing two antibiotics were used to ensure that only transformed cells expressing newly introduced plasmids survived. Upon successful transformation, selected colonies were used to inoculate liquid cultures and overexpression of PrP-encoding plasmid was ensured either by IPTG induction (MoPrP) or phosphate depletion (SHaPrP). Succesfull expression of PrP was confirmed using SDS-PAGE (see Figure 2.4). Since overexpressed prion protein aggregated within the inclusion bodies, harvested cells were disrupted and solubilised in 8 M GdnHCl

solution with 100 mM DTT added. Consequently, solubilised proteins were unfolded and had their disulfide bond reduced.

In order to isolate prion proteins from cell extract, a two-step purification protocol was used.

The first step of purification involved using size-exclusion chromatography (SEC) under denaturing conditions to separate PrP from *E. coli* proteins with higher molecular weight. Size-exclusion fractions containing PrP were identified using SDS-PAGE analysis (see Figure 2.5) which also allowed for the purity of PrP to be estimated.

Due to the fact that DTT was separated from protein sample during size exclusion chromatography, PrP could oxidise in air following the first purification step. Consequently, PrP-containing fractions isolated at the end of SEC protocol consisted of a mixture of oxidised and reduced prion proteins. It has been demonstrated that while purification of oxidised PrP yields protein with high α-helical content, isolating the same protein under reducing conditions generates PrP with elevated β-structure content (Mehlhorn *et al.* 1996, Kazlauskaite *et al.* 2003). It was therefore vital to ensure that PrP in SEC fractions was oxidised prior to second purification step. In order to achieve this, PrP-containing fractions were incubated with either copper sulfate (MoPrP) or glutathione (SHaPrP).

During the second step of purification protocol reverse-phase HPLC was used to further separate PrP from *E. coli* proteins with molecular weight too close to that of prion protein to be resolved by size-exclusion chromatography. Upon binding to the column, PrP can only be eluted using 35-37% acetonitrile which is then removed by dialysis at the end of purification protocol. HPLC fractions containing PrP are again identified using SDS-PAGE which also allows for the final purity to be determined (see Figure 2.6).

PrP samples were considered suitable for experimental use when their purity exceeded 90%. If the estimated final purity of PrP sample was insufficient, additional size-exclusion chromatography step was performed. The final yield of PrP varied between consecutive expressions, usually between 6-9 mg per one litre of liquid culture.

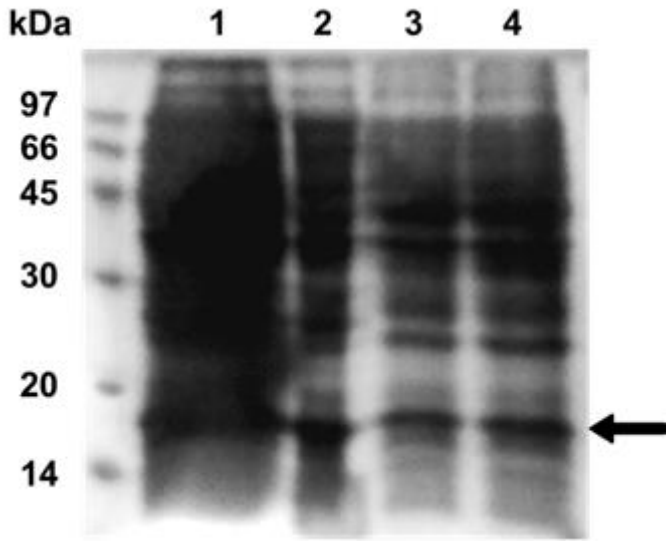

Figure 2.4 Picture of SDS-PAGE gel used for analysis of cell extract from *E. coli* cells expressing single tryptophan mutant of MoPrP(Met91-230). Lines 1 and 2 were loaded with cell extract while columns 3 and 4 were loaded with aliquots of solubilised inclusion bodies.

The band corresponding to PrP is indicated with black arrow.

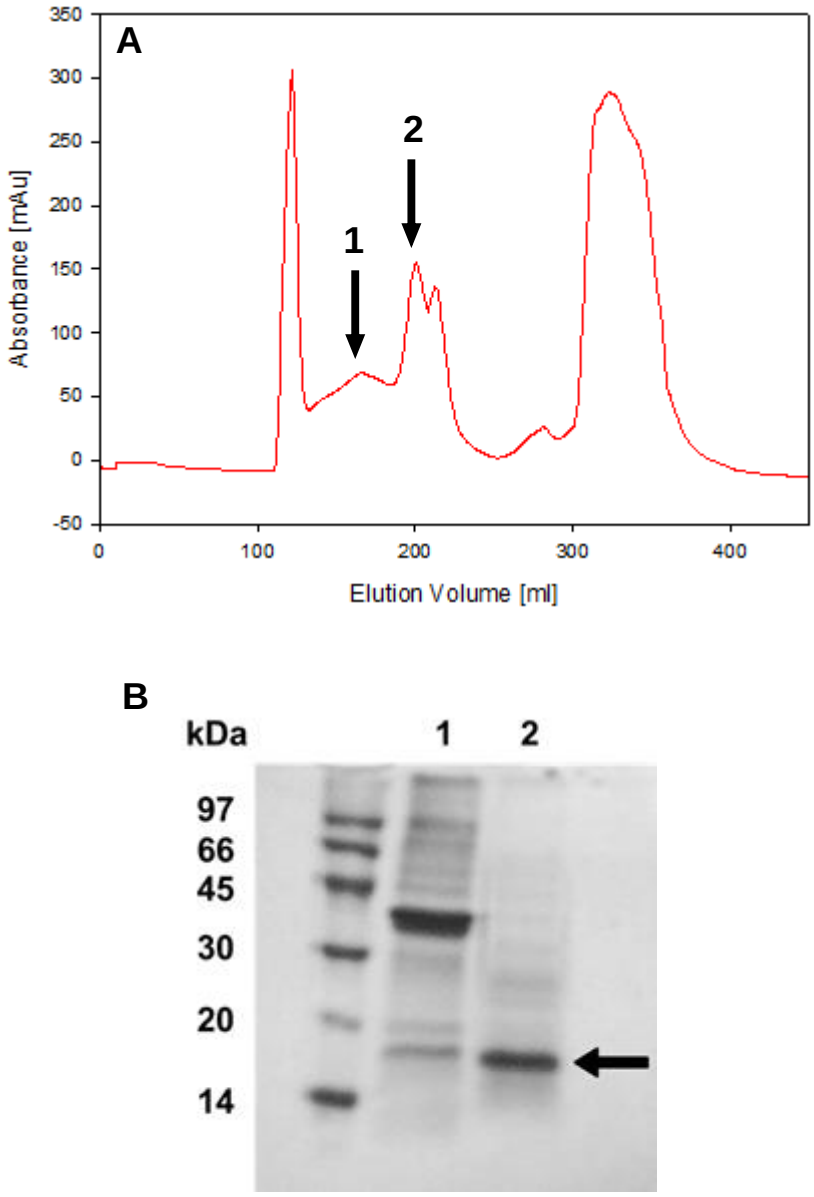

Figure 2.5 First step of PrP purification: isolation of prion protein from cell extract using size-exclusion chromatography.

Panel A depicts elution profile of MoPrP recorded during size-exclusion chromatography. Fractions corresponding to peaks 1 and 2 (indicated with black arrows) were suspected to contain PrP and were analysed by SDS-PAGE.

Panel B shows picture of SDS-PAGE gel used for analysis size-exclusion fractions. Lines 1 and 2 correspond to pooled fractions from peaks 1 and 2 in Panel A. The band corresponding to PrP is indicated with black arrow.

The purity of MoPrP isolated through size-exclusion chromatography was estimated to be between 75 and 80 %.

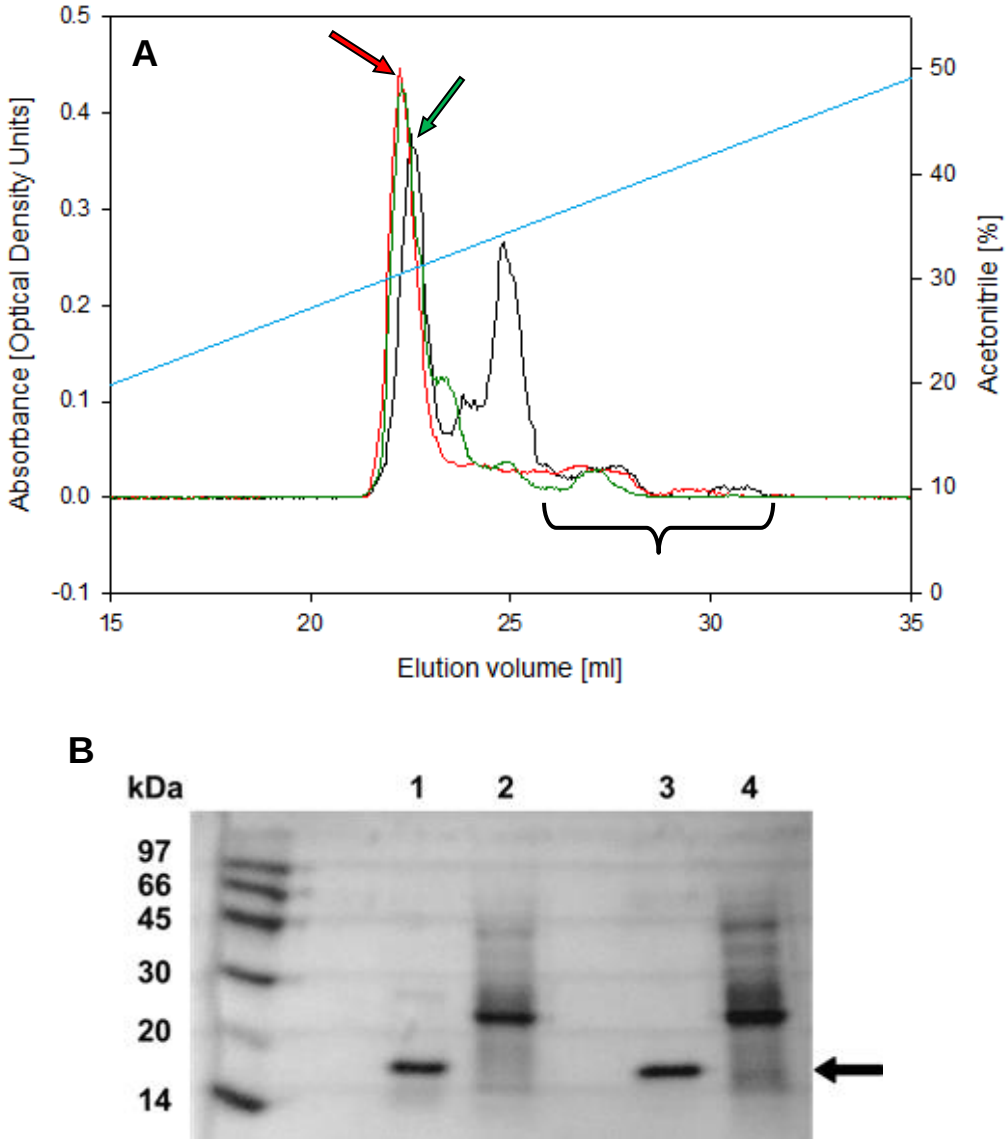

Figure 2.6 Second step of PrP purification: isolation of prion protein from similarly sized proteins present in SEC fractions using HPLC.

Panel A depicts elution profile of PrP prior to oxidation (black line), MoPrP oxidised using copper (red line) and SHaPrP oxidised with glutathione. Acetonitrile gradient used to elute PrP is represented by blue line and corresponds to the y-axis on the right hand side.

Panel B shows picture of SDS-PAGE gel used for analysis HPLC fractions. Line 1 corresponds to pooled fractions from MoPrP peak indicated with red arrow on the chromatogram. Line 3 corresponds to SHaPrP fractions indicated with green arrow. Lines 2 and 4 show contents of multiple small peaks indicated in chromatogram by black bracket. The SDS-PAGE band corresponding to PrP is indicated with black arrow. The purity of PrP isolated by HPLC was estimated to be around 95 %.

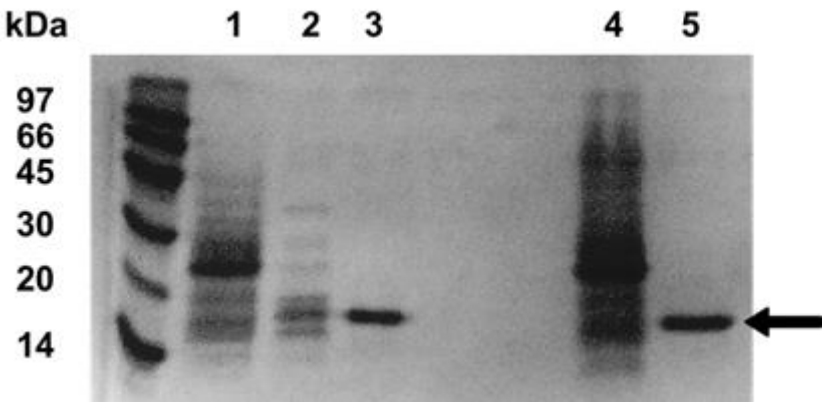

Figure 2.7 Photograph of SDS-PAGE gel showing comparison of MoPrP purity at different purification steps.

Line 1 corresponds to cell extract from E. coli expressing MoPrP, line 2 corresponds to size-exclusion fractions containing MoPrP and line 3 shows the final purity of refolded MoPrP after HPLC.

Lines 4 and 5 correspond to aliquots taken before (line 4 – cell extract) and after (line 5 – post-HPLC) the purification of SHaPrP.

The SDS-PAGE bands corresponding to PrP are indicated with black arrow.

The final purity of both MoPrP and SHaPrP was estimated to be over 95 %.

2.3.2 Characterisation of purified PrP

Upon successful purification, molecular weight of isolated prion proteins was confirmed using electrospray-ionisation mass spectrometry (ESI-MS).
Mass of mouse PrP single tryptophan mutant F197W was estimated as 16,104 Da, that of disease-related single tryptophan mutant Q167R as 16,132 Da and that of single-tryptophan Syrian hamster PrP as 16,201 Da. All of the molecular masses are in agreement with those determined through ESI-MS (see Figures 2.8 and 2.9).
Note that actual masses of single-tryptophan mutants F197W and Q167R given by deconvoluted ESI-MS spectra are 15,972 Da and 16,001 Da respectively. The difference between predicted and estimated mass is due to the cleavage of N-terminal methionine residues of both species of mouse PrP. The cleavage occurs during a post-translational modification catalysed by methionine aminopeptidase which targets specific amino acids adjacent to N-terminal methionine. In both prion constructs this position is occupied by glycine which is one of the substrates of methionine aminopeptidase and is therefore cleaved. Upon taking the post-translational modification into account, estimated masses of F197W and Q167R should be 15,972 Da and 16,001 Da respectively, which agrees with masses determined experimentally by mass spectrometry.

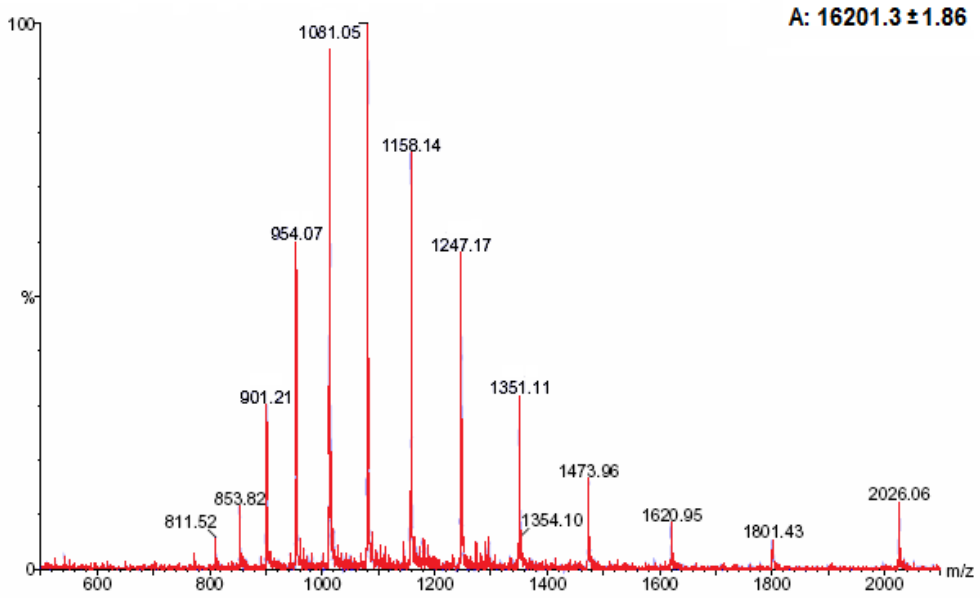

Figure 2.8 ESI mass spectrometry of single tryptophan mutant SHaPrP(90-231) F198W. Molecular mass estimated from the spectrum is 16201.3±1.86 Da which is well in agreement with calculated mass.

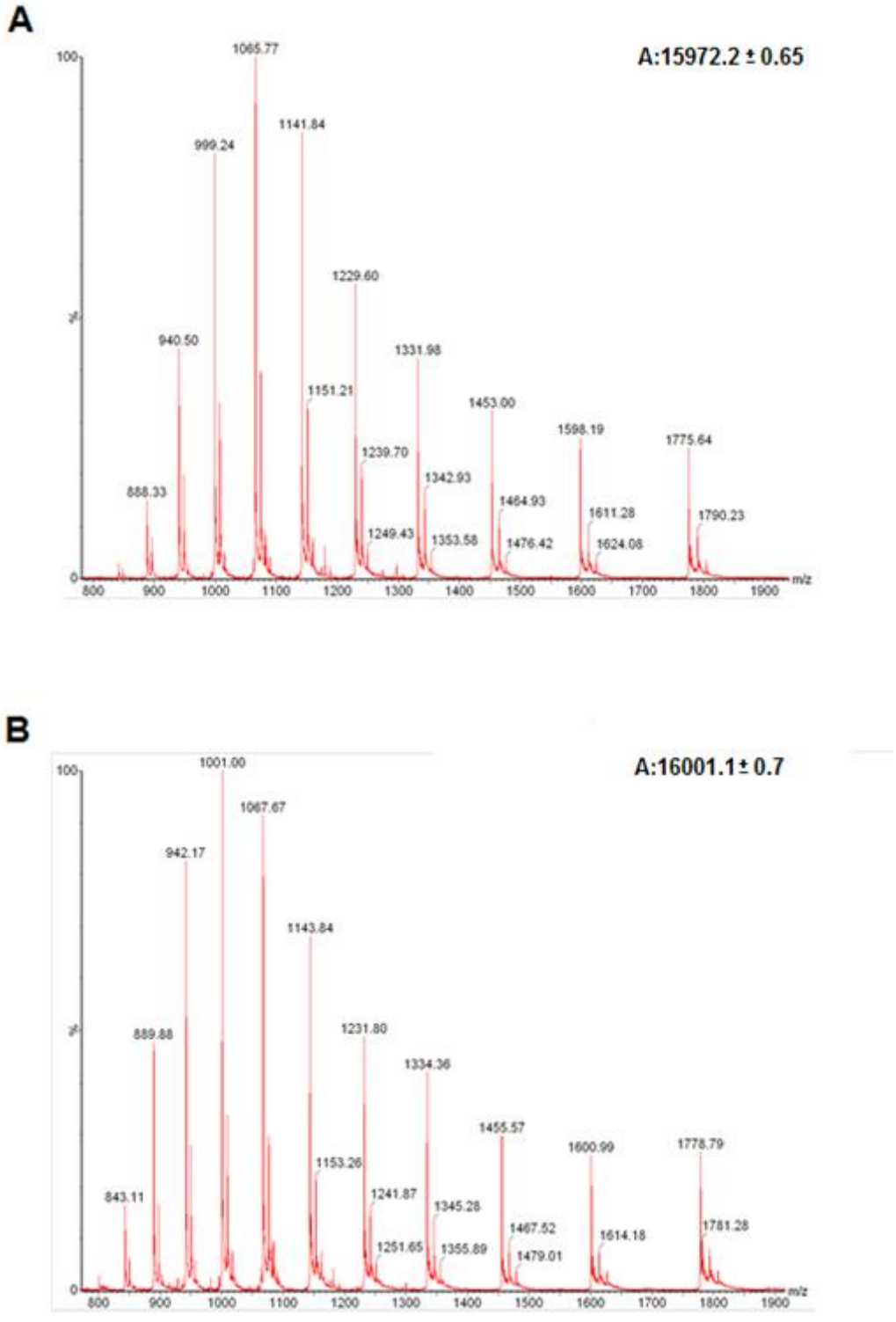

Figure 2.9 ESI mass spectrometry of single tryptophan mutant MoPrP(91-230) F197W (panel A) and disease-related single tryptophan mutant MoPrP(91-230) Q167R. Molecular masses estimated from the spectra are 15972.2±0.65 Da for F197W and 16001.1±0.7 for Q167R which corresponds to calculated masses.

While mass spectrometry allowed to confirm that molecular mass of purified proteins agrees with calculated mass of all three PrP constructs, further characterisation of obtained prion proteins was necessary to ensure they were expressed and purified correctly. Circular Dichroism was used in order to confirm that purified PrP has been successfully refolded to native α-helical form (PrP^C) upon its dialysis from HPLC buffer into 2 mM pH 5.5 MES buffer used for storage. Since removing native tryptophans and introducing fluorescent probe in place of phenylalanine was already determined to have no effect on secondary or tertiary structure of neither two MoPrP constructs nor SHaPrP one (Jenkins D., 2006, Robinson P., 2009), circular dichroism was used exclusively to confirm the structure of prion proteins prior to their experimental use.

The main components of the circular-dichroism spectrum characteristic for α-helical proteins are negative bands at 208 and 222 nm and a positive band at 195 nm. All of these bands are clearly visible in CD spectra of both mouse constructs (F197 and Q167R) as well as that of Syrian hamster (F198W) indicating that all of the proteins adopted correct α-helical conformation (see Figures 2.10 and 2.11).

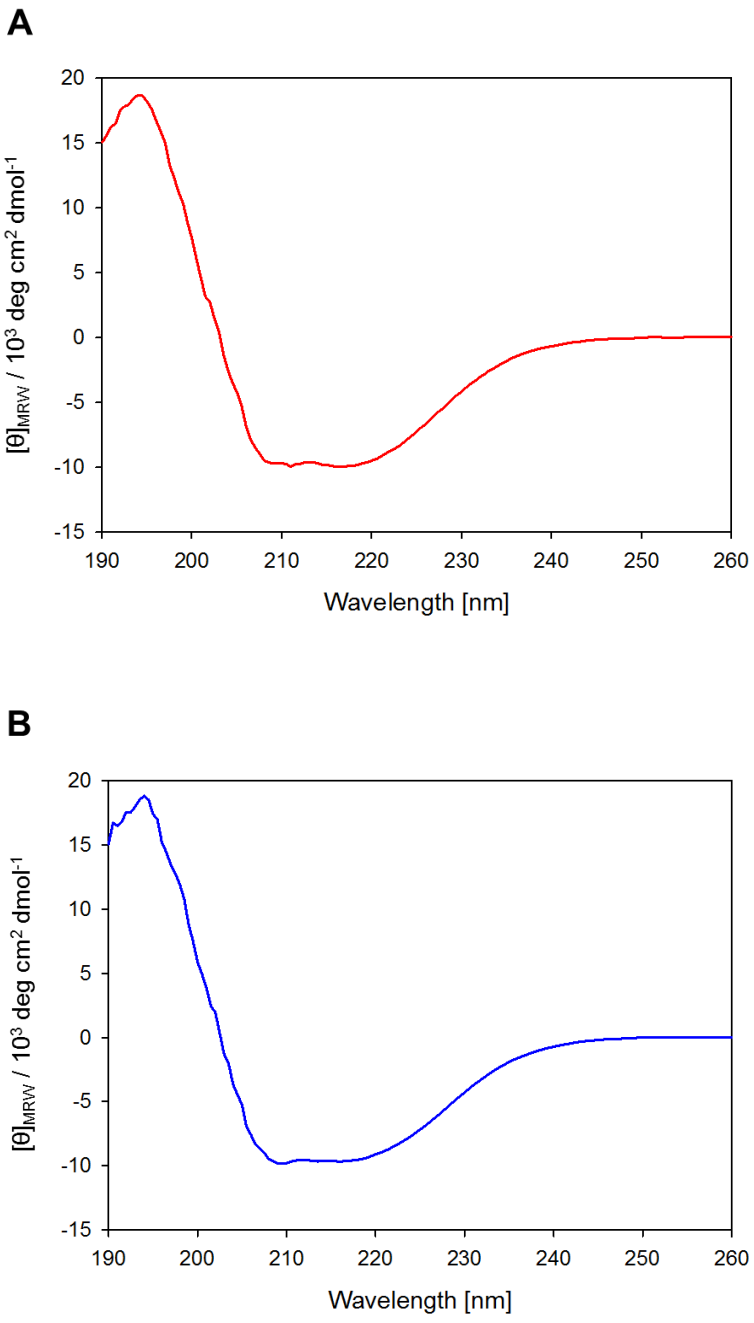

Figure 2.10 Far-UV circular dichroism spectra of single tryptophan mutants of MoPrP. Panel A shows spectrum of single tryptophan mutant F197W while panel B depicts spectrum of disease-related mutant Q167R. Note the presence of two negative peaks at 222 and 208 nm and single positive peak at 195 nm characteristic for proteins with high α-helical content.

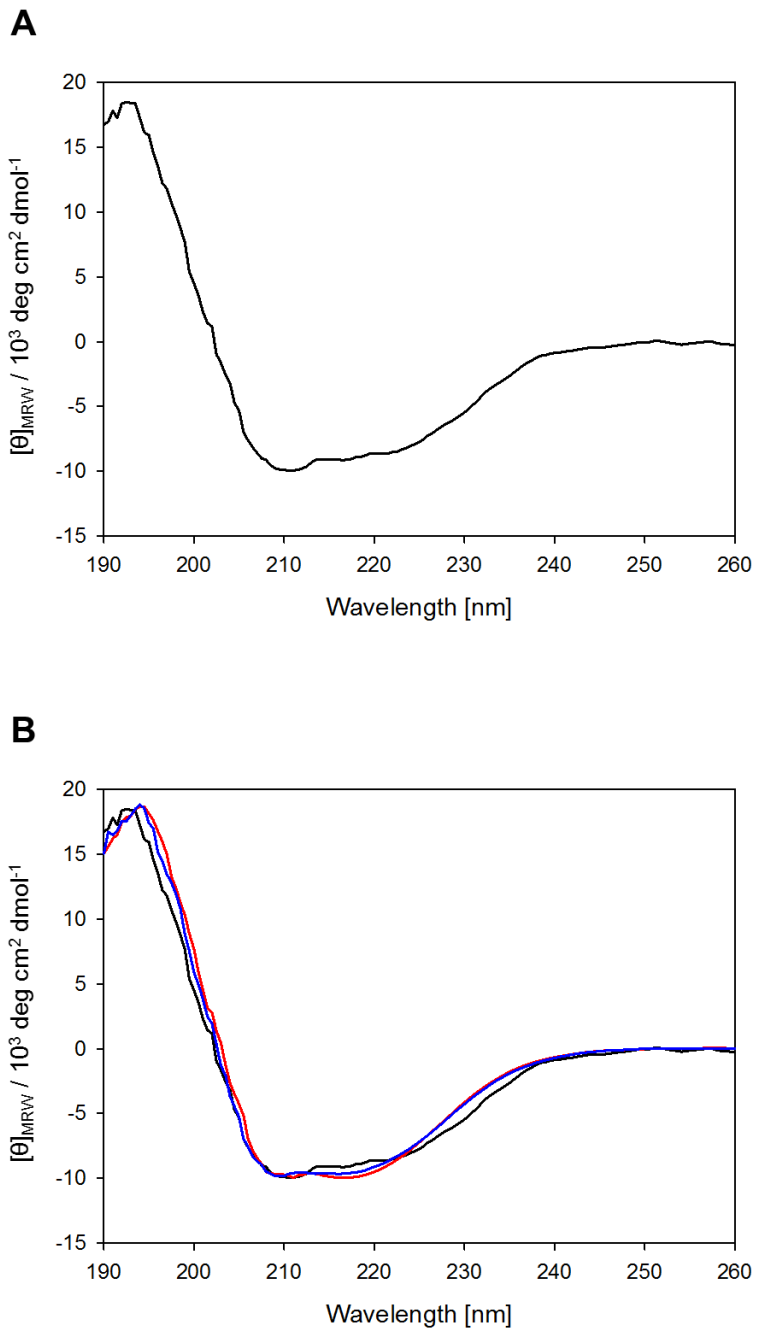

Figure 2.11 Far-UV circular dichroism spectra of single tryptophan mutant of SHaPrP (panel A) and an overlay of CD spectra of MoPrP F197W, MoPrP Q167R and SHaPrP F198W (panel B).While all three proteins have clearly α-helical secondary structure, minor differences between mouse PrP and Syrian hamster prions are visible. Note that the structure of MoPrP F197W and that of MoPrP Q167R are virtually identical, indicating that additional point mutation in disease-related prion strain does not affect the structure of the protein.

2.4 Summary

Two recombinant prion proteins - mouse PrP(Met91-230) and Syrian hamster PrP(90-231) have been successfully expressed and purified according to well-established two-step protocol combining size-exclusion chromatography and HPLC. Purity and identity of all three constructs was confirmed by SDS-PAGE analysis. Final purity of 95% for all three constructs and the average yield of 6-9 mg / L were satisfactory and proved that purification protocol was effective.
Electrospray-ionisation mass spectrometry was used to confirm molecular weight of purified proteins. Molecular mass of all constructs determined experimentally corresponded to theoretical mass calculated from their sequences, however cleavage of mouse prions by methionine aminopeptidase had to be accounted for.
Circular dichroism spectroscopy confirmed that all of the proteins were refolded to native, predominantly α-helical conformation and were ready for experimental studies detailed in chapters 3 and 4.

Chapter 3: Investigation of mechanisms of species barrier and disease-altering polymorphism by pressure-jump spectroscopy and fibrilisation studies.

3.1 Introduction

It has been recently reported that the key difference in PrP folding between different species known for their vastly different prion susceptibility is the ability of PrP to form a β-structured state under slightly destabilizing conditions such as low urea concentration or mildly acidic pH (Khan *et al.*, 2010). It has also been proposed that the β-state was in fact a folding intermediate which lies between the native and unfolded state on the PrP folding pathway (Zhang *et al.*, 1997; Hornemann and Glockshuber, 1998; Swietnicki *et al.*, 2000). Should the β-state of PrP play a role in the mechanism underlying prion diseases, as has been suggested (Collinge and Clarke, 2007), the propensity to form the β-state may be a major determinant of prion disease susceptibility.

Consequently, investigating the folding properties of PrP from different species, as well as disease-associated mutants should increase our understanding of both the misfolding mechanisms associated with the disease's occurrence and the phenomenon of the species barrier and varied disease susceptibility.

While certain spectroscopic techniques such as stopped-flow can be used to investigate later events in PrP folding pathway (Apetri *et al.*, 2006), the earliest folding events occur well within a millisecond, which is beyond the timescale accessible by stopped-flow instrument. Consequently, a different spectroscopic method, capable of achieving the dead time an order of magnitude shorter than stopped-flow is necessary. One of the few instruments capable of investigating the full extent of rapid reactions such as PrP folding is continuous-flow. It should be noted that while the author had direct access to one such instrument, it was undergoing re-evaluation, reconfiguration and upgrading as a separate part of this project (see Chapter 5) and was therefore unavailable for kinetic studies.

3.1.1 Principles of pressure-jump spectroscopy

Pressure-jump is a spectroscopic technique capable of probing submilisecond processes. While the basic principles of method itself are not new (Davis and Gutfreund, 1976), it is recent developments in the field of pressure-jump instruments that allow very rapid processes to be studied. This method has been successfully used in previous studies to investigate folding of Syrian Hamster PrP (Jenkins, 2006), demonstrating its capability to follow early events of PrP folding.

Pressure-jump spectroscopy utilizes rapid changes in hydrostatic pressure in order to perturb the equilibrium of the system. Consequently, the method can be used in protein folding studies, in research into protein-ligand interactions and many other processes in which reversible substrate-product equilibrium exists. In case of folding studies, pressure application induces protein unfolding, while pressure release shifts the equilibrium of the system back towards the folded state resulting in refolding of the protein (Jacob *et al.,* 1999).

Any changes in protein conformation resulting from shifting the equilibrium upon pressure application or release are followed using a relevant spectroscopic technique. Fluorescence spectroscopy is commonly employed due to its sensitivity, allowing for a number of biochemical processes, such as protein conformational changes and protein-protein and protein-ligand interactions to be studied (Gross and Jaenike, 1994; Jenkins *et al.,* 2009).

The underlying principle of the pressure-jump is equilibrium perturbation, as mentioned before. Application of pressure to a system at dynamic equilibrium will cause the equilibrium to shift in order to compensate for the effect of pressure, as predicted by Le Chatelier`s principle (Atkins, 1999). This shift in equilibrium is physically manifested as a decrease in the volume of investigated system. Such phenomenon can be commonly observed in a number of biochemical processes such as protein folding and unfolding, protein-ligand interactions and protein isomerisation.

In case of protein folding, the energetics depend on the relationship between changes in conformational entropy of a protein, changes in enthalpy due to side-chain interactions and the entropy change in hydrophobic group environments (Fersht, 1999). Changes in volume upon pressure application to the system in which an equilibrium between folded and unfolded protein exists are largely attributable to solvation effects. When sufficiently high pressure is applied, water molecules become compressed around ions

in a process known as electrostriction. This process contributes to weakening of electrostatic interactions and overall solvation, consequently contributing to unfolding of the protein (Mozhaev *et al.*, 1996).

Changes in Gibbs free energy of given system (ΔG) can be expressed as:

$$\Delta G = - RT \ln K \quad (3.1)$$

where R is the gas constant (8.314 J K^{-1} mol^{-1}), T is the absolute temperature in Kelvins and K is the equilibrium constant of the process.

Alternatively, the same change in free energy can be expressed in terms of change in internal energy and entropy as:

$$\Delta G = \Delta E + \Delta(pV) - (\Delta TS) \quad (3.2)$$

where ΔE is the change in internal energy, p is the pressure, ΔV is the change in volume, T is the absolute temperature and ΔS is the change in entropy.

By combining equations 3.1 and 3.2 the following equation can be obtained:

$$-RT \ln K = \Delta E + \Delta(pV) - \Delta(TS) \quad (3.3)$$

The relationship between change in pressure (p), volume (V) and equilibrium constant (K) indicates that any change in pressure will influence the position of the equilibrium of the system as well as the volume.

This relationship can be used to reveal any changes in volume of the system upon pressure application and release and therefore equilibrium perturbation. Changes in volume over the course of reactions such as protein folding and unfolding or protein-ligand interactions may reveal previously unobserved steps in the reaction. Pressure dependence of the rate of the reaction can be used to determine the so-called activation volume, which is the difference between partial molar volumes of the reactants at the same temperature and pressure (Muller, 1994). Hence, activation volume can be interpreted as a kinetic barrier that has to be overcome in order for the reaction to progress, much like activation energy (Cordeiro *et al.*, 2005b).

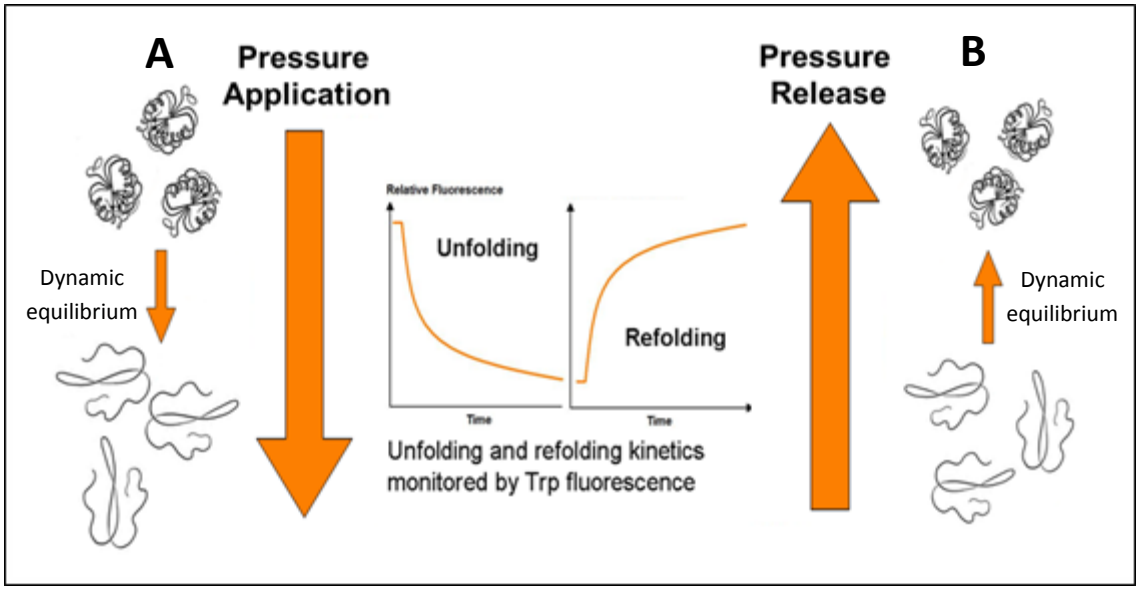

Figure 3.1 Schematic representation of the basic principles underlying the investigation of protein folding and unfolding kinetics by pressure-jump.
The method utilizes rapid changes in hydrostatic pressure in order to perturb the equilibrium of the system. In the system consisting of folded and unfolded proteins at dynamic equilibrium application of pressure induces protein unfolding (A), while pressure release shifts the equilibrium of the system back towards the folded state resulting in refolding of the protein (B).
Changes in protein conformation upon shifting the equilibrium are followed by fluorescence spectroscopy.

Unlike stopped-flow or continuous-flow techniques where physical mixing of the reactants is one of the key factors determining instrumental dead time, pressure-jump relies only on the shift in equilibrium to initiate a reaction, be it unfolding, refolding on protein-ligand interaction. Thus, the dead time of pressure-jump instrument is only limited by the time it takes for the pressure to stabilize following its rapid increase or decrease. In many modern instruments, the pressure is fully stabilized within a hundred microseconds, allowing for the very earliest events to be observed. Since pressure-jump does not rely on mechanical agitation or harsh radiation or heating but only on pressure alteration, the entire process of equilibrium perturbation is relatively gentle, allowing sensitive reactants to be studied. Moreover, the entire process of pressure application and release can be rapidly cycled, allowing for fluorescence transients from dozens of equilibrium perturbations to be accumulated within minutes. By averaging such high number of individual repeats, a very high signal-to-noise ratio can be achieved.

While it is possible for the pressure alone to induce shift in equilibrium and thus perform folding kinetics studies (Tan *et al.,* 2005, Torrent *et al.,* 2006), it is quite often the case that pressure alone is insufficient to denature a protein. In such instances, a chemical denaturant such as urea or GdnHCl is included in the reaction mixture. The presence of denaturant allows the equilibrium of the system to be poised at suitable point on the equilibrium transition curve which favours the presence of partially unfolded conformations. When coupled with pressure application, presence of denaturant is sufficient to induce equilibrium shift necessary for protein unfolding to take place. The combination of denaturant and pressure alteration has been successfully used in several studies, such as folding of stabilized mutants of staphylococcal nuclease (Vidugiris *et al.,* 1996), fast-folding of cold-shock protein (Jacob *et al.,* 1999) or rapid folding of Syrian hamster prion protein (Jenkins *et al.,* 2006).

Kinetic studies using methods such as pressure-jump spectroscopy can provide invaluable insight into earliest kinetic events of protein folding pathway. In prion folding, they can be used to identify protein folding intermediates (Hosszu *et al.,* 2005) or to determine differences in folding kinetics between prions from different species. Investigation of such differences and detection of previously unidentified kinetic intermediates may contribute to our understanding of phenomena such as species barrier and disease resistance. While pressure-jump experiments can provide kinetic data such as whether energy needed to unfold prion variant associated with increased

disease susceptibility is lower than wild type, or if there is a large difference in stability between species which may account for inability of PrP^{Sc} from certain species to convert PrP^{C} from other, it cannot provide details on conformation or propensity to form aggregates.

Recent findings suggest that disease resistance may also be linked to structural features of PrP such as stability of a compact loop region encompassing residues 166-175, which plays important role in aggregation and formation of the infectious particles in several species including bank vole, elk, sheep and mice (Scouras and Daggett, 2012). Consequently, investigation of fibrilisation properties of PrP may reveal a link between early kinetic behaviour of prions, the presence of folding intermediates and propensity to form fibrils.

Thus, the pressure-jump studies of kinetics of early folding pathway of PrP detailed in this chater were supplemented by fibrilization studies of prion proteins, in order to identify key processes involved in both species barrier and disease resistance.

Fibril formation can be investigated in a series of fibrilisation and oligomeristaion studies utilizing ThT fluorescence (Gill *et al.* 2009). Positively charged ThT is known to bind to negatively charged nucleic acids as well as fibrils formed by α-synucleins and prion proteins. Upon binding, ThT molecules exhibiting low fluorescence in water show several-fold enhancement in fluorescence intensity. This increase in emission is characteristic only for bound ThT and therefore is often used as a marker of fibril formation.

The aim of this project is to investigate whether the physical folding properties of PrP are influenced by the Q167R mutation which is known to confer decreased susceptibility, by comparing the unfolding and refolding kinetics of wild type PrP and Q167R mutant under native and mildly denaturing conditions using pressure-jump spectroscopy.

Moreover, fibrilisation studies of MoWT, Q167R mutant and SHaPrP are conducted at a range of denaturant concentrations and pHs known to induce PrP conversion into β-state intermediate, in an attempt to answer the question of species variation and disease-modulating mutations in the folding properties of the prion protein.

All of the pressure-jump experiments conducted during this project were carried out in collaboration with Professor Mike Geeves and Dr Dave Pearson from Department of Biosciences, University of Kent, Canterbury.

3.2 Materials and Methods

3.2.1 Materials

All chemicals were purchased from Sigma-Aldrich (Poole, UK) unless stated otherwise.

3.2.2 Expression and purification of PrP.

The three piron constructs MoWT (Met91-230), disease-associated mutant Q167R (Met91-230) as well as SHaWT (Met91-231) were expressed and purified according to protocols described in chapter 2, sections 2.2.1.7 to 2.2.1.14.

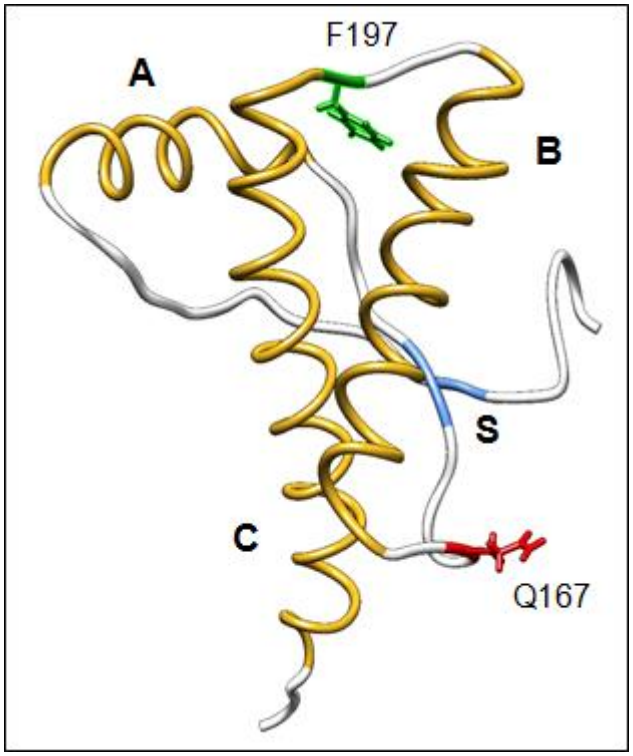

Figure 3.2 Ribbon representation of the structure of the C-terminal globular domain of mouse prion protein (residues 120–230) based on the NMR structure (Gossert *et al.*, 2005). Main structural features are highlighted in colour with key residues shown using stick representation. Three main α-helices A, B and C running from C to N terminus of the polypeptide are shown in yellow, with short antiparallel β-sheet S highlighted in blue. Residues Q167 and F197 are highlighted in red and green respectively.

The NMR structure was drawn from PDB file 1XYX using UCSF Chimera package from the Resource for Biocomputing, Visualization and Informatics at the University of California, San Francisco (supported by NIH P41 RR-01081) (Pettersen *et al.*, 2004)

3.2.3 Tryptophan fluorescence spectroscopy

Urea unfolding curves of MoWT Q167R and SHaWT were constructed through a series of tryptophan fluorescence measurements of each of the proteins in increasing urea concentration at two different pH values.

A stock solution of 10 M urea was prepared and treated with Amberlite deionising resin (Merck, Darmstadt, Germany) for several hours. For each experiment a folded and unfolded stock solutions of relevant PrP species were constructed. For pH 7, the folded stock solution contained 10 μM PrP in 20 mM phosphate buffer and no urea, while unfolded stock solution consisted of 10 μM PrP in 20 mM phosphate buffer and 8 M urea.

For pH 4, the folded stock consisted of 10 μM PrP in 20 mM sodium acetate and no urea with unfolded stock containing 10 μM PrP in 20 mM sodium acetate and 8 M urea.

For each unfolding curve a series of measurements was carried out during which an aliquot of the folded stock was withdrawn from a 1 cm pathlength quartz cuvette and replaced with an aliquot of unfolded stock so that the PrP concentration remained the same but urea concentration was increased.

All fluorescence spectra were recorded using Photon Technology International spectrofluorimeter. The tryptophan residues in PrP-containing samples were selectively excited using excitation wavelength of 295 nm with the emission spectra collected between 305 and 450 nm. The bandwidth of both excitation and emission light was set to 2 nm. Four scans were averaged per spectrum and corresponding buffer backgrounds were collected and subtracted prior to data analysis.

3.2.3.1 Fluorescence data analysis

Fluorescence unfolding curves were constructed by following the change in tryptophan fluorescence intensity and shift in the wavelength of maximum fluorescence in increasing urea concentrations.

The two-state unfolding process of PrP in presence of urea can be represented by the following equation:

$$K_F = [F] / [U] \qquad (3.4)$$

Where [F] is the concentration of the folded protein, [U] is the concentration of unfolded protein and K_F is the folding constant. Upon reaching equilibrium between the two states, the free energy of folding can be expressed by equation 3.1. Consequently, the free energy of folding in the absence of denaturant (ΔG_0) can be calculated using the linear extrapolation method (Santoro and Bolen, 1988). Assuming that free energy of the folding observed in the transition region of the folding curve is linearly dependent on denaturant concentration, the following formula can be applied:

$$\Delta G = \Delta G_0 - m\,[denaturant] \tag{3.5}$$

where ΔG is the free energy of folding and m is the constant reflecting the gradient of plot of free energy against denaturant concentration.

Thus, the folding constant at specific denaturant concentration can be calculated from combined equations 3.1 and 3.5:

$$K_F = e^{-(\Delta G_0 - m\,[denaturant] / RT)} \tag{3.6}$$

where K_F is the folding constant, R is the gas constant and T is the absolute temperature.

By calculating the values of the folding constant, the fraction of folded PrP (f_F) can be determined using the following equation:

$$f_F = K_F / (K_F + 1) \tag{3.7}$$

and the theoretical blue shift of the tryptophan fluorescence spectrum can be defined as:

$$S = f_F (S_F - S_U) + S_U \tag{3.8}$$

Where S is the theoretical blue shift of Trp fluorescence spectrum, S_F is the blue shift in λ max of the completely folded protein and S_U is the blue shift in λ max of the completely unfolded protein (Greenfield, 2006).

It should be noted that the formula 3.8 applies only to the transition region of the folding curve, and thus the following correction has to be applied to take into account the linear slopes observed in the pre-unfolding baseline:

$$S = f_F (S_F + [denaturant] \times m_U - S_U) + S_U \quad (3.9)$$

Prior to data analysis, recorded fluorescence spectra were normalised. The values of the blue shift in maximum fluorescence of tryptophan residues for both fully folded and fully unfolded proteins were calculated from plots of raw experimental data and used to normalise each individual data set to fraction of folded protein:

$$f_F = (S - S_U) / (S_F - S_U) \quad (3.10)$$

where S is the value of blue shift in tryptophan fluorescence.
The fraction of folded PrP was then plotted against urea concentration to construct folding transition curves.

3.2.4 Circular dichroism spectroscopy

A stock solution of 10 M urea was prepared and treated with Amberlite resin. For each CD experiment a folded and unfolded stocks of relevant PrP species were constructed. For pH 7, the folded stock contained 10 μM PrP in 20 mM phosphate buffer and no urea, while unfolded stock consisted of 10 μM PrP in 20 mM phosphate buffer in 8 M urea.
For pH 4, the folded and unfolded stocks consisted of 10 μM PrP in 20 mM sodium acetate with no urea and 10 μM PrP in 20 mM sodium acetate in 8 M urea respectively. For each unfolding curve a series of measurements was carried out during which an aliquot of the folded stock was withdrawn from a 1 mm pathlength quartz cuvette and replaced with an aliquot of unfolded stock so that the PrP concentration remained the same but urea concentration was increased.
The far-UV (190–260 nm) circular dichroism spectra were measured using JASCO J-815 spectropolarimeter. All spectra were measured using 1 mm path length quartz cuvettes, with a scanning rate of 100 nm / minute, response time of one second,

bandwidth of 1.0 nm, and resolution of 0.5 nm. Typically 16 scans were averaged per spectrum and corresponding buffer backgrounds were subtracted from the final spectra. Buffer systems consisting of 20 mM MES and 20 mM sodium acetate were used to maintain a constant pH of 7.0 and 4.0 respectively. All measurements were carried out at 20 °C.

For far-UV CD measurements, mean residue ellipticity ($[\theta]_{MRW}$) was calculated using Equation 3.11:

$$[\theta]_{MRW} = \frac{\theta}{Ncl \times 10} \tag{3.11}$$

where [θ] is the observed ellipticity (millidegrees), *N* is the number of peptide bonds in the protein, *c* is the molar protein concentration, and *l* the pathlength of the cuvette used (cm).

The mean residue ellipticity at 222 nm wavelength was then determined for each CD spectrum recorded and normalised to fraction unfolded according to equation 3.10, with ellipticity values at 8 M urea corresponding to fully unfolded state (S_U) and those at 0 M urea to fully folded state (S_F).

3.2.5 Pressure-jump instrument

3.2.5.1 Components of pressure-jump instrument

All of the pressure-jump experiments were performed using apparatus described by Pearson *et al.* (Pearson *et al.*, 2002; Pearson *et al.*, 2008) with some modifications, mentioned below. The heart of the instrument is a sample chamber consisting of small sapphire ring closed off at either end by polyimide membranes. At one end, a piezoelectric pressure sensor (6158A from Kistler Instrumente AG, Winterthur, Switzerland) is used to detect changes in pressure, whilst at the other a piston distorts the membrane in order to induce fast pressure changes. The piston is driven by a piezoelectric crystal stack (P-245.70, Physik Instrumente GmbH, Waldbronn, Germany) capable of delivering pressure changes of up to 45 MPa in as little as 100 μs.

Fluorescence transients resulting from both pressure application (up to 45 MPa) and release (to 1-2 MPa) are monitored at 90º to the light guide using a R928HA Hammamatsu photomultiplier with signal conditioning provided by a modified stopped-flow instrument with an added transimpedance pre-amp stage, provided by TgK Scientific (Bradford-on-Avon, UK). Excitation light was provided by a 75 W Xe/Hg arc lamp (Hamamatsu Photonics, Enfeld, UK), delivered to the cell via a liquid light guide abutting directly onto the sample chamber. The modified configuration uses a new A/D board (DT3010-268, Data Translation Ltd) and specially developed software (D. S. Pearson, developed using LabVIEW) to collect pressure and fluorescence data side-by-side. The new configuration allows sequential fast repeats followed by a data offload phase during which an automated shutter is closed to reduce sample photobleaching. This detection and data processing system allows for multiple transients to be averaged providing hundreds of averaged spectra per minute, contributing to very low signal/noise ratio of the data.

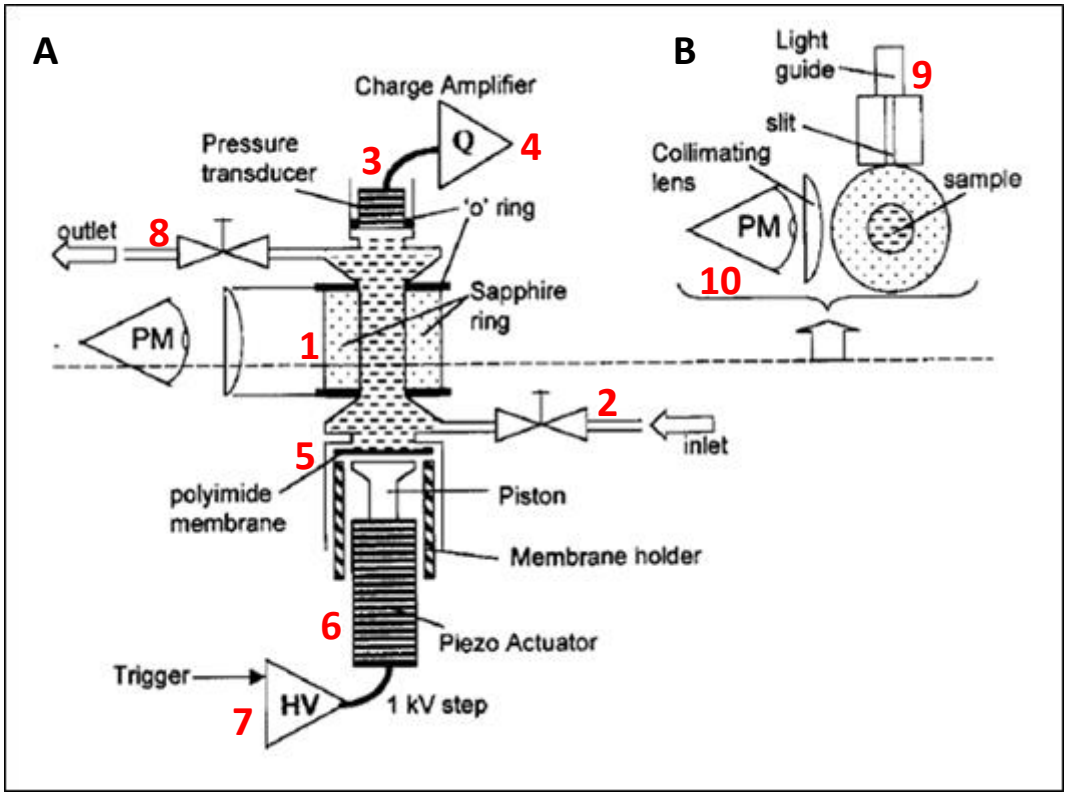

Figure 3.3 Schematic diagram illustrating key components of the pressure-jump instrument located at the University of Kent.

Side view (A) highlights both sample delivery and pressure application systems. The sample is introduced into the 50 µl optical chamber (1) via the inlet valve (2). The chamber consists of a sapphire ring sealed at the top end by pressure transducer (3) coupled to charge amplifier (4), and at the bottom end by elastic polyimide membrane (5). The pressure necessary to perturb equilibrium in the sample is provided by a piston attached to a piezoelectric actuator (6). Upon application of electric current through high-voltage power switch (7), the piston protrudes upwards, deforming the polyimide membrane and decreasing the volume of the optical chamber. Upon completion of the experiment, the chamber may be emptied through the outlet valve (8). The sample chamber is surrounded by a water jacket (not shown), allowing for temperature to be thermostatically controlled. Section view (B) provides details of the detection setup used to monitor changes in fluorescence of the sample. The fiber-optic light guide (9) supplies monochromatic light used to excite the sample in optical chamber. The fluorescence emitted by the sample is passed through appropriate optical filter, focussed by a collimating lens and collected by the photomultiplier (10) at 90° to the excitation light (adapted from Pearson *et al.*, 2002).

3.2.5.2 Equilibrium perturbation and its effect on protein fold

A change in pressure changes the free energy of a reaction ($\Delta G°$) in which there is a difference in volume between the reactants and products ($\Delta V°$) so that the reaction must do enthalpic work (given by $P\ \Delta V°$) against the external pressure to proceed. The pressure perturbation function is given by the differential of the work done with respect to pressure: $\Delta V° = -RT\ \partial \ln K / \partial P$. Pressure jump using our equipment uses relatively little material and is able to access fast reactions because the pressure rise time is ~100 μs. Fast reactions can be conveniently measured using repeated averages that are not possible over short time periods using temperature jump due to long cooling times necessary between temperature jump measurements. Pressure jump can selectively perturb steps on a reaction pathway (Málnási-Csizmadia *et al.,* 2001; Málnási-Csizmadia *et al.,* 2007; Kintses *et al.,* 2007), can measure the volume change and affinity for second order reactions by titrating the total concentration of protein and ligand (Pearson *et al.,* 2002; Pearson *et al.,* 2008) and has been used previously in protein folding studies (Jacob *et al.,* 1999; Dumont *et al.,* 2009; Jenkins *et al.,* 2009).

3.2.6 Pressure-jump experiments

During a typical experiment a 50 μl sample was loaded into the chamber via the inlet valve into the bottom of the chamber. Prior to the measurement itself a small pre-pressure (1–2 MPa) was applied in order to remove elasticity from the system and to deform the polyimide membrane into intimate contact with the piston. Once the inlet valve was closed measurements were obtained by rapid application and release of pressure (up to 35 MPa in ~100 μs).

A protein concentration of 10 μM was used throughout the experiment, with a fluorescence transients obtained during each measurement consisting of at least 1,000 averages. Protein tryptophan fluorescence was measured using an excitation wavelength of 295 nm with a monochromator bandwidth of 1.8 nm. The emitted fluorescence light was collected through a WG320 cut-off filter (Schott GmbH, Mainz, Germany), in order to block scattered excitation light below 320 nm. For each denaturant concentration used, a corresponding blank measurement was performed and used for

the calculation of relative change in fluorescence. This was done to account for the effect of urea on the refractive index of the solution, which could alter the light path of the cell. Buffer systems consisting of 20 mM MES and 20 mM sodium acetate were used to maintain a constant pH of 7.0 and 4.0 respectively.

3.2.6.1 Data analysis

Raw signal transients resulting from pressure-jump experiments were expressed as a percentage change in fluorescence according to the formula:

$$F(t) = 100((B_t - S_t) / (B_0 - S_0) - 1) \quad (3.12)$$

where F(t) is the fluorescence as a function of time, S_t and B_t are the signal and blank measurements over time, respectively whereas S_0 and B_0 are the signal and mean blank measurements averaged over the pretrigger time before initiation of the jump (Pearson *et al*., 2002).

Fluorescence transients resulting from pressure-jump experiments were fitted to a single exponential decay function with equation:

$$F(t) = F_\infty + A[1 - \exp(-t/\tau)] \quad (3.13)$$

where F(t) is the fitted fluorescence function, F_∞ is the end-point, A is the amplitude and τ is the time constant (Pearson *et al*., 2002). The fluorescence data included an early phase too fast to resolve, due to its time course coinciding with the fast pressure step. Consequently, the exponential function was only used to fit the slower phase beginning at the end of the initial fast pressure step, about 100 μs after the pressure application.

The inverse time constants ($1/\tau$) resulting from pressure-jump measurements over a range of urea concentrations were fitted to a two-state folding model using the following formula:

$$1/\tau = k_f \exp(m_f [D] / RT) + k_u \exp(m_u [D] / RT) \quad (3.14)$$

where m_f and m_u are the kinetic folding and unfolding fragility parameters respectively, k_f and k_u are the folding and unfolding rate constants in the absence of denaturant, [D] is the concentration of denaturant, R is the gas constant, and T is the absolute temperature (293 K) (Pearson *et al*., 2002).

Fitting was carried out using data transformed to $\ln(1/\tau)$ in order to avoid undue bias towards large τ values. The minima of the chevron plots were determined using the following expression:

$$[D]_{min} = RT / (m_f - m_u) \ln(-m_u \times k_u / m_f \times k_f) \quad (3.15)$$

which was obtained by solving the differential (Pearson *et al*., 2002). The mid-point of the corresponding equilibrium ($[D]_{50\%}$) unfolding curve was calculated using to the following formula:

$$[D]_{50\%} = RT / (m_f - m_u) \ln (k_u / k_f) \quad (3.16)$$

The amplitudes resulting from pressure jump experiments were fitted by calculating the change in fluorescence predicted upon application of pressure (Pearson *et al*., 2002). The denaturant dependent folding equilibrium constant, K_D was calculated according to the formula:

$$K_D = K_0 \exp(-m / RT) \quad (3.17)$$

where K_0 is the equilibrium constant in water and m is the fragility parameter.

The fraction unfolded given by the formula

$$(\alpha = K_D / K_D + 1) \quad (3.18)$$

was used to calculate the equilibrium fluorescence as a function of denaturant (F_D) according to the following formula:

$$F_D = 1 + \alpha(Q-1) \quad (3.19)$$

where Q is the ratio of fluorescence in the fully folded to the fully unfolded state, with a value of 3.2 used in all cases (Gill and Von Hippel, 1989). The pressure perturbation function was used to calculate the change in the equilibrium constant upon application of pressure, and thus the change in fluorescence. The values of K_0, m and $\Delta V°$ were free parameters in this calculation.

Obtaining realistic confidence limits for the fitted parameters resulting from fits to chevron plots is challenging without repeating entire sets of experimental data for the purpose of statistical analysis. We fitted the high and low [urea] data separately as linear functions in $\ln(1/\tau)$ and propagated the relative error in the slope and intercept into an estimate of error in fragility and aqueous rate constants, respectively, in order to provide a low threshold estimate of the uncertainties. Error estimates in the derived parameters *m* and $[D]_{50\%}$ come from error propagation. Uncertainties in the amplitude fits were standard errors derived directly from the fitting program (Microcal Origin).

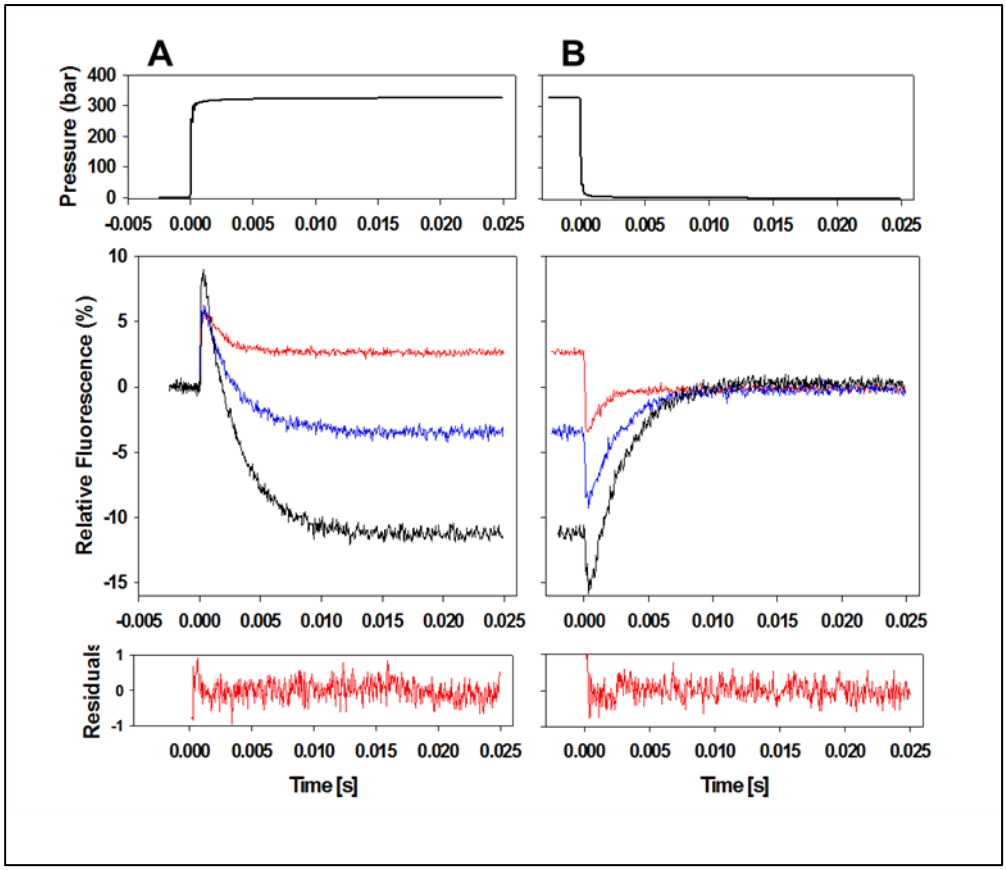

Figure 3.4 Example of data yielded by the pressure-jump experiment. Top panels show the pressure profile upon pressure application (A) and release (B). Middle panels show examples of three overlaid tryptophan fluorescence transients recorded at different urea concentrations, as well as single exponential fits by linear regression to said fluorescence transients. upon pressure application and release are shown in left and right-hand side panels respectively. Residuals from fitting fluorescence transient coloured in red are shown in the bottom panels.

3.2.7 Fibrilization of PrP

Recombinant mouse PrP was fibrillized according to published protocol (Breydo *et al.* 2008). Aliquots of MoWT, Q167R and sHaWT PrP were lyophilized and briefly dissolved in 6 M guanidine HCl, pH 6.0, at a concentration of 3 mg/ml. A range of fibrillization reactions consisting of 6-5M urea, 10 mM thiourea, 120 μg/ml recPrP, 50 mM MES, pH 7.0 and pH 4.0, and 10 μM thioflavin T was prepared. 160 μl aliquots of reaction mixtures were placed into individual wells of a 96-well plate, and 3 Teflon spheres were added to aid mixing (Graham *et al.,* 2010). In some reactions 0.1% (w/w) of preformed PrP seed was added to the reaction wells. The 96-well plate was incubated in a plate reader at 37 °C with constant shaking (900 rpm, 1-mm diameter). The fluorescence from thioflavin T (ThT) was monitored every 30 min by use of a fluorescence plate reader (Fluoroskan Ascent, Thermo Scientific) with excitation at 444 nm and emission at 485 nm. Background fluorescence was calculated from three replicate wells containing no PrP and was subtracted from sample readings. Sigmoidal curves were fitted to the data where possible by a least squares approach. Fluorescence, *F*, at time, *t* was calculated from the equation:

$$F(t) = A + (B + C) / (1 + e^{(k(tm-t))}) \quad (3.20)$$

where A is the initial level of ThT fluorescence, B is the peak level of fluorescence, t_m is the mid point of the transition, and k is the rate of increase of fluorescence. C is an empirical parameter describing changes in fluorescence after fibril formation (Graham *et al.*, 2010).

The lag time, t_1, is calculated as

$$t_1 = t_m - 2 / k \quad (3.21)$$

3.3 Results and Discussion

3.3.1 Equilibrium denaturation of PrP followed by tryptophan fluorescence

Tryptophan fluorescence is the most common spectroscopic technique used to monitor protein folding and refolding, relying on changes in fluorescence of reporter Trp residues located in the key structural regions of investigated protein. In this study single- tryptophan mutants of MoPrP, Q167R disease-associated mutant and SHaPrP were used. Each of the constructs had its two native tryptophan residues at positions 98 and 144 mutated to phenylalanine residues, with phenylalanine residue at position 197 (mouse PrP) or 198 (hamster PrP) mutated to tryptophan which acted as a fluorescent probe.

Prior to pressure-jump experiments, the denaturant unfolding transition curves for all three species were constructed to determine the range of denaturant concentrations at which perturbing the equilibrium would be most effective. Since pressure-jump spectroscopy, as an equilibrium perturbation technique, relies on shifting the equilibrium between unfolded and folded protein conformations, its effect should be most pronounced near the midpoint of the transition curve where populations of unfolded and folded states are relatively equal. On the other hand, the further from the midpoint, the lower the population of folded/unfolded protein in which conformational change can be induced upon pressure application or release and thus lower the fluorescence signal. Since pressure values achievable by pressure-jump instrument used in this study are insufficient to unfold PrP without denaturant present (Jenkins, 2006), determination of behavior of all thee prion proteins along the denaturant unfolding curve is of vital importance.

In order to investigate whether the increased propensity to form β-state intermediate in mildly acidic and denaturing conditions can be characterised kinetically, pressure-jump experiments with all three PrP species were conducted at two pH values (pH 7.0 and pH 4.0). Consequently, denaturant folding curves of MoWT, Q167R and SHaWT at both pH 7.0 and pH 4.0 were constructed.

Comparison of tryptophan fluorescence spectra of three prion species collected at increasing urea concentrations (see Figures 3.5, 3.6 and 3.7) reveals key similarities shared by investigated proteins. Upon increase in denaturant concentration, the

unfolding-sensitive tryptophan residue becomes solvent exposed, resulting in shift in wavelength at which maximum fluorescence can be observed (λ_{max}) towards the higher energy region of the spectrum – a process referred to as red-shift. For all three proteins, the maximum fluorescence under native conditions occurs at 337 nm at pH 7.0 and 339 nm at pH 4.0, while in presence of 7.5 M urea the λ_{max} is shifted to 351 nm at both pH values. The slightly lower total red-shift value of 12 nm at pH 4.0, compared to 14 nm at pH 7.0, can be easily attributed to mildly denaturing conditions of low pH, resulting in the PrP being slightly destabilized even in absence of urea. This is consistent with the total changes in fluorescence intensity in absence of denaturant and in highest concentration of urea being lower at pH 4.0 compared to pH 7.0. At neutral pH, the fluorescence intensity of fully unfolded protein is approximately 70% lower than that of folded protein, while at pH 4.0 fluorescence of unfolded protein is 60% lower.

It should be noted that this behavior is true for mouse prions MoWT and Q167R, while for Syrian hamster PrP (SHaWT) the process is reversed – the fluorescence intensity is not decreased upon unfolding but increased, which is consistent with previous folding studies of Syrian hamster PrP (Jenkins, 2006). Consistently with the destabilization of structure at lower pH, the total increase in fluorescence between fully folded and unfolded states is approximately 5% larger at pH 7.0 than at pH 4.0.

While typically upon unfolding of the protein the fluorescence of tryptophan residues is quenched (Lakowicz, 1999), in some cases the local environment of the tryptophan residue acts as quencher when protein is folded. In such case, unfolding of the protein results in de-quenching of the tryptophan and consequently increased fluorescence. Such effect has been observed in single-tryptophan mutant of E.coli aporepressor protein (Royer *et al.*, 1993).

Both changes in maximum fluorescence intensity and the red-shift can be used to monitor protein folding. However, while in case of prion proteins the tryptophan fluorescence can be both quenched and increased upon unfolding depending on the local environment of the residue, as illustrated above, the red-shift is universally unidirectional and associated with unfolding. Thus, for the sake of clarity and uniform data processing, the red shift of maximum tryptophan fluorescence was used to construct denaturant unfolding transition curves.

For both mouse prion proteins, MoWT and Q167R (see figure 3.8, panels A and B respectively), at neutral pH the major unfolding transition occurs between 5 M urea and 7 M urea. Such narrow transition range is indicative of the cooperative two-state

transition. Moreover, the mid-point of the transition curve of Q167R protein occurs at slightly lower urea concentration (see Table 3.1), which is indicative of slight structural destabilization conferred by this mutation (Robinson and Pinheiro, 2009).

The transition region of Syrian hamster PrP is noticeably broader than both mouse prions (see Figure 3.9), occurring between 3.5-4 M and 7 M urea. While it can be fitted to two-state model by linear regression, the protein which folds via two-state transition should exhibit much steeper transition. This suggests that the Syrian hamster PrP does not exhibit the cooperativity observed in mouse prions and other proteins that fold via essentially two-state mechanism.

Interestingly, at pH 4.0 all three proteins exhibit extremely broad transition regions stretching between 2 M and 6 M urea concentrations. Such broad transitions strongly suggest that lowering the pH affects the folding of all three prion species so that they no longer clearly follow the two-state mechanism. This in turn might be indicative of the presence of a β-state intermediate in low-pH folding pathways of both mouse and hamster prions.

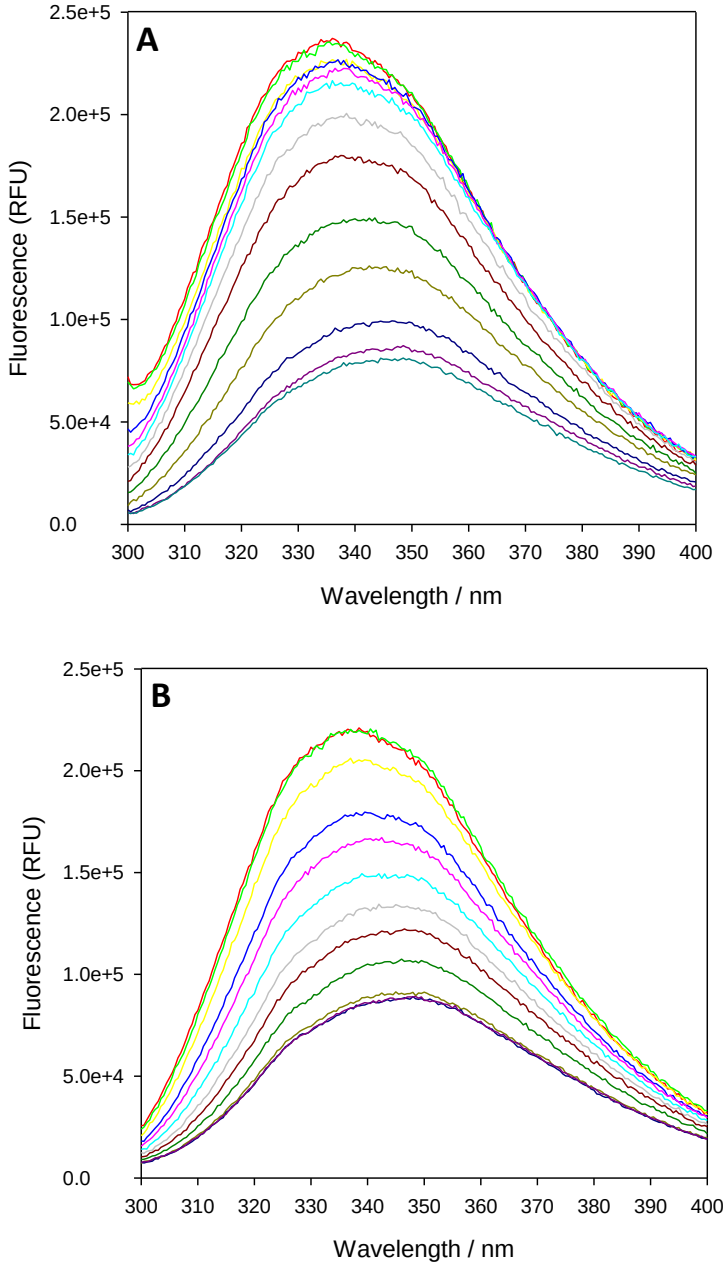

Figure 3.5 Fluorescence spectra of single-tryptophan mutant of mouse PrP (MoWT) at increasing urea concentrations across the folding transition curve at pH 7.0 (A) and 4.0 (B).

The fluorescence spectra at 0 M urea (red), 1.0 M urea (green), 2.0 M urea (yellow), 3.0 M urea (blue), 3.5 M urea (pink), 4.0 M urea (cyan), 4.5 M urea (grey), 5.0 M urea (brown), 5.5 M urea (dark green), 6.0 M urea (dark yellow), 6.5 M urea (dark blue), 7.0 M urea (purple) and 7.5 M urea (teal) are shown.

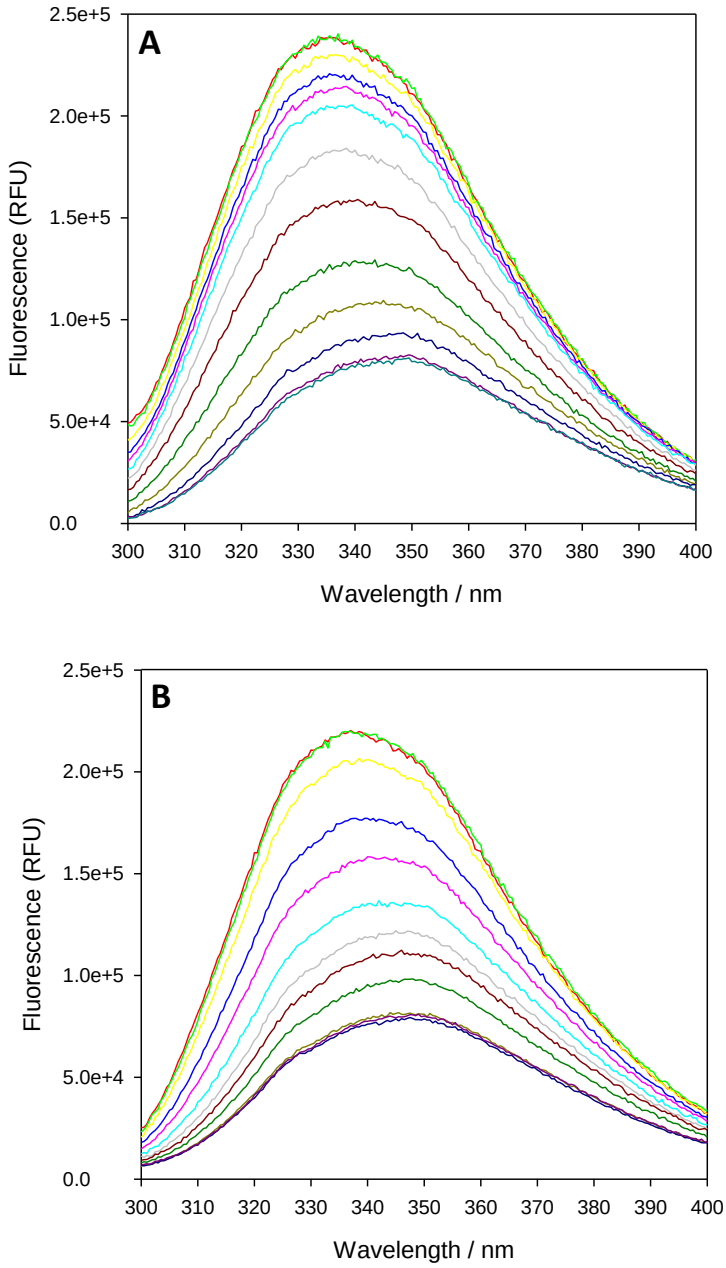

Figure 3.6 Fluorescence spectra of single-tryptophan construct of disease-associated mutant of mouse PrP (Q167R) at increasing urea concentrations across the folding transition curve at pH 7.0 (A) and 4.0 (B).

The fluorescence spectra at 0 M urea (red), 1.0 M urea (green), 2.0 M urea (yellow), 3.0 M urea (blue), 3.5 M urea (pink), 4.0 M urea (cyan), 4.5 M urea (grey), 5.0 M urea (brown), 5.5 M urea (dark green), 6.0 M urea (dark yellow), 6.5 M urea (dark blue), 7.0 M urea (purple) and 7.5 M urea (teal) are shown.

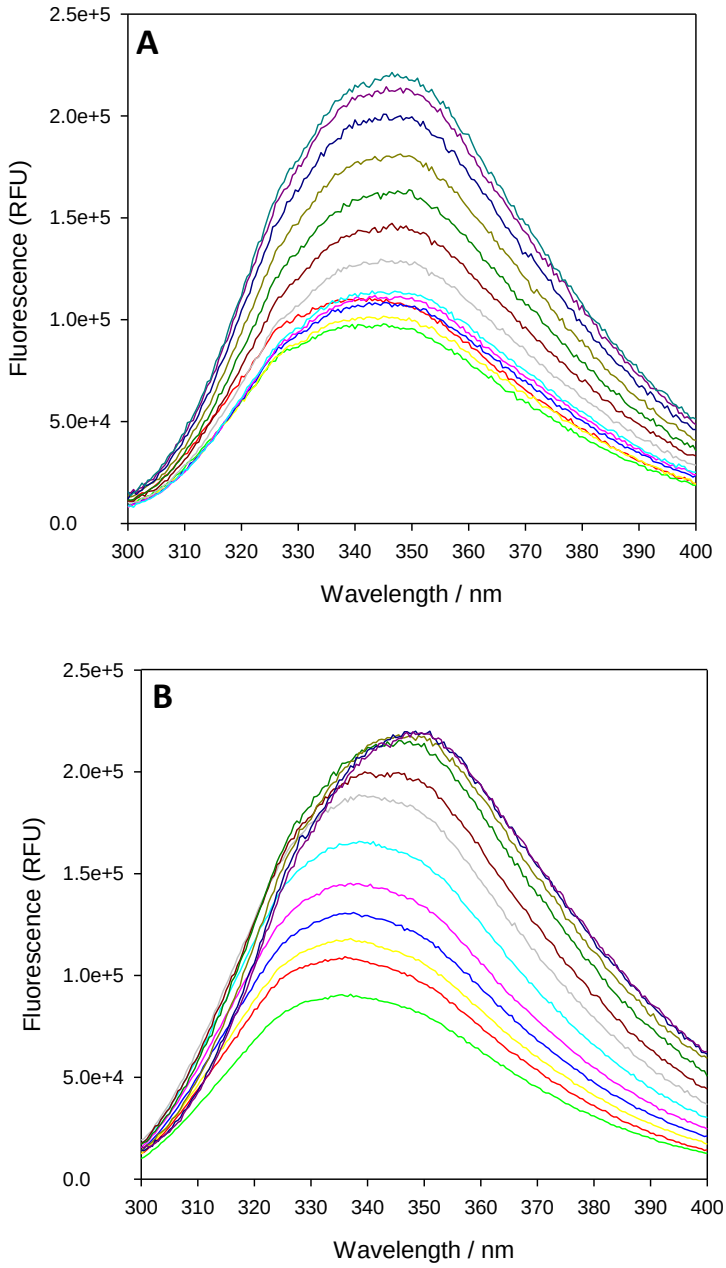

Figure 3.7 Fluorescence spectra of single-tryptophan mutant of Syrian hamster PrP (SHaWT) at increasing urea concentrations across the folding transition curve at pH 7.0 (A) and 4.0 (B).

The fluorescence spectra at 0 M urea (red), 1.0 M urea (green), 2.0 M urea (yellow), 3.0 M urea (blue), 3.5 M urea (pink), 4.0 M urea (cyan), 4.5 M urea (grey), 5.0 M urea (brown), 5.5 M urea (dark green), 6.0 M urea (dark yellow), 6.5 M urea (dark blue), 7.0 M urea (purple) and 7.5 M urea (teal) are shown.

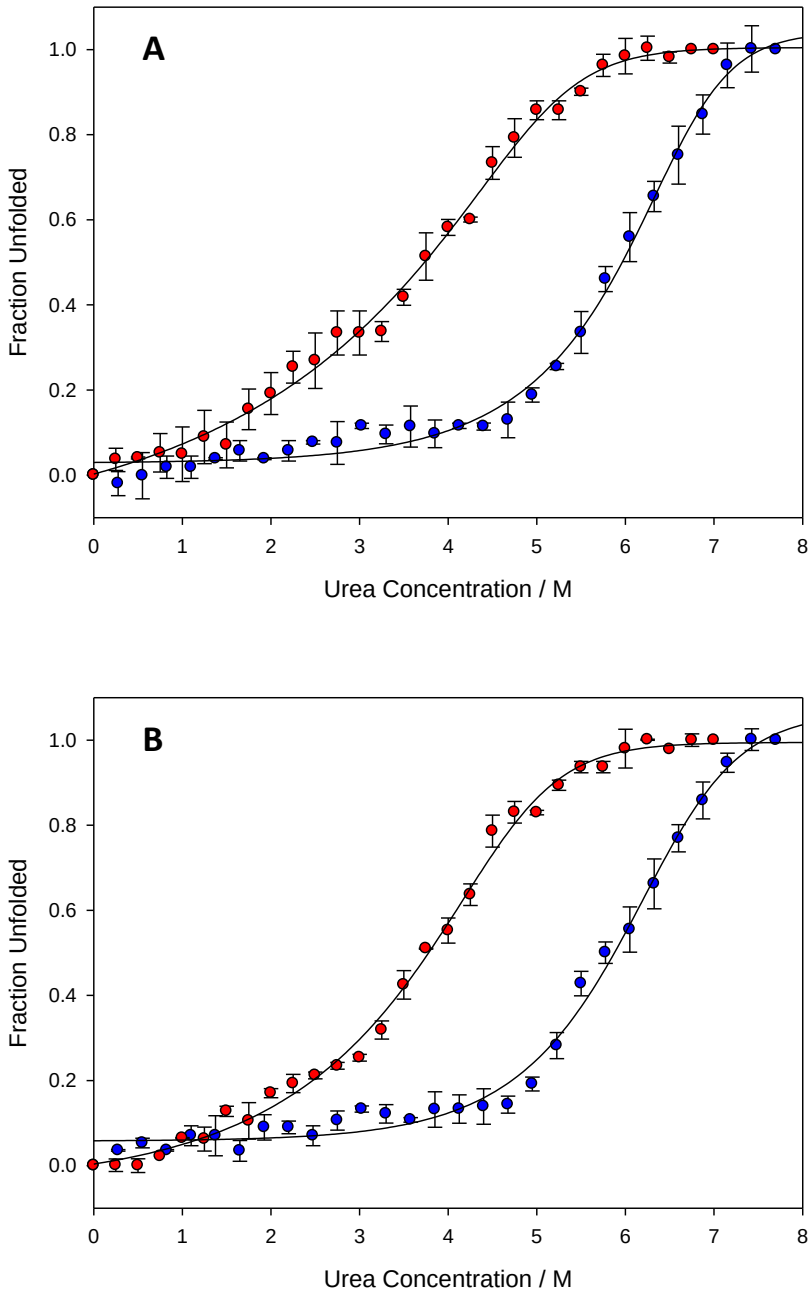

Figure 3.8 Denaturant unfolding transition curves of MoWT (A) and Q167R (B) followed by red-shift in tryptophan fluorescence. For each variant of prion protein two curves were constructed: at pH 7.0 (blue) and at pH 4.0 (red). Each data point represents the value of red-shift in λ_{max} normalized to fraction unfolded as described in section 3.2.3.1. Error bars show the standard deviation of two independent experiments.

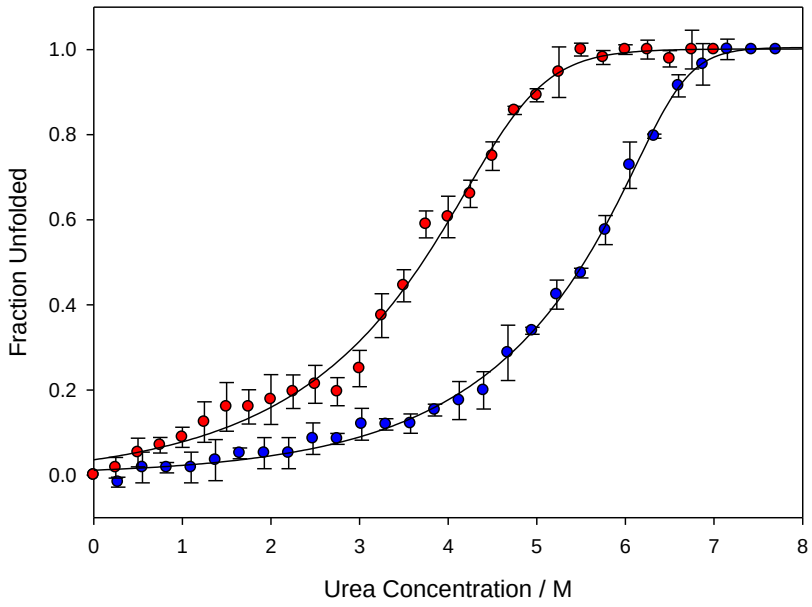

Figure 3.9 Denaturant unfolding transition curve of SHaWT followed by red-shift in tryptophan fluorescence. Two transition curves constructed at pH 7.0 and at pH 4.0 are shown in blue and red respectively. Each data point represents the value of red-shift in λ_{max} normalized to fraction unfolded as described in section 3.2.3.1. Error bars show the standard deviation of two independent experiments.

PrP construct	pH	ΔG_0 kJ mol^{-1}	*m* kJ mol^{-1} M^{-1}	$[D]_{50\%}$
MoWT (F197W)	7.0	30.2 ± 2.7	5.4 ± 0.5	6.0 ± 0.3
	4.0	25.6 ± 2.3	5.1 ± 0.4	3.7 ± 0.1
Q167R	7.0	29.4 ± 1.9	4.8 ± 0.4	5.8 ± 0.3
	4.0	27.3 ± 2.2	4.5 ± 0.3	3.7 ± 0.2
SHaWT (F198W)	7.0	18.4 ± 1.1	8.8 ± 0.5	5.5 ± 0.2
	4.0	12.5 ± 0.9	6.5 ± 0.3	3.5 ± 0.1

Table 3.1 Thermodynamic parameters extracted from denaturant unfolding transition curves of MoWT, Q167R and SHaWT.
The free energy of unfolding in the absence of urea (ΔG_0) and *m* values were calculated from the two-state analysis of denaturant unfolding transition curves.

PrP construct	ΔG_0 kJ mol^{-1}	*m* kJ mol^{-1} M^{-1}	$[D]_{50\%}$
MoWT (F197W)	1.82	0.66	10.29
Q167R	1.02	0.85	8.24
SHaWT (F198W)	5.87	5.58	12.56

Table 3.2 T-parameter values obtained via statistical analysis of thermodynamic parameters from Table 3.1 using T-test. For each PrP construct the thermodynamic parameters at pH 7.0 and pH 4.0 were compared in order to identify any statistically significant differences. T-parameter values exceedint 2.920 allow for the null hypothesis to be rejected, thus confirming the statistically significant difference between thermodynamic parameters. For values below 2.920 the null hypothesis cannot be rejected, and consequently no statistically significant difference can be claimed.

3.3.2 Equilibrium denaturation of PrP followed by far-UV circular dichroism

Far-UV circular dichroism was used to construct denaturant unfolding transition curves complementary to those obtained by tryptophan fluorescence spectroscopy. Moreover, it could potentially determine the presence of elusive β-state intermediate in mildly acidic and denaturing conditions, which may not be detectable through tryptophan fluorescence. Thus, denaturant folding curves of MoWT, Q167R and SHaWT at pH 4.0 were constructed.

In absence of urea, all three spectra show clear characteristics of predominantly α-helical structure: two negative bands at 208 and 222 nm. The third band at 195 nm is not visible due to spectral properties of the sodium acetate buffer used to maintain low pH, which prevent any reliable data to be collected below 200 nm.

Upon increase in denaturant concentration, the two bands indicative of α-helical structure lose their intensity, and a single strongly negative band appears below 205 nm, which is characteristic for random coil structure. At urea concentrations exceeding 6 M any traces of α-helical structure are absent and entire spectrum corresponds to that of a fully unfolded protein.

The spectra of both mouse prions (MoWT and Q167R) follow the essentially two-state transition model, however, in both cases the transition region is unusually broad, ranging from 2 M urea to 6 M urea (see Figure 3.10 and 3.11), with midpoints occurring at 4.4 and 4.3 M urea respectively.

All of the transition curves at pH 4.0 exhibit sloping baselines compared to pH 7.0 (Figures 3.8 and 3.9), which may reflect the lower protein stability at acidic conditions and some minimal protein aggregation. The latter seems unlikely, however, due to the fact that fluorescence spectra show no significant difference between minimal fluorescence at pH 7.0 and pH 4.0 (see Figures 3.5, 3.6 and 3.7), which would be visible if some of the protein aggregated, hence decreasing the total fluorescence signal. Moreover, possible aggregation at lower pH was accounted for during the process of sample preparation. All samples were centrifuged prior to measurements in order to eliminate any possible aggregates. No visible pallets were collected and supernatants were clear.While there is no clear indication of accumulation of a β-state intermediate at urea concentrations between 3 and 5 M, which is characteristic for both mouse and hamster prions (Khan *et al.,* 2010), the broadness of the transition itself strongly suggests that neither MoWT nor Q167R follow two-state transition model.

Consequently, while the presence of β-state intermediate cannot be directly inferred from unfolding transition curves, the two-state model characteristic for mouse prions at higher pH cannot account for their behaviour at pH 4.0.

The transition curve of Syrian hamster PrP (see Figure 3.12) differs from two mouse spectra, in that while it exhibits similarly wide transition uncharacteristic for two-state model, it also contains an unusual feature in form of a plateau region between 3.5 M and 4 M urea which is consistent with the presence of β-state intermediate. It should be noted that the plateau region observed is narrower than expected – previously reported plateau region extends between 2.5 and 4 M urea (Khan *et al.,* 2010). The relatively narrow plateau region of hamster PrP, which has by far the highest propensity to form the intermediate,may explain why no such feature is visible in mouse PrP spectra, which have lower propensity to form β-structured intermediate. All three transition curves are visibly shifted towards lower urea concentrations in comparison to transition curves collected at pH 7.0 (see Figure 3.13) which is consistent with overall structural destabilisation characteristic for lower pH.

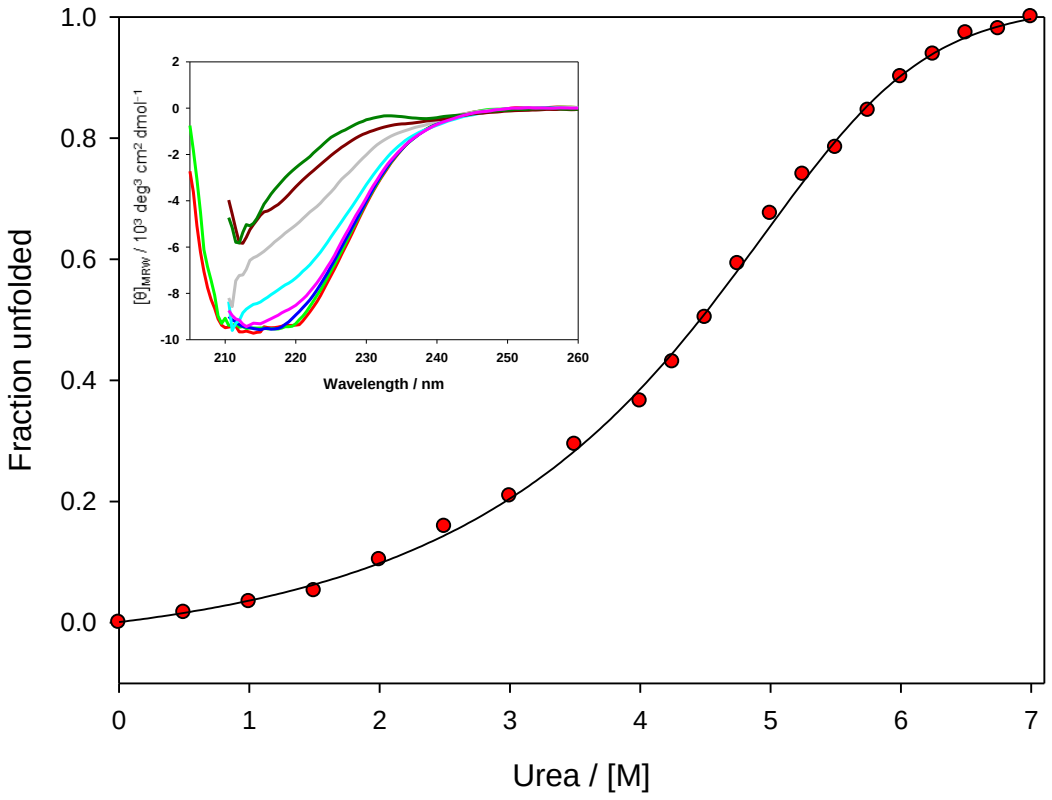

Figure 3.10 Denaturant unfolding transition curve of single-tryptophan mutant of mouse PrP (MoWT) followed by far-UV circular dichroism at pH 4.0. The inset shows CD spectra of 10 μM MoWT in 20 mM sodium acetate buffer collected in absence of denaturant (red), in presence of 1M urea (green), 2 M urea (blue), 3 M urea (pink), 4 M urea (cyan), 5 M urea (grey), 6 M urea (brown) and 7 M urea (dark green).

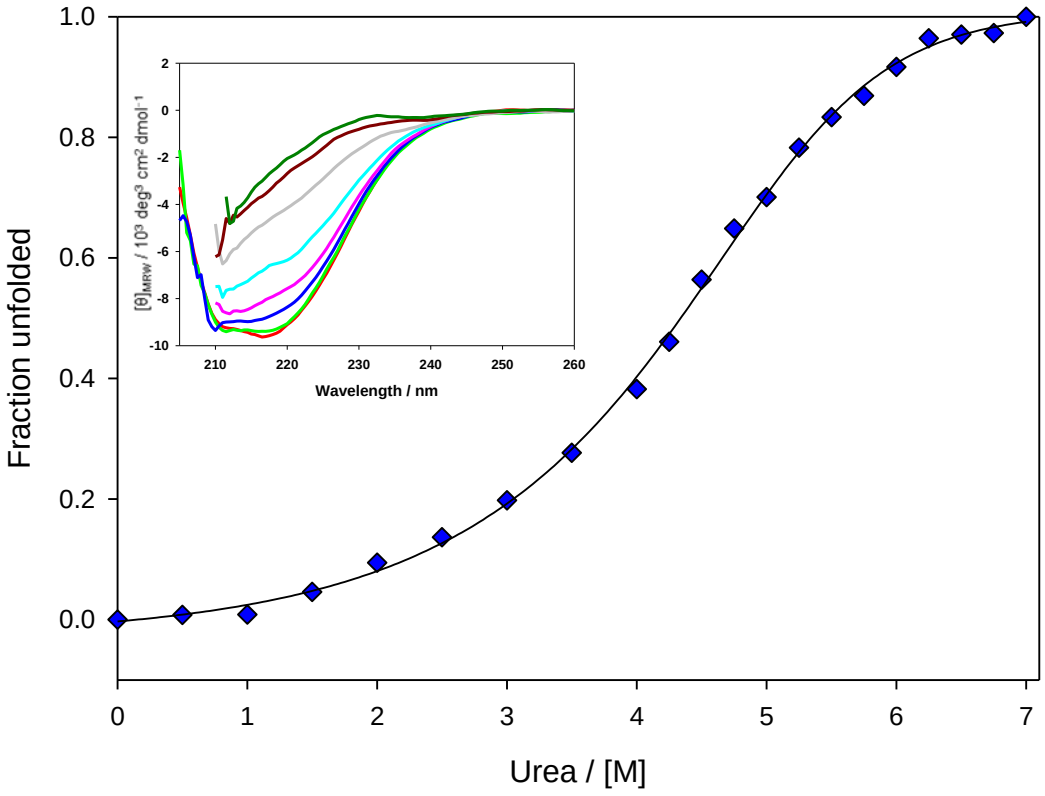

Figure 3.11 Denaturant unfolding transition curve of single-tryptophan construct of disease-associated mutant of mouse PrP (Q167R) followed by far-UV circular dichroism at pH 4.0. The inset shows CD spectra of 10 μM Q167R in 20 mM sodium acetate buffer collected in absence of denaturant (red), in presence of 1M urea (green), 2 M urea (blue), 3 M urea (pink), 4 M urea (cyan), 5 M urea (grey), 6 M urea (brown) and 7 M urea (dark green).

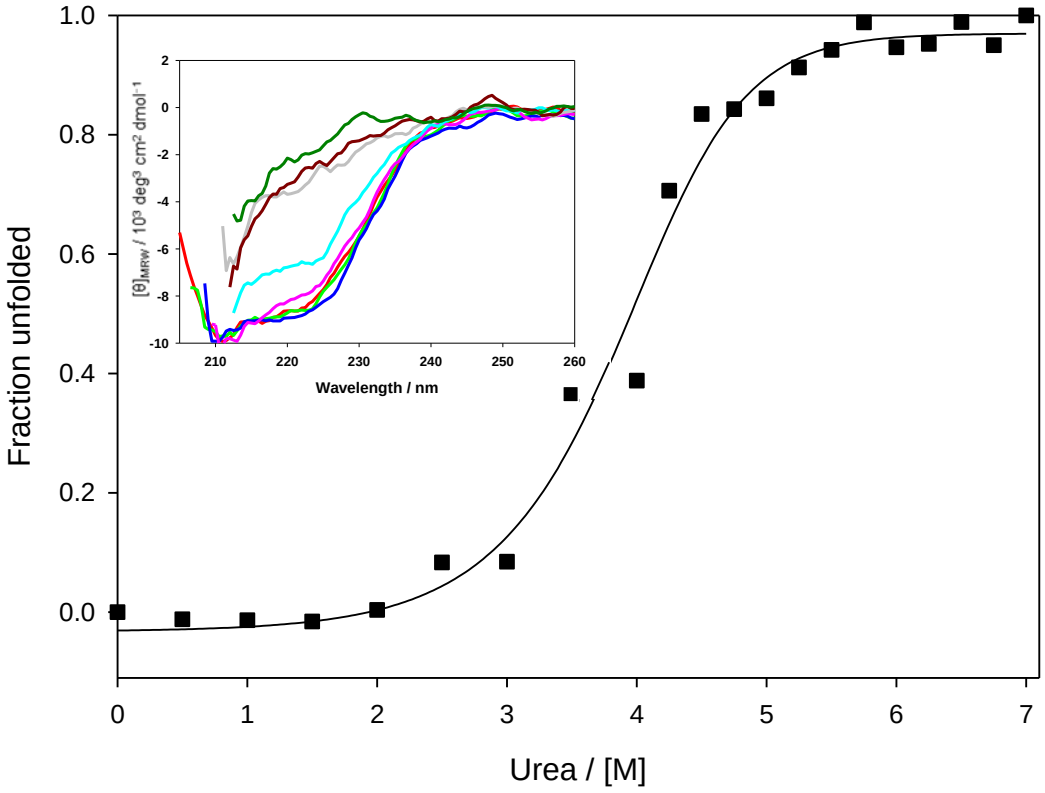

Figure 3.12 Denaturant unfolding transition curve of single-tryptophan mutant of Syrian hamster PrP (SHaWT) followed by far-UV circular dichroism at pH 4.0. The inset shows CD spectra of 10 μM SHaWT in 20 mM sodium acetate buffer collected in absence of denaturant (red), in presence of 1M urea (green), 2 M urea (blue), 3 M urea (pink), 4 M urea (cyan), 5 M urea (grey), 6 M urea (brown) and 7 M urea (dark green).

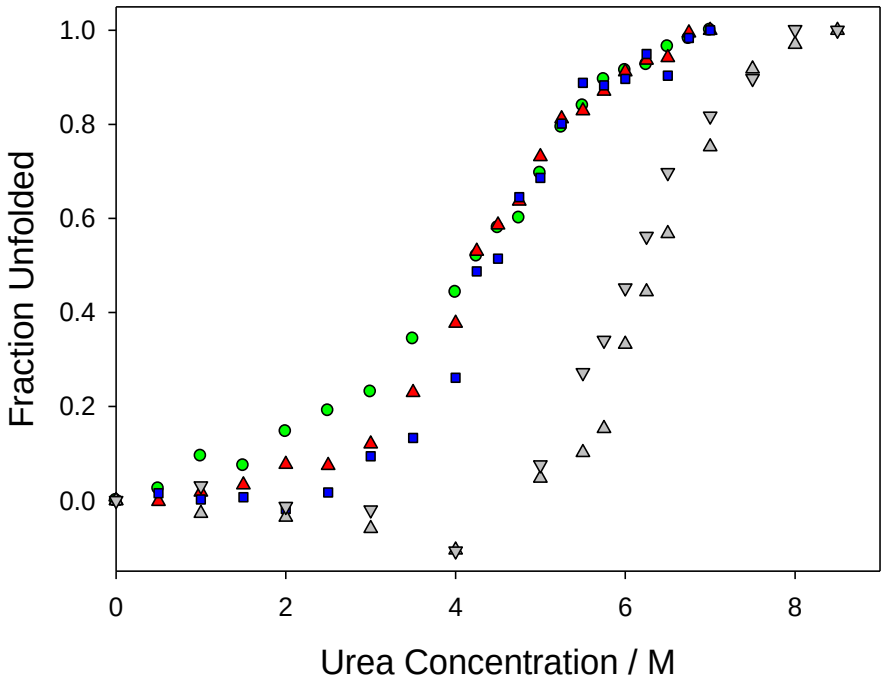

Figure 3.13 Comparison of CD denaturant unfolding transition curves of of 10 μM MoWT (green circles), Q167R (red traingles) and SHaWT (blue squares) collected in sodium acetate buffer at pH 4.0 with CD transition curves of MoWT (upward traingles) and Q167R (downward triangles) collected in 20 mM phosphate buffer at pH 7.0.

3.3.3 Fast folding kinetics investigated by pressure jump

Investigation of folding properties of PrP was performed using the truncated form of Syrian hamster and mouse PrP with native tryptophan residues removed and extra tryptophan inserted in key structural areas to act as a fluorescent probe sensitive to the folding state of PrP. Previous far-UV circular dichroism studies on Mo-PrP using a folding sensitive mutant with the tryptophan residue located at position 197 produced transition curves almost identical to those of wild type protein, indicating that folding is not affected by the position of tryptophan residue used to monitor the folding pathway (Robinson and Pinheiro, 2009). An orthologous mutant protein from Syrian hamster, SHaWT F198W, has also been used. It is similar to the protein studied previously (Jenkins *et al.*, 2009), with the exception of having its native tryptophan residues removed in order to reduce the background fluorescence. All of these measurements were conducted at pH 7.0 and pH 4.0, using urea as the denaturant.

3.3.3.1 Folding kinetics at varying denaturant concentrations

The PrP folding kinetics were investigated over a broad range of urea concentrations, ranging from 3.5 M up to 8.5 M for pH 7.0 and 3.0 M to 7.0 M for pH 4.0. Lower urea concentrations were required for pH 4.0 due to inherent destabilizing effect of decreased pH on the prion protein. In order to ensure that only relevant kinetic data will be captured, said concentrations were chosen following a careful investigation of published denaturant folding and refolding transition curves for pH 7.0 (Robinson and Pinheiro, 2009) as well as folding and refolding curves determined experimentally for pH 4.0 by monitoring red shift in Tryptophan fluorescence (Figures 3.8 and 3.9).

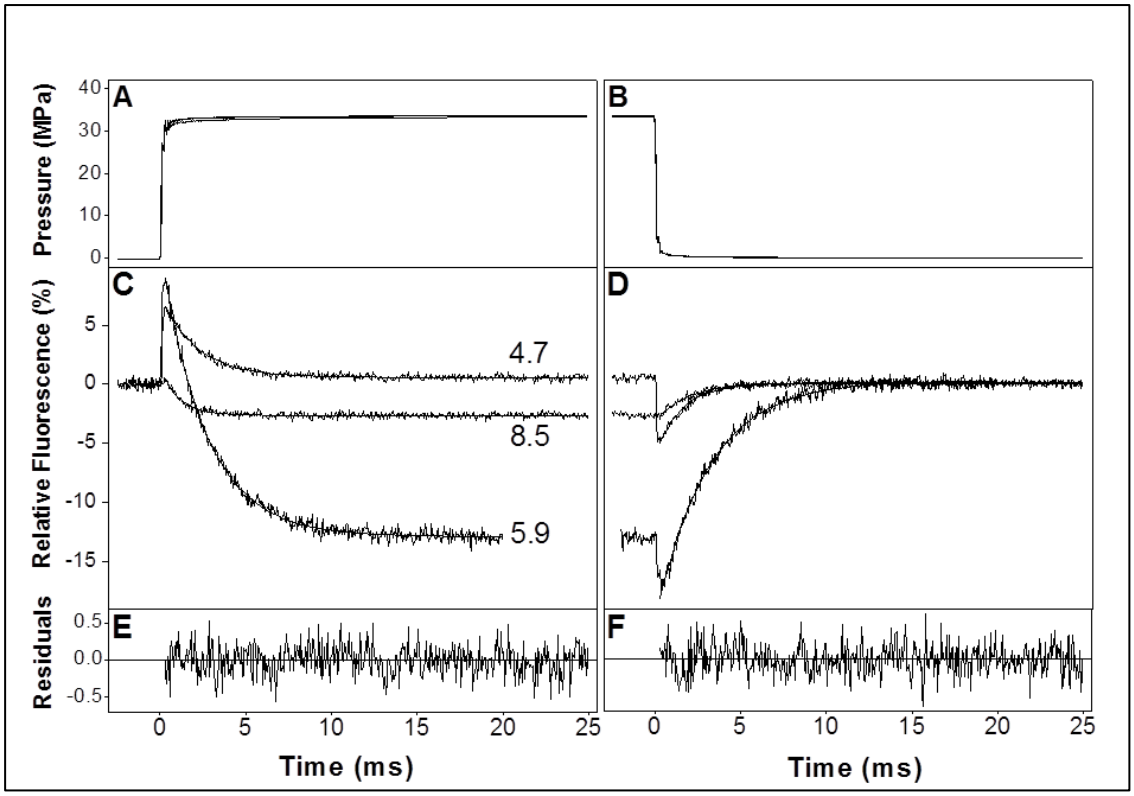

Figure 3.14 Folding kinetics of 10 μM MoWT monitored by fluorescence during a pressure-jump experiment. Unfolding and refolding of MoWT protein at 20^{o} C, pH 7.0 following pressure application and release. Top panels show the pressure profile upon pressure application (A) and release (B). Middle panels show three overlaid fluorescence transients acquired at different urea concentrations as well as single exponential fits by linear regression to saidfluorescence transients.Urea concentrations at which particular transients were obtained are shown as numbers next to curves in panel C). Data collected upon pressure application and release are shown in panels C and D respectively. Residuals from fitting to 4.7 M urea data are shown in the bottom panels (E and F).

Pressure application resulted in overall decrease in fluorescence which reverted to original state upon pressure release (Figure 3.14). This not only confirmed that pressure application shifts equilibrium towards the unfolded state, but also allowed us to determine that the process is fully reversible, again in accordance with published reports (Zhang *et al.*, 1997).

Recorded fluorescence transients were fitted to a single exponential function, with rates of fluorescence decrease upon pressure application of around $1/\tau$ = ~10,000 s^{-1} at both pH 7.0 and pH 4.0 depending on the PrP variant (Table 3.3). Upon pressure release the fluorescence transients measured at pH 7.0 follow the reverse pattern, with kinetic parameters being only slightly different than parameters derived from unfolding curves ($1/\tau$ = ~13,000 s^{-1} upon pressure release compared to $1/\tau$ = ~10,000 s^{-1} upon pressure application). Interestingly, at pH 4.0 the difference in rates of fluorescence decrease upon pressure application and release can only be observed for MoWT, with Q167R and SHaWT rates being very similar (Table 3.3).

It should be noted that both folding and unfolding constants (K_f and K_u) can be calculated for both pressure application (protein unfolding) and pressure release (protein refolding) experiments (see Table 3.3 and 3.4). While obtaining folding constant from unfolding experiment seems counter-intuitive, it is a direct consequence of perturbation of the equilibrium of the system.

Upon change in pressure the folding-unfolding equilibrium constant is altered as well, allowing for measurement of rate constant (inverse time constant, 1/tau) for the exponential relaxation process:

$$Y = A \exp(-t/\tau)$$

This $1/\tau$ value depends on the sum of the forward and backward rate constants, under the final conditions of the experiment (pressure, denaturant concentration etc.):

$$1/\tau = ku(D) + kf(D)$$

where the unfolding equilibrium constant, K(D) is given by

$$K(D) = ku(D)/kf(D)$$

Each of these rate constants depend exponentially on the denaturant concentration, a fragility parameter and the value of the rate constant in water (no denaturant):

$$ku(D) = ku(0) \exp(-mu\ [D]/RT)$$

and

$$kf(D) = kf(0) \exp(-mf\ [D]/RT)$$

There is thus also an equilibrium constant of unfolding under native conditions, which would be expected to be a very small number (as seen in first column of Table 3.3 and 3.4):

$$K(0) = ku(0)/kf(0)$$

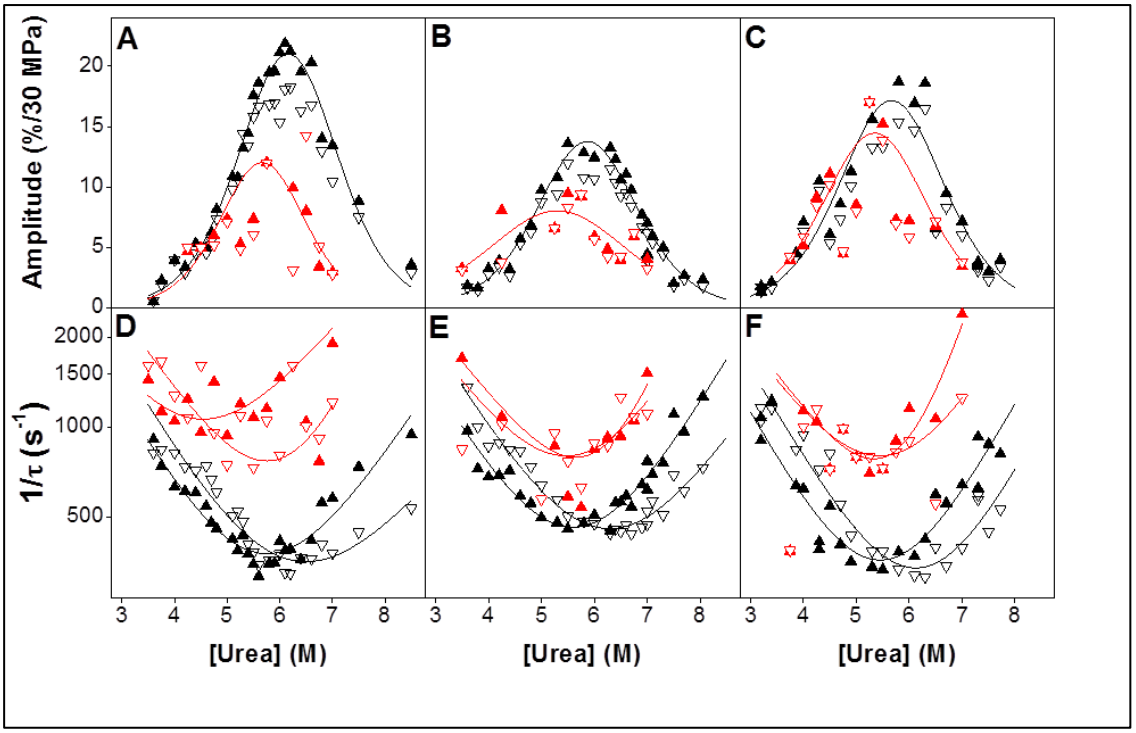

Figure 3.15 Effect of urea concentration on amplitudes (A, B, C) and inverse relaxation times (D, E, F) resulting from single exponential fits to pressure-jump relaxation transients. Results from MoWT are shown in panels A and D; Q167R are shown in panels B and E and SHaWT are shown in panels C and F. Black lines represent data obtained at pH 7.0, while red lines correspond to data yielded by experiments at pH 4.0. Upward pointing triangles indicate results of pressure increase and downward pointing triangles to pressure decrease. Smooth curves indicate fits to a two-state model – parameters obtained from fits are shown in Table 3.3 (pH 7.0) and Table 3.4 (pH 4.0).

Amplitudes of the exponential phase plotted against denaturant concentration (Figure 3.15) follow the bell-shaped curve characteristic for single step reactions for all three variants of PrP. The maxima of the amplitude plots occur where the equilibrium constant is closest to 1 and correspond to the minima of inverse time constants plotted against denaturant concentrations.

At pH 7.0 the amplitude maxima occur at denaturant concentrations of approximately 6.0, 5.9 and 5.7 M urea for MoWT, Q167R and SHaWT respectively, close to the minima of corresponding chevron plots and midpoints of denaturant unfolding transition curves (5.6 and 6.1 M Urea for pressure application and release for MoWT, 5.5 and 6.4 M urea for Q167R and 5.5 and 6.2 M urea for SHaWT). At lower pH the maxima occur at urea concentrations of 5.7, 5.3 and 5.2 M urea for MoWT, Q167R and SHaWT respectively, again close to the minima of corresponding chevron plots. This shift of parameters towards lower urea concentration is consistent with the destabilizing effect of decreased pH on protein stability.

It should be noted that for both pH 7.0 and pH 4.0 the pressure jump experiments were not performed along the entire range of denaturant unfolding transition curves, as at both very low and very high denaturant concentrations (below 3.5 and above 8.5M urea for pH 7.0 and 3.0 and 7.0M urea for pH 4.0) the amplitudes of the exponential phase were below 1% and hence too small to measure reliably. This is clearly visible on the amplitude plots, where both arms approach 0% amplitude as the measurements move further from the maximum.

Inverse time constants plotted against denaturant concentrations yielded well-defined two-state curves at both pH 7.0 and pH 4.0. As expected, at pH 7.0 the pressure increase and resulting shift in equilibrium towards unfolded state moved the midpoint of unfolding curves towards lower denaturant concentration, which is reflected by pressure application chevron curves being shifted towards lower urea concentration. The minima of chevron plots occurred at 5.64 and 6.13 M urea for MoWT for pressure application and release respectively, while corresponding values for Q167R were 5.51 and 6.38 M urea and 5.45 and 6.19 for SHaWT. The large difference between unfolding and refolding chevron arms at higher denaturant concentrations compared to lower denaturant concentrations hints at $\Delta Vu^{\ddagger}$ being negative and larger than -20 $mL.mol^{-1}$ which was confirmed by activation volume calculations.

Similar position of chevron minima of three PrP variants is surprising, taking into account the overall different shapes of chevron plots (particularly the MoWT and

Q167R curves) as well as the fact that MoPrP reportedly folds via two-state transition as opposed to SHaPrP folding via intermediate.

At pH 4.0 the chevron plots are much more superposable, particularly for Q167R and SHaWT, which is reflected in the minima of chevron plots for both pressure application and pressure release being much closer. This indicates that the population of folded states being shifted towards unfolded states upon pressure application is lower than at pH 7.0 due to overall decrease in stability induced by lower pH.

Independently on pH, the inverse relaxation times resulting from pressure release at low denaturant concentrations were faster than those resulting from pressure application, with the trend being reversed at higher urea concentrations. The minima of the refolding curves obtained during the pressure release are shifted to consistently higher denaturant concentrations than the minima of unfolding curves (eg. 5.64 M urea for pressure application and 6.13 M urea for pressure release for MoWT). The results of kinetic analysis of both amplitude and chevron plots are summarized in Tables 3.3 and 3.4, where the equilibrium fragility (*m*) is the sum of the two values from the two arms of the chevron.

As change in pressure influences the volume of the system, it allows the volume changes and pressure dependence of rate constants to be investigated, potentially revealing the activation volume of the reaction. This was achieved by plotting rates of unfolding and refolding against the net pressure change occurring upon pressure application (Figure 3.16). As expected, the relaxation times observed upon pressure release are very similar, since they are effectively measured at the same pressure of 1 bar. For pressure application, however, plots of intrinsic rate constant ($k_f(D)$ of $k_u(D)$) show strong pressure dependence. While at low pressure (1 bar) the $1/\tau$ is completely pressure-independent and depends only on final protein concentration, it does exhibit strong pressure dependence at high pressure values. This linear relationship between pressure and observed rate constants allows to define $\Delta V^{\ddagger}$ (change in volume between start of step and activated complex given by –RTdlnk/dP) for pressure application. The $\Delta V^{\ddagger}$ values calculated for different PrP constructs are shown in Table 3.3. Interestingly, while activation volumes of both mouse MoWT and hamster SHaWT are quite similar (-69 ± 2 and -57 ± 4 $mL.mol^{-1}$ respectively) the activation volume of Q167R is much lower (-39 ± 1 $mL.mol^{-1}$) hinting at decreased stability of the construct.

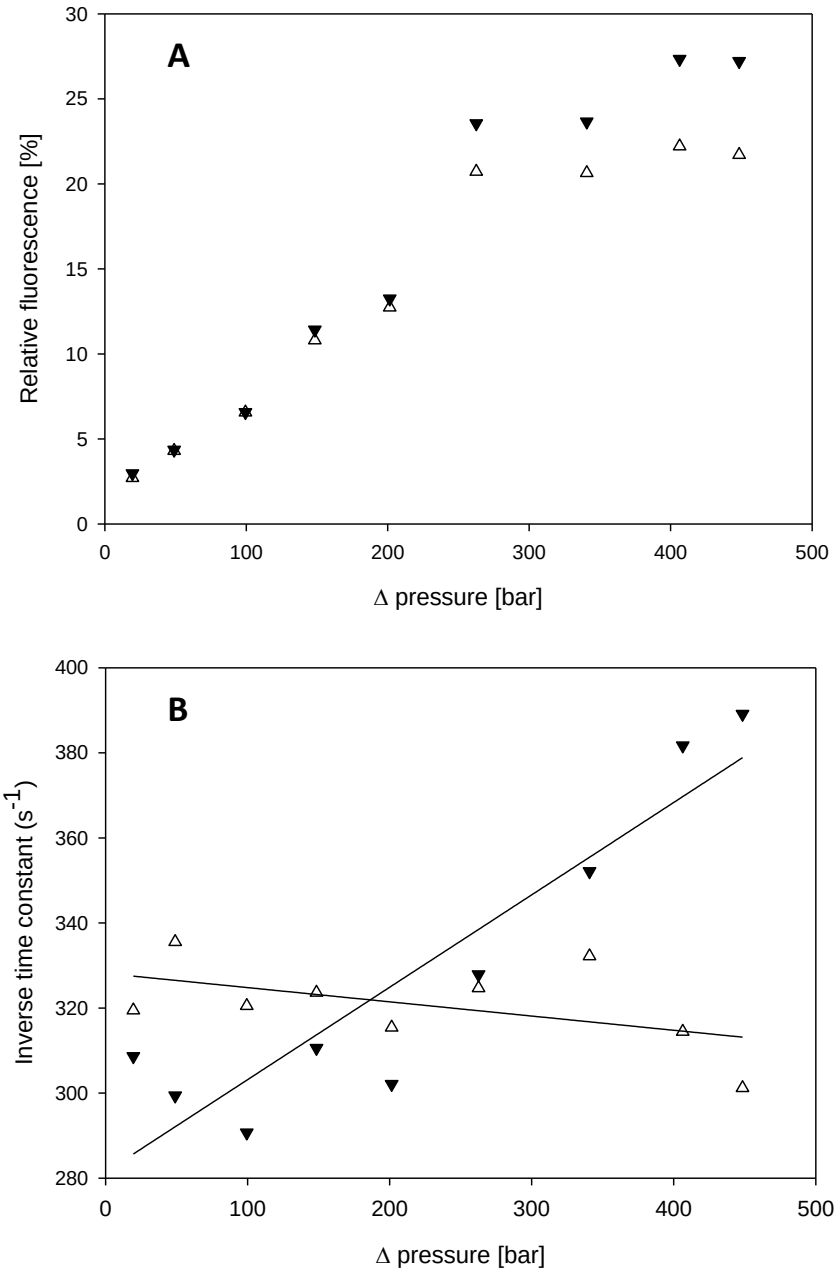

Figure 3.16 Effect of size of pressure jump on amplitude of change in relative fluorescence (A) and rate constant (B). Both fluorescence and rate constants upon pressure application (downward black triangles) and pressure release (upward white triangles) of 10 μM MoWT were recorded at 5.5 M urea, pH 7.0. Linear regression fits for both pressure application and pressure release data are represented in panel B as straight solid lines.

Table 3.3 Kinetic parameters of the folding of MoWT, Q167R and SHaWT at pH 7.0

	MoWT		**Q167R**		**SHaWT**		
	Pressure application	**Pressure release**	**Pressure application**	**Pressure release**	**Pressure application**	**Pressure release**	**Stopped-Flow**
k_u (s^{-1})	6.16 ± 0.03	10.97 ± 0.65	7.0 ± 0.2	7.0 ± 0.2	3.3 ± 0.7	1.5 ± 0.3	0.69 ± 0.04
k_f (s^{-1})	10 000 ± 1100	13 000 ± 560	10 000 ± 2700	13 000 ± 1900	10 000 ± 390	12 400 ± 380	12 000 ± 160
m_u ($kJ.mol^{-1}.M^{-1}$)	1.48 ± 0.15	1.11 ± 0.20	1.56 ± 0.22	1.38 ± 0.18	1.79 ± 0.32	1.87 ± 0.44	2.21 ± 0.34
m_f ($kJ.mol^{-1}.M^{-1}$)	-1.71± 0.19	-1.70± 0.30	-1.65 ± 0.24	-1.59 ± 0.31	-1.80 ± 0.25	-1.69 ± 0.21	-1.67 ± 0.04
$\Delta V°$ ($mL.mol^{-1}$)	-69 ± 2		-39 ± 1		-57 ± 4		N/A
m ($kJ.mol^{-1}.M^{-1}$)	3.19 ± 0.34	2.81 ± 0.50	3.21 ± 0.46	2.97 ± 0.49	3.59 ± 0.57	3.56 ± 0.65	3.88 ± 0.38
$[D]_{50\%}$ (M)	5.64 ± 0.63	6.13 ± 1.18	5.51	6.38	5.45 ± 1.03	6.19 ± 1.27	6.14 ± 0.65

Table 3.4 Kinetic parameters of the folding of MoWT, Q167R and SHaWT at pH 4.0

	MoWT		**Q167R**		**SHaWT**	
	Pressure application	**Pressure release**	**Pressure application**	**Pressure release**	**Pressure application**	**Pressure release**
k_u (s^{-1})	68	1.26	0.51	8.44	0.26	7.45
k_f (s^{-1})	9988	13056	9977	9737	9997	9766
m_u ($kJ.mol^{-1}.M^{-1}$)	1.18	2.30	2.68	1.67	3.11	1.73
m_f ($kJ.mol^{-1}.M^{-1}$)	-1.68	-1.40	-1.26	-1.38	-1.33	-1.38
$\Delta V°$ ($mL.mol^{-1}$)	-37		-25		-47	
m ($kJ.mol^{-1}.M^{-1}$)	2.86	3.71	3.94	3.06	4.44	3.11
$[D]_{50\%}$ (M)	4.24	6.08	6.11	5.62	5.79	5.63

A key molecular event in prion diseases is the conversion of cellular PrP to disease-associated form of the protein called PrP^{Sc}. For PrP^{C} to be able to convert to its misfolded isoform, it must undergo at least partial unfolding. Consequently, obtaining detailed information on the unfolding and folding properties of PrP may provide invaluable insight into the mechanism of misfolding.

Fast pressure-jump fluorimetry was used to investigate early events of the PrP folding pathway, as previous folding studies proved it to be an effective and reliable method capable of high time resolution, not relying on lowering the temperature to slow down the observed reaction (Jenkins *et al.*, 2009). As expected from earlier pressure-jump studies, the data collected during experiments on different PrP variants displayed similar characteristics, with produced transients compatible with equilibrium perturbation of three comparable single tryptophan PrP constructs.

All pressure-jump traces exhibited a characteristic decrease in fluorescence upon pressure application, which reverted to the original state upon pressure release, providing strong evidence that the equilibrium perturbation is fully reversible. Moreover, since the shape of fluorescence curves shows the relationship between pressure application and relaxation and equilibrium perturbation, it can be concluded that the equilibrium is perturbed momentarily, its changes depending only on pressure application and not other physical factors.

Independently of denaturant concentration, the PrP unfolding upon pressure application can easily be fitted to single exponential function (as shown in Figure 3.14) suggesting a single-step transition with little dependence on the denaturant concentration. However, very rapid fluorescence change occurring immediately after pressure application as well as fast amplitude imply a fast hidden step. The presence of such a fast phase may be indicative of the formation of a folding intermediate early in the folding pathway.

Variation in amplitude displayed by fluorescence curves is clearly dependant on the denaturant concentration, and hence the positions of the equilibrium along the folding curve. The largest amplitude changes occur at denaturant concentrations closest to the midpoint of the folding curve, confirming their dependence on the relative size of unfolded/folded populations of the protein that can be “recruited” in re-establishing equilibrium upon its perturbation by a rapid pressure change. This is confirmed by characteristic bell-shaped curves produced by plotting amplitude against urea concentration, where the maximum value of those curves corresponds with the midpoint

of folding curves. The overall shape, as well as a single, well-defined peak of those curves both supports the single-step model of PrP folding. Pressure-dependence of amplitude changes is more linear in nature, indicating marginal concentration changes upon pressure application. This linear relationship can be explained by larger pressure jumps allowing for greater equilibrium perturbation by increasing the population of PrP molecules that can change their folded/unfolded state and thus generating larger amplitude. Complete lack of any intermolecular interactions (such as dimerization) as part of the pathway was confirmed by flat lines obtained upon plotting amplitudes and rates against PrP concentration. Folding/unfolding kinetics as well as denaturant concentration dependence of rate constants of sHa were confirmed by subsequent stopped-flow measurements.

The amplitude curves obtained from wild-type single-tryptophan mouse and hamster proteins (MoWT and SHaWT respectively) show larger amplitudes than for mutated mouse variant Q167R, with maximum amplitude changes occurring at 6.1M urea for mouse PrP and ~5.8M for hamster PrP. Lower amplitude changes in Q167R mutant seem to indicate that the unfolded/folded populations of the protein are smaller with respect to MoWT and SHaWT, resulting in lower populations being available for folding state transition upon equilibrium perturbation.

The apparent difference in folding kinetics between MoWT and Q167R mutant is also visible in chevron plots. While for all the PrP variants the rate constants calculated from recorded transients follow a single-step unfolding model depicting a typical chevron shape, the rates themselves differ significantly with Q167R unfolding and refolding significantly faster than two other PrP variants ($1/\tau_{min}$ ~ 450 $s^{-}1$ for Q167R compared with $1/\tau_{min}$ ~ 350 s^{-1} for two other constructs). This difference is reflected by kinetic parameters calculated for different PrP constructs, with $\Delta V°$ of MoWT and SHaWT being 69 $mL.mol^{-1}$ and 57 $mL.mol^{-1}$ respectively, compared with only 39 $mL.mol^{-1}$ for Q167R, suggesting lower stability of disease-resistant mutant. These findings are consistent with structural interpretation of a hydrogen bond existing between R167 and Q171 which stabilizes the loop region between strand S2 and helix HB and which is missing in Q167R variant where R167 and R171 repel each other (Figure 3.17), destabilizing the loop region and consequently decreasing overall protein stability (Robinson and Pinheiro, 2009).

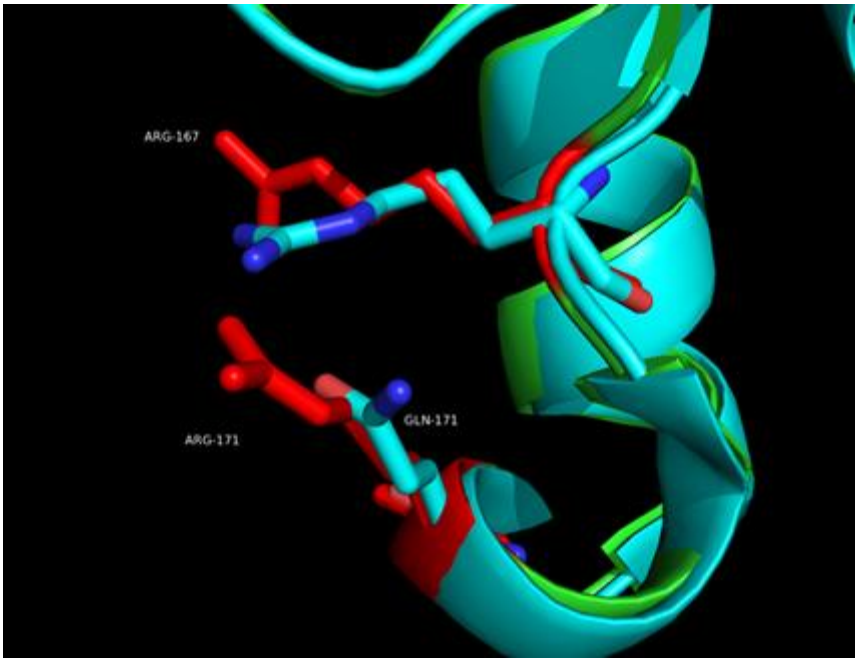

Figure 3.17 Overlay of the loop region of crystal structures of ovine Q171 (blue) and R171 (red) variants with residues 167 and 171 highlighted.
The NMR structure was drawn from PDB file 1TPX (Q variant) and 1TQC (R variant) using UCSF Chimera package as stated in legend of Figure 3.2.

3.3.4 Fibrilisation studies of PrP

While kinetic studies using spectroscopic methods such as pressure-jump can provide invaluable insight into earliest kinetic events of protein folding pathway, they cannot provide details on conformation or propensity to form aggregates. Independently of any differences in folding kinetics, the disease resistance and species barrier may not be linked directly with the early folding pathway. They may instead be associated with propensity of PrP to form neurotoxic oligomers as well as amyloid-like fibrils. Thus, the pressure-jump studies of kinetics of early folding pathway of PrP were supplemented with fibrilization studies of prion proteins in order to identify key processes involved in both species barrier and disease resistance.

Fibril formation of single-tryptophan constructs of MoWT, Q167R and SHaWT was investigated in a series of fibrilisation studies utilizing ThT fluorescence (Gill *et al.* 2009).

In order to determine whether conditions which promote formation of β-state intermediate affect the rate of fibril formation as well as morphology of formed fibrils, the fibrilisation experiments for all three PrP constructs (MoWT, Q167R and SHaWT) were conducted at pH 4.0 which is known to promote the formation of intermediate, as well as at pH 7.0 where the intermediate was not observed.

Fibrilisation experiments were conducted at 6 M urea concentration for pH 7.0 and 4 M urea for pH 4.0 Initial fibrilization experiments were conducted with and without 200 mM NaCl which mimicked the salt concentrations present in cells. The presence or absence of salt was determined to have no quantifiable effect on length of lag phase, rate of fibril formation or their morphology. The ThT fluorescence traces obtained during fibrilisation experiments are shown in Figures 3.18, 3.19 and 3.20.

Both species of mouse PrP – MoWT and Q167R – form fibrils after approximately 50-80 hours from onset of incubation, as indicated by rapid increase in ThT fluorescence (see Figures 3.18 and 3.19). In both cases the lag phase observed at neutral pH is noticeably shorter than the lag phase at pH 4.0 (see Table 3.5). This is consistent with observation that mildly destabilising conditions result in longer lag phase (Birkmann and Reisner, 2008).

At pH 7.0 the observed lag phase of MoWT is slightly shorter than that of Q167R (57.4 h and 77.2 h respectively); however at pH 4.0 the length of both lag phases is similar (see Table 3.5). Interestingly, lag phase of Q167R seems to be affected by change in pH

to a lesser extent than that of MoWT. Taking into account that conditions which destabilise protein may result in lag phase extension, this seems to be consistent with lower overall stability of PrP conferred by Q167R mutation compared to MoWT, independently of pH.

Unlike mouse prions, the formation of fibrils by Syrian hamster PrP could not be successfully induced at either pH 7.0 or pH 4.0 (see Figure 3.20). However after approximately 80-90 hours the ThT fluorescence exhibits minor increase from approximately 1.5 to 3.0-3.5 fluorescence units, which may be indicative of slow protofibril formation in the reaction mixture.

Upon seeding with fibrillous material, both MoWT and Q167R exhibit significant reduction in length of average lag phase, from approximately 57 hours to 17 hours for MoWT and approximately 77 to 8 hours for Q167R at pH 7.0. At lower pH, the lag phases are similarly reduced from 83 hours to 9 hours for MoWT and from 82 hours to 10 hours for Q167R.

This is consistent with short PrP oligomers obtained from mature fibrils used in seeding providing a template for conversion of PrP^{C} into PrP^{Sc} and its subsequent aggregation and fibrilisation (Jones and Surewicz, 2005; Graham *et al.,* 2010).

In case of Syrian hamster, the minor change in ThT fluorescence attributed to protofibril formation also occurs significantly faster upon addition of pre-formed fibrils to the reaction mixture. The estimated length of average lag phase is decreased from 100 hours to just above 30 hours.

Consecutive seeding of reaction mixture with fibrilous material obtained at the end of first seeding experiment did not reduce the lag phase any further, independently of PrP construct (see Table 3.5), indicating that the presence of the seeding material itself is a key factor in PrP fibrilisation.

Morphology of fibrils formed during secondary seeding experiment was investigated by electron microscopy (see Figure 3.21).

Both MoWT and Q167R form elongated fibrils characteristic for prion aggregation in solution. While pH in general does not seem to have a significant effect on the rate of fibril formation and relatively mild effect on the duration of the lag phase, upon inspection of EM images it is clear that fibrils formed at pH 4.0 are shorter but much more abundant than those formed at pH 7.0 The fibrils of both MoWT and Q167R formed at pH 7.0 are longer but less abundant compared to pH 4.0. At lower pH, the

sheer number of short fibrils indicates that the total population of PrP molecules forming fibrils is higher.

In case of Syrian hamster, while no fibrillous material seems to be present at pH 7.0, the short protofibrils are clearly visible in pH 4.0 sample.

These findings are of utmost interest if one considers the prevailing opinion that formation of fibrils and their aggregation as well as subsequent formation of plaques is a protective mechanism evolved to avoid high toxicity of soluble oligomers (Buccianti *et al.,* 2002; Kirkitadze *et al.,* 2002; Caughey *et al.,* 2003). Indeed, a growing body of evidence indicates that small, soluble oligomers are primary cytotoxic mechanism as opposed to fibril formation and deposition on cellular membranes (Chisea *et al.,* 2001; Novitskaya *et al.,* 2005).

Consequently, increased propensity of fibril formation of mouse PrP could explain lower susceptibility of mice to prion diseases, compared to Syrian hamster. Since the Q167R mutant of mouse PrP exhibits higher propensity to form fibrils and the length of its lag phase is less affected by change in pH compared to wild-type construct, the structural destabilisation conferred by the point mutation seems to play a key role in disease-resistance mechanism.

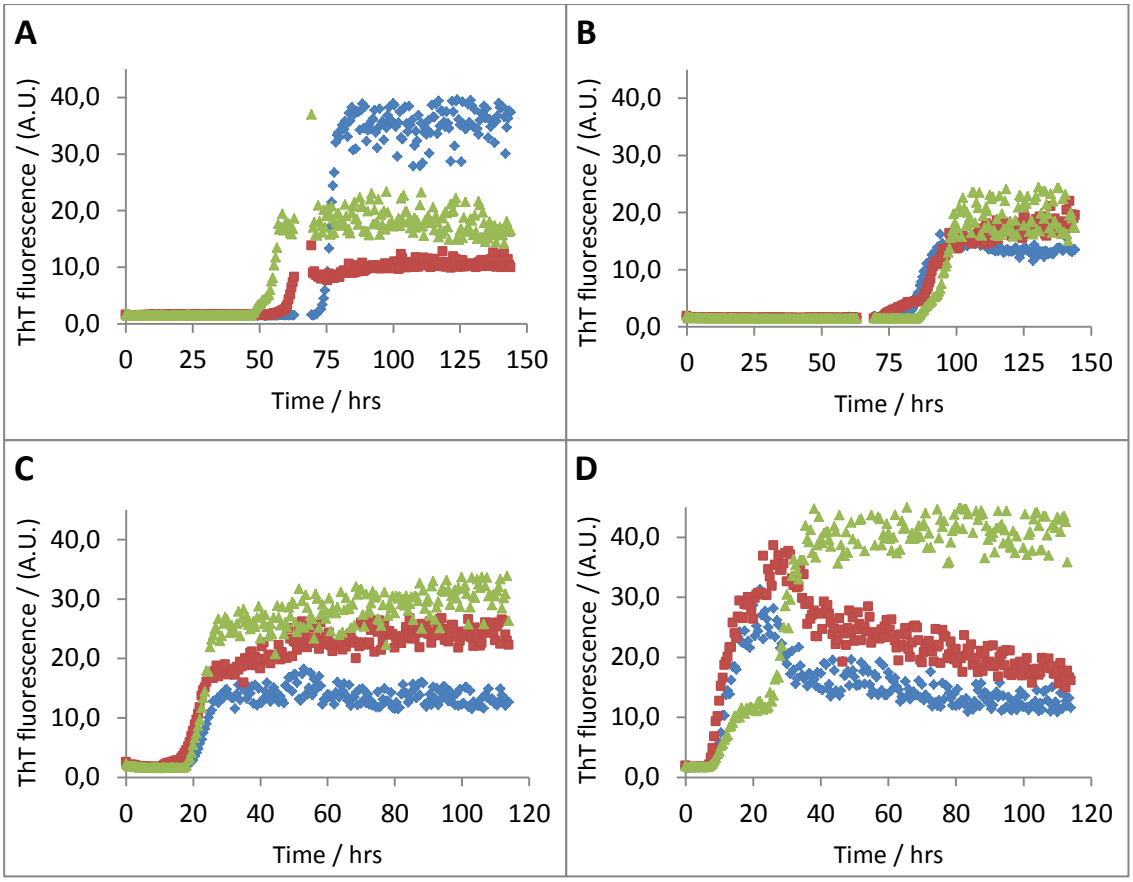

Figure 3.18 Triplicates of ThT fluorescence curves of 120 μg/ml MoWT (see section 3.2.7 for details on sample preparation) obtained as a result of three independent fibrilisation experiments conducted at pH 7.0 (A and C) and pH 4.0 (B and D). Panels A and B show fluorescence traces obtained as a result of unseeded fibrilisation. Panels C and D depict ThT fluorescence curves collected upon secondary seeding - that is seeding with fibrillous material obtained at the end of first seeding experiment.

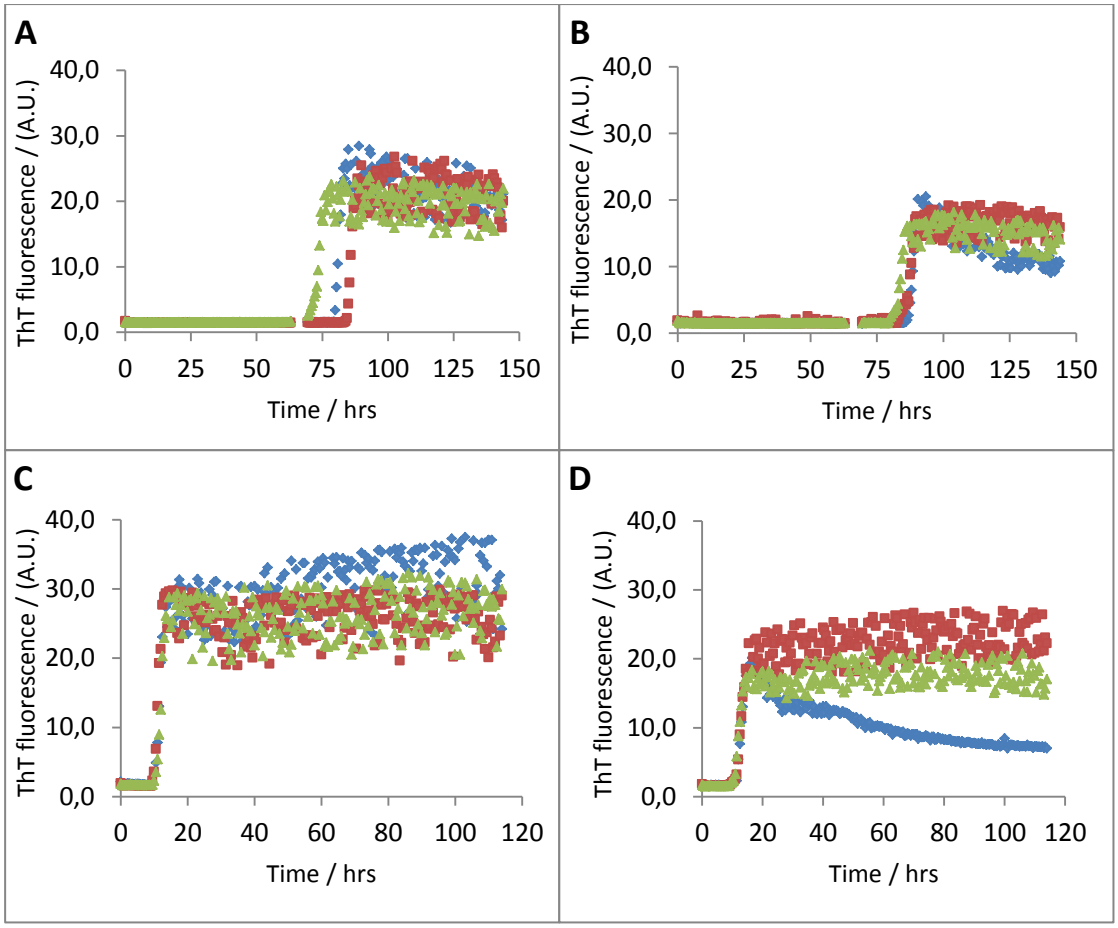

Figure 3.19 Triplicates of ThT fluorescence curves of 120 μg/ml Q167R obtained as a result of three independent fibrilisation experiments conducted at pH 7.0 (A and C) and pH 4.0 (B and D). Panels A and B show fluorescence traces obtained as a result of unseeded fibrilisation.

Panels C and D depict ThT fluorescence curves collected upon secondary seeding - that is seeding with fibrillous material obtained at the end of first seeding experiment.

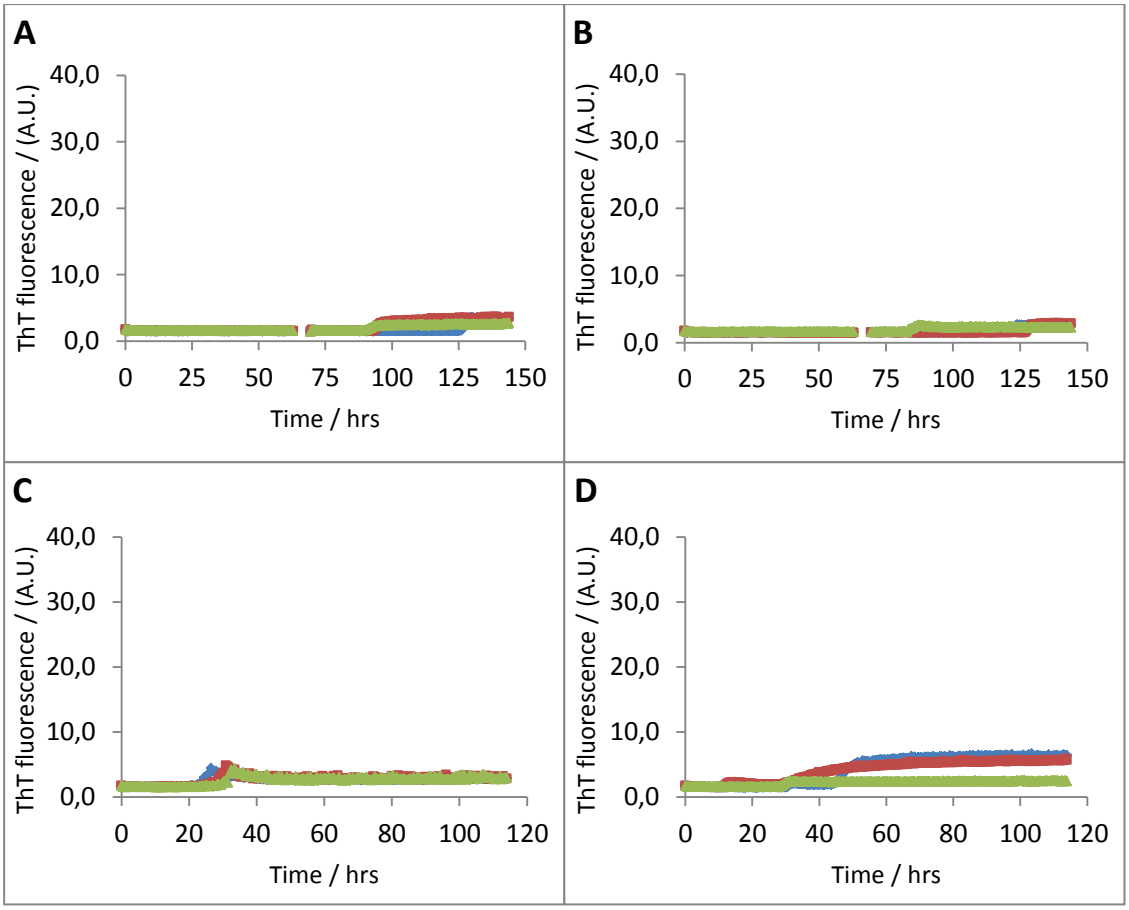

Figure 3.20 Triplicates of ThT fluorescence curves of 120 μg/ml SHaWT obtained as a result of three independent fibrilisation experiments conducted at pH 7.0 (A and C) and pH 4.0 (B and D). Panels A and B show fluorescence traces obtained as a result of unseeded fibrilisation.

Panels C and D depict ThT fluorescence curves collected upon secondary seeding - that is seeding with fibrillous material obtained at the end of first seeding experiment.

PrP construct	pH	Lag phase duration (h)	Lag phase duration primary seeding (h)	Lag phase duration secondary seeding (h)
MoWT	7.0	57.4 ± 7.6	16.5 ± 2.9	17.2 ± 2.1
	4.0	82.8 ± 4.2	8.5 ± 2.0	7.3 ± 1.3
Q167R	7.0	77.2 ± 4.7	7.8 ± 2.1	8.6 ± 1.7
	4.0	81.5 ± 2.3	10.2 ± 3.1	9.2 ± 1.1
SHaWT	7.0	101.5 ± 15.6	36.7 ± 7.1	32.7 ± 9.7
	4.0	104.3 ± 18.0	33.6 ± 6.6	29.6 ± 8.5

Table 3.5 Average lag phase duration observed during fibrilisation experiments of MoWT, Q167R and SHaWT at two different pH values. The length of each average lag phase was calculated by averaging the duration of lag phases from six independent fibrilisation experiments. Errors represent the standard error.

PrP construct	pH	A	B
MoWT	7.0	12.32	0.48
	4.0	39.12	1.23
Q167R	7.0	33.02	0.73
	4.0	45.25	0.74
SHaWT	7.0	9.26	0.82
	4.0	9.03	0.91

Table 3.6 T-parameter values obtained via statistical comparison of length of unseeded lag time with length of lag time upon primary seeding (column A) and length of lag time upon primary seeding with that of secondary seeding (column B) using T-test. T-parameter values exceedint 1.812 allow for the null hypothesis to be rejected, thus confirming the statistically significant difference between thermodynamic parameters. For values below 1.812 the null hypothesis cannot be rejected, and consequently no statistically significant difference can be claimed.

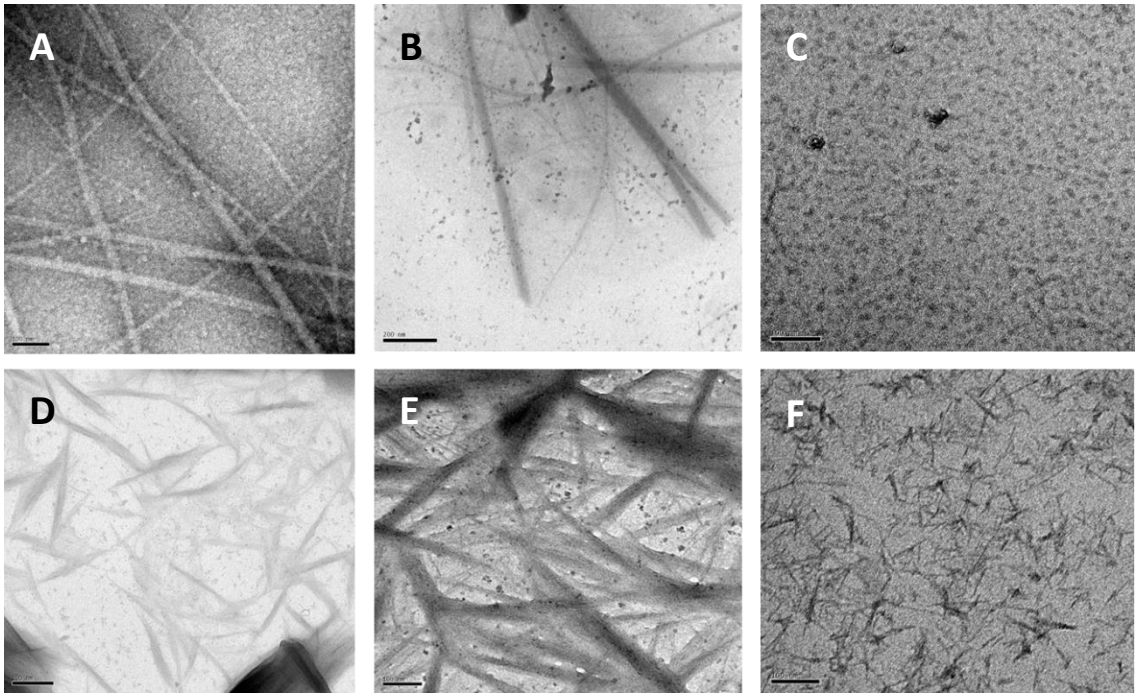

Figure 3.21 Electron microscope images of fibrils formed by secondary seeding of MoWT (panels A and D), Q167R (panels B and E) and SHaWT (panels C and F). Panels A, B and C depict fibrils formed at pH 7.0, while panels D, E and F show fibrils formed at pH 4.0.
The thin black bar visible in bottom left corner of each image represents a scale bar of 100 nm.

3.4 Summary

In this study, three single tryptophan mutants of prion proteins from two different species – mouse prion constructs MoWT and Q167R and Syrian hamster PrP SHaWT - were used to investigate the kinetics early folding pathways as well as fibrilisation properties in an attempt to explain the mechanism of species barrier and disease resistance. All of the experiments were conducted at neutral pH as well as pH 4.0 at which both mouse and Syrian hamster prions exhibit increased propensity to form a β-state intermediate which has been linked with disease susceptibility (Khan *et al.*, 2010).

Equilibrium denaturation studies of PrP by urea showed that while at pH 7.0 both mouse constructs exhibit a transition characteristic for two-state mechanism, at pH 4.0 the same transition is too broad to be explained by a two-state model. This indicates that at pH 4.0 mouse PrP may fold via an intermediate state which is not present at higher pH.

The denaturant unfolding transition curve of Syrian hamster shows the propensity to form the β-state intermediate at pH 4.0, although at a lower extent than reported (Khan *et al.*, 2010).

The pressure-jump studies of early folding kinetics of PrP determined that while at pH 4.0 the overall stability of all three PrP constructs is lower than at pH 7.0, the presence of β-state intermediate at lower pH is not visible in terms of folding kinetics. Lower fluorescence amplitudes as well as faster folding and unfolding rates of Q167R confirmed that the point mutation negatively affects overall stability of the protein. This effect was more pronounced at pH 7.0 than at pH 4.0.

Fibrilisation studies demonstrated that both MoWT and Q167R have significantly higher propensity to form fibrils compared to Syrian hamster PrP, particularly at pH 4.0. The total fibre amount at the end of fibrilisation experiment is highest for Q167R, indicating that the disease resistance mechanism conferred by this point mutation may be tied to its fibrilisation properties. Since formation of fibrils and their aggregation as well as subsequent formation of plaques is considered as a protective mechanism evolved to avoid high toxicity of soluble oligomers, highest total fibre amount may be indicative of increased propensity to form fibrils, which is a valid mechanism of increased disease resistance.

Chapter 4: Equilibrium and fibrilisation studies of Elk PrP

4.1 Introduction

Chronic wasting disease (CWD) is a prion disease of free-ranging wildlife, affecting a number of cervid species such as deer, elk and moose. It is the only prion disease identified so far which affect wild animals, which coupled with its high transmission rate and the fact that the exact prevalence remains currently unknown is of major concern in terms of epidemiology. While the possibility of transmission of CWD to other species remains unknown, only a handful of occurrences in human population could result in a new disease, much like transmission of bovine prions to humans resulted in an emergence of a variant of Creutzfeld-Jakobs disease.

In transmission experiments, inoculation of squirrel monkeys with CWD prions induced the disease, yet transgenic mice expressing human PrP remained unaffected, indicating that the species barrier effect between humans and cervids is stronger than between cattle and humans (Kong *et al.*, 2005; Sandberg *et al.*, 2010).

Although these findings reduced the perceived threat of cervid prion disease transmission to humans, recent protein misfolding cyclic amplification (PMCA) study showed that PrP^{Sc} generated *in vitro* by PMCA is infectious to wild-type animals and maintains the strain properties. PMCA is a technique which mimics prion replication *in vitro* at an accelerated speed, and can be used to generate, adapt, and stabilize new prion strains upon crossing species barriers *in vitro* (Green *et al.*, 2008; Castilla *et al.*, 2008). It was determined that serial round of PMCA produce the same adaptation of natural CWD prion strain as serial passages *in vivo*.

These findings are of great importance in terms of current understanding of emergence and adaptation of new prion strains. Based on the available knowledge, two main routes of prion strain appearance may be defined: spontaneous route through interspecies transmission or by genetic mutations. These “first generation” prions are unstable strains that begin a progressive and gradual process of adaptation that may take several passages and years or decades to complete (Barria *et al.*, 2011). Consequently, it is possible that the CWD prions spreading among the wildlife may at some point adapt to other species including humans, as demonstrated by PMCA experiments.

It is therefore of vital importance to understand the mechanism underlying CWD, particularly the conversion of cervid PrP^{C} into PrP^{Sc} and its transmission between individuals, as well as the species barrier existing between humans and cervids.

Despite differences in primary sequence, the prion proteins from different species share almost identical tertiary and secondary structures composed of unstructured region and a small globular domain, with three α-helices and two short β-sheets being the primary features (see Figure 4.1). Cervid prions, however, of which Elk PrP is a prime example, possess a unique structural feature which is not encountered in other species such as mice, hamsters, cats, dogs, bovine or humans (Gossert *et al.*, 2005; Lysek *et al.*, 2005). The loop region located between α-helix referred to as α2 and one of the short β-sheet strands known as β2 is very precisely defined in Elk PrP, while in other species it exhibits a high structural disorder (Gorfe and Caflisch, 2007).

The source of this highly ordered structure can be traced to two amino acid substitutions at positions 170 and 174 with respect to PrP from other species. These findings are confirmed by the fact that upon introduction of the sequence of elk loop region into mouse PrP, the elk-mouse hybrid S170N/N174T is created, which contains a rigid loop region exactly mimicking that of Elk PrP (Gossert *et al.*, 2005). Moreover, the loop region of Syrian hamster prion protein containing Asn residue at position 170 is also partially stabilised, similarly to S170N variant of human PrP. Unlike mutation at position 170, the introduction of Thr residue at position 174 in the loop region of mouse PrP if not coupled with second stabilising mutation, does not induce noticeable increase in stability. This indicates that it is the presence of serine residue at position 170 which is the key factor determining the stability of the entire loop region (Gorfe and Caflisch, 2007).

The stabilising effect of point mutations described above is a result of side-chain hydrogen bonds formed by residues within the loop region. Interestingly, the residues 170 and 174 do not interact directly, but instead play key roles in formation of two separate groups of hydrogen bonds. The first group of two backbone hydrogen bonds is formed between residues 165–169, while the second group forms between side chains of residues 171 and 174 (Gossert *et al.*, 2005).

While the structural effects of both mutations may seem unimportant, a growing body of evidence suggests that the stability of the loop region may be important for the species barrier effect. The loop, and in particular the residue 170, are thought to play a

critical role as a ‘molecular switch’ modulating prion transmission (Sigurdson *et al.*, 2009, 2010).

Moreover, the higher flexibility of the loop region may be an important factor in the species barrier between cervids and other mammals.

Recent molecular dynamics simulations suggest that a compact loop encompassing residues 166-175 is necessary for aggregation and formation of the infectious particles in elk, sheep and mouse prion strains. In the protofibril model, the stabilised turn is buried between two PrP monomers and makes contact with 35 neighboring residues. In absence of S170N and N174T mutations, the loop region is destabilised, and the resulting flexible, expanded loop disrupts the packing of the adjacent monomers, consequently impairing their incorporation into the protofibril (Scouras and Daggett, 2012). Another potential disease-resistance mechanism is based on the possibility that if the PrP variants carrying loop-destabilising mutations become parts of the infectious seeds, the altered stability of their conformation prevents further oligomerisation (Ott *et al.*, 2008).

Due to the fact that mouse PrP carrying S170N and N174T mutations is structurally very similar to elk PrP, it provides a valuable model for further investigations into the effects of loop-stabilising mutations. Interestingly, molecular dynamics simulations predicted the formation of elk-like rigid loop in MoPrP at pH 7.0, but not at pH 5.0 or pH 3.0, suggesting that the pH itself may affect oligomerisation and fibrilisation properties of some PrP species.

Consequently, investigating equilibrium folding and fibrilization properties of a series of mouse PrP mutants carrying either or both loop-stabilising point mutations (S170N, N174T and double mutant S170N/N174T) and their comparison with wild-type mouse PrP should yield to our understanding of both the misfolding mechanisms associated with the disease’s occurrence and the phenomenon of the species barrier and varied disease susceptibility.

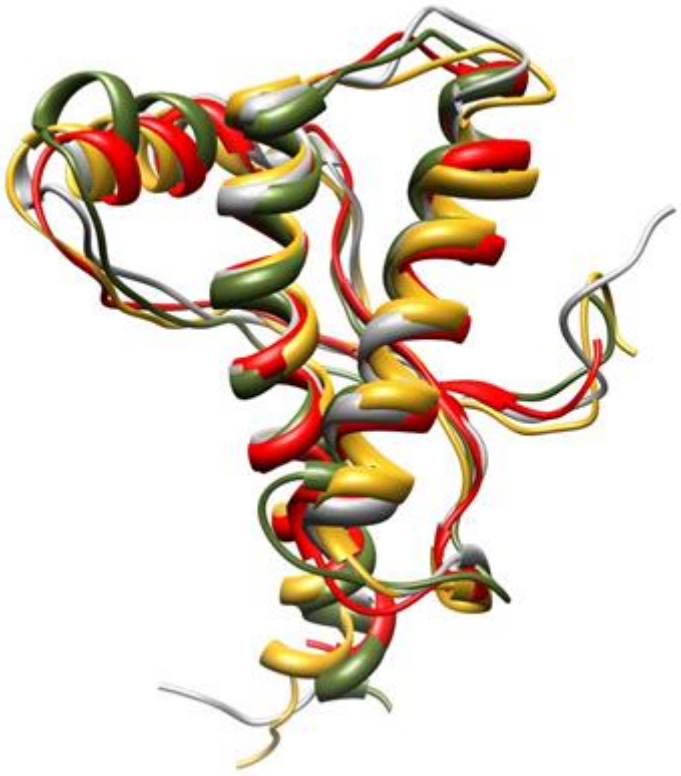

Figure 4.1 Overlay of NMR structures of human PrP (olive), mouse PrP (yellow), Syrian hamster PrP (red) and elk PrP (grey) showing remarkable conservation of secondary and tertiary structure across different species.

NMR structures were drawn from PDB files 1B10, 1QM0, 1XYW and 1XYX using UCSF Chimera package from the Resource for Biocomputing, Visualization and Informatics at the University of California, San Francisco (supported by NIH P41 RR-01081) (Pettersen *et al.*, 2004).

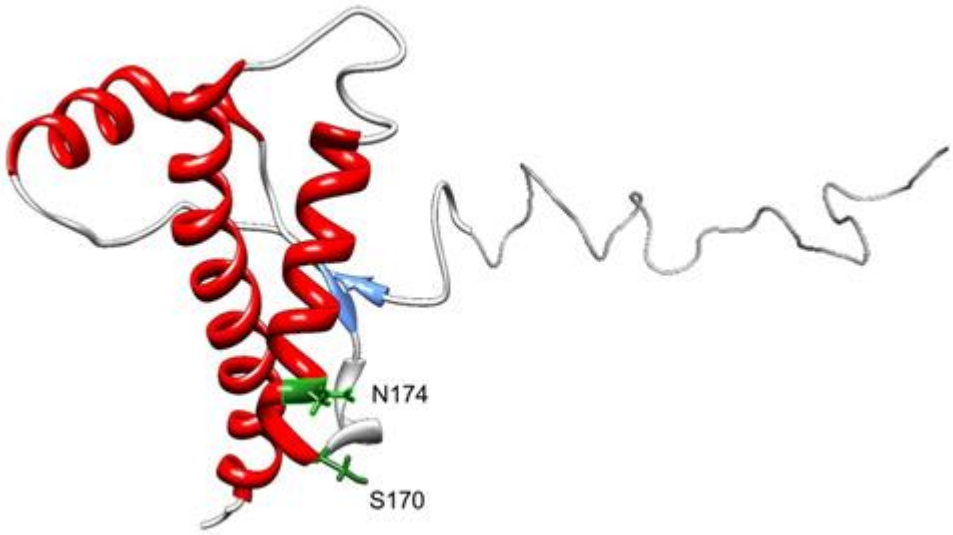

Figure 4.2 Ribbon representation of NMR structure of globular domain of murine prion protein (residues 91-230). Main structural features are highlighted in colour with locations of two elk mutations highlighted using stick representation. Three main α-helices are shown in red, with short antiparallel β-sheet highlighted in blue. Residues N174 and S170 are highlighted in green.

The NMR structure was drawn from PDB file 1XYX using UCSF Chimera package from the Resource for Biocomputing, Visualization and Informatics at the University of California, San Francisco (supported by NIH P41 RR-01081) (Pettersen *et al.*, 2004).

4.2 Materials and Methods

4.2.1 Materials

All chemicals were purchased from Sigma-Aldrich (Poole, UK) unless stated otherwise.

During the study, four full length mouse constructs carrying point mutations characteristic for elk PrP were used. The full length wild type mouse PrP is referred to as MoPrP in this chapter to avoid confusion with MoWT designation given to single tryptophan truncated construct Mo(91-230)F197W used in other chapters. Two constructs carrying single point mutations at positions 170 and 174 are named S170N and N174T respectively. Double mutant with both substitution mutations is referred to as S170N/N174T.

Note that all of the mutations are described using elk numbering rather than mouse numbering, as commonly used in literature.

All of the full-length prion protein constructs described above were supplied by Dr Andrew Gill (Roslin Institute, University of Edinburgh).

4.2.2 Circular dichroism spectroscopy

Urea unfolding curves of MoPrP, N174T, S170N and S170N/N174T were constructed through a series of circular dichroism measurements similar to those described in section 3.2.3, with the following differences:

Stock solutions of unfolded prion proteins were prepared in 9 M urea instead of 8 M urea used in section 3.2.3; other stock solutions, buffers, measurement procedures and data processing methods were identical.

4.2.3 Fibrilization of PrP

Fibrilization studies of MoPrP, N174T, S170N and S170N/N174T were carried out according to the protocol stated in section 3.2.7. All buffers, measurement procedures and data processing methods were identical.

4.3 Results and Discussion

4.3.1 Equilibrium denaturation of elk PrP followed by far-UV circular dichroism

Far-UV circular dichroism was used to construct denaturant unfolding transition curves of MoPrP, N174T, S170N and S170N/N174T at pH 7.0 and pH 4.0 in order to determine the range of denaturant concentrations best suited for fibrilisation experiments.

Since fibril formation of PrP occurs in mildly denaturing conditions (Breydo *et al.*, 2008), urea concentrations corresponding to mid points of transition curves were selected.

Two different pH values were used throughout the experiment in order to determine the effect of formation of rigid elk-like loop observed in mouse PrP at pH 7.0, but absent at lower pH (Scouras and Daggett, 2012).

In absence of urea, all CD spectra show clear characteristics of predominantly α-helical structure: two negative bands at 208 and 222 nm and a positive band at 195 nm (see Figures 4.3, 4.4, 4.5 and 4.6, panels B and C).

Upon increase in denaturant concentration, the two bands indicative of α-helical structure lose their intensity, and a single strongly negative band appears around 205 nm, which is characteristic for random coil structure. Changes in the third band at 195 nm are not visible due to spectral properties of urea present in solutions at increasing concentrations, which prevented any reliable data to be collected below 200 nm. At urea concentrations exceeding 6 M at pH 4.0 and 7 M at pH 7.0 any traces of α-helical structure are absent and entire spectrum corresponds to that of fully unfolded protein.

The spectrum of wild type mouse PrP collected at pH 7.0 follows a typical the two-state transition model, characteristic for proteins which fold without any intermediates. The transition region visible in spectrum collected at pH 4.0 is much broader, stretching between 2.0 M and 6.5 M urea compared to 4.5 M and 7.0 M urea at pH 7.0 (see Figure 4.3). Such dramatic increase in the width of transition suggests that at lower pH the MoPrP can no longer be described by a two-state model. Moreover, a small plateau region visible at pH 4.0 between 4.5 M and 5.5 M urea concentrations indicates a presence of intermediate which is absent at higher pH. While unexpected,

these findings are consistent with the presence of β-state intermediate characteristic for truncated mouse and hamster PrP at low pH conditions (Khan *et al.*, 2010).
The folding curve collected at pH 4.0 is visibly shifted towards the lower urea concentration - at pH 7.0 the midpoint of the transition curve occurs at 5.9 M urea while at pH 4.0 it is shifted to 4.4 M urea. This difference can be easily explained by partial structural destabilisation of PrP in low pH conditions.

The behaviour of N174T construct at both pH values (Figure 4.4) is similar to that of MoPrP. The transition region of N174T at pH 7.0 is only marginally broader than that of MoPrP (between 4.0 M and 7.0 M for the latter compared to 4.5 M and 7.0 M urea for the former), suggesting that both variants follow a two-state transition. Similarities between MoPrP and N174T extend to pH 4.0, at which the transition region of single mutant extends from 2.0 M urea to 6.5 M urea, much like in wild type mouse PrP. The presence of plateau region between 4.5 M and 5.5 M urea closely follows similar feature exhibited by MoPrP, and the midpoints of both transition curves (5.9M urea at pH 7.0 and 4.3 M urea at pH 4.0) occur at similar urea concentrations indicating almost identical structural destabilisation resulting from decrease in pH. All of these findings demonstrate that N174T substitution mutation has hardly any effect on stability and overall behaviour of mouse PrP, which is consistent with molecular dynamics simulations (Scouras and Daggett, 2012).

The equilibrium folding transition curves of S170N construct (Figure 4.5) fit well into a pattern set by MoPrP and N174T. The transition region of S170N at pH 7.0 is slightly broader than N174T (3.5 M to 7.0 M for S170N and 4.0 M to 7.0 M urea for N174T), with the transition region at pH 4.0 remaining the same (2.0 M to 6.5 M urea). Interestingly, the plateau region occurs at slightly lower denaturant concentration (between 4.0 M and 5.0 M urea), but is quite well defined much like in two previous constructs.
The decrease in stability conferred by the S170N mutation is much more visible, with midpoints of transition curves occurring at 5.5M urea at pH 7.0 and 3.8 M urea at pH 4.0

As expected, the mutant S170N/N174T exhibits broadest transition at pH 7.0 (3.0 M to 7.0 M urea), with pH 4.0 transition very similar to that of wild type and single mutants (see Figure 4.6). The broadness of transition region at both pH 7.0 and pH 4.0 suggests that unlike MoPrP and N174T, the double mutant does not follow a typical

two-step transition, instead behaving much like Syrian hamster PrP which is known to fold via intermediate.

The plateau region of pH 4.0 folding curve occurs between 4.5 M and 5.5 M urea, much like in N174T and MoPrP, again hinting at the presence of intermediate unique to low pH conditions. It should be noted that the plateau region observed in all constructs at pH 4.0 is narrower than expected - previously reported plateau region extends between 2.5 and 4 M urea (Khan *et al.*, 2010).

All of the above findings are of particular interest in terms of the effect of loop-stabilizing mutations on overall stability of the protein. Upon comparison of transition curves of MoPrP, N174T, S170N and S170N/N174T it becomes apparent that the mutations which stabilize the loop region result in expansion of the transition region of the folding curves constructed at pH 7.0. This in turn suggests that stabilisation of the loop region increases the overall propensity of given protein to from an intermediate, as implied by the increase in width of the transition region of folding curves.

From recent studies of truncated constructs of PrP from different species including mouse and Syrian hamster, it is known that the increased propensity to form β-state intermediate correlates with increased disease susceptibility (Khan *et al.*, 2010). Consequently, it is possible that increased loop stability results in higher propensity to form such intermediate, which leads to increased disease susceptibility. Such mechanism corresponds to the differences in susceptibilities between mouse and Syrian hamster. Since wild type mouse PrP lacks any stabilising mutations in the loop region, it exhibits lower propensity to form β-state intermediate and lower disease susceptibility compared to Syrian hamster PrP in which Asn residue at position 170 increases loop stability. Alternatively, the propensity to form intermediate could be an observable side effect rather than a direct cause of loop stabilisation, which correlates with susceptibility to prion disease

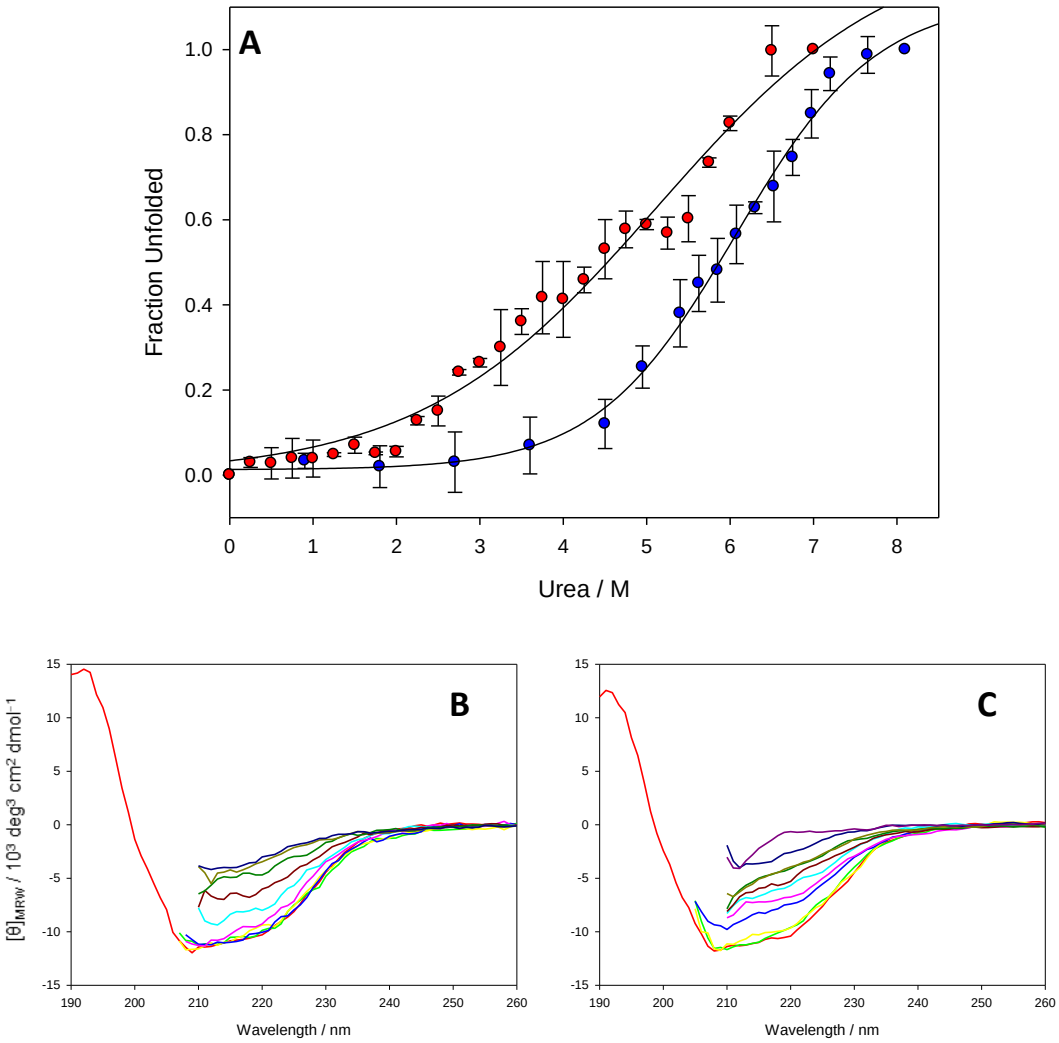

Figure 4.3 Denaturant unfolding transition curves of MoPrP (A) followed by far-UV circular dichroism at pH 7.0 (blue) and at pH 4.0 (red). Each data point represents the value of $[\theta]_{MRW}$ at 222 nm normalized to fraction unfolded as described in section 3.2.3. Error bars show the standard error of two independent experiments

Panels B shows CD spectra collected at pH 7.0 in absence of denaturant (red), in presence of 1M urea (green), 2 M urea (yellow), 3 M urea (blue), 4 M urea (pink), 5 M urea (cyan), 6 M urea (brown), 7 M urea (dark green), 8 M urea (dark yellow) and 9 M urea (dark blue).

Panels C shows CD spectra collected at pH 4.0 in absence of denaturant (red), in presence of 1M urea (green), 2 M urea (yellow), 3 M urea (blue), 3.5 M urea (pink), 4 M urea (cyan), 4.5 M urea (brown), 5.0 M urea (dark green), 5.5 M urea (dark yellow) 6 M urea (dark blue) and 7 M urea (purple).

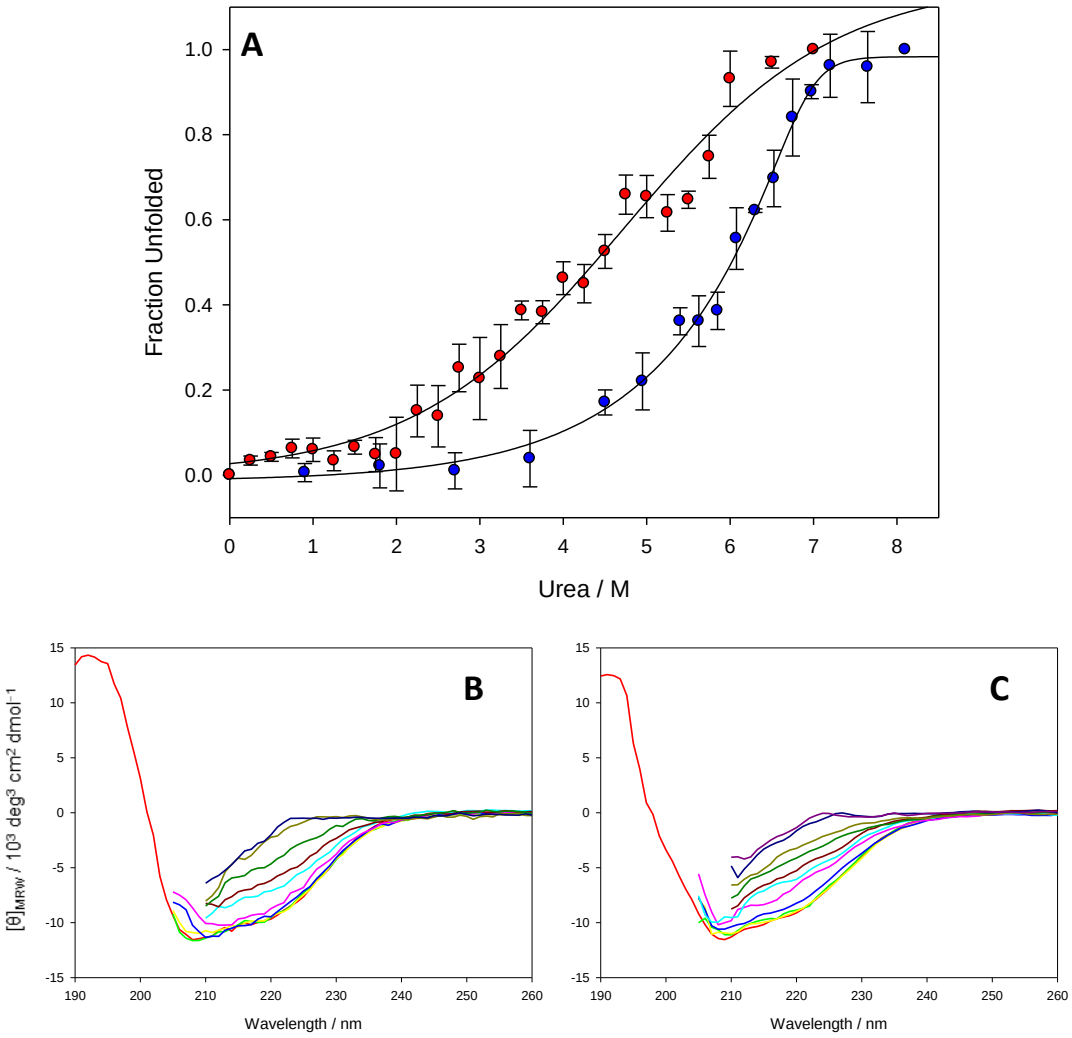

Figure 4.4 Denaturant unfolding transition curves of N174T (A) followed by far-UV circular dichroism at pH 7.0 (blue) and at pH 4.0 (red). Each data point represents the value of $[\theta]_{MRW}$ at 222 nm normalized to fraction unfolded as described in section 3.2.3. Error bars show the standard error of two independent experiments
Panels B shows CD spectra collected at pH 7.0 in absence of denaturant (red), in presence of 1M urea (green), 2 M urea (yellow), 3 M urea (blue), 4 M urea (pink), 5 M urea (cyan), 6 M urea (brown), 7 M urea (dark green), 8 M urea (dark yellow) and 9 M urea (dark blue).
Panels C shows CD spectra collected at pH 4.0 in absence of denaturant (red), in presence of 1M urea (green), 2 M urea (yellow), 3 M urea (blue), 3.5 M urea (pink), 4 M urea (cyan), 4.5 M urea (brown), 5.0 M urea (dark green), 5.5 M urea (dark yellow) 6 M urea (dark blue) and 7 M urea (purple).

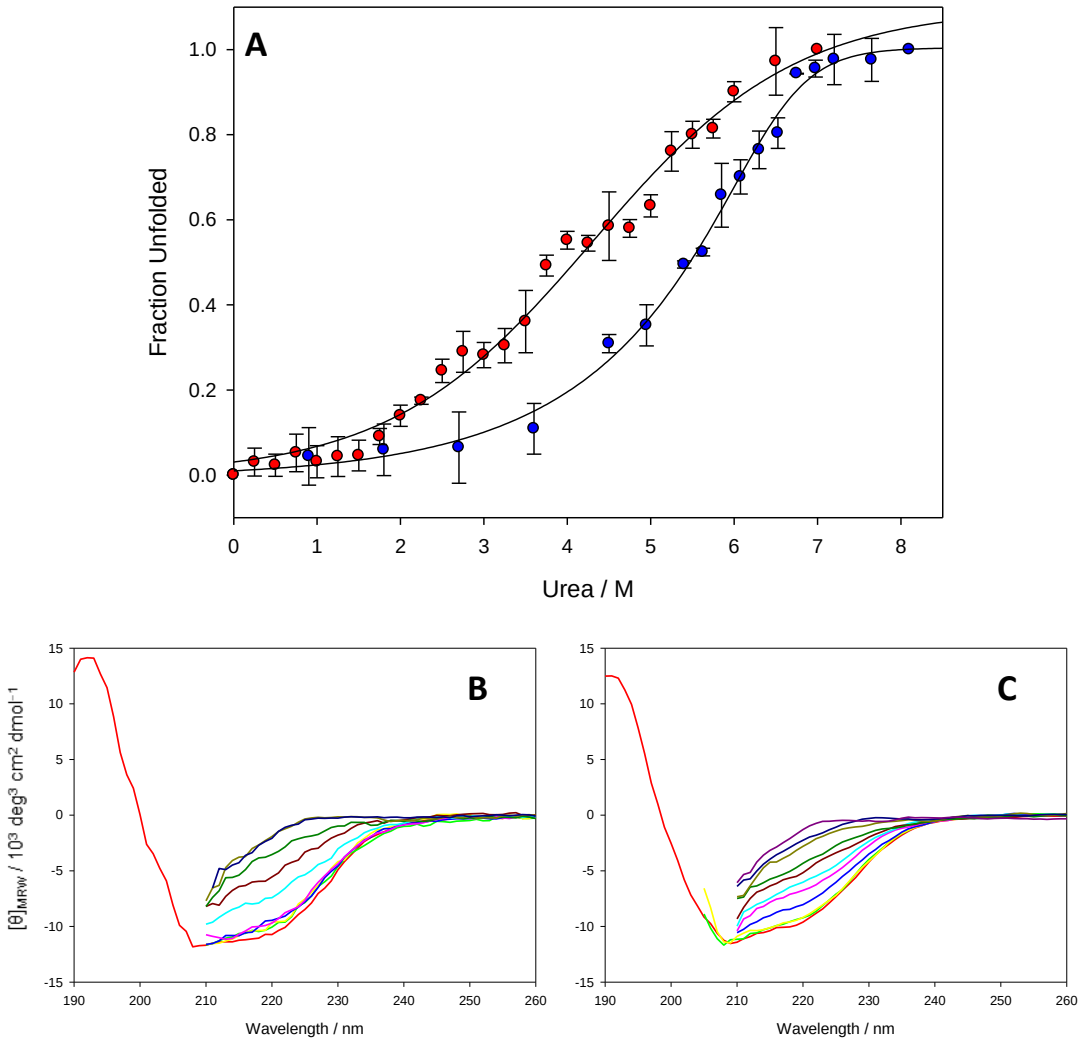

Figure 4.5 Denaturant unfolding transition curves of S170N (A) followed by far-UV circular dichroism at pH 7.0 (blue) and at pH 4.0 (red). Each data point represents the value of $[\theta]_{MRW}$ at 222 nm normalized to fraction unfolded as described in section 3.2.3. Error bars show the standard error of two independent experiments

Panels B shows CD spectra collected at pH 7.0 in absence of denaturant (red), in presence of 1M urea (green), 2 M urea (yellow), 3 M urea (blue), 4 M urea (pink), 5 M urea (cyan), 6 M urea (brown), 7 M urea (dark green), 8 M urea (dark yellow) and 9 M urea (dark blue).

Panels C shows CD spectra collected at pH 4.0 in absence of denaturant (red), in presence of 1M urea (green), 2 M urea (yellow), 3 M urea (blue), 3.5 M urea (pink), 4 M urea (cyan), 4.5 M urea (brown), 5.0 M urea (dark green), 5.5 M urea (dark yellow) 6 M urea (dark blue) and 7 M urea (purple).

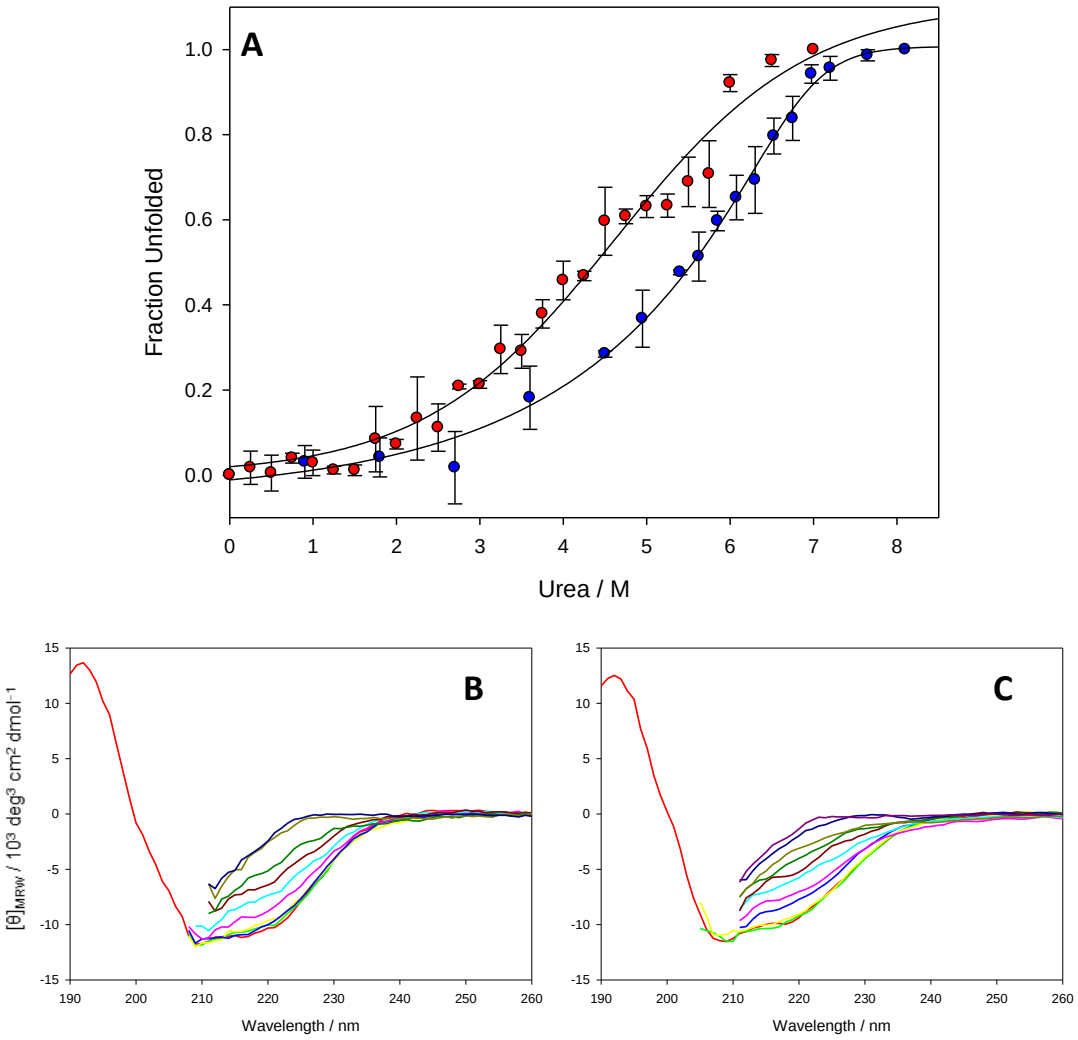

Figure 4.6 Denaturant unfolding transition curves of S170N/N174T (A) followed by far-UV circular dichroism at pH 7.0 (blue) and at pH 4.0 (red). Each data point represents the value of $[\theta]_{MRW}$ at 222 nm normalized to fraction unfolded as described in section 3.2.3. Error bars show the standard error of two independent experiments Panels B shows CD spectra collected at pH 7.0 in absence of denaturant (red), in presence of 1M urea (green), 2 M urea (yellow), 3 M urea (blue), 4 M urea (pink), 5 M urea (cyan), 6 M urea (brown), 7 M urea (dark green), 8 M urea (dark yellow) and 9 M urea (dark blue).

Panels C shows CD spectra collected at pH 4.0 in absence of denaturant (red), in presence of 1M urea (green), 2 M urea (yellow), 3 M urea (blue), 3.5 M urea (pink), 4 M urea (cyan), 4.5 M urea (brown), 5.0 M urea (dark green), 5.5 M urea (dark yellow) 6 M urea (dark blue) and 7 M urea (purple).

PrP construct	pH	ΔG_0 kJ mol^{-1}	$[D]_{50\%}$
MoPrP	7.0	27.8 ±2.2	5.9 ± 0.2
	4.0	22.1 ±1.8	4.4 ± 0.2
N174T	7.0	26.4 ± 1.9	5.9 ± 0.3
	4.0	20.5 ± 2.0	4.3 ± 0.2
S170N	7.0	23.9 ± 2.1	5.5 ± 0.2
	4.0	15.2 ± 1.4	4.0 ± 0.1
S170N/N174T	7.0	17.1 ± 0.9	5.3 ± 0.3
	4.0	13.3 ± 0.8	4.0 ± 0.1

Table 4.1 Thermodynamic parameters extracted from denaturant unfolding transition curves of MoPrP, N174T, S170N and S170N/N174T.
The free energy of unfolding in the absence of urea (ΔG_0) was calculated from the two-state analysis of denaturant unfolding transition curves.

PrP construct	ΔG_0 kJ mol^{-1}	$[D]_{50\%}$
MoPrP	2.94	7.5
N174T	3.02	6.28
S170N	4.87	9.49
S170N/N174T	4.46	5.81

Table 4.2 T-parameter values obtained via statistical analysis of thermodynamic parameters from Table 4.1 using T-test. For each PrP construct the thermodynamic parameters at pH 7.0 and pH 4.0 were compared in order to identify any statistically significant differences. T-parameter values exceedint 2.920 allow for the null hypothesis to be rejected, thus confirming the statistically significant difference between thermodynamic parameters. For values below 2.920 the null hypothesis cannot be rejected, and consequently no statistically significant difference can be claimed.

4.3.2 Fibrilisation studies of PrP

In this study, a series of fibrilisation experiments was conducted in an attempt to correlate the effects of mutations which alter the stability of the unstructured loop connecting helix α2 with β-strand β2 of prion protein with propensity to form fibrils. Fibrilisation experiments involving MoPrP, N174T, S170N and S170N/N174T were carried out at pH 7.0 at which the elk-like stabilised loop is known to form in mouse PrP, as well as at pH 4.0 which destabilizes the loop.

Formation of fibrils was monitored by ThT fluorescence assays (Gill *et al.* 2009).

A series of urea concentrations were used throughout the experiment in order to determine the optimal conditions for fibril formation at given pH (see Figure 4.7). As expected, denaturant concentrations corresponding to the midpoint of denaturant transition curves were determined to be most effective in terms of promoting fibrilisation.The length of the lag phase was not affected in any significant manner, however the lag phases were slightly shorter for 6M urea at pH 7.0 and 4 M urea at pH 4.0 (data not shown). This was most likely due to the fact that at urea concentration close to midpoint of unfolding curve, the equilibrium between folded and unfolded conformations of proteins in solution would be poised in such a way that population of partially unfolded PrP molecules which could be recruited into fibril formation was highest. Consequently, subsequent experiments were conducted at 6 M urea concentration for pH 7.0 and 4 M urea for pH 4.0. Initial fibrilization experiments were conducted with and without 200 mm NaCl which mimicked the salt concentrations present in cells, however presence or absence of salt was determined to have no quantifiable effect on length of lag phase, rate of fibril formation or their morphology. The ThT fluorescence traces obtained during fibrilisation experiments are shown in Figures 4.8, 4.9, 4.10 and 4.11.

In unseeded experiments, both MoPrP and N174T failed to form fibrils within 200 hours of incubation, at any of investigated urea concentrations and pH values. S170N exhibited limited fibrilisation capacity, with slow fibril formation after approximately 20 hours at pH 7.0 and 40-60 hours at pH 4.0. The double mutant of S170N/N174T showed by far the highest propensity to form fibrils, with ThT fluorescence indicating fibril formation after 40-60 hours at pH 4.0 and 90+ hours at pH 7.0. These data correlate well with structural effects of each mutation, with mutations conferring highest loop rigidity also exhibiting highest propensity to form fibrils.

As mentioned before, if the loop region is flexible, the packaging of monomers and their oligomerisation and incorporation into protofibrils is impaired (Ott *et al.*, 2008; Scouras and Daggett, 2012). The lower the loop rigidity, the higher the negative effect on fibril formation, as demonstrated by MoPrP and N174T. In both of these constructs, the loop is not stabilised at all and consequently the formation of oligomers and protofibrils occurs very slowly. The S170N construct, with partially rigid loop exhibits limited fibril formation and the double mutant in which the loop is fully stabilised forming elk-like turn fibrilizes well.

Consequently, subsequent experiments involved seeding of all of the constructs with fibrillous material obtained at the end of S170N/N174T fibrilisation in order to test whether loop rigidity affects formation of fibrils even in presence of pre-formed protofibrils.

Both MoPrP and N174T formed fibrils upon seeding, although the ThT fluorescence traces suggest that the process was somewhat irregular, particularly at low pH.

The S170N construct responded well to addition S170N/N174T seeds, with fibrils forming within 20 hours at pH 7.0 and 30-40 hours at pH 4.0.

Adding seeds to reaction mixture of double mutant decreased the lag phase significantly, particularly at pH 4.0 (see Table 4.3) which is consistent with short PrP oligomers obtained from mature fibrils providing a template for conversion of PrP^{C} into PrP^{Sc} and subsequent aggregation and fibrilisation (Jones and Surewicz, 2005; Graham *et al.*, 2010).

Morphology of fibrils formed during seeding experiment was investigated by electron microscopy (see Figure 4.12).

As suggested by ThT fluorescence traces, no fibrils were observed in unseeded samples of MoPrP and N174T, independently of pH. Upon addition of S170N/N174T seeds, MoPrP formed several relatively sparse clusters of straight fibrils, indicating that increased flexibility of loop region impairs fibril formation to limited extent, even if pre-formed protofibrils are present. The fibrils formed by N174T during seeding experiments were slightly longer than those formed by MoPrP, while also forming denser network.

The S170N mutant was the first construct (in order of increasing loop stability) observed to form fibrils at both pH 7.0 and pH 4.0 even without seeding. Although scarce and very short, the fibrils nonetheless demonstrated that increasing the stability

of the loop region is necessary for oligomerisation and formation of protofibrils. Addition of S170N/N174T seeds resulted in formation of much greater number of longer and more pronounced fibrils.

The double mutant S170N/N174T was the only construct which demonstrated high fibrilisation propensity in absence of seeding material. Fibrils formed in unseeded experiments are very similar in appearance to those formed after addition of pre-formed fibrillous material. This indicates that except for providing additional templates for PrP^{Sc} recruitment and incorporation therefore decreasing lag phase, seeds have little impact on the quality of fibrils themselves. Interestingly, some of the EM images of S170N/N174T samples seem to reveal the presence of small oligomeric particles (see Figure 4.13), consistently with high fibrilisation propensity exhibited by the construct.

All of the above findings, while unexpected, provide a fascinating insight into structural features of PrP which may be key factors determining disease susceptibility. Molecular dynamics simulations strongly suggest that a compact loop between helix α2 and β-sheet β2 is necessary for aggregation and formation of the infectious protofibrillar species in several different species, particularly elk and sheep. Nearly all of the point mutations which confer increased disease resistance perturb the structure of the loop, preventing the initial formation of infectious oligomers (Scouras and Daggett, 2012).

Thus, it is possible that while flexibility of loop region affects nucleation and oligomerisation, consequently preventing fibril formation from "free" PrP molecules, its effect may be limited if the pre-formed protofibrils are already present in the reaction mixture. In such case loop stability would affect spontaneous generation of prions in the organism, as well as disease transmission via small oligomers. While flexible loop region would be likely to prevent spontaneous nucleation and/or oligomerisation and thus protofibril formation due to impaired packaging of PrP monomers, it would not affect pre-formed protofibrils originating from external source.

Consequently, the disease-resistant, mutations which decrease loop rigidity would have significant effect on fibril formation in unseeded fibrilisation, but their impact on fibril formation in presence of seeds would be much more limited. The difference would be due to the fact that already pre-formed seeds may recruit PrP^{C} from environment and incorporate it into growing fibril without the need for nuclei and oligomers to form first from free PrP^{C} molecules. Such model correlates well with the experimental data obtained in this study.

These findings seem to be counterintuitive, if one considers the prevailing opinion that formation of fibrils and their aggregation as well as subsequent formation of plaques is a protective mechanism evolved to avoid high toxicity of soluble oligomers (Buccianti *et al.*, 2002; Kirkitadze *et al.*, 2002; Caughey *et al.*, 2003). Loop destabilisation, being a potential protective mechanism, should not affect fibrilisation and decrease its potential to trap neurotoxic particles. It is these soluble oligomers, however, that are thought to be the primary cytotoxic mechanism as opposed to fibril formation and deposition on cellular membranes (Chisea *et al.*, 2001; Novitskaya *et al.*, 2005). Consequently, while the protective mechanism based around loop-destabilizing mutations could potentially lead to increased susceptibility to the disease due to the fact that the neurotoxic species are not trapped in fibrils, it is the oligomer formation that is primarily affected.
Thus, proposed source of disease resistance conferred by loop-destabilising mutations is the decreased formation of neurotoxic particles in the organism as well as diminished ability of infectious oligomers from both inside and outside to propagate oligomerisation of PrP.

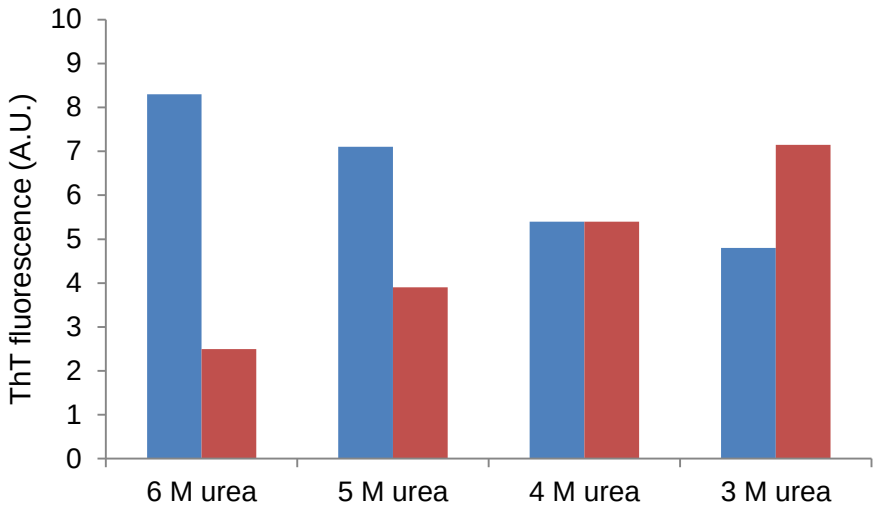

Figure 4.7 Total fibre load of S170N at pH 7.0 (blue) and pH 4.0 (red) across a range of denaturant concentrations. Bars represent the final ThT fluorescence observed in each sample which corresponds to total fibre load after 190 hours of incubation. All bars show the average ThT fluorescence values from three independent fibrilisation experiments.

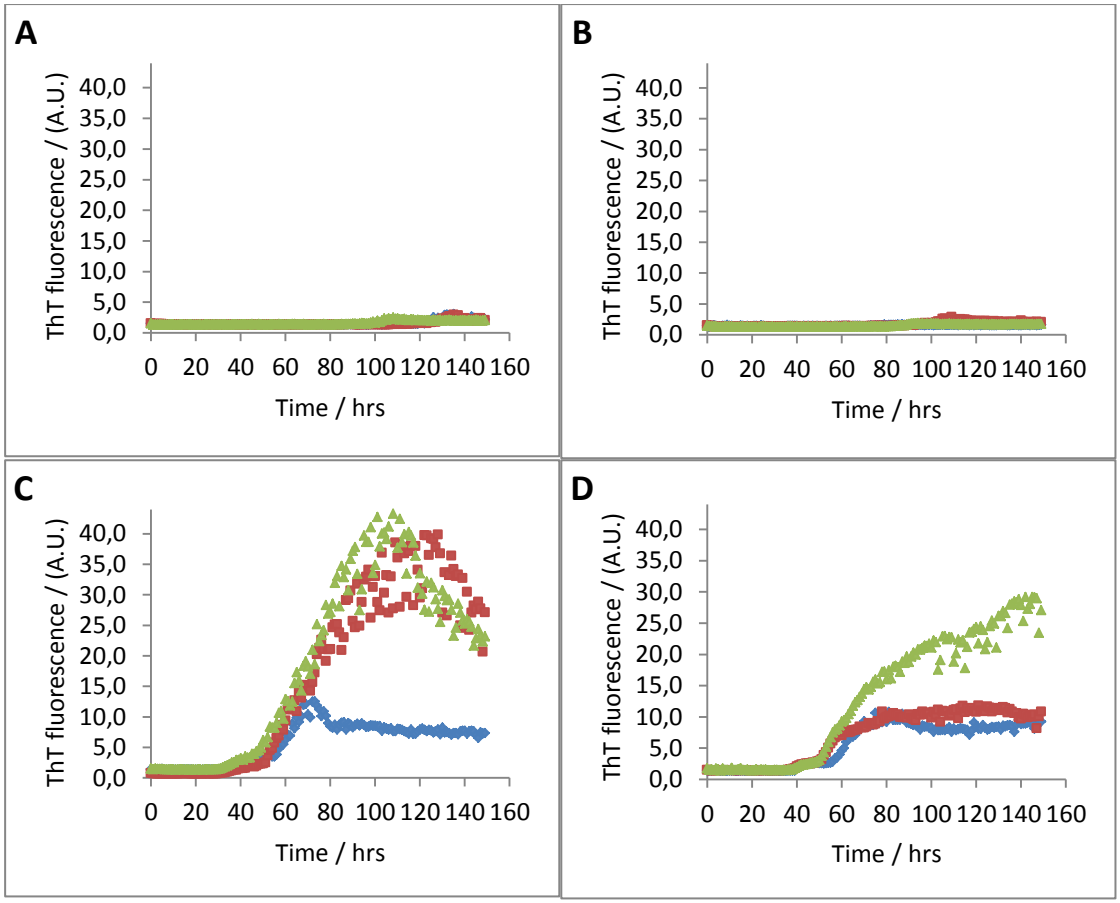

Figure 4.8 Triplicates of ThT fluorescence curves of MoPrP obtained as a result of three independent fibrilisation experiments conducted at pH 7.0 (A and C) and pH 4.0 (B and D). Panels A and B show fluorescence traces obtained as a result of unseeded fibrilisation.

Panels C and D depict ThT fluorescence curves collected upon seeding with S170N/N174T fibrillous material.

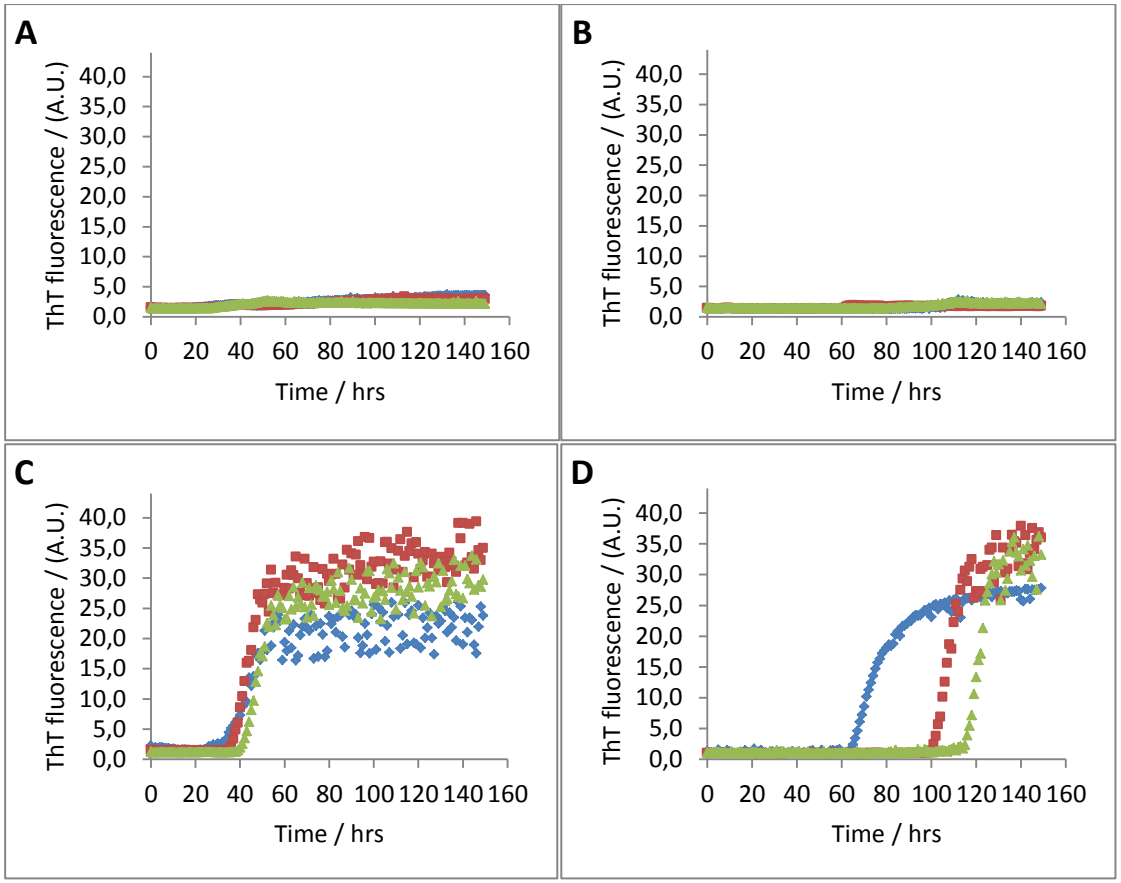

Figure 4.9 Triplicates of ThT fluorescence curves of N174T obtained as a result of three independent fibrilisation experiments conducted at pH 7.0 (A and C) and pH 4.0 (B and D). Panels A and B show fluorescence traces obtained as a result of unseeded fibrilisation.

Panels C and D depict ThT fluorescence curves collected upon seeding with S170N/N174T fibrillous material.

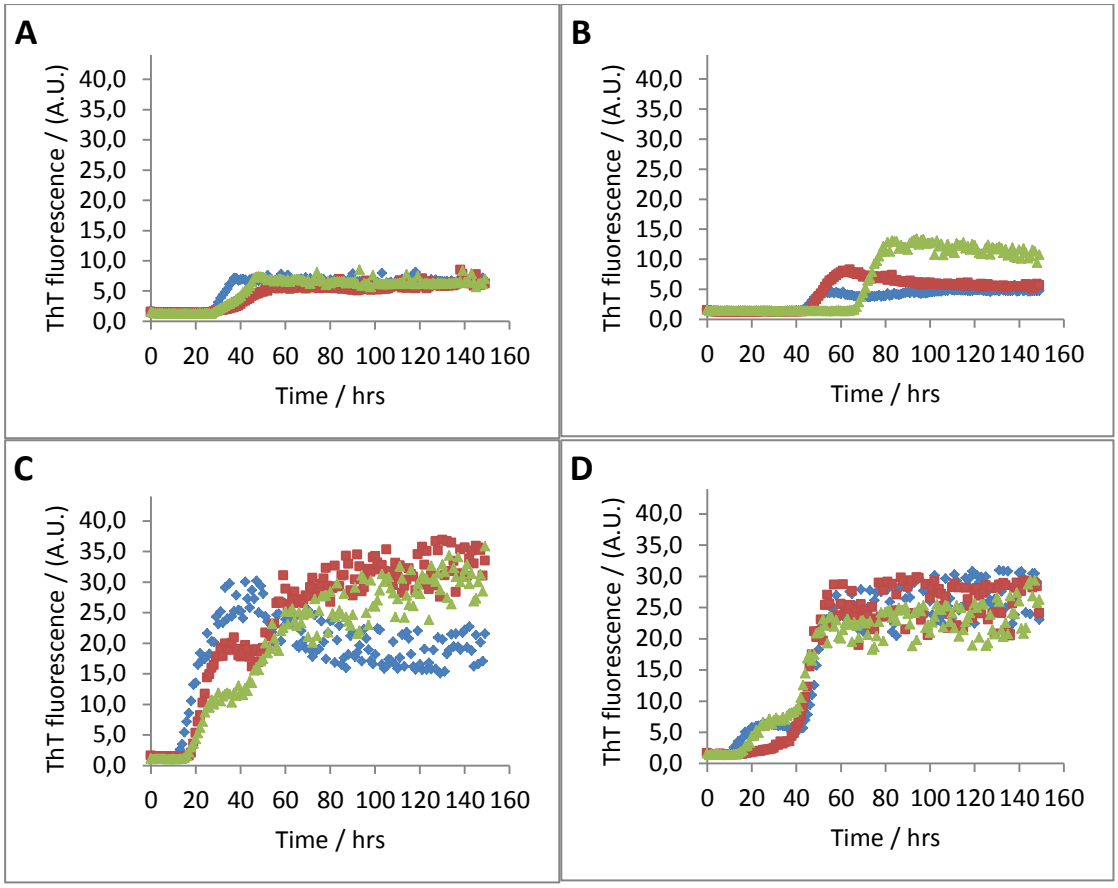

Figure 4.10 Triplicates of ThT fluorescence curves of S170N obtained as a result of three independent fibrilisation experiments conducted at pH 7.0 (A and C) and pH 4.0 (B and D). Panels A and B show fluorescence traces obtained as a result of unseeded fibrilisation.

Panels C and D depict ThT fluorescence curves collected upon seeding with S170N/N174T fibrillous material.

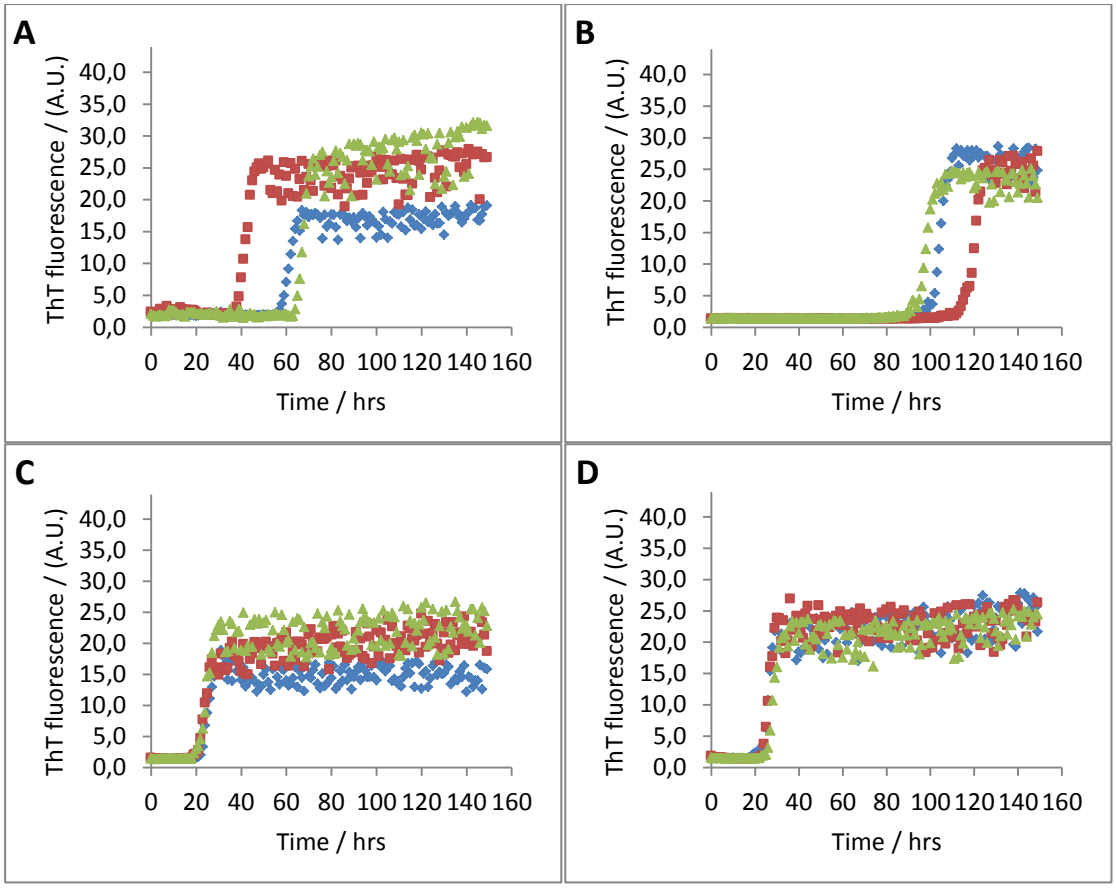

Figure 4.11 Triplicates of ThT fluorescence curves of S170N/N174T obtained as a result of three independent fibrilisation experiments conducted at pH 7.0 (A and C) and pH 4.0 (B and D). Panels A and B show fluorescence traces obtained as a result of unseeded fibrilisation.

Panels C and D depict ThT fluorescence curves collected upon seeding with S170N/N174T fibrillous material.

PrP construct	pH	Lag phase duration (h)	Lag phase duration of seeded fibrilisation (h)
MoPrP	7.0	N/A	47.6 ± 4.2
	4.0	N/A	52.3 ± 5.1
N174T	7.0	N/A	36.7 ± 4.7
	4.0	N/A	95.3 ± 17.5
S170N	7.0	38.8 ± 7.6	18.1 ± 3.8
	4.0	51.3 ± 9.4	24.2 ± 8.7
S170N/N174T	7.0	53.2 ± 10.8	20.5 ± 2.7
	4.0	97.5 ± 7.9	24.6 ± 3.1

Table 4.3 Average lag phase duration observed during fibrilisation experiments of MoPrP, N174T, S170N and S170N/N174T at two different pH values. The length of each average lag phase was calculated by averaging the duration of lag phases from three independent fibrilisation experiments. Errors represent the standard error.

PrP construct	pH	A
MoPrP	7.0	N/A
	4.0	N/A
N174T	7.0	N/A
	4.0	N/A
S170N	7.0	4.22
	4.0	3.66
S170N/N174T	7.0	5.09
	4.0	14.88

Table 4.4 T-parameter values obtained via statistical analysis of thermodynamic parameters from Table 4.1 using T-test. T-parameter values exceedint 1.812 allow for the null hypothesis to be rejected, thus confirming the statistically significant difference between thermodynamic parameters. For values below 1.812 the null hypothesis cannot be rejected, and consequently no statistically significant difference can be claimed.

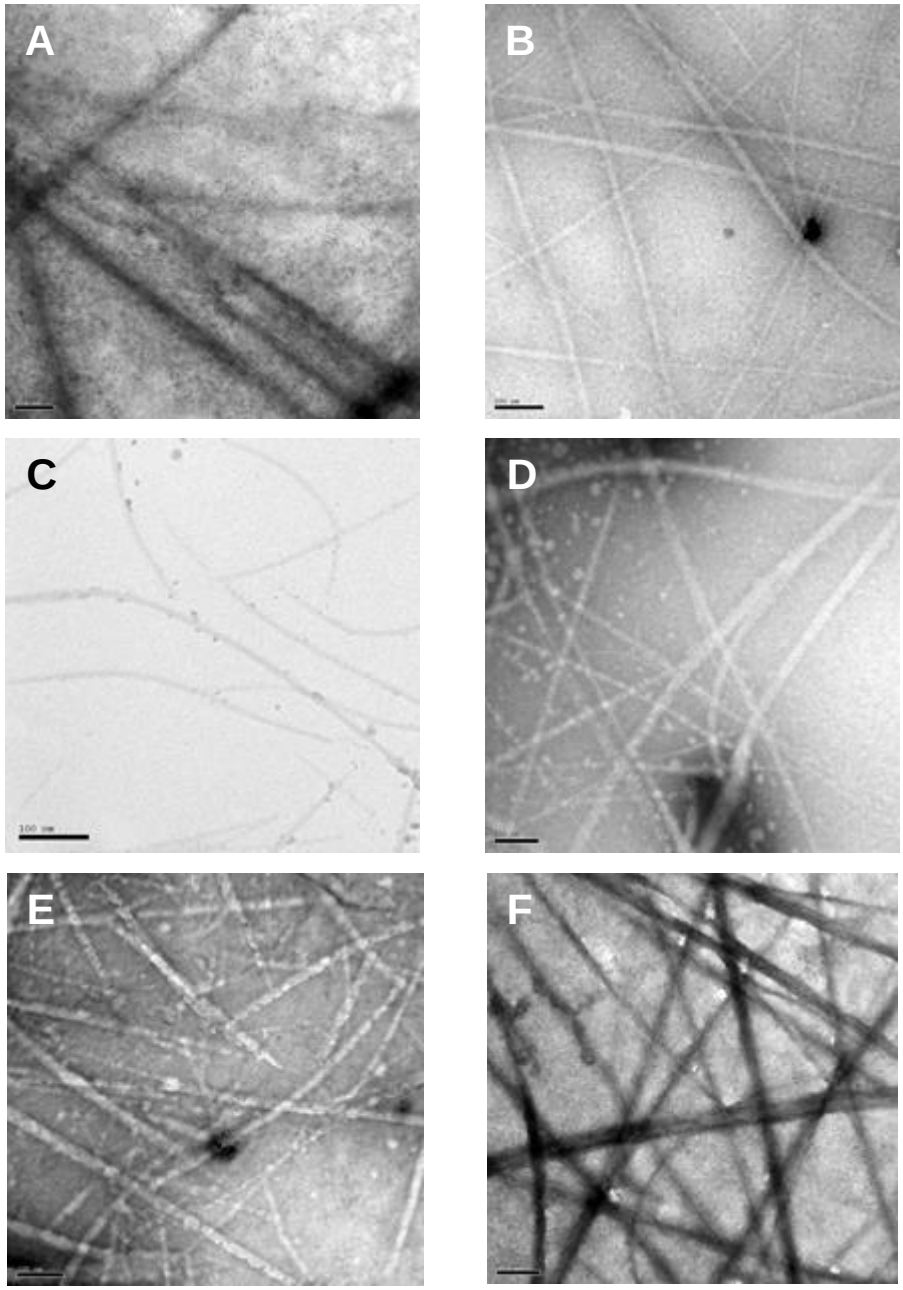

Figure 4.12 Electron microscope images of fibrils formed upon seeding of MoPrP (A), N174T (B), S170N (D) and S170N/N174T (F). Fibrils formed by S170N and S170N/N174Tduring unseeded experiments are shown in panels C and E respectively. All panels depict fibrils formed at pH 7.0. The thin black bar visible in bottom left corner of each image represents a scale bar of 100 nm.

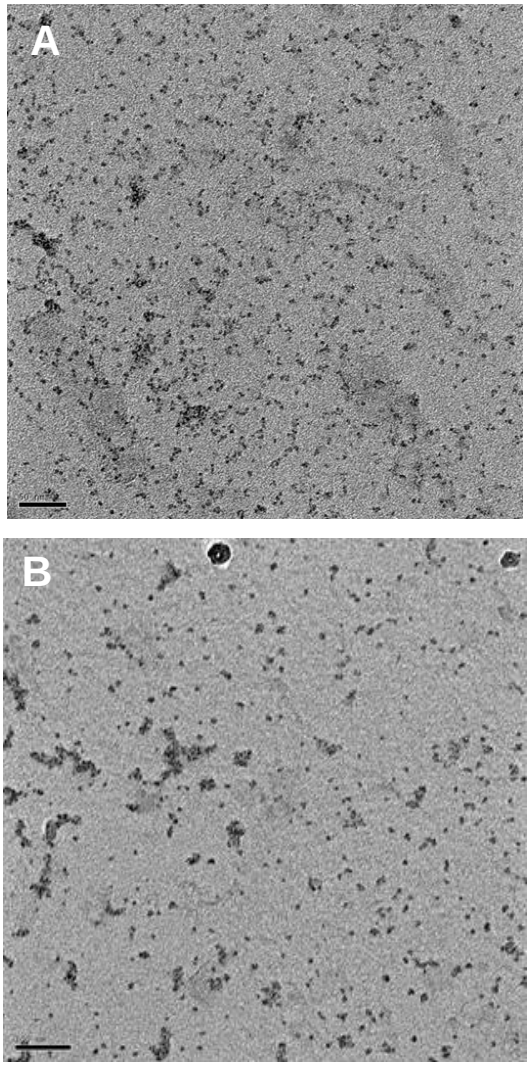

Figure 4.13 Electron microscope images of possible small oligomeric particles present in S170N/N174T sample.

Panel A depict particles present at pH 7.0, panel B at pH 4.0.

The thin black bar visible in bottom left corner of each image represents a scale bar of 50 nm (A) and 100 nm (B).

4.4 Summary

In this study, three mutants and wild type mouse prion proteins were used to investigate the effects of several loop-stabilising mutations on equilibrium folding and fibrilization properties or PrP.

Equilibrium denaturation studies of the four constructs showed that mutations which confer increased loop rigidity (S170N and S170N/N174T) result in expansion of the transition region of the folding curves constructed at pH 7.0. This in turn suggests that higher rigidity of the loop region increases the overall propensity of given protein to from an intermediate, while at the same having a net negative effect on overall protein stability, as implied by the increase in width of the transition region of folding curves and decrease in $[D]_{50\%}$. From recent studies of truncated constructs of PrP from different species including mouse and Syrian hamster, it is known that the increased propensity to form β-state intermediate correlates with increased disease susceptibility (Khan *et al.*, 2010). Consequently, it is possible that increased loop rigidity results in higher propensity to form such intermediate, which leads to increased disease susceptibility. Such mechanism corresponds to the differences in susceptibilities between mouse PrP in which the loop region is fully flexible and Syrian hamster which carries loop stabilizing Asn residue at position 170.

Fibrilisation studies demonstrated that increasing loop rigidity correlates negatively with propensity to form fibrils, irrespective of pH, but only in the absence of seeding material. Upon addition of seeds, all of the constructs demonstrated good fibrilisation capacity only slightly dependent on flexibility of the loop region.
These findings are consistent with molecular dynamics simulations which suggest that a compact loop between helix α2 and β-sheet β2 is necessary for aggregation and formation of infectious protofibrils. Point mutations which confer increased disease resistance perturb the structure of the loop, preventing the initial formation of infectious oligomers (Scouras and Daggett, 2012). Thus, proposed source of disease resistance conferred by loop-destabilising mutations is the decreased formation of neurotoxic particles in the organism as well as diminished ability of infectious oligomers from both inside and outside to propagate oligomerisation of PrP.

Chapter 5: Development and Testing of a Continuous-Flow Instrument for Investigation of Sub-millisecond Reactions

5.1 Introduction

From the simplest enzymatic reactions to complex folding processes associated with formation of multimeric protein complexes, important information can be gained about the pathways of chemical and biological reactions by studying the rates at which they occur.

Vast majority of biological and chemical reactions are studied in aqueous environment or other relevant solution as this not only offers a convenient working medium, but also reflects the conditions in which those processes take place *in vivo*.

A great number of biochemical processes occurs in sub-second timescale, therefore requiring a specialised instrumentation for efficient and effective study.

Stopped-flow is one of the most common and effective methods of investigating rapid reactions in aqueous environment thanks to its flexibility, sample economy (usually requiring only few millilitres of sample to yield reliable data) and adaptability. It relies on physical mixing of two or more reagents to initiate a reaction which can then be followed using a number of spectroscopic techniques such as tryptophan fluorescence and Raman spectroscopy (Sergiu *et al.,* 2006).

An important aspect of stopped-flow systems is the long observation window they provide, allowing them to monitor the progress of the reaction from one millisecond up to a few minutes. The earliest time at which scientifically reliable data can be collected following the onset of the reaction (referred to as "dead time" of the instrument) depends primarily on how quickly and effectively the two or more reagents can be mixed, making efficient and thorough mixing one of the most important aspects of the method.

Even with most recent developments in the field, SF instruments cannot reliably investigate processes shorter than 1 millisecond such as the earliest events of protein folding pathways. This is due to the fact that factors associated with flow of the reagents such as mixing and dissipation of mixing artefacts after the solution is stopped. Although one millisecond dead time is sufficient for most applications, a number of biologically important reactions such as the earliest processes of protein folding

pathways take place within the dead time of stopped-flow instruments. Thus, considerable efforts were made to create instruments capable of accessing the sub-millisecond timescale and shed light some light on those elusive events.
Currently there are only three methods capable of following sub-millisecond reactions: temperature-jump, pressure-jump and continuous-flow, all of which have successfully been used to investigate very rapid protein folding (Jacob *et al.*, 1999; Nolting *et al.*, 1997).

A continuous-flow instrument relies on the same principle as stopped-flow – that is mixing of two or more reagents to initiate a reaction and utilizing a number of spectroscopic methods to follow its progress. While in case of a stopped-flow instrument the data collection can only begin after the flow of mixing reactants has stopped and any mixing artefacts thus created have cleared, in continuous-flow the data are collected by imaging a whole flow-channel through which the reagents travel. This allows both the onset and progress of the reaction to be observed at once, as the distance the mixed solution has travelled through the flow channel correspond to the progress of the reaction. As the reagents are continuously pumped through the flow channel, no mixing artefacts are created as a result of rapidly stopping the flow, allowing for the data collection to begin as soon as the reagents are fully mixed. This allows considerably faster reactions to be monitored, at the expense of increased sample consumption, as the reagents have to be continuously delivered throughout the course of the measurement.
Another potential disadvantage is the reduced timeframe at which the reaction can be monitored, as the observation window is limited by the length of the flow channel and flow rate of the solutions. Continuous-flow instruments are thus not suitable for investigating reactions longer than few seconds, as longer observation time would require unsuitably long flow channels.

In order to access the sub-millisecond timescale and observe reactions inaccessible to stopped-flow, mixing in continuous flow must be as rapid and thorough as possible, making an efficient and effective mixer the most important part of the instrument and at the same time a main limiting factor as far as performance is concerned.
A continuous-flow instrument requires a delivery system for reagents, a mixer coupled to an observation channel, as well as an appropriate light source and a detection system (Figure 2). Solutions are delivered to the mixer from at least two separate reservoirs

(usually syringes) driven preferably by a stepper-motor device (this offers more stable flow velocities than those generated by pressure-driven devices). Upon reaching the mixer, solutions are mixed as rapidly and as efficiently as possible starting the reaction, and enter the observation channel where reaction progresses as it travels down the channel. The reaction is then measured through an appropriate spectroscopic method. The most common observation methods widely used in biological and chemical applications rely on absorbance or fluorescence changes during the reaction.

A typical layout of a continuous-flow instrument assembled for reactions detected through fluorescence changes is shown in Figure 5.1. In this configuration a light source, typically a strong mercury or mercury-xenon arc lamp, is used and specific wavelengths selected with a monochromator. Fluorescence from the sample is collected through a set of lenses and optical filters on the sensor of a CCD camera. The output of a continuous-flow instrument is an image of the reaction progressing along the observation channel.

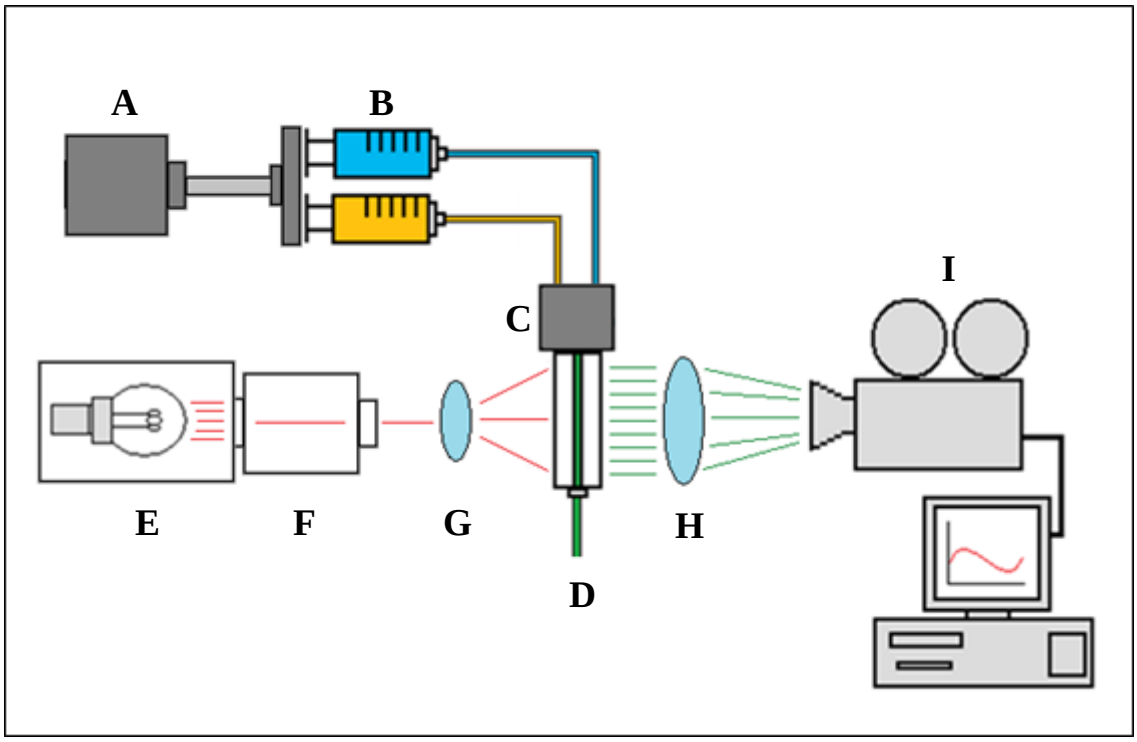

Figure 5.1. Schematic diagram of a continuous-flow instrument which uses fluorescence measurements to follow the reaction. The stepper motor (A) drives two syringes (B) which supply reactant solutions to the mixer (C). The mixed solution flows up the flow-channel (D) where it is illuminated by monochromatic light provided by mercury-xenon lamp (E) coupled to the monochromator (F). Excitation light is focussed by the cylindrical lens (G). Fluorescence is collected at right-angles to the incident light, passes through filters (H), is focussed by a lens and collected by the CCD (I).

Protein folding involves a number of submillisecond processes, such as secondary structure formation and intrachain diffusion (Bieri and Kiefhaber, 1999) which are too rapid to be reliably investigated using stopped-flow instruments, but can be easily followed by continuous-flow. Studies such as investigation of early folding pathways of β-lactoglobulin (Kuwata *et al.*, 2001), acyl-CoA binding protein (Teilum *et al.*, 2002), and cytochrome c (Takahashi *et al.*, 1997) have all benefited greatly from application of continuous flow method. Another protein, kinetics of which could be reliably investigated using continuous-flow instrument, is the prion protein.

It is known that at 20 °C prion proteins fold within 1-2 miliseconds, which is well within the dead time of most commercial stopped-flow instruments (Wildegger *et al.*, 1999). Thus, characterisation of kinetics of early folding pathways of PrP requires application of techniques capable of accessing the sub-milisecond timescale, such as pressure jump or continuous-flow.

Therefore, in collaboration with Warwick School of Engineering and the company TgK Scientific (Salisbury, UK), the aim of this study was to further develop a CF instrument assembled in-house (Pinheiro *et al.*, 2001). Previous studies (Pinheiro *et al.*, 2001, Jenkins, 2006) have highlighted the requirement of thorough understanding of mixing process itself in order to decrease the dead time of continuous-flow apparatus well below a milisecond. Thus, in collaboration with Warwick School of Engineering a simultnaneous study into turbulent mixing in micromixers was conducted, and its findings utilized in designing and manufacturing new continuous-flow apparatus. This new apparatus would be capable of accessing the microsecond timeframe necessary to characterise the kinetic folding pathway of PrP. The instrument would also have wider applications for any sub-millisecond process detectable by fluorescence.

This chapter describes the process of designing, microfabricating and testing of the efficiency of different new mixers developed jointly with TgK Scientific, as well as proving the effectiveness and reliability of its hardware components and custom-written computer software, with the view of developing a commercially applicable CF instrument.

Tests described in this chapter make use of a fluorescence quenching reaction of a soluble, monomeric derivative of the amino acid tryptophan N-acetyl-L-tryptophanamide (NATA) with N-bromosuccinimide (NBS) which is widely considered a standard fluorescence decay reaction (Peterman, 1979).

5.2 Materials and Methods

5.2.1 Materials

All solutions used in the continuous-flow instrument were made using distilled water passed through a cellulose acetate filter with 0.2 μM pore size (Whatman, Clifton, NJ, USA). Prepared solutions were filtered again directly prior to their introduction into the continuous-flow apparatus in order to prevent the entry of any particulate matter into the system which could potentially obstruct the narrow tubing used to carry solutions. Both NATA and NBS were purchased from Sigma in powdered form. Solutions of NBS were made fresh on the day of the experiment by first dissolving the necessary quantity of NBS powder into a small amount (roughly 0.5 - 1 ml) of dimethylformamide (DMF) (BDH, Poole, UK). The NBS solution was then diluted with filtered distilled water to the desired concentration and stored in the dark and cool.

5.2.2 Components and assembly of the continuous-flow instrument

The continuous-flow instrument assembled in this group (Pinheiro *et al.*, 2001) which served as the basis for new, upgraded apparatus (Figure 1) was originally based on that of a collaborator's (Shastry *et al.*, 1998).

5.2.2.1 Instrument layout

The instrument described in this chapter follows a typical layout of continuous-flow apparatus assembled for investigating reactions which can be followed by monitoring detected fluorescence changes in reaction mixture.
Excitation light used to induce fluorescence in the sample is provided by a 103 Watt mercury-xenon (Hg-Xe) arc lamp (Osram, Germany) and gathered by a half-spherical reflector and directed towards the water filter which blocks the infrared part of the light spectrum. The light beam is then passed through monochromator (Photon Technology International, Birmingham, NJ, USA) which is used to select the relevant wavelength for fluorescence excitation.

A cylindrical lens (Oriel, Stratford, CT, USA) positioned between the monochromator and the flow-cell is used to focus the incident beam exiting the monochromator into the "heart" of the machine which is a single-piece unit which combines the mixer (microfabricated by Warwick School of Engineering) coupled to a quartz flow-cell (Hellma Cells, Inc.) using a stainless steel holder.

A stepper-motor drive unit (TgK Scientific) is used to deliver reactants from solution reservoirs (usually two 5 ml and one 0.5 ml syringes) to the mixer and flow-cell. The mixer is oriented so that the mixed solutions flow upwards against gravity and under the force of the drive, allowing to minimise any cavitation or gravity effects on the flow of the reagents. The stepper-motor drive is capable of delivering a precisely controlled and consistent flow over the course of experiment, and its gearing provides access to a range of flow velocities varying from 4 ms^{-1} up to 14 ms^{-1}.

Reactants are carried to the mixer through a PEEK tubing (Upchurch Scientific, WA, USA) from three syringes driven by the stepper-motor drive unit.

Mixing of the solution takes place in the microfabricated mixer, with the flow forcing the reaction mixture down the channel in the quartz flow-cell (also referred to as observation channel) where progress of the reaction can be monitored.

Fluorescence from the sample passes through a selective filter which blocks light with wavelengths shorter than 320 nm (WG320 filter, Schott GmbH, Mainz, Germany). Filtered fluorescent light is then focussed by another lens (Oriel), and collected at 90° to the incident excitation light by a digital camera (Retiga-2000R, QImaging Scientific, Surrey, Canada). The camera is equipped with a charge coupled device (CCD) sensitive to ultra-violet light (model Kodak Sensors KAI-2020), with an array of 1600 × 1200 pixels. The camera system was electrically cooled to 25 °C below ambient temperature to prevent thermally-induced noise.

The entire instrument is assembled on an optical bench for stability (Melles Griot, Irvine, CA, USA).

Evaluations of the mixing efficiency and dead time of the instrument were carried out using the so-called asymmetric mixing mode typical of protein folding experiments. In such an experiment an aqueous solution containing unfolded protein in denaturant would be loaded at a relatively high concentration into the small 0.5 ml syringe and then rapidly diluted by an excess of buffer, supplied from the two larger syringes (2.5 ml each).

Due to the fact that the output of two larger syringes containing buffer is combined at a PEEK tubing junction before reaching the mixer, only two input lines into the mixer are required (consequently simplifying its design).
Such configuration gives a final mixing ratio of buffer to denaturant of 10:1 (a dilution factor of 11-fold), which is usually adequate for protein folding experiments. Alternative dilution factors can be achieved by filling only a single syringe with buffer or by replacing small 0.5 ml syringe used to store protein solutions with larger one.
All of the syringes are contained within a sealed compartment on the top of the stepper-motor drive unit where water from a thermostatically controlled water bath is circulated around the syringes. The local temperature is monitored by a platinum resistance thermometer (Digitron 2024T, SIFAM instruments, Devon UK). The same water is circulated through a copper pipe in order to control the temperature of the solution in the PEEK tubing leading to the mixer. It was deemed unnecessary to apply thermostatic control to the flow-cell itself due to the very brief contact time the mixed solution has with it. The camera, focusing lenses and cell holder are all contained within a darkened light-proof box.

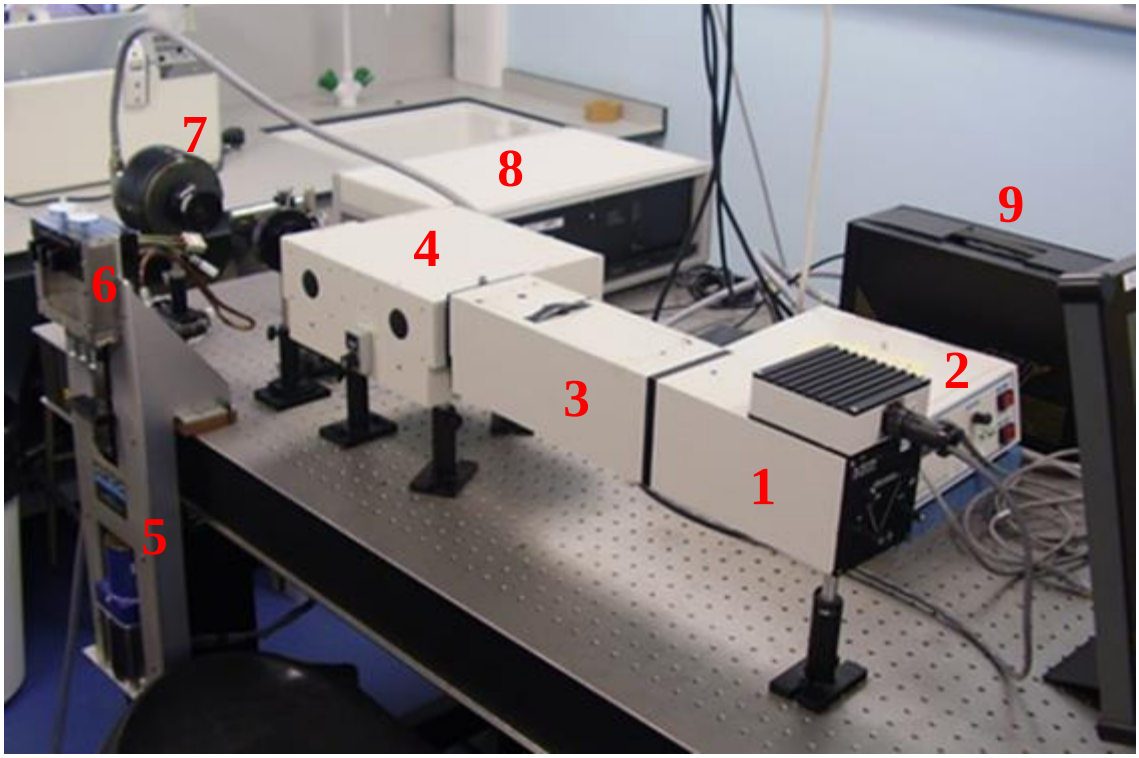

Figure 5.2 Photograph of an early configuration of continuous-flow instrument on the optical bench showing the main components: lamp housing (1) with ignition and power control (2), water filter compartment (3), monochromator (4), stepper motor drive (5) with syringe compartment (6) and old model CCD camera (7) replaced since with Retiga-2000R. Note the presence of two large external units (8 and 9) required to synchronise the old camera with a stepper-motor drive (8) and process the output of the CCD chip into a format recognisable by the computer (9).

The flow cell is not visible as it was removed for maintenance.

Note the unusual position of the camera which is facing the monochromator rather than being positioned at 90°. This is due to the fact that at the time of taking the photograph a number of different optical configurations were considered, one of which was positioning the camera to face the excitation light and use several filters to block any incident light other than fluorescence (see section 5.2.3.1).

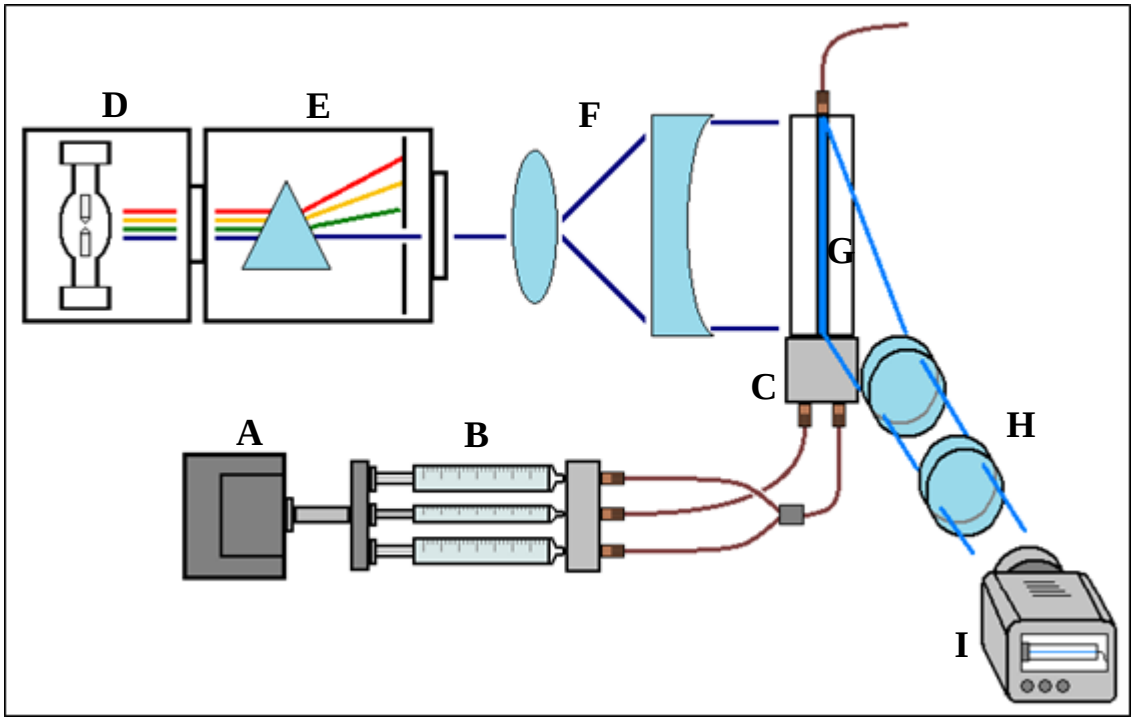

Figure 5.3 Schematic diagram of a 90° detection configuration of continuous-flow instrument developed over the course of this study.

A stepper motor drive (A) delivers reagents from solution reservoirs (B) into the microfabricated mixer (C) where reaction is initiated. A light source (D) provides illumination selected by a monochromator (E). Focusing lenses (F) focus the light exiting the monochromator into a narrow band aligned with the observation channel inside the flow cell coupled to the mixer (G). As the reaction progresses, fluorescence emitted from the flow cell is gathered by focusing lenses and filters (H) before reaching the CCD camera (I).

5.2.2.2 Current and potential light sources

An important aspect of this study, in addition to designing a novel, highly efficient micromixer, was to enhance the detection capabilities of the instrument in order to improve the quality of collected data and increase sample economy.
This was achieved by replacing the old CCD camera with a newer, more user-friendly model boasting enhanced sensitivity and durability. This aspect was accomplished by purchasing Retiga-2000R CCD camera equipped with high sensitivity chip (see section 5.3.1.1 for comparison with the old Micromax camera).
A second method of improving data quality and enhancing detection is to increase the strength of fluorescence in the flow cell. This could be achieved by either increasing the fluorophore concentration and thus sample consumption (a method both undesirable and counter-productive) or by increasing the intensity of excitation light reaching the sample by replacing the light source. The latter option was deemed attractive and consequently pursued.

Before a new light source could be considered, potential areas for improvement had to be identified. Current light source, a 103 Watt mercury-xenon arc lamp, provides intense light which can be focused into the flow cell by a system of cylindrical and convex lenses. However, the lamp itself emits a broad spectrum of light of different wavelengths which have to be filtered by a monochromator and a set of filters. While such system allows one to narrow down the wavelengths present in the excitation beam to just a few nanometres (e.g. 500 nm ± 1 nm), it also reduces the intensity of the excitation light. Moreover, if the arc lamp is to be used for Tryptophan fluorescence detection, it requires particular care while selecting wavelength with a monochromator. This is due to the fact that the output of the arc lamp is uneven across different wavelengths (see Figure 5.4) and its application to Tryptophan fluorescence relies on selecting particular mercury spike at 281 nm. If care is not taken, this particular spike can be missed – setting monochromator to 282 nm could easily result in decreasing the light intensity of the excitation beam by half. Any excitation light exiting the monochromator would be dispersed into a cone, much like a flashlight light. This necessitates the use of focusing lenses which gather the excitation light and focus it into the flow cell. As single focusing lens could never provide homogenous illumination along the entire flow-channel, complex multi-lens systems are often required to ensure even light distribution increasing both cost of instrument and its complexity.

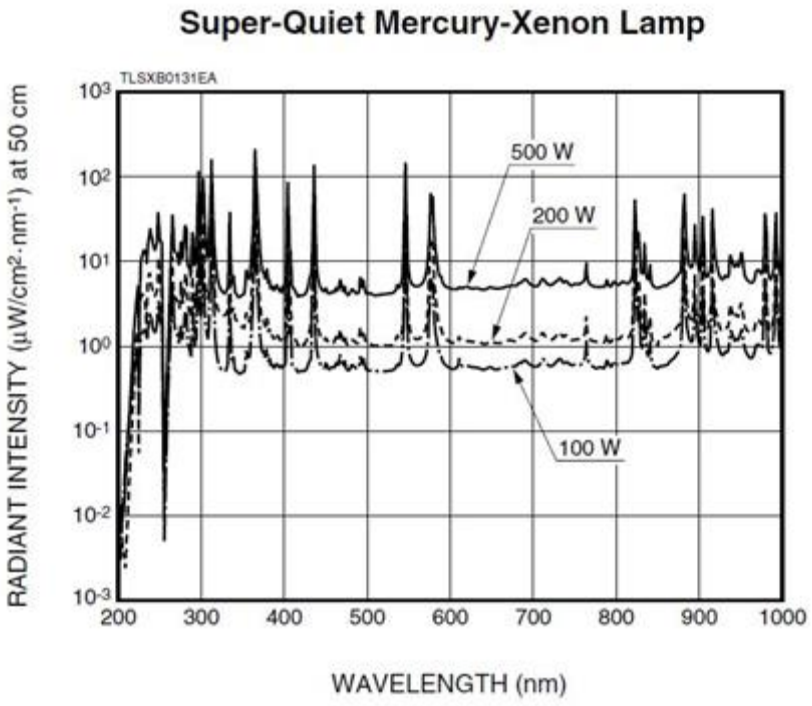

Figure 5.4 Radiant intensity profile of a mercury-xenon arc lamps of different power across a range of wavelengths. Numerous peaks across the spectrum correspond to spectrum lines of xenon (peaks above 800 nm) and mercury (peaks between 230-800 nm). Note logarithmic scale on vertical axis illustrating the intensity of the lines and importance of careful calibration of monochromator used with the lamp.

An ideal light source should have none of those limitations. It should be tunable to a single wavelength, should emit tightly focussed beam which could be easily focused along the channel using single cylindrical lens and should provide higher light intensity than Hg-Xe lamp resulting in stronger excitation and therefore increased fluorescence of the sample.

All of the above features are characteristic for laser-based light sources and consequently lasers were the first alternative to be considered. Two possible setups were considered: a deep UV laser tuned to 280 nm (such as DUV manufactured by Laser 2000, Stockholm, Sweden) or tunable visible light laser coupled to frequency doubler (e.g. MBR family by Coherent, Santa Clara, USA).

While both setups offered similar advantages over a mercury-xenon arc lamp, they also shared a common disadvantage: their price. Deep UV lasers are much more expensive than visible light lasers, however the latter is only applicable for fluorescence studies when coupled to a frequency doubler which decreases the wavelength of emitted light into the deep-UV region. In both cases financial costs associated with purchasing the laser, installing it in a dedicated workroom in accordance to health and safety regulations and finally personnel training required to operate them safely proved to be well beyond the financial scope of the grant.

It should be noted, however, that laser light sources remain a very attractive and viable option as far as future developments and instrument improvements are concerned.

Following rejection of lasers as prospective light source for the new instrument, attention was shifted to ultraviolet diodes. Recent developments in LED technology allowed for construction of deep UV diodes with wavelengths varying from near-UV down to 240 nm.

For this study, a 280 nm UVTOP diodes manufactured by Sensor Electronic Technology, Inc. (Columbia, SC, USA) were considered. Among numerous advantages offered by this particular light source are adaptability (diodes are offered in a variety of wavelengths ranging from 400 nm to 240 nm in 5 nm increments), very long life span (between 40-50,000 hours compared to 500 hours for Hg-Xe arc lamp) and low price. They can be manufactured in different shapes, providing either dispersed illumination or very focussed, narrow cone of light. Moreover, since individual diodes are small, having diameter of 3-4 mm, several diodes can be arranged into an array and positioned along the flow channel in order to provide homogenous illumination without the need for focusing lenses.

The only disadvantage of diodes is the intensity of light they provide, which is an order of magnitude lower than that of mercury-xenon arc lamp, particularly at 280 nm where a mercury spike in an arc lamp spectrum is often used for biological and biochemical applications such as Trp fluorescence.
Lower output of diode array would result in decreased fluorescence intensity, negatively affecting the quality of the data gathered. Due to this reason, the concept of using diode array as a source of excitation light was discarded and decision was made to continue the use of mercury-xenon lamps, despite their many shortcomings.

5.2.2.3 Computer software and data analysis

An important advance in reliability and consistency of operation of the continuous-flow instrument used in this study was the introduction of the custom-written software 'μHi Flow' (TgK Scientific) by previous PhD student Dr David Jenkins (Jenkins, 2006). This software was used to control the stepper motor drive unit via drive unit controller custom-built by our industrial collaborator (TgK Scientific). The controller interfaced with the computer by a PCI-bus card.
The μHi Flow software allowed for a specification of most important parameters such as the linear flow velocity of the solution pushed through the flow-channel (from 4 to 16 ms^{-1} in increments of 2 ms^{-1}), the time delay between the start of the flow (i.e. activation of stepper motor drive) and the onset of data collection by CCD camera, and finally the total volume of reactants to be displaced in particular experiment.
The volume of solutions displaced during each run also specified the duration of measurement, with higher flow velocities resulting in shorter time span and increased sample consumption.
While the Micromax CCD camera was installed, the μHi Flow software could interact directly with camera control and data collection software WinView/32 (Roper Scientific) allowing for data collection to be automatically triggered each time stepper-motor drive was activated, greatly adding to ease of use of the instrument.
With a replacement of CCD camera came the necessity to re-wire the drive unit controller so that it could interface with new hardware. Fortunately, the QImaging Suite software provided with Retiga-2000R proved to be flexible and was easily adapted for

μHi Flow, allowing data collection to be synchronised with stepper motor drive activation.

The QImaging Suite software was used to both interface the camera with drive unit controller and to process raw data acquired during continuous-flow experiments. Fluorescence intensity profiles made from flow-channel images (see Section 5.2.3) were imported into QImaging Suite and converted into relative fluorescence traces. The final kinetic trace could be exported from the QImaging Suite software as an XLS file and easily loaded into Excel (Microsoft, Redmond, WA, USA), SigmaPlot (Systat Software, Richmond, CA, USA) or Kinetasyst 3 (Hi-Tech Scientific) for curve-fitting by non-linear regression.

5.2.3 Continuous-flow mixer

Continuous-flow relies greatly on rapid and complete mixing of reactants in order to initiate the reaction as quickly as possible and thus decrease the dead time after which viable data can be collected. It is therefore not surprising that efficient and robust mixer is a key element of every continuous-flow instrument, being the limiting factor in terms of performance.

Since there are currently no continuous-flow instruments available commercially, every single apparatus assembled to date was custom made by respective research group. Consequently, every mixer was also assembled in-house, leading to very poor reproducibility of the results between groups making use of different instruments. Careful handling and very regular maintenance were required, as spare mixers were unavailable.

Thus, a specific market niche was formed, which could be filled by a simple, cheap and easy to handle mixer that could be discarded in case of critical failure and replaced with identical one.

By far the easiest way of manufacturing large quantities of simple, non-mechanical components such as mixers is microfabrication, which was therefore incorporated into the study. Mass produced microfabricated mixers made from chemically inert, durable materials would be a very attractive alternative to hand-crafted devices. However, due to technological limitations microfabrication is essentially limited to production of two-

dimensional objects, rendering most common mixer designs difficult to manufacture. Thus a completely new design suitable for mass production was required.
Extensive literature review yielded particularly interesting design of single-plane mixer which followed the T-mixer geometry widely used in stopped-flow instruments, where two delivery channels and an observation channel machined in a thin sheet of chemically inert polymer were sandwiched between two layers of glass (Billsel *et al.*, 2005).
This particular designed served as a basis for the development of very first prototype of planar continuous flow mixer manufactured by collaborators from Warwick School of Engineering (see Section 5.2.3.1).

5.2.3.1 Initial prototypes of planar continuous-flow mixers

A first prototype of continuous-flow mixer served as a technology demonstrator to test the feasibility of manufacturing device based on selected design (see Figure 5.5). The central part of the prototype was a planar PEEK sheet in a form of a square with side length of 25.4 mm and thickness of 100 μm. Two 100 μm wide delivery channels were cut along the sides, intersecting at one of the corners, their meeting point serving as a mixing chamber. A single 100 μm wide observation channel was cut along the diagonal of the sheet, stretching from the mixing chamber to the opposite corner.
Such configuration was a result of careful analysis of fluid flow dynamics in microscopic channels performed by a collaborator Ching-Hsien Cheng from Warwick School of Engineering. It was discovered that placing two delivery channels at 90° to each other and the flow channel along the diagonal results in increased turbulent flow in the mixing chamber itself, as well as in the initial section of flow channel. This in turn should increase mixing efficiency and therefore decrease instrumental dead time.
The PEEK layer was then sandwiched between two 5 mm thick, 25.4 x 25.4 mm quartz windows placed above and below the PEEK sheet, thus forming a flow channel with square cross-section and side length of100 μm. Upper quartz window had three holes drilled in it which coincided with the ends of delivery channels and observation channel and thus served as reagent inlets and reaction mixture outlet.
Two 1.6 mm thick 25.4 mm x 25.4 mm Teflon gaskets located at the top and bottom of glass-PEEK sandwich served as a seal between the mixer and a stainless steel holder.

The holder consisted of two 5 mm thick plates each 40 mm long and wide held together by 4 screws. The plates also had a simple alignment system manufactured into them: eight 1 mm thick pillars protruding from the surface of the bottom plate would fit tightly into eight holes drilled through the upper plate guaranteeing perfect alignment of all elements of the mixer.

Delivery lines were connected to the upper plate of the steel holder via standard 10-32 HPLC fittings.

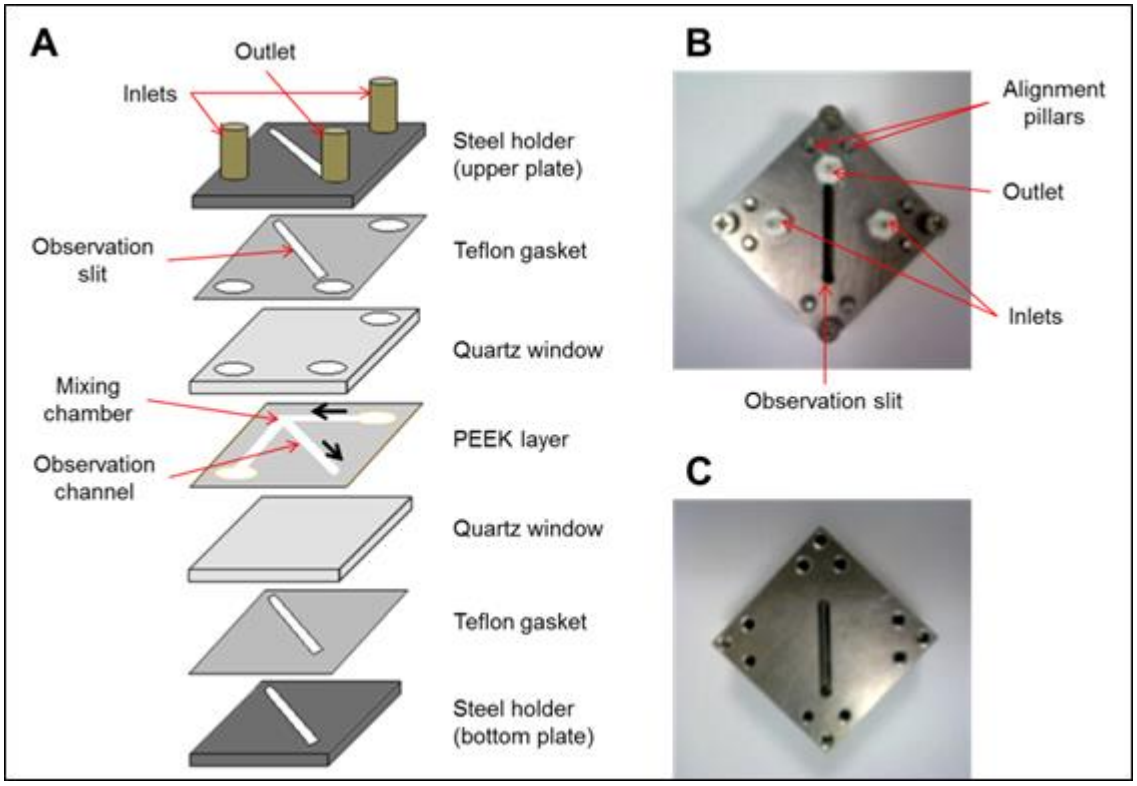

Figure 5.5 First prototype of continuous flow mixer manufactured at Warwick School of Engineering. Schematic diagram (A) demonstrates details of the design, while photographs of upper plate (B) and bottom plate (C) show outer features of the mixer. Black arrows on the PEEK layer in panel A indicate the direction of the flow of reagents.

Having successfully demonstrated the feasibility of microfabrication for the manufacture of continuous-flow mixer, the design was modified to facilitate its incorporation into the instrument.

While PEEK-quartz glass sandwich forming the core of the mixer was unchanged, the steel holder was significantly strengthened in order to withstand high pressure exerted by solutions pumped through narrow channels of the mixer at high flow rates. The bottom plate of the holder was enlarged to 60 mm x 60 mm and its thickness increased to 10 mm to withstand greater pressure. The shape of the upper plate was modified to accommodate horizontal bar used to position the mixer in the instrument (see Figure 5.6). Four screws holding upper and bottom plates together were replaced with eight bolts with hex nuts to increase durability of the holder.

Following its assembly, second prototype underwent a series of pressure and leakage tests in order to verify its suitability for integration into the continuous-flow apparatus. Prior to live testing with fluorophores, the entire optical setup of continuous-flow apparatus had to be revised. This was due to the fact that new mixer prototype relied on 180° detection as opposed to 90° detection characteristic for mixers previously installed in the instrument.

In 180° detection the CCD camera is facing the light source, with the mixer positioned between the light source and the camera. Such method is not commonly used as any excitation light exiting the monochromator is focussed into the flow channel and upon passing through the channel may reach the camera. Since the intensity of excitation light is several orders of magnitude higher than fluorescence emitted by the sample, the excitation light can easily blind the CCD sensor rendering collection of data impossible. Thus a set of two 320 mm cut-off filters was installed between the camera lens and the mixer in order to eliminate any incident light passing through the flow channel (see Figure 5.6). Since both NATA and Tryptophan fluoresce at higher wavelengths, the CCD camera can detect their emissions unhindered.

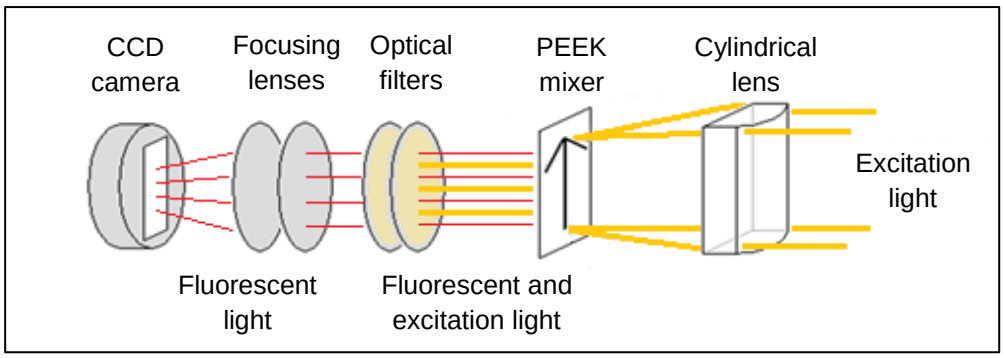

Figure 5.6 Optical setup of continuous flow instrument revised in order to accommodate new microfabricated mixer requiring 180° detection. Excitation light focussed by cylindrical lens passes through the flow channel of PEEK mixer exciting fluorophore mixture. Upon exiting the flow cell fuorescent light emitted by the sample is mixed with much stronger excitation light which has to be blocked by a selection of cut-off or bandpass filters. Fluorescent light passing through the filters freely is then focussed into the CCD camera by focusing lenses to facilitate detection.

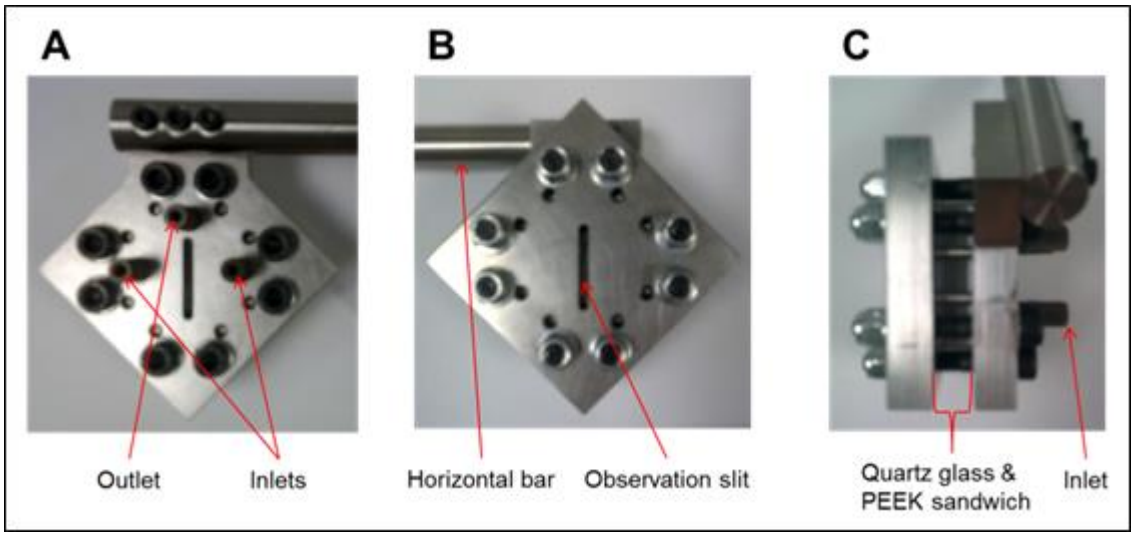

Figure 5.7 Second prototype of a continuous-flow mixer demonstrating enlarged steel casing and horizontal bar used to integrate the mixer into the instrument. Front plate (A) was modified in order to accommodate the horizontal bar while the layout of the back plate (B) remained largely unchanged. The side view of the mixer (C) demonstrates the thickness of steel holder necessary to withstand high pressure generated during instrument operation.

With newly installed mixer prototype and revised optical setup, experimental evaluation of effectiveness of the instrument carried out. It was immediately revealed that fluorescence emitted by the sample at working concentration was too weak compared to excitation light. Optical filters designed to block intense excitation light were also blocking fluorescence. This was due to the fact that no optical filter is 100% transparent to light of any wavelength, and even light of wavelength which can pass through the filter would lose some of its intensity. Reducing a number of optical filters from two to one did not reduce the intensity of excitation light sufficiently enough to prevent saturation of CCD chip thus preventing the camera from gathering any useful data. Removing this shortcoming required re-designing the mixer and was accomplished in the third prototype.

5.2.3.2 Microfabricated planar T-mixer

With 180° observation proved impossible, alternate solution was quickly implemented. The observation slit of the mixer was widened in order to facilitate a 150° observation. Such angle allowed the camera to be moved outside the excitation light beam while simultaneously allowing for unhindered observation of flow channel (see Figures 5.8 and 5.9). Thus a third and final prototype of the mixer was manufactured.

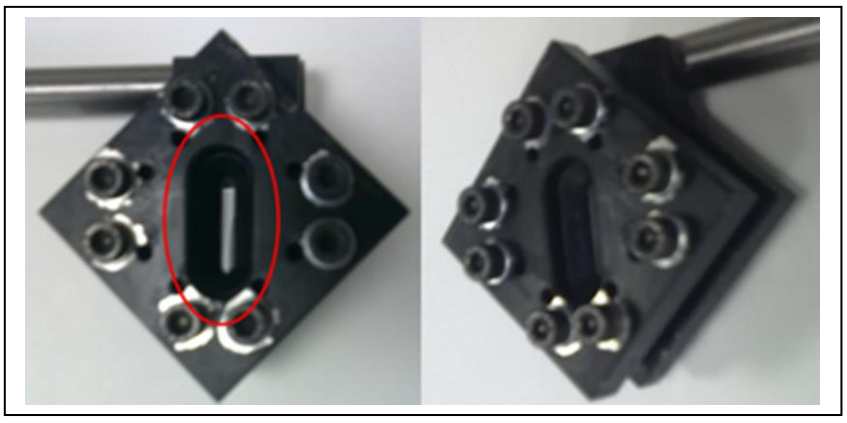

Figure 5.8 Photographs of the back plate of third prototype of continuous flow mixer demonstrating widened observation slit to facilitate wide-angle detection. Front plate remained unchanged and is not shown. Note black coating of the entire steel holder designed to minimise internal light scattering from metallic surfaces and glass/metal interfaces.

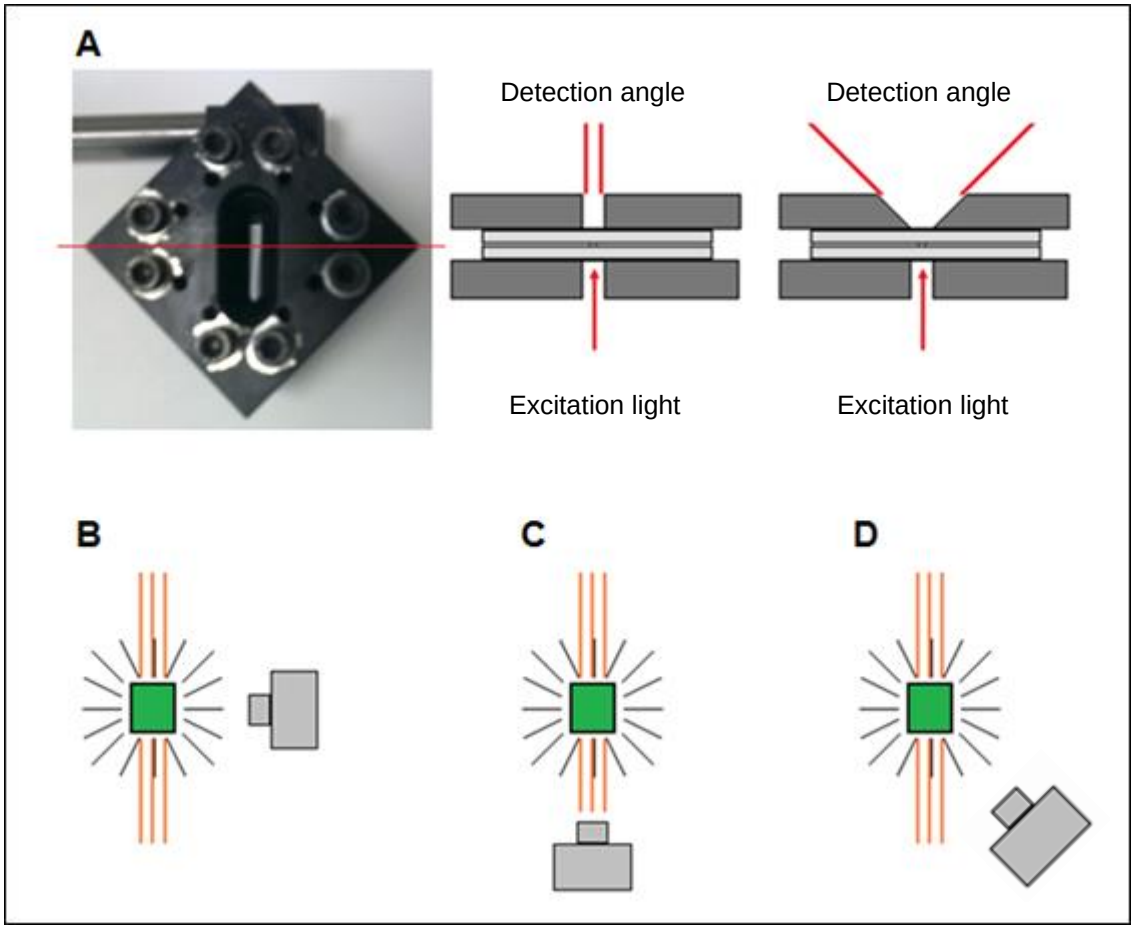

Figure 5.9 Schematic representation of modifications introduced in third mixer prototype in order to facilitate 150° detection. Panel A shows how widening the observation slit on the back plate of the mixer allowed the detection angle to be altered, compared to unmodified mixer. Panels B illustrates the basic principle of 90° detection which relies on positioning the camera (grey shape) at 90° angle to excitation light (orange lines) allowing for fluorescence (black lines) emitted by the sample flowing through the flow channel (green square) to be easily detected. Panel C represents the camera positioned at 180° being blinded by excess excitation light reaching CCD sensor despite the use of filters. Panel D demonstrates how decreasing the detection angle to 150° allows for the camera to be moved beyond the beam of excitation light and thus collect reliable data.

Initial stages of third prototype evaluation involved leakage and pressure resistance tests which proved that the mixer can operate without problems at flow velocities of up to 12 ms^{-1}, much like the second prototype. At 14 ms^{-1} minor leaking occurred, but this was not considered an issue since flow dynamics simulations showed that for this particular mixer configuration most efficient mixing occurred at flow velocities of 6-8 ms^{-1}. Below 6 ms^{-1} the flow of reactants changed from turbulent to laminar and thus mixing efficiency was severely decreased. Similarly, at flow velocities exceeding 10 ms^{-1} simulated mixing efficiency decreased.

Live tests of third prototype aimed at both verifying the conclusions drawn from flow dynamics simulations and evaluating mixing efficiency of the mixer itself quickly revealed that although no excitation light was reaching the camera positioned at 150° to the light source, no fluorescence decay could be observed during NATA/NBS quenching experiments.

Thorough investigation of the phenomenon led to a conclusion that light scattering occurring at interfaces between quartz windows and metal surfaces of the steel holder, as well as additional scattering at the edges of the flow channel produced enough refracted light to swamp NATA fluorescence (see Figure 5.10).

Any modifications to the third prototype aimed at eliminating light scattering such as coating the entire steel holder with black paint proved unsuccessful. Similarly, altering the detection angle between 130° (smallest angle which positioned the camera beyond the excitation light beam) and 160° (largest observation angle achievable with widened observation slit of the third prototype) yielded no positive results.

Due to the fact that the wavelengths of scattered light and those of NATA or tryptophan fluorescence overlapped greatly (see Figure 5.10, panel B) introduction of additional optical filters to block scattered light was deemed impossible.

In such circumstances, a decision was made to abandon the planar geometry of microfabricated mixers and adopt a completely new design which included a three-dimensional geometry and 90° fluorescence detection.

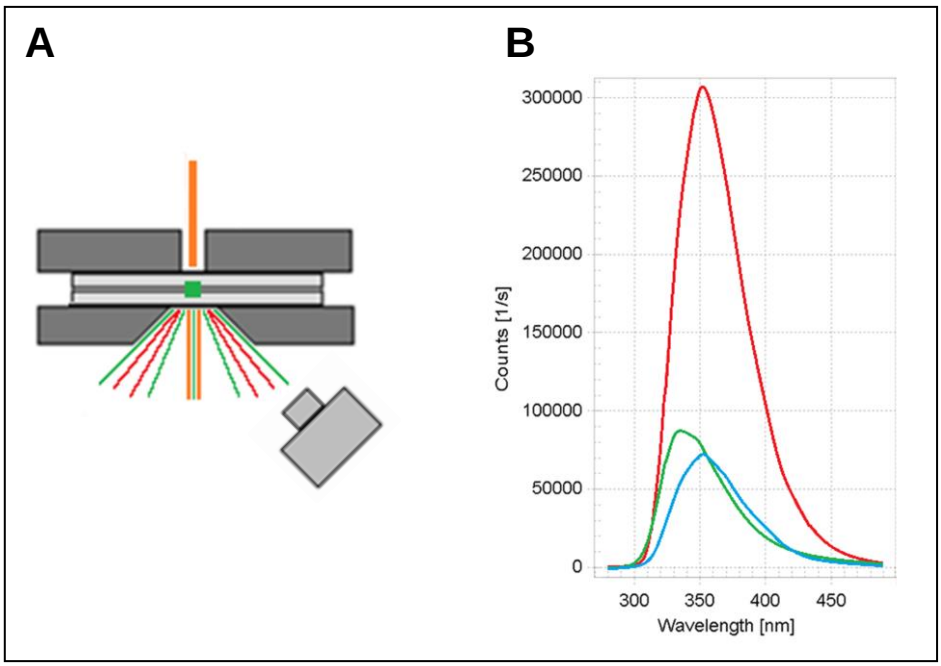

Figure 5.10 Diagram illustrating light scattering occurring during continuous-flow experiment. Panel A demonstrates how scattered light interferes with fluorescence measurements in 150° detection. Although excitation light (orange lines) can pass freely through the mixer and does not reach the CCD sensor (grey shape), light scattered (red lines) at glass/metal interfaces and flow channel edges can easily reach the camera and interfere with detection of fluorescence (green lines). Panel B shows a graph created by quantifying both fluorescence (blue line) and scattered light (green line) using handheld fibre-optic spectrometer. Red line in panel B represents fluorescence intensity in previous generation of ball-mixer and T-mixers used in previous study by Dr David Jenkins (Jenkins, 2006). Flow channels in those devices were significantly wider - 250 μm by 250 μm allowing for larger volume of fluorophore to be visible to the camera and therefore stronger signal to be detected.

5.2.3.3 Hybrid T-mixer with vertical flow cell

Three prototypes of planar mixers, while successfully demonstrated suitability of microfabrication for production of continuous flow mixers and mechanical robustness of the design, were also unsuitable for fluorescence data collection. While solving the problem of light scattering was achievable in the long term, it would require dramatic re-designing of the entire prototype, and was therefore deemed to time and resource-consuming. Thus a decision was made to design a completely new prototype using knowledge gained from previous prototypes as well as flow dynamics simulations.

New mixer design combined elements of microfabricated planar mixers such as steel holder, and PEEK layer with delivery channels arranged in planar geometry, with a three-dimensional layout and 90° detection offered by more typical continuous-flow mixers.

Much like in previous prototypes, the central part of the prototype was a planar PEEK sheet 25.4 mm long and 25.4 mm wide. While thickness of the layer remained unchanged, the width of both delivery channels was increased from 100 μm to 250 μm. Geometry of delivery channels, each 100 μm high and 250 μm wide, was also altered. They no longer ran along the sides of the layer to meet at 90° in one of the corners, but rather stretched from opposite corners of the layer along the diagonal and met head-on in the middle of the sheet (see Figure 5.11).

Unlike previous prototypes, flow-channel was not machined in the layer along with delivery channels, but was formed by placing PEEK sheet on top of 20 mm long quartz cuvette (see Figures 5.11 and 5.12). The cuvette made from fused silica contained a 250 μm x 250 μm flow-channel positioned so that one of its ends would coincide with the meeting point of two delivery channels. Increasing the diameter of flow channel allowed for larger volume of the sample to be viewed by the camera, increasing fluorescence intensity.

Quartz cuvette was encased in the bottom part of stainless steel holder with four observation windows machined in each of its sides to facilitate 90° detection. Steel holder was held together by four screw-in bolts, allowing for precise regulation of mechanical pressure applied to all of the components.

In order to increase durability of the mixer the PEEK layer was not placed directly on top of the quartz cuvette, but sandwiched between upper plate of the steel holder and

100 μm-thick tungsten plate. While this generated a gap between the mixing chamber and visible part of the flow channel (see Figures 5.11 and 5.12), it also offered necessary rigidity and pressure resistance vital for instrument operation at high flow velocities.

The seal between PEEK, tungsten plate and upper plate of the holder was provided by PEEK itself upon pressing all of the elements together by four bolts in the steel holder. Entire configuration was again subjected to simulations of flow dynamics which suggested virtually no loss in turbulence of the flow mainly due to head-on collision of two reactants flowing through delivery channel, and thus no noticeable change in mixing efficiency of the design.

Upon assembly, the mixer was subjected to standard leakage and pressure tests which verified its pressure and flow velocity operation range. At flow velocities of up to 12 ms^{-1}, no leaking was detected, while at 14 ms^{-1} only minor leaking occurred. Much like with previous mixer prototypes, this was deemed satisfactory.

Live tests with fluorophore revealed no unexpected problems such as light scattering, which was expected given 90° detection utilised in this design.

Thus a fully functional mixer was created, mixing efficiency and dead time of which could be experimentally verified.

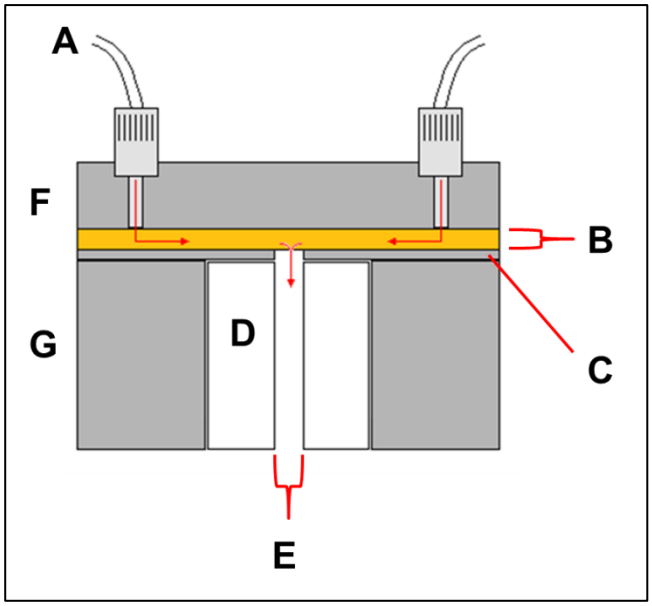

Figure 5.11 General layout of the hybrid T-mixer with vertical flow cell. Ferrules and tubing (A) are used to deliver reagents to the mixer. The reagents flow through the 250 µm wide channel cut in the 100 µm thick PEEK layer. The PEEK layer sits atop the 100 µm thick tungsten plate which provides necessary durability. The entire PEEK-tungsten sandwich is placed atop the quartz flow cell (D) with 250 x 250 µm wide channel running through its centre (E). The PEEK layer, tungsten plate and the flow cell are pressed together by a two-part stainless steel holder consisting of upper plate which houses the delivery system (F) and bottom plate which encases the flow cell (G).

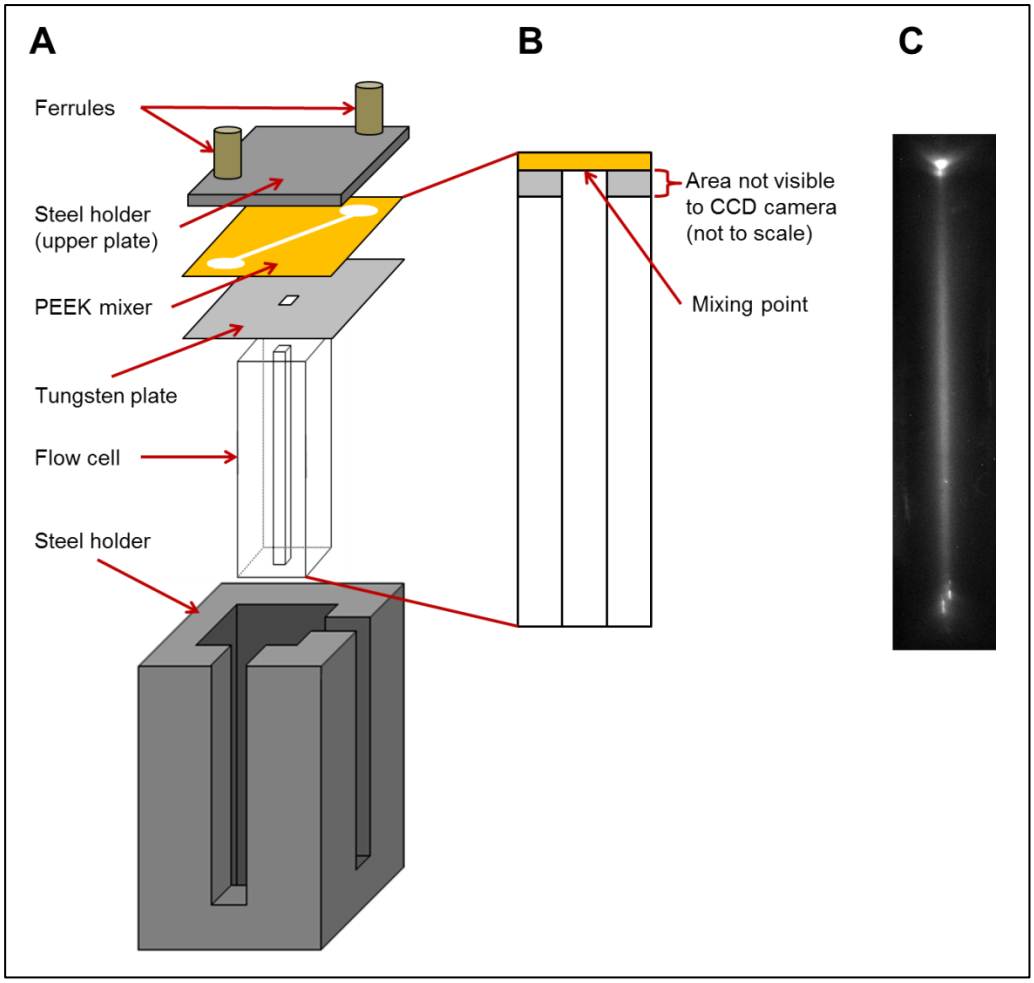

Figure 5.12 Detailed structure of a hybrid T-mixer with vertical flow cell. Panel A illustrates the details of the design and its assembly. The PEEK mixer is squeezed between upper plate of the steel holder and thin tungsten plate. This sandwich is in turn placed on top of the quartz flow cell encased in steel holder with observation slits cut in its sides. Panel B highlights a small dead volume created by tungsten plate located between the PEEK mixer and quartz flow cell. Panel C shows an actual image of the channel filled with 20 μM NATA.

5.2.4 Mixing efficiency

5.2.4.1 Data collection and analysis

During a typical continuous-flow experiment fluorescence emitted by the sample passing through the flow-channel of the mixer is monitored by the CCD camera. The chip of the camera is sensitized in the deep-UV region allowing for detection of NATA and tryptophan fluorescence. Fluorescence data are collected in a form of digital images of the flow channel and stored on PC hard drive for further analysis. All of the experimental variables (excluding reactant concentrations) were controlled by μHi Flow software together with QImagin Suite facilitating easy and efficient collection of the data.

The exposure time during each of the experiments detailed in this chapter was set to 5 seconds, allowing clear images of the flow-cell with high signal to noise ratio to be obtained. A time interval of 0.5 second was set between activation of stepper-motor drive and thus flow initiation and the onset of data collection. This time delay was necessary to ensure that the flow channel was filled with reaction mixture prior to data collection as well as to provide enough time for any residual solution leftover from previous runs to be flushed from the observation channel by fresh reactants.

While QImaging Suite software was capable of manipulating variables such as gain and contrast of acquired images, it was deemed unnecessary to manipulate any of those settings and hence throughout all of the experiments they remained set to default values. The linear flow velocity controlled by μHi Flow software could be set to a number of values ranging from 4 to 14 ms^{-1} in 2 ms^{-1} increments. Similarly, the total reactant volume displaced during each individual experiment could be set to a value which allowed for a run time of at least 5.5 s. The run time itself was calculated by the μHi Flow software from the flow velocity and the volume displaced, based on the knowledge of the dimensions of the flow-channel provided prior to the experiment. Following the run, data acquired over the entire five-second runtime were immediately displayed by QImaging Suite in a form of an image showing the fluorescence intensity of the mixed solution travelling up the flow-channel (see Figure 5.13, panel A). Since fluorescence intensity of individual pixels in the entire image was recorded automatically by the software, the only processing needed to obtain average fluorescence profile of the flow-cell was to select the outline of the channel visible in

the image. Upon selection of channel outline, average fluorescence values in every row or every column of pixels could be calculated by the software (this corresponds to averaging fluorescence along or across the channel respectively) and exported in form of XLS or ASCII file. For continuous-flow experiments detailed in this chapter, averaging columns of pixels allowed for construction of fluorescence profile along the channel (see Figure 5.13, panel B). Between 18 and 20 pixels in each column were typically used in the calculation of average fluorescence.

Once calculated, mean fluorescence intensity was plotted against pixel number to give a fluorescence intensity profile for each flow-cell image. Using fluorescence values from these profiles together with Equation 5.1 allowed for calculation of normalised fluorescence decay relative to initial (unquenched) NATA fluorescence:

$$\text{Relative fluorescence} = \frac{F_{(\text{reaction})} - F_{(\text{background})}}{F_{(\text{initial})} - F_{(\text{background})}} \tag{5.1}$$

where $F_{(\text{reaction})}$ is the fluorescence profile of NATA quenched by NBS, $F_{(\text{background})}$ is the profile of distilled water alone, and $F_{(\text{initial})}$ is the profile of unquenched NATA. The profile of distilled water was used to account for any background signal reported by the CCD not attributable to NATA fluorescence (such as scattered or reflected excitation light, background levels of the CCD or "dead" pixels).

Prior to mixing efficiency or dead time estimation, the x-axis scale of relative fluorescence graphs had to be converted from pixel number to kinetic time-base. This was achieved by implementing Equation 5.2

$$\Delta t = \frac{A \times L}{\gamma} \tag{5.2}$$

where Δt is the change in time in seconds over the distance of flow-channel viewed by the CCD camera, A is the area of the cross-section of the flow-cell measured in mm^2, L is the length in mm of the channel observed by the CCD, and γ is the flow-rate in mls^{-1}, calculated by μHi Flow software on the basis of the linear flow-velocity set for particular run and dimensions of the flow-cell specified prior to the experiment.

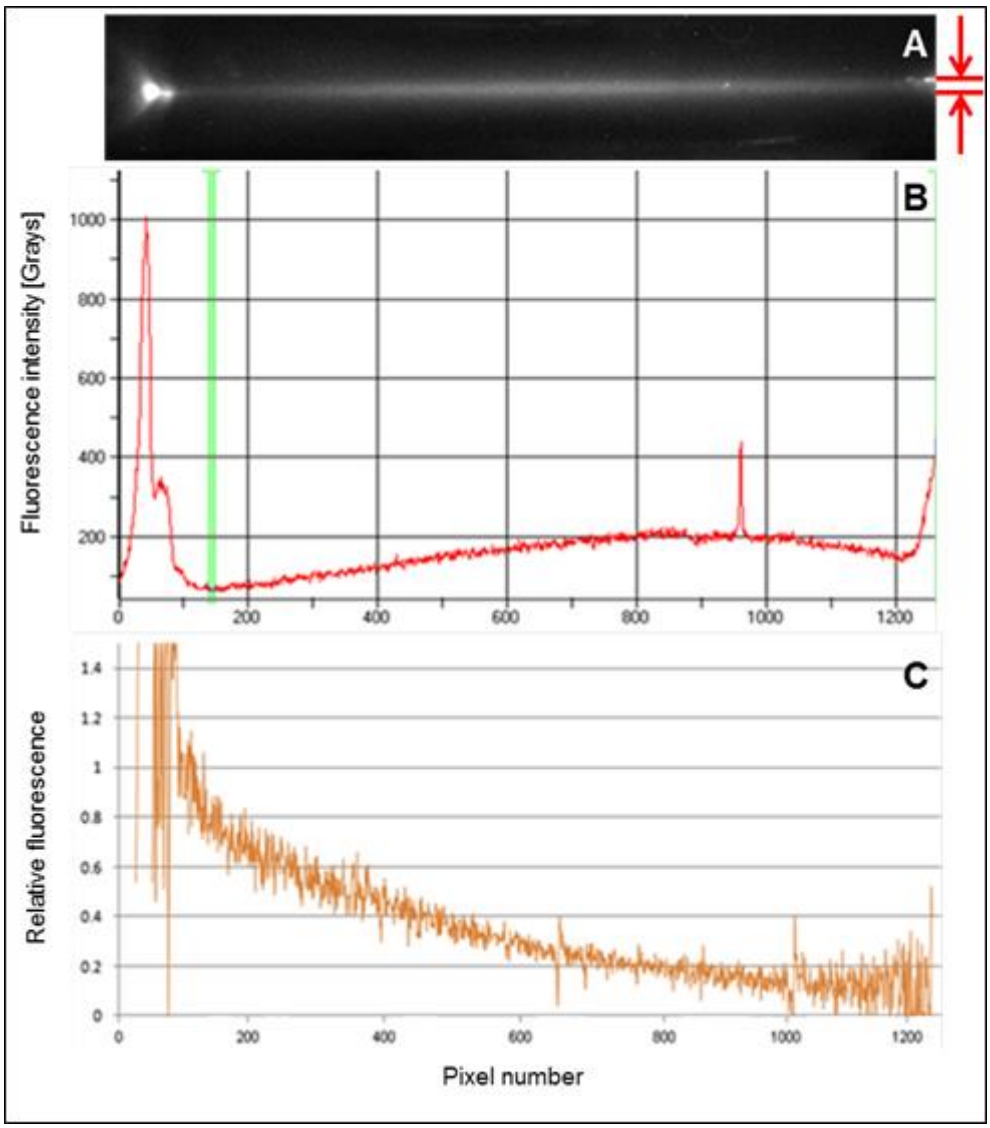

Figure 5.13 Illustration of the method of data processing from image to relative fluorescence profile. Panel A shows an image of the flow-cell acquired during experiment which involved quenching 20 μM NATA fluorescence with 0.5 mM NBS. Red lines and arrows indicate the boundaries of the flow-channel between which columns of pixels were averaged to construct fluorescence intensity profile by QImaging Suite software as shown in panel B. Panel C represents relative fluorescence profile calculated from fluorescence intensity profile in panel B using Equation 5.1. Note that fluorescence profile in panel B shows uneven fluorescence intensity along the flow-channel resulting from non-uniform illumination.

5.2.4.2 Mixing efficiency tests

In order to confirm suitability of new mixer for investigation of very rapid reactions such as folding of PrP, both mixing efficiency and instrumental dead time had to be evaluated. Estimation of mixing efficiency was performed by comparison of fluorescence profiles of NATA recorded in two separate experiments.

During the first experiment 220 μM solution of NATA was diluted with distilled water to a final concentration of 20 μM. Diluted fluorophore was then loaded into all three syringes serving as reactant reservoirs and pushed through the mixer at flow velocities of 4, 6, 8 and 10 ms^{-1}. This was done in order to evaluate whether mixing efficiency varies depending on the flow velocity and if so, which flow velocity provides optimal mixing. Recorded fluorescence profile of pre-mixed NATA served as a reference of "ideal mixing".

Intensity profile of distilled water alone was also recorded and processed to account for any background noise.

Second experiment involved loading 220 μM solution of NATA into the smallest 0.5 ml syringe with distilled water being loaded into two 2.5 ml syringes. Over the course of the experiment NATA was diluted by distilled water in 1:10 ratio, resulting in final concentration of 20 μM. Flow-cell image obtained during the experiment was then processed into fluorescence intensity profile using Equation 5.1 and compared with the profile recorded during the first experiment. The more similar the fluorescence profile from second experiment was to the profile from first experiment, the greater the mixing efficiency. If the mixer was 100% efficient, the two profiles would be identical, indicating no difference between fluorescence profile of pre-mixed fluorophore with the profile recorded *in vivo* during the mixing experiment.

5.2.4.3 Determination of instrumental dead time

Dead time of the instrument equipped with newly developed mixer was determined using a well-established procedure of following the kinetics of the first-order reaction of NATA fluorescence quenching by NBS (Peterman, 1979; Shastry *et al.,* 1998) upon their mixing within the instrument under evaluation.

The experiment itself involved mixing of 20 μM NATA with a range of NBS concentrations varying from 0.25 mM to 5.0 mM. In order to achieve desired fluorophore concentration, 220 μM NATA was loaded into the smallest syringe (fluorophore reservoir), with NBS loaded into Larger syringes (quencher reservoirs). Upon mixing initiation NATA was diluted by NBS in 1:10 ratio, resulting in final concentration of 20 μM. In order to account for minor dilution of NBS with NATA, concentrations of solutions loaded into the reservoirs were 10% higher than desired final concentration (e.g. in order to achieve 5.0 mM final concentration, 5.5 mM NBS was loaded into quencher reservoirs).

Progress of the reaction was monitored by CCD camera and recorded in form of flow-cell images. The images obtained during the experiment were then processed into fluorescence intensity profiles using QImaging Suite and Equation 5.1, with Equation 5.2 later used to calculate the time-base of the reaction. Resulting kinetic profiles were imported as XLS files into statistical analysis software (SigmaPlot 9.0) for curve-fitting, and plotted as a graph for visual inspection. In order to account for any turbulences or mixing artefacts present in the earliest stages of fluorescence profile, the earliest time-base coordinate at which the data deviated from an exponential decay was determined and only the data further down the x-axis were used to determine key kinetic parameters of the reaction. One of such artefacts can be seen in Figure 5.13, panel A as circular-shaped are of intense fluorescence between pixels 0 and 100, as well as in resulting fluorescence profiles (Figure 5.13, panels B and C).

In order to determine the key kinetic parameters, the data were fitted by a single exponential decay function, of the form

$$F_t = F_0 + a^{(-kt)} \tag{5.3}$$

where *Ft* is the fitted fluorescence function, *F0* is the end-point, *a* is the amplitude, *k* is the rate constant and *t* is time.

Following the fitting, relative fluorescence curves obtained during given experiment were re-plotted on a single semi-logarithmic plot, and the fit lines extrapolated back to a common intersection with a y-axis value close to 1, which corresponds to the value of relative fluorescence of NATA in the absence of NBS. The x-axis difference between the common intersection and the first data point of fitted curves provided an estimation length of the dead time of the instrument at given flow velocity.

5.3 Results and discussion

5.3.1 Fluorescence signal intensity enhancement

5.3.1.1 Increased sensitivity CCD camera

Over the course of the project multiple methods of improving the overall sensitivity of the instrument were considered. The issue of low sensitivity of Micromax camera became particularly important following the evaluation of third prototype of microfabricated mixer, when relatively low levels of excitation light scattered into the camera produced as strong a signal as NATA fluorescence in the channel. Thus, prior to mixing efficiency and dead time evaluation of the final prototype of the mixer, a decision was made to replace ageing Micromax camera with a newer, more sensitive and efficient model. Several commercially available models were evaluated and a Retiga-2000R model boasting enhanced deep-UV sensitivity was purchased (for comparison between Micromax camera and Retiga-2000R see Figure 5.14). As a side-effect of changing the camera from 15-year old model to a 2-year old one, a bulky signal processing unit (see #9, Figure 5.2) could be discarded, as the new camera could be connected to the computer via USB cable. This significantly increased the reliability of the system, as the old camera had to be connected to the signal processing unit with a specialised connector cable custom made by Micromax, which in case of failure would be both expensive and time-consuming to replace as it is only manufactured in the USA.

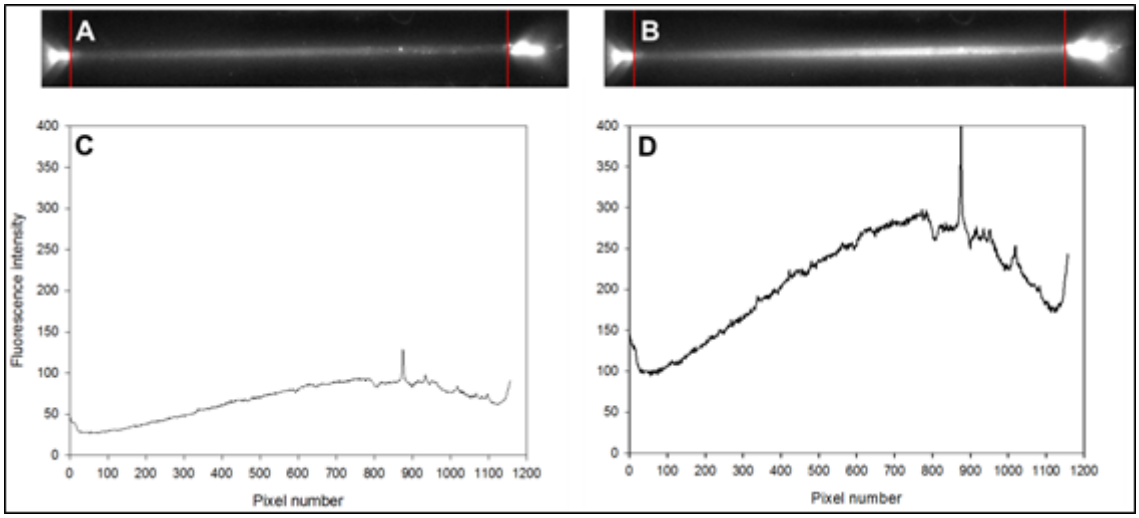

Figure 5.14 Comparison of sensitivites of Micromax CCD camera with SenSys: 1401E chip (A) and Retiga-2000R camera equipped with Kodak Sensors KAI-2020 chip (B). The channel inside the flow-cell is visible as a bright horizontal band roughly in the centre of each image. Both images were acquired over the course of one second with 220 μM NATA filling the channel.

Panels C and D show numerical values of fluorescence intensity distribution across the fragment of each image indicated by red lines. Although fluorophore concentration was identical, Retiga-2000R detected much stronger signal of 260-280 Grays as opposed to Micromax, which registered only 80-90 Grays.

Note that this particular test was conducted with a flow channel blocked at both ends and filled with stationary fluorophore solution. This allowed for exactly the same channel to be viewed by both cameras to facilitate sensitivity comparison.

5.3.1.2 Fluorescence enhancement by light reflection

An important aspect of any instrument used for biological studies is sample economy.

Protein solutions used in experiments often take weeks to prepare, particularly if expression of given protein in prokaryotic system and subsequent purification are required. Therefore, it is of great importance for the instrument to offer greatest possible sensitivity, thus limiting sample consumption.

While replacing the camera with a more robust model increased detection capabilities of the instrument, a second method of improving data quality and enhancing detection was available, which involved increasing the strength of fluorescence in the flow cell. As mentioned in Section 5.2.2.2, this could be achieved by either increasing fluorophore concentration in the sample or by increasing the intensity of excitation light reaching the sample. The latter could be achieved not only by replacing the light source, but also by reflecting any incident light transmitted through the sample and the walls of the flow-cell back into the quartz cuvette. This could be achieved by installing mirrors in the flow-cell holder to reflect transmitted light back towards the flow-channel. Upon closer inspection of the holder housing both the mixer and the flow cell, it became apparent that installation of mirrors would require re-designing the entire steel frame. Thus, another solution was implemented: two walls of the quartz cuvette were mirror-coated by depositing silver on cuvette surfaces, one opposite to the face exposed to incident light, and the other opposite the face observed by the CCD (see Figure 5.15). In order to assess the extent of fluorescence intensity increase upon coating two sides of the cuvette with silver, a typical continuous-flow experiment was set up in which 220 μM NATA was diluted in 1:10 ratio by distilled water at linear flow velocity of 6 ms^{-1}. Several channel images for both non-coated and coated cuvettes were recorded and fluorescence intensity profiles constructed using QImaging Suite software (see Figure 5.16).

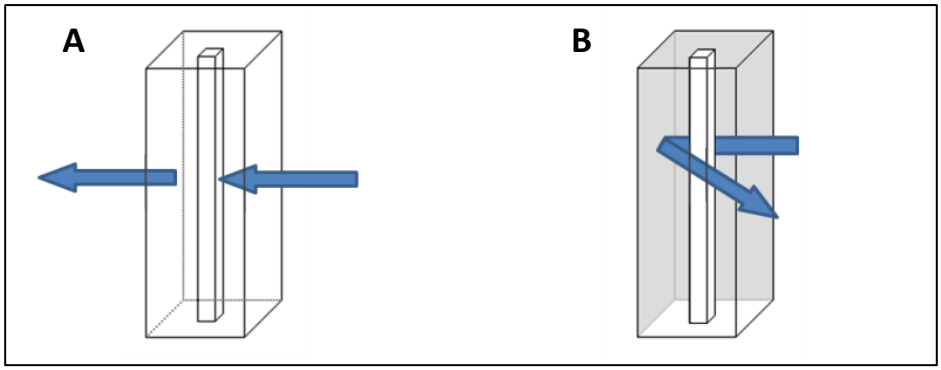

Figure 5.15 Comparison of excitation light transduction through non-coated and mirror-coated quartz cuvette. In non-coated cuvette (A) any incident light not focussed into the fluorophore-filled flow-channel may pass freely through the cuvette and is therefore lost into the environment. Upon coating two sides of the cuvette with silver, any excitation light missing the channel and passing through the flow-cell is now reflected back into the cell with high probability of passing through the flow-channel again, therefore increasing the overall intensity of excitation light reaching the sample.

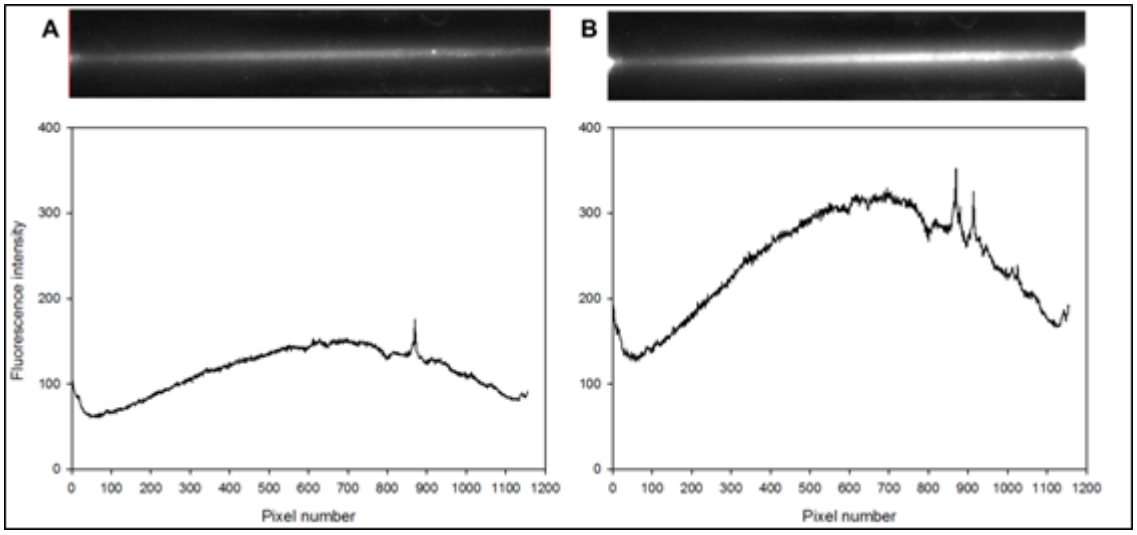

Figure 5.16 Flow cell images and fluorescence intensity profiles collected during the experiment aimed to compare fluorescence intensity in non-coated and mirror-coated cuvettes. Panel A shows image of the flow-channel acquired by CCD camera (top) as well as fluorescence intensity profile along the channel (bottom) of the non-coated cuvette. In comparison, fluorescent light visible in the photograph of the flow-channel of coated cuvette (panel B, top) is much more intense. This is confirmed by the fluorescence profile constructed for that image (panel B, bottom).
Note that in both flow cell images recorded during the test, fluorescence intensity is significantly higher towards the centre of the flow-channel (between pixels 600 and 800) than at the entrance and exit of the channel (pixels 0 and 1200 respectively). This effect again highlights the uneven intensity profile of the excitation light beam which has to be corrected for by subtraction of background profiles, as described in section 5.2.4.1.

Upon comparison of the fluorescence intensity profile of NATA flowing through non-coated cuvette with corresponding profile for mirror-coated cuvette, significant signal enhancement achieved by silver coating two sides of a quartz flow-cell becomes apparent.

While in non-coated cuvette a 20 μM NATA solution yielded observed fluorescence intensity of approximately 150 Grays, the very same fluorophre concentration flowing through mirror-coated cuvette provided signal of 300-350 Grays, demonstrating an enhancement of approximately 250 % of the total fluorescence intensity.

These data clearly indicate that by silver-coating two sides of the quartz flow-cell significant increase in fluorescence signal can be achieved, consequently improving both sample economy during CF experiments and detection capabilities of the apparatus.

5.3.2 Dimensions of the flow channel visible to the CCD camera

Precise evaluation of key parameters, such as instrumental dead time as well as analysis of kinetics of monitored reaction requires an accurate measurement of the time-base.

In continuous-flow the time-base of the experiment is determined by the length of the flow-channel visible to the CCD camera. Thus, an accurate determination of the time-base (Δt) as calculated by Equation 5.2 requires the exact length of the flow-channel viewed by the camera (L) to be known.

In this study, the field of view of the camera itself was used to determine how many pixels in the image of the mixer are occupied by the flow channel. Estimating what part of the channel is visible to the camera was not necessary, since observation windows cut in the frame of steel holder allowed for entire 20 mm flow channel to be visible. Thus by correlating the length of the channel with the number of pixel it stretches across the image, length of the channel in pixels can be estimated.

With the pixel resolution of the screen being 1600 x 1200 pixels, the flow channel was positioned to occupy exactly 1300 pixels. Approximately 100 pixels at the very end of the channel usually had to be cut due to large light scattering artefact occurring at the interface between the quartz glass cuvette and the steel holder (see Figure 5.14, panels A and B) this however had minimal effect on the time base since any reactions

observed by the camera were usually finished by the time the reaction mixture reached far end of the flow cell.
Thus, a total of 1300 pixels were visible for 20 mm long channel, resulting in a calculated conversion factor of 65 pixels per millimetre of the channel. This was slightly less than 86 pixels mm-1 obtained in previous study (Jenkins, 2006). Unlike previous study, however, the entire flow channel was visible to the CCD camera, allowing for longer time-base to be observable.

5.3.3 Determination of dead time and efficiency of a hybrid T-mixer

By far the most important parameter of continuous-flow instrument is the "dead time", which is a time between the initiation of investigated reaction and collection of first reliable data. Shortest possible dead time may determine whether important early events of the reaction pathway are observed or not, greatly influencing the outcome of the research.
Key factors determining the length of the dead time of continuous-flow instrument are undoubtedly the mixing efficiency and robustness of its mixer. Thus, dead time evaluation was of great significance to the project, defining its success upon achieving dead times comparable to published mixer designs, or failure should the dead time be unacceptably long.
The hybrid T-mixer developed jointly with TgK Scientific and Warwick School of Engineering was tested using two standard methods of mixer efficacy evaluation (Shastry *et al.*, 1998). The first of these tests assessed mixing efficiency of the design by comparing fluorescence intensity profiles of premixed solutions of NATA with fluorescence profiles of fluorophore mixed *in vivo* in the mixer. The second test provided estimates of the dead time of the instrument by monitoring the first order reaction of NATA fluorescence quenching with NBS (Peterman, 1979). Both of these tests were carried out at linear flow velocities of 4, 6, 8, and 10 ms^{-1} to assess the effects of flow velocity alteration on mixer performance, as well as to determine the optimal flow rate for mixer operation.

5.3.3.1 Mixing efficiency test

In order to evaluate mixing efficiency of continuous-flow mixer design, fluorescence intensity profiles of 220 μM NATA diluted by distilled water in 1:10 ratio and mixed both prior to injection into the apparatus and during the instrument run were constructed. Ratio of fluorescence intensities observed for pre-mixed solutions to those recorded during the mixing in-vivo allowed to determine the overall mixing efficiency for particular flow velocities.

Should the mixer perform with 100% efficiency, the ratio of fluorescence intensities would form a straight line with value of 1 across the length of the channel (see Figure 5.17).

Upon inspection of mixing efficiency estimates presented in the figure, it becomes apparent that mixing is by far more efficient at flow velocities of 6 and 8 ms^{-1} with much lower efficiency at both 4 and 10 ms^{-1}. Those estimates confirm the conclusions drawn from flow dynamics simulations conducted during the process of designing hybrid T-mixer prototype with vertical flow cell, that at 4 ms^{-1} flow of reactants is not turbulent enough to facilitate efficient mixing, while at 10 ms^{-1} it is the velocity of the fluids themselves that reduces mixing efficiency by forcing two streams of reactants to spiral around each other rather than mix turbulently through head-on collision. While mixing efficiencies at both 6 and 8 ms^{-1} flow velocities are close to unity, it should be noted that at 6 ms^{-1} the mixer efficacy is slightly higher across the entire channel.

At each of the flow-rates a considerable noise in the relative fluorescence profile can be seen between pixels 0 and 200. Such behaviour can be attributed to turbulences generated in the mixing chamber extending into the entrance of the flow-channel which is visualised in this region.

It should be noted that no attempt was made to determine the efficiency of the mixer at a linear flow velocity of 12 ms^{-1}. This was due to the fact that according to flow dynamics simulations mixing efficiency at 12 ms^{-1} would be even lower than at 10 ms^{-1}. Since simulations proved very reliable in the 4 ms^{-1} – 10 ms^{-1} region, it was decided not to expose the only working prototype of the new mixer to mechanical stress involved in pumping reactants through the mixer at 12 ms^{-1} flow velocity and thus risk any mechanical damage.

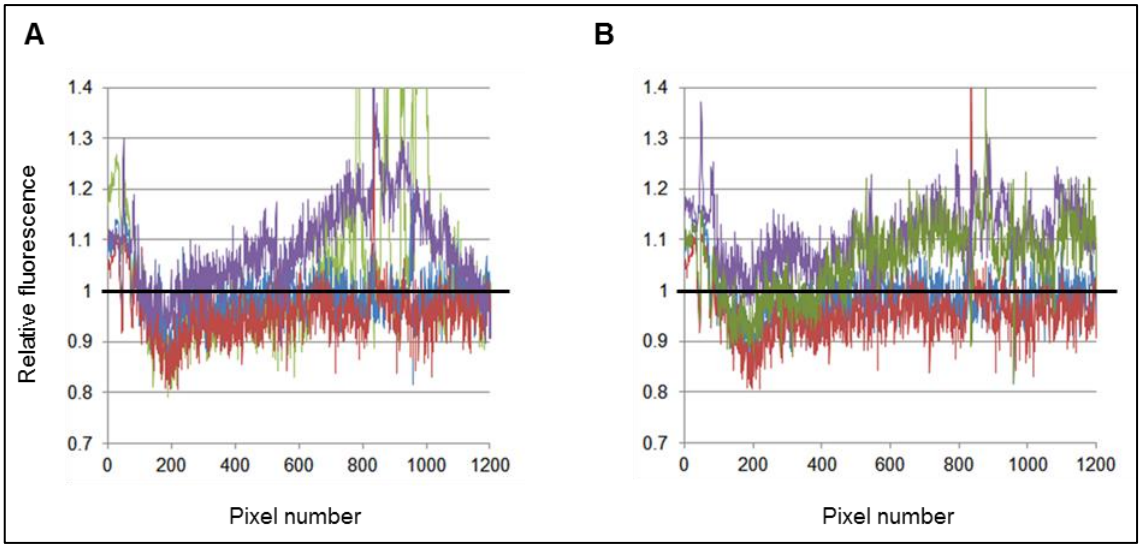

Figure 5.17 Ratios of fluorescence intensity profiles of reactants mixed *in vivo* to pre-mixed solutions of 20 μM NATA at 4, 6, 8 and 10 ms^{-1} flow velocities. Two separate repeats of mixing efficiency estimation are represented on panels A and B to verify validity of conclusions drawn from the experiment. Solid black line represents a constant at 1 and thus ideal mixing.

It is apparent that at both very low flow velocity of 4 ms^{-1} (green line) and very high velocity of 10 ms^{-1} (purple line) the mixing is far from optimum. In contrast, medium flow velocities of 6 ms^{-1} and 8 ms^{-1} (blue and red lines respectively) provide much better performance along the entire flow-cell.

5.3.3.2 Dead time determination

Instrumental dead time was estimated by monitoring the quenching of NATA fluorescence upon its mixing with NBS. A solution of 220 μM NATA was mixed in 1:10 ratio with solutions of NBS with concentration increasing from 0.25 mM to 5 mM. Four sets of dead time measurements were carried out in total at the same range of flow velocities as those used for mixing efficiency tests (4 ms^{-1}, 6 ms^{-1}, 8 ms^{-1}, and 10 ms^{-1}). All measurements were made at 20 °C.

Flow cell images recorded during the experiment were processed according to methods described in Sections 5.2.4.1 and 5.2.4.3 and plotted in form of relative fluorescence kinetic traces (see Figures 5.18 to 5.21, upper panels). Fitted single exponential functions determined by nonlinear regression are shown as black lines. The absolute value of time difference between the point of intersection of the fitted lines and the first recorded data point (represented by 0 on the time axis in figures 5.18 to 5.21) gives a dead time estimate. At each of the four flow-rates the fit lines extrapolate back to a common relative fluorescence close to 1, which is the expected initial fluorescence of NATA in the absence of quenching by NBS.

For every set of data, obtained graphs were re-plotted on a logarithmic fluorescence scale, in order to allow more precise estimation of the point of intersection.

The estimated dead times for different flow velocities are summarised in Table 1.

At 4 ms^{-1} flow velocity the fit lines cross over a relatively broad time range, making a precise estimate of the dead time difficult, which is reflected in high reported error. Similarly at 10 ms^{-1} the fit lines do not form a clear crossover point, indicating less thorough and reliable mixing in comparison to intermediate flow-velocities of 6 ms^{-1} and 8 ms^{-1}. This confirms the mixing efficiency estimates which clearly indicate less efficient mixing at either extremely low or extremely high flow-velocities.

The smallest dead time estimated by the quenching of NATA fluorescence by NBS was 130 ± 35 μs achieved at 8 ms^{-1}, with 170 ± 25 μs achieved at 6 ms^{-1} falling close behind.

Although this is well within the desired time frame of less than a millisecond, it is greater than was anticipated, compared for instance to the dead time of 100 μs reported for another CF instrument equipped with a T-mixer, working at a flow-rate of 2 ms^{-1} (Takahashi *et al.*, 1997).

Linear flow velocity [ms^{-1}]	Volumetric flow rate [mls^{-1}]	Dead time [μs]
4	0.18	460 ± 110
6	0.27	170 ± 25
8	0.36	130 ± 35
10	0.45	270 ± 160

Table 5.1 Estimated dead times of continuous-flow instrument equipped with hybrid T-mixer with vertical flow-cell.

Dead time for each of four linear flow velocities was estimated by following the kinetics of fluorescence quenching of 20 μM NATA upon its mixing with varying concentrations of NBS.

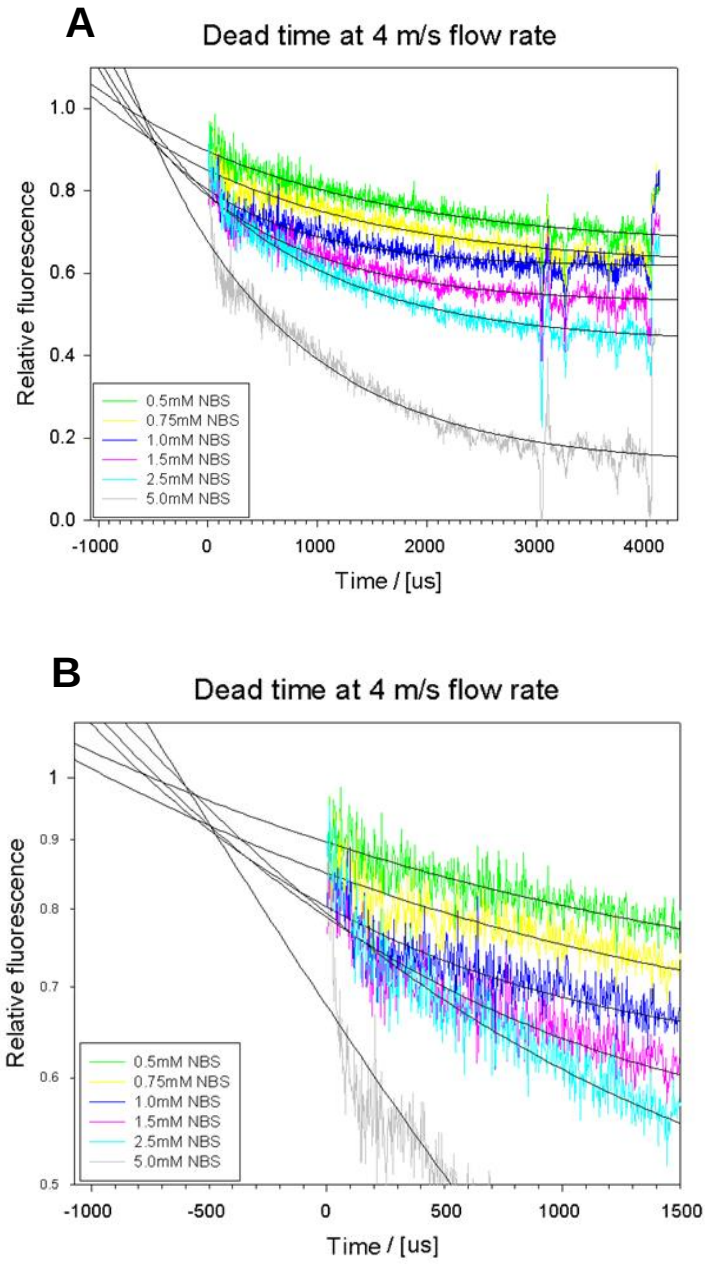

Figure 5.18 Dead time determination of continuous-flow instrument at a linear flow velocity of 4 ms^{-1}.

Fluorescence traces illustrate kinetics of quenching of 20 μM NATA with a range of final concentrations of NBS: 0.5 mM (green line), 0.75 mM (yellow), 1.0 mM (dark blue), 1.5 mM (pink), 2.5 mM (light blue) and 5 mM (grey). Kinetic trace obtained at NBS concentration of 0.25 mM not shown, as concentration of regent was insufficient to induce quenching and thus produce reliable kinetic data.

Single exponential decays fitted to the data are represented by solid black lines. Initial fits were plotted on a linear relative fluorescence scale (panel A) and re-plotted on a semi-logarithmic chart (panel B), for more precise dead time estimation.

Estimated dead time at 4 ms^{-1} linear flow velocity: 460 ± 110 μs.

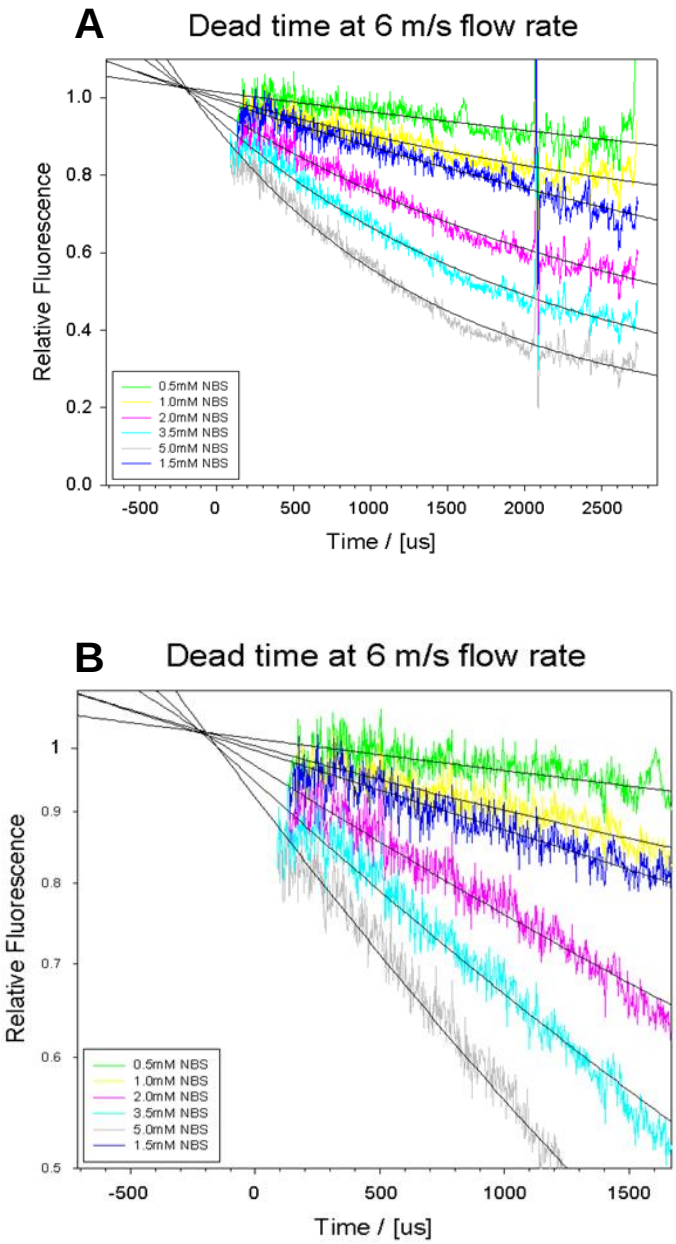

Figure 5.19 Dead time determination of continuous-flow instrument at a linear flow velocity of 6 ms^{-1}.

Fluorescence traces illustrate kinetics of quenching of 20 μM NATA with a range of final concentrations of NBS: 0.5 mM (green line), 1.0 mM (yellow), 1.5 mM (dark blue), 2.0 mM (pink), 3.5 mM (light blue) and 5 mM (grey). Kinetic trace obtained at NBS concentration of 0.25 mM not shown, as concentration of regent was insufficient to induce quenching and thus produce reliable kinetic data.

Single exponential decays fitted to the data are represented by solid black lines. Initial fits were plotted on a linear relative fluorescence scale (panel A) and re-plotted on a semi-logarithmic chart (panel B), for more precise dead time estimation.

Estimated dead time at 4 ms^{-1} linear flow velocity: 170 ± 25μs.

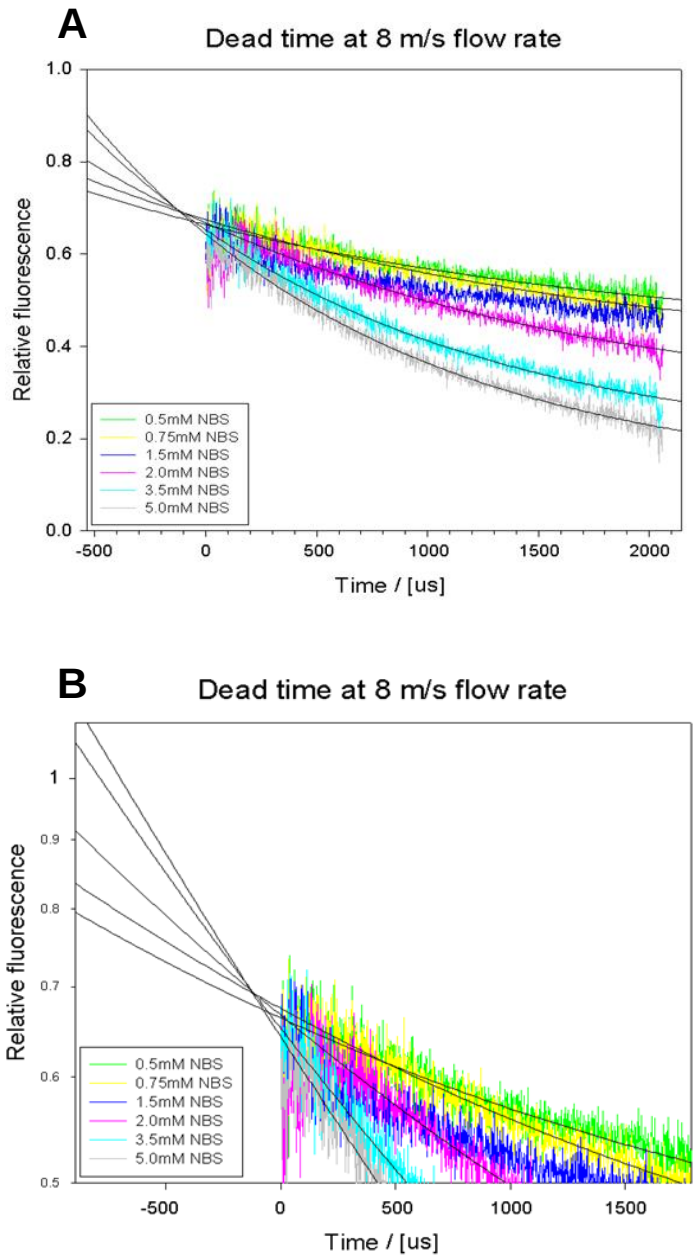

Figure 5.20 Dead time determination of continuous-flow instrument at a linear flow velocity of 8 ms^{-1}.

Fluorescence traces illustrate kinetics of quenching of 20 μM NATA with a range of final concentrations of NBS: 0.5 mM (green line), 0.75 mM (yellow), 1.5 mM (dark blue), 2.0 mM (pink), 3.5 mM (light blue) and 5 mM (grey). Kinetic trace obtained at NBS concentration of 0.25 mM not shown, as concentration of regent was insufficient to induce quenching and thus produce reliable kinetic data.

Single exponential decays fitted to the data are represented by solid black lines. Initial fits were plotted on a linear relative fluorescence scale (panel A) and re-plotted on a semi-logarithmic chart (panel B), for more precise dead time estimation.

Estimated dead time at 4 ms^{-1} linear flow velocity: 130 ± 35μs.

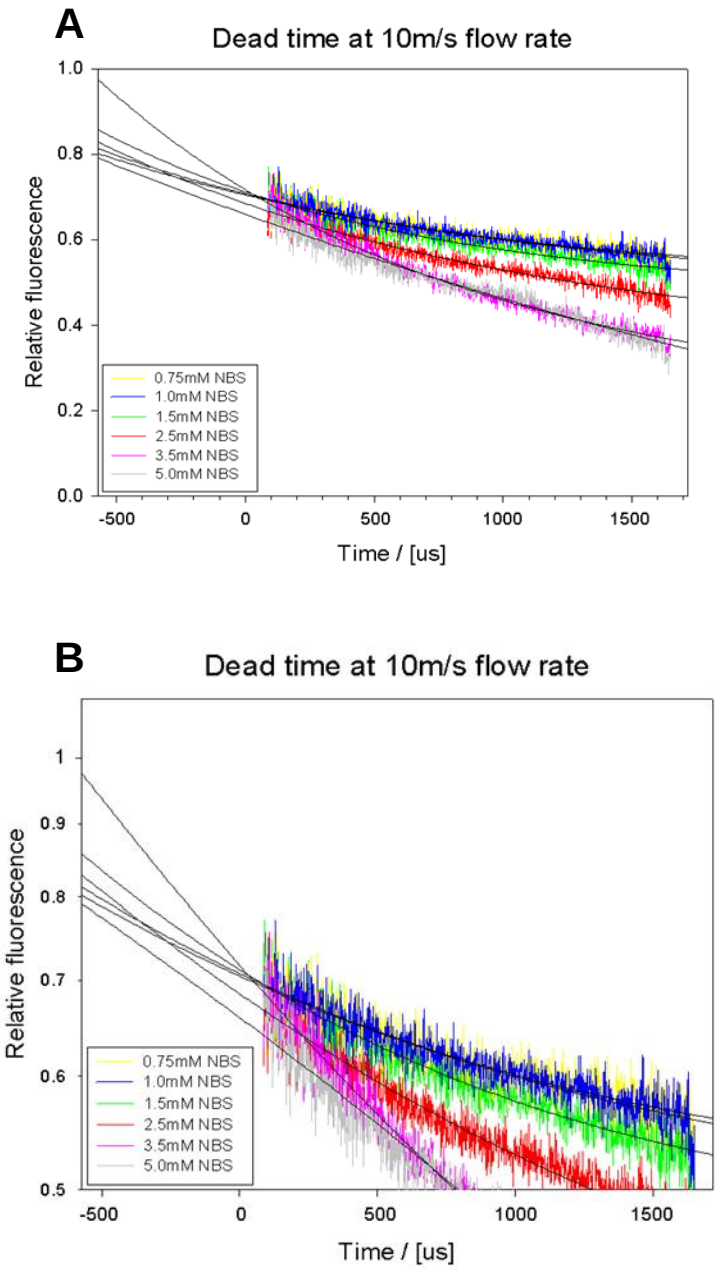

Figure 5.21 Dead time determination of continuous-flow instrument at a linear flow velocity of 10 ms^{-1}.

Fluorescence traces illustrate kinetics of quenching of 20 μM NATA with a range of final concentrations of NBS: 0.75 mM (yellow), 1.0 mM (dark blue), 1.5 mM (green), 2.5 mM (red), 3.5 mM (pink) and 5 mM (grey). Kinetic trace obtained at NBS concentration of 0.5 mM not shown, as concentration of regent was insufficient to induce quenching and thus produce reliable kinetic data.

Single exponential decays fitted to the data are represented by solid black lines. Initial fits were plotted on a linear relative fluorescence scale (panel A) and re-plotted on a semi-logarithmic chart (panel B), for more precise dead time estimation.

Estimated dead time at 4 ms^{-1} linear flow velocity: 270 ± 160μs.

5.4 Summary

5.4.1 Summary of instrument development

Development of continuous-flow mixer detailed in this chapter provided a wealth of new information on the subject of microfluidic mixers.

Three consecutive prototypes of mixers developed in the initial stages of the study proved that microfabrication can be successfully utilized as a method of cheap mass production of durable, identical devices such as simple mixers or mixer components. Since one of the key aspects of any commercially available instrument second only to performance is its price, optimizing mass-production technology was of significant benefit. Moreover, by adapting the entire instrument for the use of cheap and widely available light source such as mercury-xenon lamps while simultaneously keeping an option of introducing more specialised light sources such as deep UV lasers, the range of potential users can be expanded.

Important lessons learned from development, testing and improving the first three prototypes were used during development of a new hybrid T-mixer which proved to be effective and robust design. Shortest dead time of only 130 μs achieved by the mixer puts the design in line with other published continuous-flow mixers (Shastry *et al.*, 1998, Pinheiro *et al.*, 2001).

Moreover, this study was the very first project which attempted to combine the design and fabrication of continuous-flow mixer with flow dynamics simulations in order to gain thorough understanding of physical the processes within the mixer and maximise efficiency of the design. As expected, flow dynamics simulations allowed for accurate predictions of the fluid behaviour within the mixer and thus not only optimise the design, but also specify optimum operation parameters such as flow velocity

Further developments in the design of continuous-flow mixer coupled with detailed knowledge of flow mechanics gained through simulations should yield even more reliable and effective mixers.

5.4.2 Future developments

While both robustness and efficiency of the mixer created in this study were proven experimentally, there is still a great potential for improvement.

Flow dynamics simulations conducted in the design phase suggested that mixing efficiency of the mixer can be further refined by the introduction of obstacles in mixing chamber. Physical obstacles such as pillars or narrowings can greatly increase turbulence in the flow of reagents and thus enhance mixing.

Further testing of the mixer with reactants more relevant to biochemical studies should be carried out, such as GdnHCl or urea solutions commonly used in protein folding experiments.

Since such solutions are much more viscous than NATA and NBS solutions in distilled water, their behaviour within the narrow delivery and observation channels of the mixer could be very different. It would be of great importance to test whether any detrimental sheer forces exist within the mixer which may physically damage a protein sample. While flow dynamics simulations could provide theoretical data on the issue, only live tests such as Cytochrome C refolding can provide definite answer to those questions.

Upon completion of further tests detailed above, investigation of the fast folding kinetics of prion proteins using continuous-flow instrument could be carried out. With a recent study (Apetri *et al.*, 2006) proving that continuous-flow can reveal important details of protein folding taking place on the timescale not accessible to stopped-flow instruments, using a rapid mixing technique would provide an excellent comparison to pressure-jump or temperature-jump studies of prion folding kinetics.

Chapter 6: General Discussion

Prion diseases, also known as transmissible spongiform encephalopathies (TSEs), are a group of fatal neurodegenerative disorders affecting numerous species, including humans. Despite their species-dependent differences, all TSEs are inadvertently associated with a conversion of native, cellular form of the prion protein (PrP^{C}) to an altered, pathological conformation known as scrapie isoform (PrP^{Sc}). The key, species-independent aspect of prion diseases is the self-perpetuating nature of PrP aggregates and their deposition in brain tissues in a form of amyloid fibrils. The template-assisted mechanism of PrP^{C} to PrP^{Sc} transformation involves refolding of PrP from its cellular form to an altered disease-associated conformation, although the details of the conversion process itself are yet to be fully understood.
In this thesis two properties of PrP which may influence the prion disease mechanism have been investigated: the kinetics of folding mechanism of PrP and the propensity to form amyloid fibrils in different conditions.

6.1 Kinetic and equilibrium folding of PrP

An interesting phenomenon associated with TSE's transmission is the apparent inability of prions to induce a disease in certain species, while retaining full infectivity upon transferring to others. The species barrier, as it is known, results in a longer incubation time and lower incidence of disease upon transfer of the infection between individuals from different species (Beringue *et al.*, 2008). Through compelling experimental evidence, it has become apparent that the mechanism of the species barrier is directly controlled by the primary sequence of prion proteins (Moore *et al.*, 2005). As the structure of PrP is highly conserved, it is unlikely that structural differences between PrP from different species are directly responsible; however, the very fact that both primary sequence and structure are conserved does not mean that the folding mechanism itself is conserved (Robinson and Pinheiro, 2009).
Consequently, investigating the folding properties of PrP from different species, as well as their disease-associated mutants should yield to our understanding of both the

misfolding mechanisms associated with the disease's occurrence and the phenomenon of the species barrier and varied disease susceptibility.

Detailed investigations of the folding pathway of PrP^C have been impaired by its rapid folding (Wildegger *et al.*, 1999). Although several successful studies of the folding pathways and intermediates have been conducted at low temperatures (Apetri and Surewicz, 2002; Apetri *et al.*, 2004; Apetri *et al.*, 2006), instruments capable of characterising the folding kinetics at more physiological temperatures have only appeared recently. One such technique which employs a pressure-jump instrument capable of perturbing the equilibrium between folded and unfolded PrP molecules within microseconds has been successfully used in this study (see Chapter 3).

The instrument originally intended to carry out these fast-folding measurements was a continuous-flow instrument developed by Dr David Jenkins in collaboration with the company Hi-Tech Scientific (Jenkins, 2006), however the original instrument was determined to be insufficiently robust to be reliably used in protein folding kinetics measurements. Consequently, a part of this study was aimed at revising the design of original instrument and improving its detection capabilities (see Chapter 5). Necessary improvements and revisions were implemented in collaboration with members of Warwick School of Engineering and the company TgK Scientific (formerly Hi-Tech Scientific). Dead time and mixing efficiency measurements proved that the instrument is both effective and reliable and can be applied to protein folding kinetics measurements.

Pressure-jump measurements of PrP folding kinetics were preceded by equilibrium folding studies of truncated single tryptophan constructs of mouse PrP (MoWT and Q167R) and Syrian hamster prion protein (SHaWT) using tryptophan fluorescence and circular dichroism. Folding studies at pH 7.0 confirmed the two-state nature of MoWT and Q167R transitions and were consistent with the presence of folding intermediate in the folding pathway of Syrian hamster PrP. Interestingly, at pH 4.0 which is known to induce the formation of a β-state intermediate (Khan *et al.*, 2010) all three proteins exhibited extremely broad transition regions stretching between 2 M and 6 M urea concentrations. Such broad transitions strongly suggest that lowering the pH affects the folding of all three prion species so that they no longer clearly follow the two-state mechanism. This in turn might be indicative of the presence of a β-state intermediate in low-pH folding pathways of both mouse and hamster prions.

The propensity to form such an intermediate has been strongly correlated with disease susceptibility exhibited by wide variety of species (Khan *et al.*, 2010). Its presence in both mouse and hamster folding pathways at low pH seems to confirm that structural destabilisation plays a role in the mechanism of disease-associated misfolding.

Pressure-jump measurements of PrP folding kinetics highlighted decreased stability of Q167R in comparison to the wild type mouse construct. This decrease in stability has been previously observed through equilibrium folding studies (Robinson and Pinheiro, 2009). The fact that a disease-resistant mutation has a destabilising effect on the protein is surprising, particularly in case of prion proteins. Since prion propagation relies on cellular PrP being partially unfolded and subsequently recruited by PrP^{Sc}, decreased stability of the native fold should make misfolding more energetically favourable and consequently enhance the disease progression. This suggests, however, that the stability of PrP not always reflects its misfolding propensity, which is supported by the fact that not all disease-inducing mutations destabilize PrP (Horiuchi and Caughey, 1999). This interpretation is further supported by fibrilization studies of mouse PrP and Q167R variant, which indicate that both constructs form fibrils at very similar rate, as indicated by very similar durations of their lag phases (see Chapter 3, Figures 3.17 and 3.18).

Interestingly, the destabilisation of Q167Rwith respect to MoWT is not reflected in folding rates upon extrapolation to 0M denaturant concentration, with k_f of MoWT, Q167R and SHaWT being approximately 12–13000 s^{-1} at 1 bar and 10000 s^{-1} at 320 bar and calculated $\Delta Vf^{\ddagger}$ in water being +14–20 $mL.mol^{-1}$ apparently independent of construct, hinting at common transition state on folding pathway. This observation contrasts strongly with significantly lower k_u values calculated for all constructs (6.16 s^{-1} at 320 bar and 10.97 s^{-1} at 1 bar for MoWT, 7.0 s^{-1} for Q167R and 3.3 s^{-1} at 320 bar to 1.5 s^{-1} at 1 bar for SHaWT) indicating that transition state for folding is different than transition state for unfolding, suggesting an on-pathway folding/unfolding intermediate present in all three proteins.

The existence of such an elusive intermediate is consistent with recent studies (Khan *et al.*, 2010) which identified β-structured monomeric states in folding pathways of prion proteins from 6 different species including both mouse and Syrian hamster. In all cases, the β-state intermediates were very elusive, visible only in moderately destabilizing conditions such as ~5M urea and low pH, which might explain why they were not detected in earlier studies performed at pH 7.0 (Jenkins *et al.*, 2008). Since in both

mouse and hamster PrP the β-state propensity is by far the highest, the mildly destabilizing conditions in which pressure-jump experiments were performed, coupled with equilibrium shift upon pressure application might have allowed to observe those intermediates indirectly through folding/unfolding rates.

Recent molecular dynamics simulations suggest that a compact loop encompassing residues 166–175 is necessary for aggregation and formation of the infectious particles in several species including bank vole, elk, sheep and mouse. Moreover, the stability of the loop region is decreased in a number of point mutations associated with increased disease resistance (Scouras and Daggett, 2012). According to the modelling studies of infectious protofibrils, the stabilised turn is buried between two interacting PrP monomers, allowing for progression of oligomerisation. In the absence of stabilising mutations, the loop region is destabilised, and the resulting flexible, expanded loop disrupts the packing of the adjacent monomers, consequently impairing their incorporation into the protofibril (Scouras and Daggett, 2012). Another potential disease-resistance mechanism is based on the possibility that if the PrP variants carrying loop-destabilising mutations are incorporated into infectious seeds, the altered stability of their conformation prevents further oligomerisation (Ott *et al.*, 2008).

Due to the fact that mouse PrP carrying S170N and N174T mutations is structurally very similar to elk PrP, it provides a valuable model for further investigations into the effects of loop-stabilising mutations. Interestingly, molecular dynamics simulations predicted the formation of elk-like rigid loop in MoPrP at pH 7.0, but not at lower pH, suggesting that the pH itself may affect oligomerisation and fibrilisation properties of some PrP species.

In order to investigate the structural effect of loop-stabilising mutations, a series of equilibrium folding studies of mouse PrP mutants carrying elk point mutations known to stabilise the loop region (S170N, N174T and double mutant S170N/N174T) were carried out, and their results compared with wild-type mouse PrP (see Chapter 4). Upon comparison of transition curves of MoPrP, N174T, S170N and S170N/N174T it becomes apparent that the mutations which stabilize the loop region result in expansion of the transition region of the folding curves constructed at pH 7.0. This in turn suggests that stabilisation of the loop region increases the overall propensity to from an intermediate. Recent studies of truncated constructs of PrP from different species including mouse and Syrian hamster, revealed the increased propensity to form β-state

intermediate which correlates with increased disease susceptibility (Khan *et al.*, 2010). Consequently, it is possible that increased loop stability results in higher propensity to form such intermediate, which in turn leads to increased disease susceptibility. This corresponds to the differences in susceptibilities between mouse and Syrian hamster. Since mouse PrP lacks any stabilising mutations in the loop region, it exhibits lower propensity to form β-state intermediate and lower disease susceptibility compared to Syrian hamster PrP in which Asn residue at position 170 is known to stabilise the loop region.

6.2 Fibrilisation and oligomerisation of PrP

Fibrilisation studies of mouse and Syrian hamster constructs were carried out throughout the course of this study to complement relevant kinetic and equilibrium folding experiments, in an attempt to correlate the kinetic behaviour of PrP with formation of amyloid fibrils.

Following the pressure-jump studies of MoWT, Q167R and SHaWT folding kinetics, fibrilisation experiments were conducted to investigate the effects of structural destabilisation conferred by Q167R on fibrilisation, and whether propensity to form β-state intermediates at low pH exhibited by both mouse and hamster PrP affects the formation of fibrils.

Both MoWT and Q167R formed elongated fibrils characteristic for prion aggregation in solution. While pH did not seem to have a significant effect on the rate of fibril formation and only a mild effect on the duration of the lag phase, inspection of EM images obtained at the end of fibrilisation experiments revealed surprising differences in morphology of fibrils formed at different conditions. Fibrils formed at pH 4.0 were found to be shorter but much more abundant than those formed at pH 7.0 Fibrils of both MoWT and Q167R formed at higher pH were longer but less abundant compared to pH 4.0, indicating that at lower pH, that the total population of PrP molecules which aggregated into fibrils was higher. In case of Syrian hamster, while no fibrillous material was detected at pH 7.0, the distincive short protofibrils were formed at pH 4.0.

These findings are interesting in the light ofprevailing opinion that formation of fibrils and their aggregation is a protective mechanism evolved to avoid high toxicity of

soluble oligomers (Buccianti *et al.*, 2002; Kirkitadze *et al.*, 2002; Caughey *et al.*, 2003). Indeed, soluble oligomers are thought to be the primary cytotoxic species as opposed to fibril formation and deposition on cellular membranes (Chisea *et al.*, 2001; Novitskaya *et al.*, 2005). Consequently, increased fibrilisation propensity of mouse PrP is concurrent with lower susceptibility of mice to prion diseases, compared to Syrian hamster. Since the Q167R mutant of mouse PrP exhibits higher propensity to form fibrils and the length of its lag phase is less affected by change in pH compared to wild-type construct, the structural destabilisation conferred by the point mutation seems to play a key role in disease-resistance mechanism.

Fibrilisation studies of mouse PrP constructs carrying elk point mutations revealed a surprising link between the stability of the loop region and formation of fibrils. Fibrilisation propensity was found to be proportional to the stability of the loop region, with the double mutant S170N/N174T which carried two loop stabilising mutations and therefore contained rigid, elk-like loop region showing by far highest propensity to form fibrils. The S170N mutation which conferred partial stability of the loop region exhibited second-highest fibrilisation propensity, and both MoPrP and N174T mutant in which the loop stability does not differ significantly from the wild type mouse PrP did not form fibrils unless seeded with S170N/N174T material. These findings were consistent with molecular dynamics simulations, which suggest that a compact loop between helix α2 and β-sheet β2 is necessary for aggregation and formation of the infectious protofibrillar species in several different species, particularly elk and sheep. Nearly all of the point mutations which confer increased disease resistance perturb the structure of the loop, preventing the initial formation of infectious oligomers (Scouras and Daggett, 2012).

Thus, it is possible that while the destabilisation of loop region affects oligomerisation, consequently preventing fibril formation from "free" PrP molecules, its effect may be limited if the pre-formed protofibrils are already present in the reaction mixture.

Loop stability would affect spontaneous generation of prions in the organism, as well as disease transmission via small oligomers. While destabilised loop region would be likely to prevent spontaneous oligomerisation and protofibril formation, it would not affect pre-formed protofibrils originating from external source.

Consequently, the disease-resistant, loop-destabilizing mutations would have significant effect on fibril formation in unseeded fibrilisation, but their impact on fibril formation in presence of seeds would be much more limited. The difference would be due to the

fact that already pre-formed seeds may recruit PrP^C from environment and incorporate it into growing fibril without the need for oligomers to form "from scratch". Such model correlates well with the experimental data obtained in this study.

These findings seem to be counterintuitive, if one considers the prevailing opinion that formation of fibrils and their aggregation as well as subsequent formation of plaques is a protective mechanism evolved to avoid high toxicity of soluble oligomers (Buccianti *et al.*, 2002; Kirkitadze *et al.*, 2002; Caughey *et al.*, 2003). Loop destabilisation, being a potential protective mechanism, should not affect fibrilisation and decrease its potential to trap neurotoxic particles. It is these soluble oligomers, however, that are thought to be the primary cytotoxic mechanism as opposed to fibril formation and deposition on cellular membranes (Chisea *et al.*, 2001; Novitskaya *et al.*, 2005). Consequently, while the protective mechanism based around loop-destabilizing mutations could potentially lead to increased susceptibility to the disease due to the fact that the neurotoxic species are not trapped in fibrils, it is the oligomer formation that is primarily affected.

Thus, proposed source of disease resistance conferred by loop-destabilising mutations is the decreased formation of neurotoxic particles in the organism as well as diminished ability of infectious oligomers from both inside and outside to propagate oligomerisation of PrP.

6.3 Summary

This study represents a substantial step in the study of mechanisms of folding of PrP and their connection with disease-related properties such as formation of amyloid fibrils.

The use of pressure-jump instrument allowed to confirm experimental observations made previously by the members authors research group (Robinson and Pinheiro, 2009). The destabilising effect of Q167R mutation previously observed via equilibrium folding studies was confirmed through direct kinetic observations.

Subsequent fibrilisation experiments performed by the author suggested a possible link between the stability of mouse prion protein and its propensity to form fibrils at neutral and mildly destabilising conditions, elucidating a potential mechanism of increased disease resistance conferred by Q167R mutation.

Equilibrium folding studies of full length mouse constructs carrying point mutations characteristic for elk which confer increased stability of the loop region encompassing residues 166-175 characteristic for cervids revealed a surprising correlation between the degree of stability of the loop and propensity to form fibrils. These finding are consistent with the recent molecular dynamics simulations, which suggest that a compact loop encompassing residues 166-175 is necessary for aggregation and formation of the infectious particles in elk, sheep and mouse prion strains.
Due to the fact that destabilisation of the region resulting in flexible, expanded loop disrupts the packing of the adjacent monomers of PrP, consequently impairing oligomerisation and formation of protofibrils (Scouras and Daggett, 2012), a disease resistance mechanism based on decreased formation of neurotoxic particles in the organism as well as diminished ability of infectious oligomers from both inside and outside to propagate oligomerisation of PrP has been proposed.

References

Adams, D.H. and Caspary, E.A. (1968). The incorporation of nucleic acid and polysaccharide precursors into a post-ribosomal fraction of scrapie-affected mouse brain, *Biochem. J.*, **108**, 38P.

Adams, H., Beck, E. and Shenkin, A. M. (1974). Creutzfeldt-Jakob disease: further similarities with kuru. *J. Neurol. Neurosurg. Psychiatry*, **37**, 195-200.

Adler, V., Zeiler, B., Kryukov, V., Kascsak, R., Rubenstein, R. and Grossman, A. (2003). Small, highly structured RNAs participate in the conversion of human recombinant PrP^{Sen} to PrP^{Res} *in vitro*. *J. Mol. Biol.*, **332,** 47-57.

Aguzzi, A. and Polymenidou M. (2004). Mammalian prion biology: One century of evolving concepts. *Cell.*, **116**(2), 313-327.

Ahmad, A., Uversky, V. N., Hong, D. and Fink, A. L. (2005). Early events in the fibrillation of monomeric insulin. *J. Biol. Chem.*, **280**, 42669-42675.

Aisenbrey, C., Borowik, T., Bystrom, R., Bokvist, M., Lindstrom, F., Misiak, H., Sani, M. A. and Grobner, G. (2008). How is protein aggregation in amyloidogenic diseases modulated by biological membranes? *Eur. Biophys. J.*, **37**, 247-255.

Akiyama, S., Takahashi, S., Ishimori, K. and Morishima, I. (2000). Stepwise formation of alpha-helices during cytochrome c folding. *Nat. Struct. Biol.*, **7**, 514-520.

Alanen, H. I., Williamson, R. A., Howard, M. J., Lappi, A.-K., Jantti, H. P., Rautio, S. M., Kellokumpu, S. and Ruddock, L. W. (2003). Functional characterization of ERp18, a new endoplasmic reticulum-located thioredoxin superfamily member. *J. Biol. Chem.*, **278**, 28912-28920.

Alper, T., Haig, D.A. and Clarke, M.C. (1978). The scrapie agent: evidence against its dependence for replication on intrinsic nucleic acid. *J. Gen. Virol.*, **41**, 503‑516

Alper, T., Haig, D. A. and Clarke, M. C. (1966). The exceptionally small size of the scrapie agent. *Biochem. Biophys. Res. Commun.*, **22**, 278-284.

Alper, T., Cramp, W.A., Haig, D.A. and Clarke, M.C. (1967). Does the agent of scrapie replicate without nucleic acid? *Nature*, **214**, 764‑766.

Anfinsen, C. B. (1973). Principles that govern the folding of protein chains. *Science*, **181**, 223-230.

Angers, R. C., Browning, S. R., Seward, T. S., Sigurdson, C. J., Miller, M. W., Hoover, E. A. and Telling, G. C. (2006). Prions in skeletal muscles of deer with chronic wasting disease. *Science*, **311**, 1117.

Apetri, A. C., Maki, K., Roder, H. and Surewicz, W. K. (2006). Early intermediate in human prion protein folding as evidenced by ultrarapid mixing experiments. *J. Am. Chem. Soc.*, **128**, 11673-11678.

Apetri, A. C., Surewicz, K. and Surewicz, W. K. (2004). The effect of disease-associated mutations on the folding pathway of human prion protein. *J. Biol. Chem.*, **279**, 18008-18014.

Apetri, A. C. and Surewicz, W. K. (2002). Kinetic intermediate in the folding of human prion protein. *J. Biol. Chem.*, **277**, 44589-44592.

Atarashi, R., Moore, R. A., Sim, V. L., Hughson, A. G., Dorward, D. W., Onwubiko, H. A., Priola, S. A. and Caughey, B. (2007). Ultrasensitive detection of scrapie prion protein using seeded conversion of recombinant prion protein. *Nat. Methods*, **4**, 645-650.

Atkins, P. W. (1999). Chemical equilibrium. In *Physical Chemistry*, 6th edn, 215- 242. Oxford: Oxford University Press.

Ball, H. L., King, D. S., Cohen, F. E., Prusiner, S. B. and Baldwin, M. A. (2001). Engineering the prion protein using chemical synthesis. *J. Pep. Res.*, **58**, 357-374.

Barria, M.A., Telling, G.C., Gambetti, P., Mastrianni, J.M. and Soto, C. (2011). Generation of a new form of human PrPSc *in vitro* by interspecies transmission from cervid prions. *J. Biol. Chem*., **286**(9), 7490–7495

Baskakov, I. V. (2004). Autocatalytic conversion of recombinant prion proteins displays a species barrier. *J. Biol. Chem.*, **279**, 7671-7677.

Baskakov, I. V., Legname, G., Baldwin, M. A., Prusiner, S. B. and Cohen, F. E. (2002). Pathway complexity of prion protein assembly into amyloid. *J. Biol. Chem.*, **277**, 21140-21148.

Baskakov, I. V., Legname, G., Prusiner, S. B. and Cohen, F. E. (2001). Folding of prion protein to its native α-helical conformation is under kinetic control. *J. Biol. Chem.*, **276**, 19687-19690.

Basler, K., Oesch, B., Scott, M., Westaway, D., Walchli, M., Groth, D. F., McKinley, M. P., Prusiner, S. B. and Weissmann, C. (1986). Scrapie and cellular PrP isoforms are encoded by the same chromosomal gene. *Cell*, **46**, 417-428.

Bass, R., Ruddock, L. W., Klappa, P. and Freedman, R. B. (2004). A major fraction of endoplasmic reticulum-located glutathione is present as mixed disulfides with protein. *J. Biol. Chem.*, **279**, 5257-5262.

Beck, K. E., Kay, J. G. and Braun, J. E. (2006). Rdj2, a J protein family member, interacts with cellular prion PrPC. *Biochem. Biophys. Res. Commun.*, **346**, 866-871.

Belay, E. D., Gambetti, P., Schonberger, L. B., Parchi, P., Lyon, D. R., Capellari, S., McQuiston, J. H., Bradley, K., Dowdle, G., Crutcher, J. M., and Nichols, C. R. (2001). Creutzfeldt-Jakob disease in unusually young patients who consumed venison. *Arch. Neurol.* **58**, 1673–1678

Belay, E. D., Maddox, R. A., Williams, E. S., Miller, M. W., Gambetti, P., and Schonberger, L. B. (2004). Chronic wasting disease and potential transmission to humans. *Emerg. Infect. Dis.*, **10,** 977–984

Belt, P. B., Muileman, I. H., Schreuder, B. E., Bos-de Ruijter, J., Gielkens, A. L. and Smits, M. A. (1995). Identification of five allelic variants of the sheep PrP gene and their association with natural scrapie. *J. Gen. Virol.* **76 (Part 3),** 509-517.

Ben-Zaken, O., Tzaban, S., Tal, Y., Horonchik, L., Esko, J. D., Vlodavsky, I. and Taraboulos, A. (2003). Cellular heparan sulfate participates in the metabolism of prions. *J. Biol. Chem.* **278,** 40041-40049.

Beringue, V., Vilotte, J. L. and Laude, H. (2008). Prion agent diversity and species barrier. *Vet. Res.* **39,** 47

Biasini, E., Turnbaugh, J.A., Unterberger, U. and Harris D.A. (2012). Prion protein at the crossroads of physiology and disease. *Trend. Neuros.,* **35**, 92-103

Bieri, O. and Kiefhaber, T. (1999). Elementary steps in protein folding. *Biol. Chem.,* **380**, 923-929.

Billeter, M., Riek, R., Wider, G., Hornemann, S., Glockshuber, R., and Wuthrich, K. (1997). Prion protein NMR structure and species barrier for prion diseases. *Proc. Natl. Acad. Sci. USA,* **94,** 7281–7285

Bishop, M. T., Hart, P., Aitchison, L., Baybutt, H. N., Plinston, C., Thomson, V., Tuzi, N. L., Head, M. W., Ironside, J. W., Will, R. G. and Manson, J. C. (2006). Predicting susceptibility and incubation time of human-to-human transmission of vCJD. *Lancet Neurol.*, **5**, 393-398.

Bocharova, O. V., Breydo, L., Parfenov, A. S., Salnikov, V. V. and Baskakov, I. V. (2005). *In vitro* conversion of full-length mammalian prion protein produces amyloid form with physical properties of PrP^{Sc}. *J. Mol. Biol.*, **346**, 645-659.

Bolton, D. C., McKinley, M. P. and Prusiner, S. B. (1982). Identification of a protein that purifies with the scrapie prion. *Science,* **218**, 1309-1311.

Boon, J. M. and Smith, B. D. (2002). Chemical control of phospholipid distribution across bilayer membranes. *Med. Res. Rev.* **22,** 251-281.

Booth, D. R., Sunde, M., Bellotti, V., Robinson, C. V., Hutchinson, W. L., Fraser, P. E., Hawkins, P. N., Dobson, C. M., Radford, S. E., Blake, C. C. F. and Pepys, M. B. (1997). Instability, unfolding and aggregation of human lysozyme variants underlying amyloid fibrillogenesis. *Nature,* **385**, 787-793.

Borchelt, D. R., Scott, M., Taraboulos, A., Stahl, N. and Prusiner, S. B. (1990). Scrapie and cellular prion proteins differ in their kinetics of synthesis and topology in cultured cells. *J. Cell Biol.,* **110**, 743-752.

Borchelt, D., Taraboulos, A. and Prusiner, S. (1992). Evidence for synthesis of scrapie prion proteins in the endocytic pathway. *J. Biol. Chem.,* **267**, 16188-16199.

Bosques, C. J. and Imperiali, B. (2003). The interplay of glycosylation and disulfide formation influences fibrillization in a prion protein fragment. *Proc. Natl. Acad. Sci. USA,* **100**, 7593-7598.

Bosque, P. J. (2002). Bovine spongiform encephalopathy, chronic wasting disease, scrapie, and the threat to humans from prion disease epizootics. *Curr. Neurol. Neurosci. Rep.* **2**, 488–495

Brachmann, A., Baxa, U. and Wickner, R. B. (2005). Prion generation *in vitro*: amyloid of Ure2p is infectious. *EMBO J.*, **24**, 3082-3092.

Branden, C. and Tooze, J. (1999). Folding and flexibility. In *Introduction to Protein Structure*, 2nd edn, 89-126. New York: Garland Publishing, Inc.

Brandner, S., Isenmann, S., Raeber, A., Fischer, M., Sailer, A., Kobayashi, Y., Marino, S., Weissmann, C. and Aguzzi, A. (1996). Normal host prion protein necessary for scrapie-induced neurotoxicity. *Nature*, **379**, 339-343.

Breydo, L., Bocharova, O. V., Makarava, N., Salnikov, V. V., Anderson, M. and Baskakov, I. V. (2005). Methionine oxidation interferes with conversion of the prion protein into the fibrillar proteinase K-resistant conformation. *Biochemistry* **44,** 15534-15543.

Breydo, L., Makarava, N. and Baskakov, I.V. (2008) Methods for conversion of prion protein into amyloid fibrils. *Methods. Mol. Biol.* **459**,105-15.

Brockwell, D. J. and Radford, S. E. (2007). Intermediates: ubiquitous species on folding energy landscapes? *Curr. Opin. Struct. Biol.*, **17**, 30-37.

Brockwell, D. J., Smith, A. S. and Radford, S. E. (2000). Protein folding mechanisms: new methods and emerging ideas. *Curr. Opin. Struct. Biol.,* **10**, 16-25.

Brown, P. (2009). An historical perspective on efforts to treat transmissible spongiform encephalopathy. *CNS Neurol. Disord. Drug. Targets.*, **8**, 316-22.

Brown, D. R. (2002). Molecular advances in understanding inherited prion diseases. *Mol. Neurobiol.*, **25**, 287-302.

Brown, D. R., Qin, K., Herms, J. W., Madlung, A., Manson, J., Strome, R., Fraser, P. E., Kruck, T., von Bohlen, A., Schulz-Schaeffer, W., Giese, A., Westaway, D. and Kretzschmar, H. (1997). The cellular prion protein binds copper *in vivo*. *Nature,* **390**, 684-687.

Brown, D. R., Schulz-Schaeffer, W. J., Schmidt, B. and Kretzschmar, H. A. (1997). Prion protein-deficient cells show altered response to oxidative stress due to decreased SOD-1 activity. *Exp. Neurol.*, **146**, 104-112.

Browning, S.R., Mason, G.L., Seward, T., Green, M., Eliason, G.A., Mathiason, C., Miller, M.W., Williams, E.S., Hoover, E. and Telling, G.C. (2004). Transmission of prions from mule deer and elk with chronic wasting disease to transgenic mice expressing cervid PrP. *J. Virol.*, **78**, 13345–133450.

Bruce, M. E. (1993). Scrapie strain variation and mutation. *Br. Med. Bull.*, **49**, 822-838.

Bruce, M. E., McConnell, I., Fraser, H. and Dickinson, A. G. (1991). The disease characteristics of different strains of scrapie in Sinc congenic mouse lines: implications for the nature of the agent and host control of pathogenesis. *J. Gen. Virol.,* **72 (Part 3)**, 595-603.

Bucciantini, M., Giannoni, E., Chiti, F., Baroni, F., Formigli, L., Zurdo, J., Taddei, N., Ramponi, G., Dobson, C. M. and Stefani, M. (2002). Inherent toxicity of aggregates implies a common mechanism for protein misfolding diseases. *Nature,* **416**, 507-511.

Bucciantini, M., Calloni, G., Chiti, F., Formigli, L., Nosi, D., Dobson, C. M., and Stefani, M. (2004). Prefibrillar amyloid protein aggregates share common features of cytotoxicity. *J. Biol. Chem.* 279, 31374–31382

Büeler, H., Aguzzi, A., Sailer, A., Greiner, R.-A., Autenried, P., Aguet, M. and Weissmann, C. (1993). Mice devoid of PrP are resistant to scrapie. *Cell,* **73**, 1339-1347.

Büeler, H., Fischer, M., Lang, Y., Bluethmann, H., Lipp, H.-P., DeArmond, S. J., Prusiner, S. B., Aguet, M. and Weissmann, C. (1992). Normal development and behaviour of mice lacking the neuronal cell-surface PrP protein. *Nature,* **356**, 577-582.

Bujdoso, R., Burke, D. F. and Thackray, A. M. (2005). Structural differences between allelic variants of the ovine prion protein revealed by molecular dynamics simulations. *Proteins* **61,** 840-849.

Bushmarina, N. A., Kuznetsova, I. M., Biktashev, A. G., Turoverov, K. K. and Uversky, V. N. (2001). Partially folded conformations in the folding pathway of bovine carbonic anhydrase II: a fluorescence spectroscopic analysis. *Chembiochem,* **2**, 813-821.

Cai, H., Wang, C. C. and Tsou, C. L. (1994). Chaperone-like activity of protein disulfide isomerase in the refolding of a protein with no disulfide bonds. *J. Biol. Chem.,* **269**, 24550-24552.

Calzolai, L., Lysek, D. A., Guntert, P., von Schroetter, C., Riek, R., Zahn, R. and Wuthrich, K. (2000). NMR structures of three single-residue variants of the human prion protein. *Proc. Natl. Acad. Sci. USA,* **97,** 8340–8345.

Calzolai, L., Lysek, D. A., Perez, D. R., Guntert, P. and Wuthrich, K. (2005). Prion protein NMR structures of chickens, turtles, and frogs. *Proc. Natl. Acad. Sci. USA,* **102**, 651-655.

Calzolai, L. and Zahn, R. (2003). Influence of pH on NMR structure and stability of the human prion protein globular domain. *J. Biol. Chem.,* **278**, 35592-35596.

Campana, V., Sarnataro, D. and Zurzolo, C. (2005). The highways and byways of prion protein trafficking. *Trends Cell. Biol.,* **15**, 102-111.

Capellari, S., Zaidi, S. I., Urig, C. B., Perry, G., Smith, M. A. and Petersen, R. B. (1999). Prion protein glycosylation is sensitive to redox change. *J. Biol. Chem.,* **274**, 34846-34850.

Caplazi, P. A., O'Rourke, K. I. and Baszler, T. V. (2004). Resistance to scrapie in PrP ARR/ARQ heterozygous sheep is not caused by preferential allelic use. *J. Clin. Pathol.* **57,** 647-650.

Castilla, J., Gonzalez-Romero, D., Saa´, P., Morales, R., De Castro, J., and Soto, C. (2008). Crossing the species barrier by PrP(Sc) replication *in vitro* generates unique infectious prions. *Cell* **134**, 757–768

Castilla, J., Morales, R., Saa´, P., Barria, M., Gambetti, P., and Soto, C. (2008). Cell-free propagation of prion strains. *EMBO J.*, **27**, 2557–2566

Castilla, J., Saá, P., Hetz, C. and Soto, C. (2005). *In vitro* generation of infectious scrapie prions. *Cell*, **121**, 195-206.

Castilla, J., Saa, P. and Soto, C. (2005). Detection of prions in blood. *Nat. Med.*, **11**, 982-985.

Caughey, B. (2000). Transmissible spongiform encephalopathies, amyloidoses and yeast prions: Common threads? *Nat. Med.* **6**, (7), 751-754.

Caughey, B. (2001). Interactions between prion protein isoforms: the kiss of death? *Trends Biochem. Sci.* **26**(4), 235-242.

Caughey, B. and Chesebro B. (2001). Transmissible spongiform encephalopathies and prion protein interconversions. *Adv. Vir. Res.,* **56**,277-311.

Caughey, B., and Lansbury, P. T. (2003). Protofibrils, pores, fibrils, and neurodegeneration: separating the responsible protein aggregates from the innocent bystanders. *Annu. Rev. Neurosci.* **26**, 267–298

Caughey, B. and Race, R. E. (1994). Scrapie-associated PrP accumulation and its inhibition: revisiting the amyloid-glycosaminoglycan connection. *Ann. N. Y. Acad. Sci.* **724,** 290-295.

Caughey, B., Race, R. E., Ernst, D., Buchmeier, M. J. and Chesebro, B. (1989). Prion protein biosynthesis in scrapie-infected and uninfected neuroblastoma cells. *J Virol*, **63**, 175-181.

Caughey, B. and Raymond, G. J. (1991). The scrapie-associated form of PrP is made from a cell surface precursor that is both protease- and phospholipasesensitive. *J. Biol. Chem.,* **266**, 18217-18223.

Caughey, B., Raymond, G. J., Ernst, D. and Race, R. E. (1991). N-terminal truncation of the scrapie-associated form of PrP by lysosomal protease(s): Implications regarding the site of conversion of PrP to the protease-resistant state. *J. Virol.*, **65**, 6597-6603.

Caughey, B. W., Dong, A., Bhat, K. S., Ernst, D., Hayes, S. F. and Caughey, W. S. (1991). Secondary structure analysis of the scrapie-associated protein PrP 27-30 in water by infrared spectroscopy. *Biochemistry*, **30**, 7672-7680.

Chakrabarti, O., Ashok, A. and Hegde, R. S. (2009). Prion protein biosynthesis and its emerging role in neurodegeneration. *Trends Biochem. Sci.*

Chan, H. S., Bromberg, S. and Dill, K. A. (1995). Models of cooperativity in protein folding. *Phil. Trans. Roy. Soc. London B.*, **348**, 61-70.

Chandler, R. L. (1961). Encephalopathy in mice produced by inoculation with scrapie brain material. *Lancet*, **1**, 1378-1379.

Chang, C. N., Key, M., Bochner, B., Heyneker, H. and Gray, G. (1987). Highlevel secretion of human growth hormone by *Escherichia coli*. *Gene,* **55**, 189-196.

Chen, Y. and Barkley, M. D. (1998). Toward understanding tryptophan fluorescence in proteins. *Biochemistry*, **37**, 9976-9982.

Chesebro, B., Race, R., Wehrly, K., Nishio, J., Bloom, M., Lechner, D., Bergstrom, S., Robbins, K., Mayer, L., Keith, J. M., Garon, C. and Haase, A. (1985). Identification of scrapie prion protein-specific mRNA in scrapie-infected and uninfected brain. *Nature,* **315**, 331-333.

Chien, P., Weissman, J. S. and DePace, A. H. (2004). Emerging principles of conformation based prion inheritance. *Annu. Rev. Biochem.,* **73**, 617-656.

Chiesa, R., and Harris, D. A. (2001). Prion diseases: what is the neurotoxic molecule? *Neurobiol. Dis.* **8**, 743–763

Chiti, F. and Dobson, C. M. (2009). Amyloid formation by globular proteins under native conditions. *Nat. Chem. Biol.* **5,** 15-22.

Chou, P. Y. and Fasman, G. D. (1974). Prediction of protein conformation. *Biochemistry,* **13**, 222-245.

Chou, S. M. and Martin, J. D. (1971). Kuru-plaques in a case of Creutzfeldt-Jakob disease. *Acta Neuropathol.*, **17**, 150-155.

Christen, B., Hornemann, S., Damberger, F. F. and Wuthrich, K. (2009). Prion protein NMR structure from tammar wallaby (Macropus eugenii) shows that the b2-a2 loop is modulated by long-range sequence effects. *J. Mol. Biol.*, **389**, 833-845.

Christen, B., Perez, D. R., Hornemann, S. and Wuthrich, K. (2008). NMR structure of the bank vole prion protein at 20 degrees C contains a structured loop of residues 165-171. *J. Mol. Biol.*, **383**, 306-312.

Clarke, A. R. and Waltho, J. P. (1997). Protein folding and intermediates. *Curr. Opin. Biotechnol.,* **8**, 400-410.

Clarke, J. and Fersht, A. R. (1993). Engineered disulfide bonds as probes of the folding pathway of barnase - Increasing the stability of proteins against the rate of denaturation. *Biochemistry,* **32**, 4322-4329.

Clarke, J., Hounslow, A. M., Bond, C. J., Fersht, A. R. and Daggett, V. (2000). The effects of disulfide bonds on the denatured state of barnase. *Prot. Sci.,* **9**, 2394-2404.

Clewley, J. P., Kelly, C. M., Andrews, N., Vogliqi, K., Mallinson, G., Kaisar, M., Hilton, D. A., Ironside, J. W., Edwards, P., McCardle, L. M., Ritchie, D. L., Dabaghian, R., Ambrose, H. E. and Gill, O. N. (2009). Prevalence of disease related prion protein in anonymous tonsil specimens in Britain: cross sectional opportunistic survey. *Br. Med. J. (Clin. Res. Ed).* **338**, b1442.

Clouscard, C., Beaudry, P., Elsen, J. M., Milan, D., Dussaucy, M., Bounneau, C., Schelcher, F., Chatelain, J., Launay, J. M. and Laplanche, J. L. (1995). Different allelic effects of the codons 136 and 171 of the prion protein gene in sheep with natural scrapie. *J. Gen. Virol.* **76 (Part 8),** 2097-2101.

Cohen, F. E., Pan, K. M., Huang, Z., Baldwin, M., Fletterick, R. J. and Prusiner, S. B. (1994). Structural clues to prion replication. *Science*, **264**, 530-531.

Collinge, J. and Clarke A.R. (2007). A general model of prion strains and their pathogenicity. *Science,* **318**, 930–936.

Collinge, J. (2001). Prion diseases of humans and animals: Their causes and molecular basis. *Annu. Rev. Neurosci.,* **24**, 519-550.

Collinge, J. (2005). Molecular neurology of prion disease. *J. Neurol. Neurosurg. Psychiatry*, **76**, 906-919.

Collinge, J., Palmer, M. S., Sidle, K. C., Gowland, I., Medori, R., Ironside, J. and Lantos, P. (1995). Transmission of fatal familial insomnia to laboratory animals. *Lancet*, **346**, 569-570.

Collinge, J., Whittington, M. A., Sidle, K. C. L., Smith, C. J., Palmer, M. S., Clarke, A. R. and Jefferys, J. G. R. (1994). Prion protein is necessary for normal synaptic function. *Nature*, **370**, 295-297.

Collins, S. J., Lawson, V. A. and Masters, C. L. (2004). Transmissible spongiform encephalopathies. *The Lancet*, **363**, 51-61.

Cordeiro, Y., Kraineva, J., Gomes, M., Lopes, M., Martins, V. R., Lima, L., Foguel, D., Winter, R. and Silva, J. L. (2005a). The amino-terminal PrP domain is crucial to modulate prion misfolding and aggregation. *Biophys. J.,* **89**, 2667-2676.

Cordeiro, Y., Kraineva, J., Winter, R. and Silva, J. L. (2005b). Volume and energy folding landscape of prion protein revealed by pressure. *Braz. J. Med. Bio. Res.,* **38**, 1195-1201.

Couzin, J. (2004). An end to the prion debate? Don't count on it. *Science*, **305**, 589.

Couzin, J. (2004). Biomedicine. An end to the prion debate? Don't count on it. *Science*, **305**, 589.

Cozzetto, D., Di Matteo, A. and Tramontano, A. (2005). Ten years of predictions...and counting. *FEBS J.,* **272**, 881-882.

Creighton, T. E. (1990). Protein folding. *Biochem. J.*, **270**, 1-16.

Critchley, P., Kazlauskaite, J., Eason, R. and Pinheiro, T. J. (2004). Binding of prion proteins to lipid membranes. *Biochem. Biophys. Res. Commun.* **313,** 559-567.

Crozet, C., Lin, Y. L., Mettling, C., Mourton-Gilles, C., Corbeau, P., Lehmann, S. and Perrier, V. (2004). Inhibition of PrP^{Sc} formation by lentiviral gene transfer of PrP containing dominant negative mutations. *J. Cell Sci.* **117,** 5591-5597.

Cuille, J. and Chelle, P.L. (1938). La tremblante du mouton est-elle determinee par un virus filtrable? *Comptes rendus hebdomadaires des seances de l' Academie des Sciences,* **206**, 1687‑1688.

Daggett, V. (2006). Protein folding - simulation. *Chem. Rev.,* **106**, 1898-1916.

Daggett, V. and Fersht, A. R. (2003). Opinion: The present view of the mechanism of protein folding. *Nat. Rev. Mol. Cell Biol.,* **4**, 497-502.

Daggett, V. and Fersht, A. R. (2003). Is there a unifying mechanism for protein folding? *Trends Biochem. Sci.,* **28**, 18-25.

Davis, J. S. and Gutfreund, H. (1976). The scope of moderate pressure changes for kinetic and equilibrium studies of biochemical systems. *FEBS Lett.,* **72**, 199-207.

Day, A. (1996). The Source of Stability in Proteins. http://www.cryst.bbk.ac.uk/PPS2/projects/day/TDayDiss/UnfoldedState.html

Dealler, S. F. and Lacey, R. W. (1990). Transmissible spongiform encephalopathies: The threat of BSE to man. *Food Microbiol.,* **7**, 253-279.

DeArmond, S. J., McKinley, M. P., Barry, R. A., Braunfeld, M. B., McColloch, J. R. and Prusiner, S. B. (1985). Identification of prion amyloid filaments in scrapie-infected brain. *Cell*, **41**, 221-235.

Deleault, N. R., Harris, B. T., Rees, J. R. and Supattapone, S. (2007). Formation of native prions from minimal components *in vitro*. *Proc. Natl. Acad. Sci. U. S. A.* **104,** 9741-9746.

Deleault, N. R., Lucassen, R. W. and Supattapone, S. (2003). RNA molecules stimulate prion protein conversion. *Nature* **425,** 717-720.

Demuro, A., Mina, E., Kayed, R., Milton, S. C., Parker, I., and Glabe, C. G. (2005) Calcium dysregulation and membrane disruption as a ubiquitous neurotoxic mechanism of soluble amyloid oligomers. *J. Biol. Chem.* **280**, 17294–17300

Desai, G., Panick, G., Zein, M., Winter, R. and Royer, C. A. (1999). Pressurejump studies of the folding/unfolding of trp repressor. *J. Mol. Biol.,* **288**, 461-475.

Diener, T.O. (1972). Is the scrapie agent a viroid? *Nature New Biology,* **235**, 218‑219.

Diener, T. O., McKinley, M. P. and Prusiner, S. B. (1982). Viroids and prions. *Proc. Natl. Acad. Sci. USA*, **79**, 5220-5224.

DiFiglia, M., Sapp, E., Chase, K. O., Davies, S. W., Bates, G. P., Vonsattel, J. P. and Aronin, N. (1997). Aggregation of huntingtin in neuronal intranuclear inclusions and dystrophic neurites in brain. *Science*, **277**, 1990-1993.

Dill, K. A. and Chan, H. S. (1997). From Levinthal to pathways to funnels. *Nat. Struct. Biol.*, **4**, 10-19.

Dill, K. A. and Shortle, D. (1991). Denatured states of proteins. *Annu. Rev. Biochem.*, **60**, 795-825.

Dima, R. I. and Thirumalai, D. (2002). Exploring the propensities of helices in PrPC to form β -sheet using NMR structures and sequence alignments. *Biophys. J.*, **83**, 1268-1280.

Dinner, A. R., Šali, A., Smith, L. J., Dobson, C. M. and Karplus, M. (2000). Understanding protein folding via free-energy surfaces from theory and experiment. *Trends Biochem. Sci.*, **25**, 331-339.

Dobson, C. M. (2003). Protein folding and misfolding. *Nature*, **426**, 884-890.

Donne, D. G., Viles, J. H., Groth, D., Mehlhorn, I., James, T. L., Cohen, F. E., Prusiner, S. B., Wright, P. E. and Dyson, H. J. (1997). Structure of the recombinant full-length hamster prion protein PrP(29- 231): the N terminus is highly flexible. *Proc. Natl. Acad. Sci. USA*, **94**, 13452-13457.

Du, Z., Park, K. W., Yu, H., Fan, Q. and Li, L. (2008). Newly identified prion linked to the chromatin-remodeling factor Swi1 in Saccharomyces cerevisiae. *Nat. Genet.*, **40**, 460-465.

Dumont, C., Emilsson, T. and Gruebele, M. (2009). Reaching the protein folding speed limit with large, sub-microsecond pressure jumps. *Nature Methods*, **6**(7),515-U70.

Dvorakova, E., Prouza, M., Janouskova, O., Panigaj, M. and Holada, K. (2011). Development of monoclonal antibodies specific for glycated prion protein. *J. Toxicol. Environ. Health. A.*, **74**, 1469-1475.

Eaton, W. A., Munoz, V., Hagen, S. J., Jas, G. S., Lapidus, L. J., Henry, E. R. and Hofrichter, J. (2000). Fast kinetics and mechanisms in protein folding. *Annu. Rev. Biophys. Biomol. Struct.*, **29**, 327-359.

Edenhofer, F., Rieger, R., Famulok, M., Wendler, W., Weiss, S. and Winnacker, E. L. (1996). Prion protein PrPC interacts with molecular chaperones of the Hsp60 family. *J. Virol.*, **70**, 4724-4728.

Eghiaian, F., Grosclaude, J., Lesceu, S., Debey, P., Doublet, B., Treguer, E., Rezaei, H. and Knossow, M. (2004). Insight into the PrPC-->PrPSc conversion from the structures of antibody-bound ovine prion scrapie-susceptibility variants. *Proc Natl Acad Sci U S A* **101,** 10254-10259.

Ellgaard, L., Molinari, M. and Helenius, A. (1999). Setting the standards: quality control in the secretory pathway. *Science*, **286**, 1882-1888.

Ellis, R. J. (2001). Macromolecular crowding: an important but neglected aspect of the intracellular environment. *Curr. Opin. Struct. Biol.,* **11**, 114-119.

Ellis, R. J. (2001). Macromolecular crowding: obvious but underappreciated. *Trends Biochem. Sci.,* **26**, 597-604.

Ellis, R. J. and Hartl, F. U. (1999). Principles of protein folding in the cellular environment. *Curr. Opin. Struct. Biol.,* **9**, 102-110.

Ellis, R. J. and Pinheiro, T. J. (2002). Medicine: danger-misfolding proteins. *Nature,* **416**, 483-484.

Ellis, R. J. and van der Vies, S. M. (1991). Molecular chaperones. *Annu. Rev. Biochem.,* **60**, 321-347.

Endo, T., Groth, D., Prusiner, S. B. and Kobata, A. (1989). Diversity of oligosaccharide structures linked to asparagines of the scrapie prion protein. *Biochemistry,* **28**, 8380-8388.

Evans, P., Slingsby, C. and Wallace, B. A. (2008). Association of partially folded lens betaB2-crystallins with the alpha-crystallin molecular chaperone. *Biochem. J.* **409,** 691-699.

Fandrich, M. and Dobson, C. M. (2002). The behaviour of polyamino acids reveals an inverse side chain effect in amyloid structure formation. *EMBO J.,* **21,** 5682–5690

Farquhar, C. F., Somerville, R. A. and Bruce, M. E. (1998). Straining the prion hypothesis. *Nature,* **391**, 345-346.

Fedorov, A. N. and Baldwin, T. O. (1997). Cotranslational protein folding. *J. Biol. Chem.,* **272**, 32715-32718.

Feldman, D. E. and Frydman, J. (2000). Protein folding *in vivo*: the importance of molecular chaperones. *Curr. Opin. Struct. Biol.,* **10**, 26-33.

Fernandez, A. and Berry, R. S. (2002). Extent of hydrogen-bond protection in folded proteins: a constraint on packing architectures. *Biophys. J.,* **83**, 2475-2481.

Fernandez, A. and Berry, R. S. (2003). Proteins with H-bond packing defects are highly interactive with lipid bilayers: Implications for amyloidogenesis. *Proc. Natl. Acad. Sci. U. S. A.,* **100**, 2391-2396.

Fersht, A. R. (1994). Characterizing transition states in protein folding: an essential step in the puzzle. *Curr. Opin. Struct. Biol.,* **5**, 79-84.

Fersht, A. R. (1997). Nucleation mechanisms in protein folding. *Curr. Opin. Struct. Biol.,* **7**, 3-9.

Fersht, A. R. (1999). Protein stability. In *Structure and mechanism in protein science: a guide to enzyme catalysis and protein folding*, 508-539. New York: W.H. Freeman and Company.

Findeis, M. A. (2007). The role of amyloid beta peptide 42 in Alzheimer's disease. *Pharmacol. Ther.,* **116**, 266-286.

Forloni, G., Angeretti, N., Chiesa, R., Monzani, E., Salmona, M., Bugiani, O. and Tagliavini, F. (1993). Neurotoxicity of a prion protein fragment. *Nature,* **362**, 543-546.

Fraser, H., McConnell, I., Wells, G. A. H. and Dawson, M. (1988). Transmission of bovine spongiform encephalopathy to mice. *Vet. Rec.*, **123**, 472-472.

Frottin, F., Martinez, A., Peynot, P., Mitra, S., Holz, R. C., Giglione, C. and Meinnel, T. (2006). The proteomics of N-terminal methionine cleavage. *Mol. Cell. Proteomics* **5,** 2336-2349.

Gabizon, R., Rosenmann, H., Meiner, Z., Kahana, I., Kahana, E., Shugart, Y., Ott, J. and Prusiner, S. B. (1993). Mutation and polymorphism of the prion protein gene in Libyan Jews with Creutzfeldt-Jakob disease (CJD). *Am. J. Hum. Genet.*, **53**, 828-835.

Gajdusek, D.C. and Zigas, V. (1957). Degenerative disease of the central nervous system in New Guinea: the endemic occurrence of ‘‘kuru’’ in the native population. *N. Engl. J. Med.,* **257**, 974–8.

Gajdusek, D.C., Gibbs, C.J. and Alpers, M. (1966). Experimental transmission of a kuru-like syndrome to chimpanzees. *Nature,* **209**, 794–6.

Galvan, C., Camoletto, P. G., Dotti, C. G., Aguzzi, A. and Ledesma, M. D. (2005). Proper axonal distribution of PrP(C) depends on cholesterol-sphingomyelin-enriched membrane domains and is developmentally regulated in hippocampal neurons. *Mol. Cell. Neurosci.*, **30**, 304-315.

Garcia, F. L., Zahn, R., Riek, R. and Wuthrich, K. (2000). NMR structure of the bovine prion protein. *Proc. Natl. Acad. Sci. USA,* **97**, 8334-8339.

Garfin, D. E. (1990). One-dimensional gel electrophoresis. In *Methods in Enzymology, Guide toProtein Purification*. **182**: pp 425-441. Edited by M. P. Deutscher. London: Academic Press.

Gianni, S., Guydosh, N. R., Khan, F., Caldas, T. D., Mayor, U., White, G. W. N., DeMarco, M. L., Daggett, V. and Fersht, A. R. (2003). Unifying features in protein-folding mechanisms. *Proc. Natl. Acad. Sci. USA,* **100**, 13286-13291.

Gibbons, R.A. and Hunter, G.D. (1967). Nature of the scrapie agent, *Nature,* **215**, 1041‑1043

Gill, S. C. and von Hippel, P. H. (1989). Calculation of protein extinction coefficients from amino acid sequence data. *Anal. Biochem.*, **182**, 319-326.

Glockshuber, R. (2001). Folding dynamics and energetics of recombinant prion proteins. *Adv. Prot. Chem.,* **57**, 83-105.

Goldmann, W. (2008). PrP genetics in ruminant transmissible spongiform encephalopathies. *Vet. Res.* **39,** 30.

Goldmann, W., Hunter, N., Smith, G., Foster, J. and Hope, J. (1994). PrP genotype and agent effects in scrapie: change in allelic interaction with different isolates of agent in sheep, a natural host of scrapie. *J. Gen. Virol.* **75 (Part 5),** 989-995.

Goldfarb, L. G., Korczyn, A. D., Brown, P., Chapman, J. and Gajdusek, D. C. (1990). Mutation in codon 200 of scrapie amyloid precursor gene linked to Creutzfeldt-Jakob disease in Sephardic Jews of Libyan and non-Libyan origin. *Lancet*, **336**, 637-638.

Gorbenko, G. P. and Kinnunen, P. K. (2006). The role of lipid-protein interactions in amyloid-type protein fibril formation. *Chem. Phys. Lipids*, **141**, 72-82.

Gorfe, A.A. and Caflisch, A. (2007). Ser170 controls the conformational multiplicity of the loop 166–175 in prion proteins: implication for conversion and species barrier. *The FASEB Journal*, **21**, 3279-3287

Gossert, A. D., Bonjour, S., Lysek, D. A., Fiorito, F. and Wuthrich, K. (2005). Prion protein NMR structures of elk and of mouse/elk hybrids. *Proc. Natl. Acad. Sci. USA*, **102**, 646-650.

Govaerts, C., Wille, H., Prusiner, S. B. and Cohen, F. E. (2004). Evidence for assembly of prions with left-handed beta 3-helices into trimers. *Proc. Natl. Acad. Sci. USA*, **101**, 8342-8347.

Green, K. M., Castilla, J., Seward, T. S., Napier, D. L., Jewell, J. E., Soto, C., and Telling, G. C. (2008). Accelerated high fidelity prion amplification within and across prion species barriers. *PLoS Pathog.*, **4**, e1000139

Greenfield, N. J. (2006). Determination of the folding of proteins as a function of denaturants, osmolytes or ligands using circular dichroism. *Nat. Protoc.* **1,** 2733-2741.

Greenfield, N. J. (2006). Using circular dichroism collected as a function of temperature to determine the thermodynamics of protein unfolding and binding interactions. *Nat. Protoc.* **1,** 2527-2535.

Griffith, J. S. (1967). Self-replication and scrapie. *Nature*, **215**, 1043-1044.

Grimsley, J. K., Scholtz, J. M., Pace, C. N. and Wild, J. R. (1997). Organophosphorous hydrolase is a remarkably stable enzyme that unfolds through a homodimeric intermediate. *Biochemistry*, **36**, 14366-14374.

Gromiha, M. M. and Selvaraj, S. (2004). Inter-residue interactions in protein folding and stability. *Prog. Biophys. Mol. Biol.*, **86**, 235-277.

Gross, M. and Jaenike, R. (1994). Proteins under pressure. The influence of high hydrostatic pressure on structure, function and assembly of proteins and protein complexes. *Eur. J. Biochem.*, **221**, 617-630.

Guex, N. and Peitsch, M. C. (1997). SWISS-MODEL and the Swiss-PdbViewer: An environment for comparative protein modelling. *Electrophoresis*, **18**, 2714-2723.

Guijarro, J. I., Sunde, M., Jones, J. A., Campbell, I. D. and Dobson, C. M. (1998). Amyloid fibril formation by an SH3 domain. *Proc. Natl. Acad. Sci. USA*, **95,** 4224–4228

Gutfreund, H. (1999). Rapid-flow techniques and their contributions to enzymology. *Trends Biochem. Sci.,* **24**, 457-460.

Hadlow, W. J. (1959). Scrapie and Kuru. *Lancet,* **274**, 289-290.

Haigh, C. L. and Brown, D. R. (2006). Prion protein reduces both oxidative and non-oxidative copper toxicity. *J. Neurochem.,* **98**, 677-689.

Haire, L. F., Whyte, S. M., Vasisht, N., Gill, A. C., Verma, C., Dodson, E. J., Dodson, G. G. and Bayley, P. M. (2004). The crystal structure of the globular domain of sheep prion protein. *J. Mol. Biol.,* **336**, 1175-1183.

Han, H., Weinreb, P. H. and Lansbury, P.T. (1995). The core Alzheimer's peptide NAC forms amyloid fibrils which seed and are seeded by beta-amyloid: is NAC a common trigger or target in neurodegenerative disease? *Chem. Biol.,* **2**, 163–169

Harper, J. D. and Lansbury, P. T., Jr. (1997). Models of amyloid seeding in Alzheimer's disease and scrapie: mechanistic truths and physiological consequences of the time-dependent solubility of amyloid proteins. *Annu. Rev. Biochem.,* **66**, 385-407.

Harris, D. A. and True, H. L. (2006). New insights into prion structure and toxicity. *Neuron,* **50**, 353-357.

Harris, D. L. and Hudson, B. S. (1990). Photophysics of tryptophan in bacteriophage T4 lysozymes. *Biochemistry,* **29**, 5276-5285.

Harrison, C. F., Barnham, K. J. and Hill, A. F. (2007). Neurotoxic species in prion disease: a role for PrP isoforms? *J. Neurochem.,* **103**, 1709-1720.

Hart, T., Hosszu, L. L., Trevitt, C. R., Jackson, G. S., Waltho, J. P., Collinge, J. and Clarke, A. R. (2009). Folding kinetics of the human prion protein probed by temperature jump. *Proc. Natl. Acad. Sci. U. S. A.* **106,** 5651-5656.

Hartl, F. U. and Hayer-Hartl, M. (2009). Converging concepts of protein folding *in vitro* and *in vivo*. *Nat. Struct. Mol. Biol.,* **16**, 574-581.

Hay, B., Barry, R. A., Lieberburg, I., Prusiner, S. B. and Lingappa, V. R. (1987). Biogenesis and transmembrane orientation of the cellular isoform of the scrapie prion protein. *Mol. Cell. Biol.,* **7**, 914-920.

Head, M. W. and Ironside, J. W. (2000). Inhibition of prion-protein conversion: a therapeutic tool? *Trends Microbiol.,* **8**, 6-8.

Hegde, R. S., Mastrianni, J. A., Scott, M. R., DeFea, K. A., Tremblay, P., Torchia, M., DeArmond, S. J., Prusiner, S. B. and Lingappa, V. R. (1998). A transmembrane form of the prion protein in neurodegenerative disease. *Science,* **279**, 827-834.

Hicks, M. R., Gill, A. C., Bath, I. K., Rullay, A. K., Sylvester, I. D., Crout, D. H. and Pinheiro, T. J. (2006). Synthesis and structural characterization of a mimetic membrane-anchored prion protein. *FEBS J.,* **273**, 1285-1299.

Hill, A. F. and Collinge, J. (2003). Subclinical prion infection. *Trends Microbiol.*, **11**, 578-584.

Hill, A. F., Desbruslais, M., Joiner, S., Sidle, K. C. L., Gowland, I., Collinge, J., Doey, L. J. and Lantos, P. (1997). The same prion strain causes vCJD and BSE. *Nature*, **389**, 448-450.

Hilton, D. A., Ghani, A. C., Conyers, L., Edwards, P., McCardle, L., Ritchie, D., Penney, M., Hegazy, D. and Ironside, J. W. (2004). Prevalence of lymphoreticular prion protein accumulation in UK tissue samples. *J. Pathol.*, **203**, 733-739.

Hope, J. (1994). The nature of the scrapie agent: the evolution of the virino. *Ann. N. Y. Acad. Sci.*, **724**, 282-289.

Hope, J., Reekie, L. J., Hunter, N., Multhaup, G., Beyreuther, K., White, H., Scott, A. C., Stack, M. J., Dawson, M. and Wells, G. A. (1988). Fibrils from brains of cows with new cattle disease contain scrapie-associated protein. *Nature*, **336**, 390-392.

Hornemann, S. and Glockshuber, R. (1998). A scrapie-like unfolding intermediate of the prion protein domain PrP(121-231) induced by acidic pH. *Proc. Natl. Acad. Sci. USA*, **95**, 6010-6014.

Hornemann, S., Korth, C., Oesch, B., Riek, R., Wider, G., Wuthrich, K. and Glockshuber, R. (1997). Recombinant full-length murine prion protein, mPrP(23-231): purification and spectroscopic characterization. *FEBS Lett.*, **413**, 277-281.

Hornemann, S., Schorn, C. and Wuthrich, K. (2004). NMR structure of the bovine prion protein isolated from healthy calf brains. *EMBO Reports*, **5**, 1159-1164.

Hornshaw, M.P., Mcdermott, J.R. and Candy J.M. (1995). Copper-Binding to the N-Terminal Tandem Repeat Regions of Mammalian and Avian Prion Protein. *Biochem Biophys Res Com.*, **207**(2), 621-629.

Horiuchi, M. and Caughey, B. (1999). Prion protein interconversions and the transmissible spongiform encephalopathies. *Structure*, **7**,R231–R240

Hosszu, L. L., Baxter, N. J., Jackson, G. S., Power, A., Clarke, A. R., Waltho, J. P., Craven, C. J. and Collinge, J. (1999). Structural mobility of the human prion protein probed by backbone hydrogen exchange. *Nat. Struct. Biol.*, **6**, 740-743.

Hosszu, L. L., Jackson, G. S., Trevitt, C. R., Jones, S., Batchelor, M., Bhelt, D., Prodromidou, K., Clarke, A. R., Waltho, J. P. and Collinge, J. (2004). The residue 129 polymorphism in human prion protein does not confer susceptibility to Creutzfeldt-Jakob disease by altering the structure or global stability of PrPC. *J. Biol. Chem.*, **279**, 28515-28521.

Hosszu, L. L., Wells, M. A., Jackson, G. S., Jones, S., Batchelor, M., Clarke, A. R., Craven, C. J., Waltho, J. P. and Collinge, J. (2005). Definable equilibrium states in the folding of human prion protein. *Biochemistry*, **44**, 16649-16657.

Howie, A. J. and Brewer, D. B. (2009). Optical properties of amyloid stained by Congo red: history and mechanisms. *Micron*, **40**, 285-301.

Hsiao, K., Baker, H. F., Crow, T. J., Poulter, M., Owen, F., Terwilliger, J. D., Westaway, D., Ott, J. and Prusiner, S. B. (1989). Linkage of a prion protein missense variant to Gerstmann-Straussler syndrome. *Nature*, 338, 342-345.

Huang, Z., Prusiner, S. B. and Cohen, F. E. (1995). Scrapie prions: a threedimensional model of an infectious fragment. *Fold. Des.,* **1**, 13-19.

Hunter, N. (2007). Scrapie: uncertainties, biology and molecular approaches. *Biochim. Biophys. Acta* **1772,** 619-628.

Hwang, C., Sinskey, A. J. and Lodish, H. F. (1992). Oxidized redox state of glutathione in the endoplasmic reticulum. *Science,* **257**, 1496-1502.

Jackson, G. S., Hill, A. F., Joseph, C., Hosszu, L. L., Power, A., Waltho, J. P., Clarke, A. R. and Collinge, J. (1999a). Multiple folding pathways for heterologously expressed human prion protein. *Biochim. Biophys. Acta,* **1431**, 1-13.

Jackson, G. S., Hosszu, L. L., Power, A., Hill, A. F., Kenney, J., Saibil, H., Craven, C. J., Waltho, J. P., Clarke, A. R. and Collinge, J. (1999b). Reversible conversion of monomeric human prion protein between native and fibrilogenic conformations. *Science,* **283**, 1935-1937.

Jacob, M., Holtermann, G., Perl, D., Reinstein, J., Schindler, T., Geeves, M. A. and Schmid, F. X. (1999). Microsecond folding of the cold shock protein measured by a pressure-jump technique. *Biochemistry,* **38**, 2882-2891.

Jahn, T. R. and Radford, S. E. (2005). The yin and yang of protein folding. *FEBS J.*, **272**, 5962-5970.

Jahn, T. R. and Radford, S. E. (2008). Folding versus aggregation: polypeptide conformations on competing pathways. *Arch. Biochem. Biophys.*, **469**, 100-117.

James, T. L., Liu, H., Ulyanov, N. B., Farr-Jones, S., Zhang, H., Donne, D. G., Kaneko, K., Groth, D., Mehlhorn, I., Prusiner, S. B. and Cohen, F. E. (1997). Solution structure of a 142-residue recombinant prion protein corresponding to the infectious fragment of the scrapie isoform. *Proc. Natl. Acad. Sci. USA*, **94**, 10086-10091.

Jarrett, J. T. and Lansbury, P. T. (1992). Amyloid fibril formation requires a chemically discriminating nucleation event: studies of an amyloidogenic sequence from the bacterial protein. *OsmB. Biochemistry*, **31**: 12345–12352

Jarret, J. T. and Lansbury, P. T. (1993). Seeding "one dimensional crystallization" of amyloid: a pathogenic mechanism in Alzheimer's disease and scrapie? *Cell,* **73**, 1055-1058.

Jenkins, D. C. Equilibrium and kinetic folding studies of the prion protein. (2006). PhD Thesis. University of Warwick

Jenkins, D. C., Pearson, D. S., Harvey, A., Sylvester, I. D., Geeves, M. A. and Pinheiro, T. J. (2009). Rapid folding of the prion protein captured by pressure-jump. *Eur. Biophys. J.* **38,** 625-635.

Jenkins, D. C., Sylvester, I. D. and Pinheiro, T. J. (2008). The elusive intermediate on the folding pathway of the prion protein. *FEBS J.* **275,** 1323-1335.

Jessop, C. E., Chakravarthi, S., Watkins, R. H. and Bulleid, N. J. (2004). Oxidative protein folding in the mammalian endoplasmic reticulum. *Biochem. Soc. Trans.*, **32**, 655-658.

Johnson, C. J., Pedersen, J. A., Chappell, R. J., McKenzie, D., and Aiken, J. M. (2007). Oral transmissibility of prion disease is enhanced by binding to soil particles. *PLoS Pathog.*, **3**, e93

Jones, E.M. and Surewicz, W.K. (2005). Fibril conformation as the basis of species- and strain-dependent seeding specificity of mammalian prion amyloids. *Cell*, **121**(1), 63-72.

Kadokura, H., Katzen, F. and Beckwith, J. (2003). Protein disulfide bond formation in prokaryotes. *Annu. Rev. Biochem.*, **72**, 111-135.

Kanaani, J., Prusiner, S.B., Diacovo, J., Baekkeskov, S. and Legname, G. (2005). Recombinant prion protein induces rapid polarization and development of synapses in embryonic rat hippocampal neurons *in vitro*. *J. Neurochem.*, **95**, 1373–1386

Kaneko, K., Zulianello, L., Scott, M., Cooper, C. M., Wallace, A. C., James, T. L., Cohen, F. E. and Prusiner, S. B. (1997). Evidence for protein X binding to a discontinuous epitope on the cellular prion protein during scrapie prion propagation. *Proc. Natl. Acad. Sci. USA*, **94**, 10069-10074.

Kang, D., Gho, Y. S., Suh, M. and Kang, C. (2002). Highly sensitive and fast protein detection with Coomassie brilliant blue in sodium dodecyl sulfatepolyacrylamide gel electrophoresis. *Bull. Korean Chem. Soc.*, **23**, 1511-1512.

Karplus, M. and Weaver, D. L. (1994). Protein folding dynamics: the diffusioncollision model and experimental data. *Prot. Sci.*, **3**, 650-668.

Kayed, R., Sokolov, Y., Edmonds, B., McIntire, T. M., Milton, S. C., Hall, J. E., and

Glabe, C. G. (2004) Permeabilization of lipid bilayers is a common conformation-dependent activity of soluble amyloid oligomers in protein misfolding diseases. *J. Biol. Chem.* 279, 46363–46366

Kazlauskaite, J., Sanghera, N., Sylvester, I., Venien-Bryan, C. and Pinheiro, T. J. (2003). Structural changes of the prion protein in lipid membranes leading to aggregation and fibrillization. *Biochemistry*, **42**, 3295-3304.

Kazlauskaite, J., Young, A., Gardner, C. E., Macpherson, J. V., Venien-Bryan, C. and Pinheiro, T. J. T. (2005). An unusual soluble β -turn-rich conformation of prion is involved in fibril formation and toxic to neuronal cells. *Biochem. Biophys. Res. Commun.*, **328**, 292-305.

Kelly, S. M., Jess, T. J. and Price, N. C. (2005). How to study proteins by circular dichroism. *Biochim. Biophys. Acta*, **1751**, 119-139.

Kelly, S. M. and Price, N. C. (1997). The application of circular dichroism to studies of protein folding and unfolding. *Biochim. Biophys. Acta,* **1338**, 161-185.

Khan, M. Q., Sweeting, B., Mulligan, V.K., Arslan, P.E., Cashman, N.R., Pai E.F. and Chakrabartty A. (2010). Prion disease susceptibility is affected by β-structure folding propensity and local side-chain interactions in PrP, *Proc Nat Acad Sci USA,* **107**(46), 19808–19813

Kim, P. S. and Baldwin, R. L. (1982). Specific intermediates in the folding reactions of small proteins and the mechanism of protein folding. *Annu. Rev. Biochem.,* **51**, 459-489.

Kimberlin, R. H., Cole, S. and Walker, C. A. (1987). Temporary and permanent modifications to a single strain of mouse scrapie on transmission to rats and hamsters. *J. Gen. Virol.* **68 (Part 7),** 1875-1881.

King, C.Y. and Diaz-Avalos R. (2004). Protein-only transmission of three yeast prion strains. *Nature,* **428**, 319-323.

Kintses, B., Gyimesi, M., Pearson, D.S., Geeves, M.A., Zeng, W., Bagshaw, C.R. and Málnási-Csizmadia A. (2007). Reversible movement of switch 1 loop of myosin determines actin interaction. *Embo J.,* **26**(1), 265-274.

Kirkitadze, M. D., Bitan, G., and Teplow, D. B. (2002). Paradigm shifts in Alzheimer's disease and other neurodegenerative disorders: the emerging role of oligomeric assemblies. *J. Neurosci. Res.* **69**, 567–577

Kitamoto, T., Iizuka, R. and Tateishi, J. (1993). An amber mutation of prion protein in Gerstmann-Straussler syndrome with mutant PrP plaques. *Biochem. Biophys. Res. Commun.*, **192**, 525-531.

Klein-Seetharaman, J., Oikawa, M., Grimshaw, S. B., Wirmer, J., Duchardt, E., Ueda, T., Imoto, T., Smith, L. J., Dobson, C. M. and Schwalbe, H. (2002). Long-range interactions within a nonnative protein. *Science*, **295**, 1719-1722.

Knight, J. B., Vishwanath, A., Brody, J. P. and Austin, R. H. (1998). Hydrodynamic focusing on a silicon chip: Mixing nanoliters in microseconds. *Phys. Rev. Lett.,* **80**, 3863-3866.

Kong, Q., Huang, S., Zou, W., Vanegas, D., Wang, M., Wu, D., Yuan, J., Zheng, M., Bai, H., Deng, H., Chen, K., Jenny, A. L., O'Rourke, K., Belay, E. D., Schonberger, L. B., Petersen, R. B., Sy, M. S., Chen, S. G., and Gambetti, P. (2005). Chronic wasting disease of elk: transmissibility to humans examined by transgenic mouse models. *J. Neurosci.* **25**, 7944–7949

Korth, C., May, B. C., Cohen, F. E. and Prusiner, S. B. (2001). Acridine and phenothiazine derivatives as pharmacotherapeutics for prion disease. *Proc. Natl. Acad. Sci. USA,* **98**, 9836-9841.

Kramer, G., Boehringer, D., Ban, N. and Bukau, B. (2009). The ribosome as a platform for co-translational processing, folding and targeting of newly synthesized proteins. *Nat. Struct. Mol. Biol.*, **16**, 589-597.

Kramer, M. L., Kratzin, H. D., Schmidt, B., Römer, A., Windl, O., Liemann, S., Hornemann, S. and Kretzschmar, H. (2001). Prion protein binds copper within the physiological concentration range. *J. Biol. Chem.*, **276**, 16711-16719.

Kubelka, J., Chiu, T. K., Davies, D. R., Eaton, W. A. and Hofrichter, J. (2006). Sub-microsecond protein folding. *J. Mol. Biol.*, **359**, 546-553.

Kubelka, J., Hofrichter, J. and Eaton, W. A. (2004). The protein folding 'speed limit'. *Curr. Opin. Struct. Biol.*, **14**, 76-88.

Kumar, T. K. S. and Yu, C. (2004). Monitoring protein folding at atomic resolution. *Acc. Chem. Res.*, **37**, 929-936.

Kuwata, K., Li, H., Yamada, H., Legname, G., Prusiner, S. B., Akasaka, K. and James, T. L. (2002). Locally disordered conformer of the hamster prion protein: a crucial intermediate to PrPSc? *Biochemistry*, **41**, 12277-12283.

Kuwata, K., Shastry, R., Cheng, H., Hoshino, M., Batt, C. A., Goto, Y. and Roder, H. (2001). Structural and kinetic characterization of early folding events in beta-lactoglobulin. *Nat. Struct. Biol.*, **8**, 151-155.

Kuznetsov, I. B. and Rackovsky, S. (2004). Comparative computational analysis of prion proteins reveals two fragments with unusual structural properties and a pattern of increase in hydrophobicity associated with disease-promoting mutations. *Prot. Sci.*, **13**, 3230-3244.

Kuznetsova, I. M., Turoverov, K. K. and Uversky, V. N. (2004). Use of the phase diagram method to analyze the protein unfolding-refolding reactions: fishing out the "invisible" intermediates. *J. Proteome Res.*, **3**, 485-494.

Laemmli, U. K. (1970). Cleavage of structural proteins during the assembly of the head of bacteriophage T4. *Nature* **227,** 680-685.

Lakowicz, J. R. (1999). Protein fluorescence. In *Principles of Fluorescence Spectroscopy*, 2nd edn, 445-486. New York: Kluwer Academic / Plenum Publishers.

Lansbury, P. T., Jr. (1992). In pursuit of the molecular structure of amyloid plaque: new technology provides unexpected and critical information. *Biochemistry*, **31**, 6865-6870.

Lasmezas, C. I., Deslys, J. P., Demaimay, R., Adjou, K. T., Lamoury, F., Dormont, D., Robain, O., Ironside, J. and Hauw, J. J. (1996). BSE transmission to macaques. *Nature*, **381**, 743-744.

Lasmezas, C. I., Deslys, J. P., Robain, O., Jaegly, A., Beringue, V., Peyrin, J. M., Fournier, J. G., Hauw, J. J., Rossier, J. and Dormont, D. (1997). Transmission of the BSE agent to mice in the absence of detectable abnormal prion protein. *Science*, **275**, 402-405.

Lawson, V. A., Collins, S. J., Masters, C. L. and Hill, A. F. (2005). Prion protein glycosylation. *J. Neurochem.*, **93**, 793-801.

Lee, C. I., Yang, Q., Perrier, V. and Baskakov, I. V. (2007). The dominant-negative effect of the Q218K variant of the prion protein does not require protein X. *Protein Sci.* **16,** 2166-2173.

Le Pichon, C. E., Valley, M. T., Polymenidou, M., Chesler, A. T., Sagdullaev, B. T., Aguzzi, A. and Firestein, S. (2009). Olfactory behavior and physiology are disrupted in prion protein knockout mice. *Nat. Neurosci.*, **12**, 60-69.

Lee, R. J., Wang, S. and Low, P. S. (1996). Measurement of endosome pH following folate receptor-mediated endocytosis. *Biochim. Biophys. Acta*, **1312**, 237-242.

Lee, S. and Eisenberg, D. (2003). Seeded conversion of recombinant prion protein to a disulfide-bonded oligomer by a reduction-oxidation process. *Nat. Struct. Biol.*, **10**, 725-730.

Lees, A. J., Hardy, J. and Revesz, T. (2009). Parkinson's disease. *Lancet*, **373**, 2055-2066.

Legname, G., Baskakov, I. V., Nguyen, H. O., Riesner, D., Cohen, F. E., DeArmond, S. J. and Prusiner, S. B. (2004). Synthetic mammalian prions. *Science*, **305**, 673-676.

Liemann, S. and Glockshuber, R. (1999). Influence of amino acid substitutions related to inherited human prion diseases on the thermodynamic stability of the cellular prion protein. *Biochemistry*, **38**, 3258-3267.

Lin, Y., Gerfen, G. J., Rousseau, D. L. and Yeh, S. R. (2003). Ultrafast microfluidic mixer and freeze-quenching device. *Anal. Chem.*, **75**, 5381-5386.

Liu, Y. and Eisenberg, D. (2002). 3D domain swapping: as domains continue to swap. *Protein Sci.*, **11,** 1285–1299

Liu, H., Farr-Jones, S., Ulyanov, N. B., Llinas, M., Marqusee, S., Groth, D., Cohen, F. E., Prusiner, S. B. and James, T. L. (1999). Solution structure of Syrian hamster prion protein rPrP(90-231). *Biochemistry*, **38**, 5362-5377.

Leopold, P. E., Montal, M. and Onuchic, J. N. (1992). Protein folding funnels: a kinetic approach to the sequence-structure relationship. *Proc. Natl. Acad. Sci. U. S. A.*, **89**, 8721-8725.

Levinthal , C. (1968). Are There Pathways for Protein Folding? *J. Chem. Phys.*, **65**, 44-45.

Lo, R.Y., Shyu, W.C., Lin, S.Z., Wang, H.J., Chen, S.S. and Li H. (2007). New molecular insights into cellular survival and stress responses: neuroprotective role of cellular prion protein (PrPC). *Mol. Neurobiol.*, **35**, 236–244

Lodish H, B. A., Zipursky SL, Matsudaira P, Baltimore D, Darnell JE (2001). Biomembrane and subcellular organizarion of eukaryotic cells. In *Molecular Cell Biology* **4th edition**, New York: W.H Freeman and Company.

Lomakin, A., Chung, D. S., Benedek, G. B., Kirschner, D. A. and Teplow, D. B. (1996). On the nucleation and growth of amyloid beta-protein fibrils: detection of nuclei and quantitation of rate constants. *Proc. Natl. Acad. Sci. USA*, **93**, 1125–1129

Lomakin, A., Teplow, D. B., Kirschner, D. A. and Benedek, G. B. (1997). Kinetic theory of fibrillogenesis of amyloid beta-protein. *Proc. Natl. Acad. Sci. USA*, **94**, 7942–7947

Lu, B. Y., Beck, P. J. and Chang, J. Y. (2001). Oxidative folding of murine prion mPrP(23-231). *Eur. J. Biochem.*, **268**, 3767-3773.

Lu, K. P., Finn, G., Lee, T. H. and Nicholson, L. K. (2007). Prolyl cis-trans isomerization as a molecular timer. *Nat. Chem. Biol.*, **3**, 619-629.

Lysek, D. A., Schorn, C., Nivon, L. G., Esteve-Moya, V., Christen, B., Calzolai, L., von Schroetter, C., Fiorito, F., Herrmann, T., Guntert, P. and Wuthrich, K. (2005). Prion protein NMR structures of cats, dogs, pigs, and sheep. *Proc. Natl. Acad. Sci. USA*, **102**, 640-645.

Maddelein, M. L., Dos Reis, S., Duvezin-Caubet, S., Coulary-Salin, B. and Saupe, S. J. (2002). Amyloid aggregates of the HET-s prion protein are infectious. *Proc. Natl. Acad. Sci. U. S. A.*, **99**, 7402-7407.

Málnási-Csizmadia, A., Pearson, D.S., Kovacs, M., Woolley, R.J., Geeves, M.A. and Bagshaw, C.R. (2001). Kinetic resolution of a conformational transition and the ATP hydrolysis step using relaxation methods with a Dictyostelium myosin II mutant containing a single tryptophan residue. *Biochemistry*, **40**(42),12727-12737.

Makarava, N. and Baskakov, I. V. (2008). The same primary structure of the prion protein yields two distinct self-propagating states. *J Biol Chem*, **283**, 15988-15996.

Makarava, N., Ostapchenko, V. G., Savtchenko, R. and Baskakov, I. V. (2009). Conformational switching within individual amyloid fibrils. *J. Biol. Chem.*, **284**, 14386-14395.

Marijanovic, Z., Caputo, A., Campana, V. and Zurzolo, C. (2009). Identification of an intracellular site of prion conversion. *PLoS Pathog.*, **5**(5): e1000426

Martins, S. M., Chapeaurouge, A. and Ferreira, S. T. (2003). Folding intermediates of the prion protein stabilized by hydrostatic pressure and low temperature. *J. Biol. Chem.*, **278**, 50449-50455.

Martin, S. J., Reutelingsperger, C. P., McGahon, A. J., Rader, J. A., van Schie, R. C., LaFace, D. M. and Green, D. R. (1995). Early redistribution of plasma membrane phosphatidylserine is a general feature of apoptosis regardless of the initiating stimulus: inhibition by overexpression of Bcl-2 and Abl. *J. Exp. Med.* **182,** 1545-1556.

Martins, V. R., Linden, R., Prado, M. A., Walz, R., Sakamoto, A. C., Izquierdo, I. and Brentani, R. R. (2002). Cellular prion protein: on the road for functions. *FEBS Lett.,* **512**, 25-28.

Martins, V. R., Mercadante, A. F., Cabral, A. L. B., Freitas, A. R. O. and Castro, R. M. R. P. S. (2001). Insights into the physiological function of cellular prion protein. *Braz. J. Med. Biol. Res.*, **34**, 585-595.

Marsh, R. F., Kincaid, A. E., Bessen, R. A., and Bartz, J. C. (2005). Interspecies transmission of chronic wasting disease prions to squirrel monkeys (Saimiri sciureus). *J. Virol.,* **79**, 13794–13796

Mathews, C. K., Van Holde, K. E. and Ahern, K. G. (2000a). Amino acids. In *Biochemistry*, 3rd edn, 126-134. San Francisco: Benjamin/Cummings.

Mathews, C. K., Van Holde, K. E. and Ahern, K. G. (2000b). From gene to protein. In *Biochemistry*, 3rd edn, 142-146. San Francisco: Benjamin/Cummings.

Mathews, C. K., Van Holde, K. E. and Ahern, K. G. (2000c). The threedimensional structure of proteins. In *Biochemistry*, 3rd edn, 161-211. San Francisco: Benjamin/Cummings.

Mathews, C. K., Van Holde, K. E. and Ahern, K. G. (2000d). Introduction to proteins: the primary level of protein structure. In *Biochemistry*, 3rd edn, 142-146. San Francisco: Benjamin/Cummings.

Matouschek, A., Kellis, J. T., Serrano, L. and Fersht, A. R. (1989). Mapping the transition state and pathway of protein folding by protein engineering. *Nature*, **340**, 122-126.

Mawhinney, S., Pape, W. J., Forster, J. E., Anderson, C. A., Bosque, P. and Miller, M. W. (2006). Human prion disease and relative risk associated with chronic wasting disease. *Emerg. Infect. Dis.*, **12**, 1527-1535.

Maxwell, K. L., Wildes, D., Zarrine-Afsar, A., De Los Rios, M. A., Brown, A. G., Friel, C. T., Hedberg, L., Horng, J. C., Bona, D., Miller, E. J., Vallee-Belisle, A., Main, E. R., Bemporad, F., Qiu, L., Teilum, K., Vu, N. D., Edwards, A. M., Ruczinski, I., Poulsen, F. M., Kragelund, B. B., Michnick, S. W., Chiti, F., Bai, Y., Hagen, S. J., Serrano, L., Oliveberg, M., Raleigh, D. P., Wittung-Stafshede, P., Radford, S. E., Jackson, S. E., Sosnick, T. R., Marqusee, S., Davidson, A. R. and Plaxco, K. W. (2005). Protein folding: defining a "standard" set of experimental conditions and a preliminary kinetic data set of two-state proteins. *Prot. Sci.,* **14**, 602-616.

McAnaney, T.B., Zeng, W., Doe, C.F., Bhanji, N., Wakelin, S., Pearson, D.S., Abbyad, P., Shi, X., Boxer, S.G. and Bagshaw. C.R. (2005). Protonation, photobleaching, and photoactivation of yellow fluorescent protein (YFP 10C): A unifying mechanism. ***Biochemistry,* 44(14),5510-5524.**

McHolland, L. E., Bryant, P. K., 3rd, Miller, M. W., Williams, E. S., Smits, M., and Caughey, B. (2000). Evidence of a molecular barrier limiting susceptibility of humans, cattle and sheep to chronic wasting disease. *EMBO J.,* **19,** 4425–4430

McKinley, M. P., Taraboulos, A., Kenaga, L., Serban, D., Stieber, A., DeArmond, S. J., Prusiner, S. B. and Gonatas, N. (1991). Ultrastructural localization of scrapie prion proteins in cytoplasmic vesicles of infected cultured cells. *Lab. Invest.*, **65**, 622-630.

Mead, S. (2006). Prion disease genetics. *Eur. J. Hum. Genet.* **14,** 273-281.

Mehlhorn, I., Groth, D., Stockel, J., Moffat, B., Reilly, D., Yansura, D., Willett, W. S., Baldwin, M., Fletterick, R., Cohen, F. E., Vandlen, R., Henner, D. and Prusiner, S. B. (1996). High-level expression and characterization of a purified 142-residue polypeptide of the prion protein. *Biochemistry,* **35**, 5528-5537.

Merz, P. A., Somerville, R. A., Wisniewski, H. M. and Iqbal, K. (1981). Abnormal fibrils from scrapie-infected brain. *Acta Neuropathol.*, **54**, 63-74.

Meyer, R. K., McKinley, M. P., Bowman, K. A., Braunfeld, M. B., Barry, R. A. and Prusiner, S. B. (1986). Separation and properties of cellular and scrapie prion proteins. *Proc. Natl. Acad. Sci. USA,* **83**, 2310-2314.

Meyerett, C., Michel, B., Pulford, B., Spraker, T. R., Nichols, T. A., Johnson, T., Kurt, T., Hoover, E. A., Telling, G. C., and Zabel, M. D. (2008). *In vitro* strain adaptation of CWD prions by serial protein misfolding cyclic amplification.*Virology,* **382**, 267–276

Milhavet, O., McMahon, H. E. M., Rachidi, W., Nishida, N., Katamine, S., Mange, A., Arlotto, M., Casanova, D., Riondel, J., Favier, A. and Lehmann, S. (2000). Prion infection impairs the cellular response to oxidative stress. *Proc. Natl. Acad. Sci. USA,* **97**, 13937-13942.

Miller, M. W., and Williams, E. S. (2004). Chronic wasting disease of cervids. *Curr. Top. Microbiol. Immunol.*, **284**, 193–214

Miller, M. W. and Williams, E. S. (2003). Prion disease: horizontal prion transmission in mule deer. *Nature*, **425**, 35-36.

Millhauser, G. L. (2004). Copper binding in the prion protein. *Acc. Chem. Res.* **37**, (2), 79-85.

Miura, T., Hori-i, A., Mototani, H. and Takeuchi, H. (1999). Raman spectroscopic study on the copper(II) binding mode of prion octapeptide and its pH dependence. *Biochemistry,* **38**, 11560-11569.

Mo, H., Moore, R. C., Cohen, F. E., Westaway, D., Prusiner, S. B., Wright, P. E. and Dyson, H. J. (2001). Two different neurodegenerative diseases caused by proteins with similar structures. *Proc. Natl. Acad. Sci. USA,* **98**, 2352-2357.

Moore, R.A., Vorberg, I. and Priola, S.A. (2005). Species barriers in prion diseases - brief review. *Arch. Virol Suppl.,* 187-202.

Moore, R. C. and Melton, D. W. (1997). Transgenic analysis of prion diseases. *Mol. Hum. Reprod.,* **3**, 529-544.

Moore, R. C., Lee, Y. I., Silverman, G. L., Harrison, P. M., Strome, R., Heinrich, C., Karunaratne, A., Pasternak, S. H., Chishti, M. A., Liang, Y., Mastrangelo, P., Wang, K., Smit, A. F. A., Katamine, S., Carlson, G. A., Cohen, F. E., Prusiner, S. B., Melton, D. W., Tremblay, P., Hood, L. E. and Westaway, D. (1999). Ataxia in prion protein (PrP)-deficient mice is associated with upregulation of the novel PrP-like protein doppel. *J. Mol. Biol.,* **292**, 797-817.

Morillas, M., Swietnicki, W., Gambetti, P. and Surewicz, W. K. (1999). Membrane environment alters the conformational structure of the recombinant human prion protein. *J. Biol. Chem.* **274,** 36859-36865.

Morjana, N. A., McKeone, B. J. and Gilbert, H. F. (1993). Guanidine hydrochloride stabilization of a partially unfolded intermediate during the reversible denaturation of protein disulfide isomerase. *Proc. Natl. Acad. Sci. USA,* **90**, 2107-2111.

Morrissey, M. P. and Shakhnovich, E. I. (1999). Evidence for the role of PrPC helix 1 in the hydrophilic seeding of prion aggregates. *Proc. Natl. Acad. Sci. USA,* **96**, 11293-11298.

Moya, K.L., Salès, N., Hässig, R., Créminon, C., Grassi, J., Di Giamberardino, L. (2000). Immunolocalization of the cellular prion protein in normal brain. *Microsc. Res. Tech.,* **50**, 58–65

Mozhaev, V. V., Heremans, K., Frank, J., Masson, P. and Balny, C. (1996). High pressure effects on protein structure. *Prot. Struct. Funct. Genet.,* **24**, 81-91.

Muller, P. (1994). Glossary of terms used in physical organic chemistry. *Pure & Appl. Chem.,* **66**, 1077-1184.

Nandi, P. K., Leclerc, E., Nicole, J. C. and Takahashi, M. (2002). DNA-induced partial unfolding of prion protein leads to its polymerisation to amyloid. *J. Mol. Biol.* **322,** 153-161.

Nathanson, N., Wilesmith, J. and Griot, C. (1997). Bovine spongiform encephalopathy (BSE): causes and consequences of a common source epidemic. *Am. J. Epidemiol.,* **145**, 959-969.

Negro, A., De Filippis, V., Skaper, S. D., James, P. and Sorgato, M. C. (1997). The complete mature bovine prion protein highly expressed in *Escherichia coli*: biochemical and structural studies. *FEBS Lett.,* **412**, 359-364.

Nelson, R., Sawaya, M. R., Balbirnie, M., Madsen, A. O., Riekel, C., Grothe, R. and Eisenberg, D. (2005). Structure of the cross-beta spine of amyloid-like fibrils. *Nature,* **435**, 773-778.

Netzer, W. J. and Hartl, F. U. (1997). Recombination of protein domains facilitated by co-translational folding in eukaryotes. *Nature*, **388**, 343-349.

Neuweiler, H., Doose, S. and Sauer, M. (2005). A microscopic view of miniprotein folding: enhanced folding efficiency through formation of an intermediate. *Proc. Natl. Acad. Sci. U. S. A.*, **102**, 16650-16655.

Nguyen, J. T., Inouye, H., Baldwin, M. A., Fletterick, R. J., Cohen, F. E., Prusiner, S. B. and Kirschner, D. A. (1995). X-ray diffraction of scrapie prion rods and PrP peptides. *J. Mol. Biol.*, **252**, 412-422.

Nicholas, K. B. and Nicholas, H. B. (2000). Genedoc: a tool for editing and annotating multiple sequence alignments.

Nolting, B., Golbik, R., Neira, J. L., Soler-Gonzalez, A. S., Schreiber, G. and Fersht, A. R. (1997). The folding pathway of a protein at high resolution from microseconds to seconds. *Proc. Natl. Acad. Sci. USA*, **94**, 826-830.

Norrby E. (2011). Prions and proteinfolding diseases. *J. Intern. Med.*, **270**,1–14.

Novitskaya, V., Bocharova, O.V., Bronstein, I. and Baskakov, I.V. (2006). Amyloid fibrils of mammalian prion protein are highly toxic to cultured cells and primary neurons. *J. Biol. Chem.* **281**(19), 13828–13836

Novitskaya, V., Makarava, N., Sylvester, I., Bronstein, I. B. and Baskakov, I. V. (2007). Amyloid fibrils of mammalian prion protein induce axonal degeneration in NTERA2-derived terminally differentiated neurons. *J. Neurochem.*, **102**, 398-407.

Oesch, B., Westaway, D., Walchli, M., McKinley, M. P., Kent, S. B., Aebersold, R., Barry, R. A., Tempst, P., Teplow, D. B., Hood, L. E. and *et al.* (1985). A cellular gene encodes scrapie PrP 27-30 protein. *Cell*, **40**, 735-746.

Ohnishi, S. and Takano, K. (2004). Amyloid fibrils from the viewpoint of protein folding, *Cell. Mol. Life Sci.*, **61**, 511–524

Oliveberg, M. (2001). Characterisation of the transition states for protein folding: towards a new level of mechanistic detail in protein engineering analysis. *Curr. Opin. Struct. Biol.*, **11**, 94-100.

Orrú, C.D., Wilham, J.M., Raymond, L.D., Kuhn, F., Schroeder, B., Raeber, A.J. and Caughey, B. (2011). Prion disease blood test using immunoprecipitation and improved quaking-induced conversion. *MBio.*, 10,**2**(3)

Ostapchenko, V. G., Makarava, N., Savtchenko, R. and Baskakov, I. V. (2008). The polybasic N-terminal region of the prion protein controls the physical properties of both the cellular and fibrillar forms of PrP. *J. Mol. Biol.*, **383**, 1210-1224.

Osvath, S., Quynh, L.M. and Smeller, L. (2009). Thermodynamics and kinetics of the pressure unfolding of phosphoglycerate kinase. *Biochemistry*, **48**(42),10146-10150.

Ott,D., Taraborrelli,C. and Aguzzi,A. (2008). Novel dominant-negative prion protein mutants identified from a randomized library. *Protein Eng. Des. Sel.*, **21**,623–629.

Pabit, S. A. and Hagen, S. J. (2002). Laminar-flow fluid mixer for fast fluorescence kinetics studies. *Biophys. J.,* **83**, 2872-2878.

Pace, C. N. (1986). Determination and analysis of urea and guanidine hydrochloride denaturation curves. *Methods Enzymol.,* **131**, 266-280.

Pace, C. N. and Creighton, T. E. (1986). The disulfide folding pathway of ribonuclease T1. *J. Mol. Biol.,* **188**, 477-486.

Palmer, M. S., Dryden, A. J., Hughes, J. T. and Collinge, J. (1991). Homozygous prion protein genotype predisposes to sporadic Creutzfeldt-Jakob disease. *Nature*, **352**, 340-342.

Paludi, D., Thellung, S., Chiovitti, K., Corsaro, A., Villa, V., Russo, C., Ianieri, A., Bertsch, U., Kretzschmar, H. A., Aceto, A. and Florio, T. (2007). Different structural stability and toxicity of PrP(ARR) and PrP(ARQ) sheep prion protein variants. *J. Neurochem.* **103,** 2291-2300.

Pan, K. M., Baldwin, M., Nguyen, J., Gasset, M., Serban, A., Groth, D., Mehlhorn, I., Huang, Z., Fletterick, R. J., Cohen, F. E. and Prusiner, S.B. (1993). Conversion of alpha-helices into beta-sheets features in the formation of the scrapie prion proteins. *Proc. Natl. Acad. Sci. USA,* **90**, 10962-10966.

Pan, K. M., Stahl, N. and Prusiner, S. B. (1992). Purification and properties of the cellular prion protein from Syrian hamster brain. *Prot. Sci.,* **1**, 1343-1352.

Parak, F. G. (2003). Proteins in action: the physics of structural fluctuations and conformational changes. *Curr. Opin. Struct. Biol.*, **13**, 552-557.

Parton, R. G. and Richards, A. A. (2003). Lipid rafts and caveolae as portals for endocytosis: new insights and common mechanisms. *Traffic*, **4**, 724-738.

Pastore, A. and Zagari, A. (2007). A structural overview of the vertebrate prion proteins. *Prion*, **1**, 185-197.

Patel, B. K., Gavin-Smyth, J. and Liebman, S. W. (2009). The yeast global transcriptional co-repressor protein Cyc8 can propagate as a prion. *Nat. Cell Biol.,* **11**, 344-349.

Patel, B. K. and Liebman, S. W. (2007). "Prion-proof" for [PIN+]: infection with *in vitro*-made amyloid aggregates of Rnq1p-(132-405) induces [PIN+]. *J. Mol. Biol.*, **365**, 773-782.

Pattison, I.H and Jones, K.M. (1967). The possible nature of the transmissible agent of scrapie. *Vet. Rec.,* **80**, 2‑9

Paulick, M. G. and Bertozzi, C. R. (2008). The glycosylfosphatidylinositol anchor: a complex membrane-anchoring structure for proteins. *Biochemistry* **47,** 6991-7000.

Pearson, D. S., Holtermann, G., Ellison, P., Cremo, C. and Geeves, M. A. (2002). A novel pressure-jump apparatus for the microvolume analysis of protein-ligand and

protein-protein interactions: its application to nucleotide binding to skeletal-muscle and smooth-muscle myosin subfragment-1. *Biochem. J.,* **366**, 643-651.

Pearson, D.S., Swartz, D.R. and Geeves, M.A. (2008). Fast pressure jumps can perturb calcium and magnesium binding to troponin C F29W. *Biochemistry,* **47**(46),12146-12158

Pelton, J. T. and McLean, L. R. (2000). Spectroscopic methods for analysis of protein secondary structure. *Anal. Biochem.,* **277**, 167-176.

Perrett, S. and Zhou, J. M. (2002). Expanding the pressure technique: insights into protein folding from combined use of pressure and chemical denaturants. *Biochim. Biophys. Acta,* **1595**, 210-223.

Perrier, V., Kaneko, K., Safar, J., Vergara, J., Tremblay, P., DeArmond, S. J., Cohen, F. E., Prusiner, S. B. and Wallace, A. C. (2002). Dominant-negative inhibition of prion replication in transgenic mice. *Proc. Natl. Acad. Sci. U. S. A.* **99,** 13079-13084.

Perutz, M. F., Johnson, T., Suzuki, M. and Finch, J. T. (1994). Glutamine repeats as polar zippers: their possible role in inherited neurodegenerative diseases. *Proc. Natl. Acad. Sci. USA*, **91,** 5355–5358

Peterman, B. F. (1979). Measurement of the dead time of a fluorescence stoppedflow instrument. *Anal. Biochem.,* **93**, 442-444.

Pettersen, E. F., Goddard, T. D., Huang, C. C., Couch, G. S., Greenblatt, D. M., Meng, E. C. and Ferrin, T. E. (2004). UCSF Chimera - a visualization system for exploratory research and analysis. *J. Comput. Chem.,* **25**, 1605-1612.

Pinheiro, T. J. and Watts, A. (1994). Lipid specificity in the interaction of cytochrome c with anionic phospholipid bilayers revealed by solid-state 31P NMR. *Biochemistry*, **33**, 2451-2458.

Pinheiro, T. J. T., Venning, J. D. and Jackson, J. B. (2001). Fast hydride transfer in proton-translocating transhydrogenase revealed in a rapid mixing continuous flow device. *J. Biol. Chem.,* **276**, 44757-44761.

Plaxco, K. W., Simons, K. T. and Baker, D. (1998). Contact order, transition state placement and the refolding rates of single domain proteins. *J. Mol. Biol.,* **277**, 985-994.

Plaxco, K. W., Simons, K. T., Ruczinski, I. and Baker, D. (2000). Topology, stability, sequence, and length: Defining the determinants of two-state protein folding kinetics. *Biochemistry,* **39**, 11177-11183.

Pohl, T. (1990). Concentration of proteins and removal of solutes. In *Methods in Enzymology, Guide to Protein Purification*. **182**: pp 78-83. Edited by M. P. Deutscher. London: Academic Press Limited.

Premzl, M., Sangiorgio, L., Strumbo, B., Marshall Graves, J. A., Simonic, T. and Gready, J. E. (2003). Shadoo, a new protein highly conserved from fish to mammals and with similarity to prion protein. *Gene*, **314**, 89-102.

Priola, S. A. and Chesebro, B. (1995). A single hamster PrP amino acid blocks conversion to protease-resistant PrP in scrapie-infected mouse neuroblastoma cells. *J. Virol.* **69,** 7754-7758.

Privalov, P. L. (1996). Intermediate states in protein folding. *J. Mol. Biol.,* **258**, 707-725.

Promega (1996). Cloning in plasmid vectors. In *Protocols and Applications Guide*, 3rd edn, 45-46. USA: Promega Corporation.

Prusiner, S. B. (1982). Novel proteinaceous infectious particles cause scrapie. *Science,* **216**, 136-144.

Prusiner, S. B. (1997). Prion diseases and the BSE crisis. *Science,* **278**, 245-251.

Prusiner, S. B. (1998). Prions. *Proc. Natl. Acad. Sci. USA,* **95**, 13363-13383.

Prusiner, S. B., Groth, D. F., Bolton, D. C., Kent, S. B. and Hood, L. E. (1984). Purification and structural studies of a major scrapie prion protein. *Cell,* **38**, 127-134.

Prusiner, S. B., McKinley, M. P., Bowman, K. A., Bolton, D. C., Bendheim, P. E., Groth, D. F. and Glenner, G. G. (1983). Scrapie prions aggregate to form amyloid-like birefringent rods. *Cell,* **35**, 349-358.

Prusiner, S. B., McKinley, M. P., Groth, D. F., Bowman, K. A., Mock, N. I., Cochran, S. P. and Masiarz, F. R. (1981). Scrapie agent contains a hydrophobic protein. *Proc Natl Acad Sci U S A,* **78**, 6675-6679.

Prusiner, S. B., Scott, M., Foster, D., Pan, K. M., Groth, D., Mirenda, C., Torchia, M., Yang, S. L., Serban, D., Carlson, G. A., Hoppe, P. C., Westaway, D. and DeArmond, S. J. (1990). Transgenetic studies implicate interactions between homologous PrP isoforms in scrapie prion replication. *Cell,* **63**, 673-686.

Prusiner, S. B., Scott, M. R., DeArmond, S. J. and Cohen, F. E. (1998). Prion protein biology. *Cell,* **93**, 337-348.

Ptitsyn, O.B. (1973). Stages in the mechanism of self-organization of protein molecules. *Dokl. Akad. Nauk. SSSR.,* **210**(5), 1213-1215.

Ptitsyn, O. B. (1992). The molten globule state. In *Protein Folding*. pp 243-300. Edited by T. E. Creighton. New York: W.H. Freeman and Company.

Qin, K., O'Donnel, M. and Zhao, R. Y. (2006). Doppel: mores rival than double to prion. *Neuroscience,* **141**, 1-8.

Radford, S. E. (2000). Protein folding: progress made and promises ahead. *Trends Biochem. Sci.,* **25**, 611-618.

Re, F., Sesana, S., Barbiroli, A., Bonomi, F., Cazzaniga, E., Lonati, E., Bulbarelli, A. and Masserini, M. (2008). Prion protein structure is affected by pH-dependent interaction with membranes: a study in a model system. *FEBS Lett.* **582,** 215-220.

Rezaei, H., Choiset, Y., Eghiaian, F., Treguer, E., Mentre, P., Debey, P., Grosclaude, J. and Haertle, T. (2002). Amyloidogenic unfolding intermediates differentiate sheep prion protein variants. *J. Mol. Biol.* **322,** 799-814.

Rezaei, H., Marc, D., Choiset, Y., Takahashi, M., Hui Bon Hoa, G., Haertle, T., Grosclaude, J. and Debey, P. (2000). High yield purification and physico-chemical properties of full-length recombinant allelic variants of sheep prion protein linked to scrapie susceptibility. *Eur. J. Biochem.* **267,** 2833-2839.

Richt, J. A., Kasinathan, P., Hamir, A. N., Castilla, J., Sathiyaseelan, T., Vargas, F., Sathiyaseelan, J., Wu, H., Matsushita, H., Koster, J., Kato, S., Ishida, I., Soto, C., Robl, J. M. and Kuroiwa, Y. (2007). Production of cattle lacking prion protein. *Nat. Biotechnol.*, **25**, 132-138.

Rieger, R., Edenhofer, F., Lasmezas, C. I. and Weiss, S. (1997). The human 37-kDa laminin receptor precursor interacts with the prion protein in eukaryotic cells. *Nat. Med.*, **3**, 1383-1388.

Riek, R., Hornemann, S., Wider, G., Billeter, M., Glockshuber, R. and Wuthrich, K. (1996). NMR structure of the mouse prion protein domain PrP(121-321). *Nature,* **382**, 180-182.

Riek, R., Hornemann, S., Wider, G., Glockshuber, R. and Wuthrich, K. (1997). NMR characterization of the full-length recombinant murine prion protein, *m*PrP(23-231). *FEBS Lett.,* **413**, 282-288.

Riek, R., Wider, G., Billeter, M., Hornemann, S., Glockshuber, R. and Wuthrich, K. (1998). Prion protein NMR structure and familial human spongiform encephalopathies. *Proc. Natl. Acad. Sci. USA,* **95**, 11667-11672.

Ritter, C., Maddelein, M. L., Siemer, A. B., Luhrs, T., Ernst, M., Meier, B. H., Saupe, S. J. and Riek, R. (2005). Correlation of structural elements and infectivity of the HET-s prion. *Nature,* **435**, 844-848.

Robinson, P.J. The folding, misfolding and aggregation of prions. (2009). PhD Thesis. University of Warwick

Robinson, P.J. and Pinheiro T.J.T. (2009). The unfolding of the prion protein sheds light on the mechanisms of prion susceptibility and species barrier. *Biochemistry*, **48**(36), 8551-8558.

Roder, H. and Colon, W. (1997). Kinetic role of early intermediates in protein folding. *Curr. Opin. Struct. Biol.,* **7**, 15-28.

Roder, H., Maki, K. and Cheng, H. (2006). Early events in protein folding explored by rapid mixing methods. *Chem. Rev.,* **106**, 1836-1861.

Roder, H., Maki, K., Cheng, H. and Shastry, M. C. R. (2004). Rapid mixing methods for exploring the kinetics of protein folding. *Methods*, **34**, 15-27.

Royer, C. A. (2006). Probing protein folding and conformational transitions with fluorescence. *Chem. Rev.,* **106**, 1769-1784.

Royer, C. A., Mann, C. J. and Matthews, C. R. (1993). Resolution of the fluorescence equilibrium unfolding profile of trp aporepressor using single tryptophan mutants. *Prot. Sci.*, **2**, 1844-1852.

Ruoppolo, M. and Freedman, R. B. (1994). Protein-S-S-glutathione mixed disulfides as models of unfolded proteins. *Biochemistry,* **33**, 7654-7662.

Ruoppolo, M. and Freedman, R. B. (1995). Refolding by disulfide isomerization: the mixed disulfide between ribonuclease T1 and glutathione as a model refolding substrate. *Biochemistry,* **34**, 9380-9388.

Ruoppolo, M., Freedman, R. B., Pucci, P. and Marino, G. (1996). Glutathionedependent pathways of refolding of RNase T1 by oxidation and disulfide isomerization: catalysis by protein disulfide isomerase. *Biochemistry*, **35**, 13636-13646.

Saa, P., Castilla, J. and Soto, C. (2006). Ultra-efficient replication of infectious prions by automated protein misfolding cyclic amplification. *J. Biol. Chem.*, **281**, 35245-35252.

Saborio, G. P., Permanne, B. and Soto, C. (2001). Sensitive detection of pathological prion protein by cyclic amplification of protein misfolding. *Nature*, **411**, 810-813.

Sadqi, M., Lapidus, L. J. and Munoz, V. (2003). How fast is protein hydrophobic collapse? *Proc. Natl. Acad. Sci. USA,* **100**, 12117-12122.

Safar, J., Roller, P. P., Gajdusek, D. C. and Gibbs, C. J. J. (1993). Conformational transitions, dissociation, and unfolding of scrapie amyloid (prion) protein. *J. Biol. Chem.*, **268**, 20276-20284.

Safar, J., Wille, H., Itri, V., Groth, D., Serban, H., Torchia, M., Cohen, F. E. and Prusiner, S. B. (1998). Eight prion strains have PrP^{Sc} molecules with different conformations. *Nat. Med.*, **4**, 1157-1165.

Sandberg, M. K., Al-Doujaily, H., Sigurdson, C. J., Glatzel, M., O'Malley, C., Powell, C., Asante, E. A., Linehan, J. M., Brandner, S., Wadsworth, J. D., and Collinge, J. (2010). Chronic wasting disease prions are not transmissible to transgenic mice overexpressing human prion protein. *J. Gen. Virol.*, **91**, 2651–2657

Sanghera, N. (2001). PhD Thesis. University of Warwick.

Sanghera, N. and Pinheiro, T. J. (2002). Binding of prion protein to lipid membranes and implications for prion conversion. *J. Mol. Biol.*, **315**, 1241-1256.

Santoro, M. M. and Bolen, D. W. (1988). Unfolding free energy changes determined by the linear extrapolation method. 1. Unfolding of phenylmethanesulfonyl alpha-chymotrypsin using different denaturants. *Biochemistry*, **27**, 8063-8068.

Santos, T.G., Silva, I.R., Costa-Silva, B., Lepique, A.P., Martins, V.R. and Lopes, M.H. (2011). Enhanced neural progenitor/stem cells self-renewal via the interaction of stress-inducible protein 1 with the prion protein. *Stem Cells*, **29**, 1126–1136

Sarnataro, D., Caputo, A., Casanova, P., Puri, C., Paladino, S., Tivodar, S. S., Campana, V., Tacchetti, C. and Zurzolo, C. (2009). Lipid rafts and clathrin cooperate in the internalization of PrP in epithelial FRT cells. *PLoS One*, **4**, e5829.

Satoh, D., Shimizu, K., Nakamura, S. and Terada, T. (2006). Folding free-energy landscape of a 10-residue miniprotein, chignolin. *FEBS Lett.*, **580**, 3422-3426.

Schätzl, H. M., Da Costa, M., Taylor, L., Cohen, F. E. and Prusiner, S. B. (1995). Prion protein gene variation among primates. *J. Mol. Biol.*, **245**, 362-374.

Schneider, K., Fangerau, H., Michaelsen, B. and Raab, W. H. (2008). The early history of the transmissible spongiform encephalopathies exemplified by scrapie. *Brain Res. Bull.*, **77**, 343-355.

Scott, M., Foster, D., Mirenda, C., Serban, D., Coufal, F., Walchli, M., Torchia, M., Groth, D., Carlson, G., DeArmond, S. J., Westaway, D. and Prusiner, S. B. (1989). Transgenic mice expressing hamster prion protein produce species-specific scrapie infectivity and amyloid plaques. *Cell*, **59**, 847-857.

Scott, M., Groth, D., Foster, D., Torchia, M., Yang, S. L., DeArmond, S. J. and Prusiner, S. B. (1993). Propagation of prions with artificial properties in transgenic mice expressing chimeric PrP genes. *Cell*, **73**, 979-988.

Scouras, A.D. and Daggett, V. (2012). Disruption of the X-loop turn of the prion proteinlinked to scrapie resistance. *Prot. Eng, Des. Sel.,* **25**(5), 243–249

Seidel, B., Thomzig, A., Buschmann, A., Groschup, M. H., Peters, R., Beekes, M., and Terytze, K. (2007). Scrapie Agent (Strain 263K) can transmit disease via the oral route after persistence in soil over years. *PLoS ONE* **2**, e435

Shaked, G. M., Meiner, Z., Avraham, I., Taraboulos, A. and Gabizon, R. (2001). Reconstitution of prion infectivity from solubilized protease-resistant PrP and nonprotein components of prion rods. *J. Biol. Chem.* **276,** 14324-14328.

Shastry, M. C., Luck, S. D. and Roder, H. (1998). A continuous-flow capillary mixing method to monitor reactions on the microsecond time scale. *Biophys. J.*, **74**, 2714-2721.

Shtilerman, M. D., Ding, T. T. and Lansbury, P. T., Jr. (2002). Molecular crowding accelerates fibrillization of alpha-synuclein: could an increase in the cytoplasmic protein concentration induce Parkinson's disease? *Biochemistry*, **41**, 3855-3860.

Shyng, S. L., Heuser, J. E. and Harris, D. A. (1994). A glycolipid-anchored prion protein is endocytosed via clathrin-coated pits. *J. Cell Biol.*, **125**, 1239-1250.

Shyng, S. L., Huber, M. T. and Harris, D. A. (1993). A prion protein cycles between the cell surface and an endocytic compartment in cultured neuroblastoma cells. *J. Biol. Chem.*, **268**, 15922-15928.

Shyng, S. L., Moulder, K. L., Lesko, A. and Harris, D. A. (1995). The N-terminal domain of a glycolipid-anchored prion protein is essential for its endocytosis via clathrin-coated pits. *J. Biol. Chem.*, **270**, 14793-14800.

Sigurdson,C.J., Nilsson,K.P.R., Hornemann,S., Manco,G., Fernandez-Borges,N., Schwarz,P., Castilla,J., Wuthrich,K. and Aguzzi,A. (2010). A molecular switch controls interspecies prion disease transmission in mice. *J. Clin. Invest.,* **120**, 2590–2599.

Sigurdson, C. J., and Aguzzi, A. (2007). Chronic wasting disease. *Biochim. Biophys. Acta* **1772**, 610–618

Sigurdson C.J. (2008). A prion disease of cervids: Chronic wasting disease. *Vet. Res.,* **39**,41

Sigurdson, C. J., Nilsson, K. P., Hornemann, S., Heikenwalder, M., Manco, G., Schwarz, P., Ott, D., Rulicke, T., Liberski, P. P., Julius, C., Falsig, J., Stitz, L., Wuthrich, K. and Aguzzi, A. (2009). De novo generation of a transmissible spongiform encephalopathy by mouse transgenesis. *Proc. Natl. Acad. Sci. U. S. A.* **106,** 304-309.

Sim, V.L. (2012). Prion disease: chemotherapeutic strategies. *Infect. Disord. Drug. Targets.,* **12**, 144-160.

Simoneau, S., Rezaei, H., Sales, N., Kaiser-Schulz, G., Lefebvre-Roque, M., Vidal, C., Fournier, J. G., Comte, J., Wopfner, F., Grosclaude, J., Schatzl, H. and Lasmezas, C. I. (2007). *In vitro* and *in vivo* neurotoxicity of prion protein oligomers. *PLoS pathogens,* **3**, e125.

Simons, K. and Ikonen, E. (1997). Functional rafts in cell membranes. *Nature,* **387**, 569-572.

Smith, C. J., Clarke, A. R., Chia, W. N., Irons, L. I., Atkinson, T. and Holbrook, J. J. (1991). Detection and characterization of intermediates in the folding of large proteins by the use of genetically inserted tryptophan probes. *Biochemistry,* **30**, 1028-1036.

Sonnino, S. and Prinetti, A. (2009). Sphingolipids and membrane environments for caveolin. *FEBS Lett.*, **583**, 597-606.

Speare, J. O., Rush, T. S., 3rd, Bloom, M. E. and Caughey, B. (2003). The role of helix 1 aspartates and salt bridges in the stability and conversion of prion protein. *J. Biol. Chem.,* **278**, 12522-12529.

Spraker, T.R., Zink, R.R., Cummings, B.A., Wild, M.A., Miller, M.W. and O'Rourke, K.I. (2002). Comparison of histological lesions and immunohistochemical staining of proteinase-resistant prion protein in a naturally occurring spongiform encephalopathy of free-ranging mule deer (Odocoileus hemionus) with those of chronic wasting disease of captive mule deer. *Vet. Pathol.,* **39**,110–119

Sreerama, N. and Woody, R. W. (2004). Computation and analysis of protein circular dichroism spectra. *Methods Enzymol.,* **383**, 318-351.

Stahl, N., Baldwin, M. A., Teplow, D. B., Hood, L., Gibson, B. W., Burlingame, A. L. and Prusiner, S. B. (1993). Structural studies of the scrapie prion protein using mass spectrometry and amino acid sequencing. *Biochemistry*, **32**, 1991-2002.

Stahl, N., Borchelt, D. R., Hsiao, K. and Prusiner, S. B. (1987). Scrapie prion protein contains a phosphatidylinositol glycolipid. *Cell*, **51**, 229-240.

Staiano, M., Scognamiglio, V., Rossi, M., D'Auria, S., Stepanenko, O. V., Kuznetsova, I. M. and Turoverov, K. K. (2005). Unfolding and refolding of the glutamine-binding protein from *Escherichia coli* and its complex with glutamine induced by guanidine hydrochloride. *Biochemistry*, **44**, 5625-5633.

Stark, G. R. (1965). Reactions of cyanate with functional groups of proteins. IV. Inertness of aliphatic hydroxyl groups. Formation of carbamyl- and acylhydantoins. *Biochemistry*, **4**, 2363-2367.

Steele, A.D., Emsley, J.G., Ozdinler, P.H., Lindquist, S. and Macklis, J.D. (2006). Prion protein (PrPc) positively regulates neural precursor proliferation during developmental and adult mammalian neurogenesis. *Proc. Natl. Acad. Sci. U.S.A.*, **103**, 3416–3421

Steele, A. D., Lindquist, S. and Aguzzi, A. (2007). The prion protein knockout mouse: a phenotype under challenge. *Prion*, **1**, 83-93.

Stefani, M. (2004). Protein misfolding and aggregation: new examples in medicine and biology of the dark side of the protein world. *Biochim. Biophys. Acta*, **1739**, 5-25.

Stockel, J., Safar, J., Wallace, A. C., Cohen, F. E. and Prusiner, S. B. (1998). Prion protein selectively binds copper (II) ions. *Biochemistry*, **37**, 7185-7193.

Studier, F. W. and Moffatt, B. A. (1986). Use of bacteriophage T7 RNA polymerase to direct selective high-level expression of cloned genes. *J. Mol. Biol.* **189,** 113-130.

Swietnicki, W., Morillas, M., Chen, S. G., Gambetti, P. and Surewicz, W. K. (2000). Aggregation and fibrillization of the recombinant human prion protein. *Biochemistry*, **39**, 424-431.

Swietnicki, W., Petersen, R., Gambetti, P. and Surewicz, W. K. (1997). pHdependent stability and conformation of the recombinant human prion protein PrP(90-231). *J. Biol. Chem.*, **272**, 27517-27520.

Swietnicki, W., Petersen, R. B., Gambetti, P. and Surewicz, W. K. (1998). Familial mutations and the thermodynamic stability of the recombinant human prion protein. *J. Biol. Chem.*, **273**, 31048-31052.

Takahashi, S., Yeh, S. R., Das, T. K., Chan, C. K., Gottfried, D. S. and Rousseau, D. L. (1997). Folding of cytochrome c initiated by submillisecond mixing. *Nat. Struct. Biol.*, **4**, 44-50.

Tan, C., Xu, C., Wong, J., Shen, J., Sakuma, S., Yamamoto, Y., Lange, R., Balny, C. and Ruan, K. (2005). Pressure equilibrium and jump study on unfolding of 23-kDa protein from spinach photosystem II. *Biophys. J.*, **88**, 1264-1275.

Tanaka, M., Chien, P., Naber, N., Cooke. R. and Weissman. J.S. (2004). Conformational variations in an infectious protein determine prion strain differences. *Nature,* **428**, 323-328.

Taraboulos, A., Scott, M., Semenov, A., Avrahami, D., Laszlo, L. and Prusiner, S. B. (1995). Cholesterol depletion and modification of COOH-terminal targeting sequence of the prion protein inhibit formation of the scrapie isoform. *J. Cell Biol.*, **129**, 121-132.

Tattum, M. H., Cohen-Krausz, S., Khalili-Shirazi, A., Jackson, G. S., Orlova, E. V., Collinge, J., Clarke, A. R. and Saibil, H. R. (2006). Elongated oligomers assemble into mammalian PrP amyloid fibrils. *J. Mol. Biol.,* **357**, 975-985.

Tattum, M. H., Cohen-Krausz, S., Thumanu, K., Wharton, C. W., Khalili-Shirazi, A., Jackson, G. S., Orlova, E. V., Collinge, J., Clarke, A. R. and Saibil, H. R. (2006). Elongated oligomers assemble into mammalian PrP amyloid fibrils. *J. Mol. Biol.*, **357**, 975-985.

Teilum, K., Maki, K., Kragelund, B. B., Poulsen, F. M. and Roder, H. (2002). Early kinetic intermediate in the folding of acyl-CoA binding protein detected by fluorescence labeling and ultrarapid mixing. *Proc. Natl. Acad. Sci. USA,* **99**, 9807-9812.

Telling, G. C., Parchi, P., DeArmond, S. J., Cortelli, P., Montagna, P., Gabizon, R., Mastrianni, J., Lugaresi, E., Gambetti, P. and Prusiner, S. B. (1996). Evidence for the conformation of the pathologic isoform of the prion protein enciphering and propagating prion diversity. *Science*, **274**, 2079-2082.

Telling, G. C., Scott, M., Mastrianni, J., Gabizon, R., Torchia, M., Cohen, F. E., DeArmond, S. J. and Prusiner, S. B. (1995). Prion propagation in mice expressing human and chimeric PrP transgenes implicates the interaction of cellular PrP with another protein. *Cell*, **83**, 79-90.

Tew, D. J. and Bottomley, S. P. (2001). Probing the equilibrium denaturation of the serpin [alpha]1-antitrypsin with single tryptophan mutants; evidence for structure in the urea unfolded state. *J. Mol. Biol.*, **313**, 1161-1169.

Tobler, I., Gaus, S. E., Deboer, T., Achermann, P., Fischer, M., Rulicke, T., Moser, M., Oesch, B., McBride, P. A. and Manson, J. C. (1996). Altered circadian activity rhythms and sleep in mice devoid of prion protein. *Nature,* **380**, 639-642.

Torrent, J., Alvarez-Martinez, M. T., Heitz, F., Liautard, J. P., Balny, C. and Lange, R. (2003). Alternative prion structural changes revealed by high pressure. *Biochemistry,* **42**, 1318-1325.

Torrent, J., Font, J., Herberhold, H., Marchal, S., Ribo, M., Ruan, K.-C., Winter, R., Vilanova, M. and Lange, R. (2006). The use of pressure-jump relaxation kinetics to study protein folding landscapes. *Biochim. Biophys. Acta,* **1764**, 489-496.

Tokuriki, N., Kinjo, M., Negi, S., Hoshino, M., Goto, Y., Urabe, I. and Yomo, T. (2004). Protein folding by the effects of macromolecular crowding. *Protein Sci.*, **13**, 125-133.

Tu, B. P. and Weissman, J. S. (2004). Oxidative protein folding in eukaryotes: mechanisms and consequences. *J. Cell Biol.,* **164**, 341-346.

Turk, E., Teplow, D., Hood, L. and Prusiner, S. (1988). Purification and properties of the cellular and scrapie hamster prion proteins. *Eur. J. Biochem.*, **176**, 21-30.

Unterberger, U., Voigtlander, T. and Budka, H. (2005). Pathogenesis of prion diseases. *Acta Neuropathol. (Berl),* **109**, 32-48.

Uversky, V. N. and Fink, A. L. (2002). The chicken-egg scenario of protein folding revisted. *FEBS Lett.,* **515**, 79-83.

Uversky, V. N. and Fink, A. L. (2004). Conformational constraints for amyloid fibrillation: the importance of being unfolded. *Biochim. Biophys. Acta*, **1698**, 131-153.

van den Berg, B., Chung, E. W., Robinson, C. V., Mateo, P. L. and Dobson, C. M. (1999a). The oxidative refolding of hen lysozyme and its catalysis by protein disulfide isomerase. *EMBO J.,* **18**, 4794-4803.

van den Berg, B., Ellis, R. J. and Dobson, C. M. (1999b). Effects of macromolecular crowding on protein folding and aggregation. *EMBO J.,* **18**, 6927-6933.

van den Berg, B., Wain, R., Dobson, C. M. and Ellis, R. J. (2000). Macromolecular crowding perturbs protein refolding kinetics: implications for folding inside the cell. *EMBO J.,* **19**, 3870-3875.

van der Kamp, M. W. and Daggett, V. (2009). The consequences of pathogenic mutations to the human prion protein. *Protein. Eng. Des. Sel.* **22,** 461-468.

Vanik, D. L. and Surewicz, W. K. (2002). Disease-associated F198S mutation increases the propensity of the recombinant prion protein for conformational conversion to scrapie-like form. *J. Biol. Chem.,* **277**, 49065-49070.

Vidugiris, G. J. A., Markley, J. L. and Royer, C. A. (1995). Evidence for a molten globule-like transition state in protein folding from determination of activation volumes. *Biochemistry*, **34**, 4909-4912.

Vidugiris, G. J. A., Truckses, D. M., Markley, J. L. and Royer, C. A. (1996). High-pressure denaturation of staphylococcal nuclease proline-to-glycine substitution mutants. *Biochemistry,* **35**, 3857-3864.

Viles, J. H., Cohen, F. E., Prusiner, S. B., Goodin, D. B., Wright, P. E. and Dyson, H. J. (1999). Copper binding to the prion protein: structural implications of four identical cooperative binding sites. *Proc. Natl. Acad. Sci. USA*, **96**, 2042-2047.

Vorberg, I., Chan, K. and Priola, S. A. (2001). Deletion of β -strand and α -helix secondary structure in normal prion protein inhibits formation of its proteaseresistant isoform. *J. Virol.*, **75**, 10024-10032.

Walmsley, A. R., Zeng, F. and Hooper, N. M. (2003). The N-terminal region of the prion protein ectodomain contains a lipid raft targeting determinant. *J. Biol. Chem.*, **278**, 37241-37248.

Wang, C. C. and Tsou, C. L. (1993). Protein disulfide isomerase is both and enzyme and a chaperone. *FASEB,* **7**, 1515-1517.

Wang, W., Xu, Q., Shan, Y. and Xu, G. (2001). Probing local conformational changes during equilibrium unfolding of firefly luciferase: Fluorescence and circular dichroism studies of single tryptophan mutants. *Biochem. Biophys. Res. Commun.*, **282**, 28-33.

Wedemeyer, W. J., Welker, E., Narayan, M. and Scheraga, H. A. (2000). Disulfide bonds and protein folding. *Biochemistry,* **39**, 4207-4216.

Weissmann, C. (2004). The state of the prion. *Nature Rev. Microbiol.,* **2**(11), 861-871.

Weissmann, C. and Aguzzi, A. (1997). Bovine spongiform encephalopathy and early onset variant Creutzfeldt-Jakob disease. *Curr. Opin. Neurobiol.*, **7**, 695-700.

Weissmann, C. and Aguzzi, A. (2005). Approaches to therapy of prion diseases. *Annu. Rev. Med.,* **56**, 321-344.

Westaway, D., Zuliani, V., Cooper, C. M., Da Costa, M., Neuman, S., Jenny, A. L., Detwiler, L. and Prusiner, S. B. (1994). Homozygosity for prion protein alleles encoding glutamine-171 renders sheep susceptible to natural scrapie. *Genes Dev.* **8,** 959-969.

Wetlaufer, D. B. (1973). Nucleation, rapid folding, and globular intrachain regions in proteins. *Proc. Natl. Acad. Sci. USA,* **70**, 697-701.

Wickner, R. B., Edskes, H. K., Roberts, B. T., Baxa, U., Pierce, M. M., Ross, E. D. and Brachmann, A. (2004). Prions: proteins as genes and infectious entities. *Genes Dev.*, **18**, 470-485.

Wickner, R. B., Edskes, H. K., Shewmaker, F. and Nakayashiki, T. (2007). Prions of fungi: inherited structures and biological roles. *Nat. Rev. Micro.*, **5**, 611-618.

Wildegger, G., Liemann, S. and Glockshuber, R. (1999). Extremely rapid folding of the C-terminal domain of the prion protein without kinetic intermediates. *Nat. Struct. Biol.,* **6**, 550-553.

Wilkinson, B. and Gilbert, H. F. (2004). Protein disulfide isomerase. *Biochim. Biophys. Acta,* **1699**, 35-44.

Will, R. G., Ironside, J. W., Zeidler, M., Cousens, S. N., Estibeiro, K., Alperovitch, A., Poser, S., Pocchiari, M., Hofman, A. and Smith, P. G. (1996). A new variant of Creutzfeldt-Jakob disease in the UK. *Lancet,* **347**, 921-925.

Wille, H., Michelitsch, M. D., Guenebaut, V., Supattapone, S., Serban, A., Cohen, F. E., Agard, D. A. and Prusiner, S. B. (2002). Structural studies of the scrapie prion protein by electron crystallography. *Proc. Natl. Acad. Sci. USA,* **99**, 3563-3568.

Williams, E. S., and Miller, M. W. (2003). Transmissible spongiform encephalopathies in non-domestic animals: origin, transmission and risk factors. *Rev. Sci. Tech. (International Office of Epizootics),* **22,** 145–156

Williams, E. S. and Young, S. (1980). Chronic wasting disease of captive mule deer: a spongiform encephalopathy. *J. Wildl. Dis.*, **16**, 89-98.

Winklhofer, K. F., Heske, J., Heller, U., Reintjes, A., Muranyi, W., Moarefi, I. and Tatzelt, J. (2003). Determinants of the *in vivo* folding of the prion protein. A bipartite function of helix 1 in folding and aggregation. *J. Biol. Chem.*, **278**, 14961-14970.

Wong, B. S., Liu, T., Li, R., Pan, T., Petersen, R. B., Smith, M. A., Gambetti, P., Perry, G., Manson, J. C., Brown, D. R. and Sy, M. S. (2001). Increased levels of oxidative stress markers detected in the brains of mice devoid of prion protein. *J. Neurochem.*, **76**, 565-572.

Wood, S. J., Wypych, J., Steavenson, S., Louis, J. C., Citron, M. and Biere, A. L. (1999). alpha-synuclein fibrillogenesis is nucleation- dependent. Implications for the pathogenesis of Parkinson's disease. *J. Biol. Chem.*, **274**, 19509–19512

Wopfner, F., Weidenhöfer, G., Schneider, R., von Brunn, A., Gilch, S., Schwarz, T. F., Werner, T. and Schätzl, H. M. (1999). Analysis of 27 mammalian and avian PrPs reveals high conservation of flexible regions of the prion protein. *J. Mol. Biol.*, **289**, 1163-1178.

Woycechowsky, K. J. and Raines, R. T. (2000). Native disulfide bond formation in proteins. *Curr. Opin. Chem. Biol.*, **4**, 533-539.

Wuthrich, K. and Riek, R. (2001). Three-dimensional structures of prion proteins. *Adv. Prot. Chem.*, **57**, 55-82.

Zahn, R., Liu, A. Z., Luhrs, T., Riek, R., von Schroetter, C., Garcia, F. L., Billeter, M., Calzolai, L., Wider, G. and Wuthrich, K. (2000). NMR solution structure of the human prion protein. *Proc. Natl. Acad. Sci. USA,* **97**, 145-150.

Zahn, R., von Schroetter, C. and Wuthrich, K. (1997). Human prion proteins expressed in *Escherichia coli* and purified by high-affinity column refolding. *FEBS Lett.*, **417**, 400-404.

Zahn, R., Liu, A., Luhrs, T., Riek, R., von Schroetter, C., Lopez Garcia, F., Billeter, M., Calzolai, L., Wider, G. and Wuthrich, K. (2000). NMR solution structure of the human prion protein. *Proc. Natl. Acad. Sci. U. S. A.* **97,** 145-150.

Zhang, C.C., Steele A.D., Lindquist S. and Lodish H.F. (2006) Prion protein is expressed on long-term repopulating hematopoietic stem cells and is important for their self-renewal. *Proc. Natl. Acad. Sci. U. S. A.* **103**(7), 2184-2189.

Zhang, H., Stockel, J., Mehlhorn, I., Groth, D., Baldwin, M. A., Prusiner, S. B., James, T. L. and Cohen, F. E. (1997). Physical studies of conformational plasticity in a recombinant prion protein. *Biochemistry,* **36**, 3543-3553.

Zhao, H., Tuominen, E. K. and Kinnunen, P. K. (2004). Formation of amyloid fibers triggered by phosphatidylserine-containing membranes. *Biochemistry*, **43**, 10302-10307.

Zhu, M., Souillac, P. O., Ionescu-Zanetti, C., Carter, S. A. and Fink, A. L. (2002). Surface-catalyzed amyloid fibril formation. *J. Biol. Chem.*, **277**, 50914-50922.

Zimmerman, S. B. and Trach, S. O. (1991). Estimation of macromolecule concentrations and excluded volume effects for the cytoplasm of *Escherichia coli*. *J. Mol. Biol.*, **222**, 599-620.

Zou, W. Q. and Cashman, N. R. (2002). Acidic pH and detergents enhance *in vitro* conversion of human brain PrPC to a PrPSc-like form. *J. Biol. Chem.*, **277**, 43942-43947.

Zwanzig, R., Szabo, A. and Bagchi, B. (1992). Levinthal's paradox. *Proc. Natl. Acad. Sci. USA*, **89**, 20-22.